



City Research Online

City, University of London Institutional Repository

Citation: Witzke, V. (2017). Shear instabilities in stellar objects: linear stability and non-linear evolution. (Unpublished Doctoral thesis, City, University of London)

This is the accepted version of the paper.

This version of the publication may differ from the final published version.

Permanent repository link: <https://openaccess.city.ac.uk/id/eprint/18239/>

Link to published version:

Copyright: City Research Online aims to make research outputs of City, University of London available to a wider audience. Copyright and Moral Rights remain with the author(s) and/or copyright holders. URLs from City Research Online may be freely distributed and linked to.

Reuse: Copies of full items can be used for personal research or study, educational, or not-for-profit purposes without prior permission or charge. Provided that the authors, title and full bibliographic details are credited, a hyperlink and/or URL is given for the original metadata page and the content is not changed in any way.

Shear Instabilities in Stellar Objects

Linear Stability and Non-Linear Evolution

Author: Veronika Witzke

Submitted in accordance with the requirements for the degree of
Doctor of Philosophy



City, University of London
Department of Mathematics

London, August 2017

Contents

List of Figures	v
List of Tables	xi
Acknowledgments	xiii
Declaration	xiv
Abstract	xv
1. Introduction	1
2. Model	10
2.1. Stellar Properties	10
2.2. Hydrodynamics	14
2.2.1. Non-dimensional Governing Equations	15
2.2.2. Boundary Conditions and Background State	17
2.2.3. Important Approximations	18
2.3. Magnetohydrodynamics	20
2.3.1. Non-dimensional MHD Equations	23
2.3.2. Boundary Conditions and Background State	23
2.4. Numerical Methods	24
2.4.1. Non-linear DNS Calculations	24
3. Pure Hydrodynamic Shear Flow Instabilities	33
3.1. Shear Flow Instabilities	34
3.1.1. Concept of Stability	34
3.1.2. Important Theorem's	36
3.1.3. Shear Flow Instabilities in Stratified Systems	38

3.2. Considering Complex Shear Flows	41
3.2.1. Shear Flow Profile	42
3.2.2. Linear Stability Analysis	44
3.3. Results	50
3.3.1. The Effect of Varying the Mach Number on the Instability Threshold	50
3.3.2. Small Péclet Number Regime	55
3.3.3. Effect of the Distance to the Onset of Convection on the In- stability	60
3.3.4. Subdominant Shear Instability	61
3.4. Conclusions	63
4. Non-linear Calculations:	
Forcing Methods Part I	65
4.1. Forcing methods	66
4.2. Exponential Growth Regime	69
4.3. Results	72
4.4. Conclusion	79
5. Non-linear Evolution:	
Forcing Methods Part II	80
5.1. Theoretical Framework for Energy Budgets	81
5.2. Results for the Non-linear Phase	84
5.2.1. Visualisation	85
5.2.2. Horizontally averaged profiles	90
5.2.3. Energy Budgets from Numerical Calculations	93
5.2.4. Comparing Total Viscous Dissipation and External Work . . .	99
5.3. Discussion and Conclusion	101
6. Non-linear Evolution of the Saturated Phase	104
6.1. Investigating the Effective Richardson Number	105
6.1.1. Setup	105
6.1.2. Results	106

6.2. Investigations of the Saturated Regime	110
6.2.1. Results: The Effect of Key Parameters on the Non-Linear Evolution	111
6.2.2. Three-Dimensional Long Time Evolution	126
6.3. Diffusive Instability	128
6.4. Discussion	134
7. Shear-Driven Kinematic Dynamo	137
7.1. Magnetic Field Generation	138
7.1.1. Magnetohydrodynamic Dynamos	139
7.1.2. Solar Dynamo Models	142
7.1.3. Different Stars	145
7.2. Setting up a Kinematic Dynamo	147
7.3. Seeking Dynamo Action: Preliminary Results	149
7.4. Small-scale Dynamo Action	154
7.5. Summary and Future Work.	158
8. Discussions and Conclusions	160
A. Derivation of Linearised Equations	166
A.1. Zero order equations	166
A.2. First Order Equations	168
B. Useful Vector Identities	174
B.1. Vector Identities I	174
B.2. Vector identities II	175
B.3. Vector identities III	175
C. Energy Budgets Detailed Calculations	176
D. Parallel Sorting	181
Bibliography	184

List of Figures

1.1. The Hertzsprung-Russell diagram. Courtesy of NASA/CXC/SAO (2015).	2
1.2. Sun's structure. Illustration of stellar layers and phenomena occurring in the upper atmosphere. Taken from Kelvinsong (2012).	3
1.3. On the left side: Solar granulation. Courtesy of JAXA/NASA/P-PARC (2010). On the right side: Solar flare. Courtesy of NASA/SDO (2016).	4
2.1. Illustration of the local domain used for the model in correlation to the solar region that is subject to investigations.	16
2.2. Example background density and temperature profiles. a) Temperature profiles for different θ , that were used. b) Density profiles for $\theta = 2$ but three different polytropic indices m . For these indices m the atmosphere is stably stratified.	18
3.1. The velocity profiles considered by Reynolds (1883). (a) Velocity profile without an inflection point. (b) Velocity profile with an inflection point.	36
3.2. Simple systems for a KH instability. (a) An interface with different density and velocity at the top layer and bottom layer is shown. (b) A three layered system, where the middle layer has a continuously changing velocity and density ρ_1 . The top layer has a constant velocity U_1 with a lower density and the bottom layer has a constant velocity U_2	39

3.3. Example background shear flow profiles for three different L_u . Shear flow profiles with very small and very large characteristic length L_u for comparison.	43
3.4. Critical Richardson number in a viscous fluid with $\mu = 10^{-6}$ for different Mach numbers, M . The corresponding wave numbers k_{max} of the most unstable mode at the onset of instability are plotted, and the wave number is normalised by the inverse of the characteristic length $1/L_u$. The horizontal line in both plots corresponds to $Ri = 0.25$. (a) Weakly stratified atmosphere with $\theta = 2$. (b) Strongly stratified atmosphere, $\theta = 10$	52
3.5. Eigenfunctions for a fixed $M = 0.1$ and a fixed characteristic length-scale $L_u = 0.05$ are found for two different θ , where $\theta = 10$ for top plots a, b, c and $\theta = 2$ for the plots d, e, f. In both cases the eigenfunctions for δw , δT and $\delta \rho$ for the most unstable mode are shown.	54
3.6. Both plots show the growth rates ζ in a weakly thermally stratified atmosphere with $\theta = 0.5$ for a Richardson number of $Ri = 0.22$. (a) the fluid is compressible with $M = 0.09$. (b) $M = 0.009$, which corresponds to a incompressible fluid. The Péclet number is varied among three orders of magnitude.	56
3.7. Plots of critical Richardson numbers for all k in a viscous fluid with a Mach number, $M = 0.009$, a) $\theta = 0.5$ and b) $\theta = 2.0$ and viscosity $\nu = 1 \times 10^{-7}$. The Péclet number is varied from 10 to 0.01.	59
3.8. Growth rate of the instability for a viscous fluid with $\theta = 2.0$ and a Mach number of order 10^{-2} . In (a) and (c) the Péclet number is $Pe = 1$. In (b) and (d) $Pe = 0.1$. Ri is varied in (a) and (b), but $Ri = 0.22$ for the top plots (c) and (d).	60
3.9. Characteristics of instabilities for a viscous fluid with $\theta = 1.0$, Péclet number of order 10^3 and $Ri = 0.3$. (a) Growth rates. (b) Eigenfunction found for the vertical velocity w in the small arch. (c) Eigenfunction for the vertical velocity w in the large arch.	62

4.1.	Vertical velocity perturbations for different forcing methods just at the end of the exponential growth regime. (a) The viscous method. (b) The averaged relaxation method with $\tau_0 = 10$. (c) The averaged relaxation method with $\tau_0 = 0.1$. (d) The local relaxation method with $\tau_0 = 10$ and in (e) with $\tau_0 = 0.1$	75
4.2.	The time evolution of the volume averaged vertical velocity, as defined in Equation (4.10), for the two-dimensional calculations for case I in (a) and for case II in (b). Different τ_0 parameters for the relaxation method are used and compared to the viscous method and unforced calculations. The vertical velocity is displayed in logarithmic scale and t is given sound-crossing time.	76
4.3.	The time evolution of the volume averaged vertical velocity for case I with the local relaxation method. (a) Cases with $\tau_0 \leq 1$. (b) Cases with $\tau_0 > 1$. The vertical velocity is displayed in logarithmic scale and t is given sound-crossing time.	78
5.1.	The time evolution of the volume averaged vertical velocity, similar to the definition in Equation (4.10) but for three-dimensional calculations. Different τ_0 parameters for the relaxation method are used and compared to the viscous method. The vertical velocity is displayed in logarithmic scale and t is given sound-crossing time.	85
5.2.	The vorticity component perpendicular to the x - z -plane for different forcing methods at two different stages during the time evolution. The plots at the top (a) and (b) show snapshots of two different times for the viscous method, where (a) is at $\tilde{t} = 7.2$ and (b) at $\tilde{t} = 40$. The middle row (c) and (d) show the relaxation method with $\tau_0 = 10$ at $\tilde{t} = 6.8$ and $\tilde{t} = 40$, respectively. In (e) and (f) the relaxation method with $\tau_0 = 0.1$ was used, where $\tilde{t} = 12.3$ in (e) and $\tilde{t} = 38$ in (f).	86
5.3.	The vertical velocity component, w , for different forcing methods after saturation. (a) Viscous method at $\tilde{t} \approx 40$. (b) Averaged relaxation method with $\tau_0 = 10$ at $\tilde{t} \approx 40$. (c) Averaged relaxation method with $\tau_0 = 0.1$ at $\tilde{t} \approx 38$	89

5.4. Turbulent Reynolds number and length-scales for three different forcing methods. (a) Re_t , as defined in Equation (5.12). (b) Turbulent length-scales, l_t . The red line indicates the horizontal extent of the domain.	91
5.5. The horizontally averaged u_x profiles at $t \approx 60$ are shown for different forcing methods.	92
5.6. The total kinetic energy, internal energy and the gravitational potential energy evolution for the viscous forcing and relaxation method by using two different τ_0 . All energies are normalised by the initial total amount of the system's energy $E_{tot}(t = 0) = 195.81$. (a) $E_{kin}(t)/E_{tot}(t = 0)$ with time. (b) $I(t)/E_{tot}(t = 0)$. (c) $E_{pot}/E_{tot}(t = 0)$	95
5.7. The available gravitational potential energy $E_{avail}(t)/E_{tot}(t = 0)$ evolution for both the viscous forcing and relaxation methods by using two different τ_0	98
5.8. Time evolution of the viscous dissipation rate of momentum, ε , and the work done by the forcing, W . (a) Viscous forcing. (b) Relaxation method with $\tau_0 = 10$. (c) Relaxation method with $\tau_0 = 1.0$	100
6.1. Density deviation from the initial background density profile, $\bar{\delta\rho}$. (a) The profiles at $\tilde{t} \approx 60$ for case I and different relaxation times. (b) Case II is displayed at $\tilde{t} \approx 250$	107
6.2. The minimal effective Richardson number obtained from the horizontally averaged profiles as in Equation (6.1) with time. (a) Case I using two different relaxations times τ_0 . (b) Case II with three different relaxation times τ_0 . The red line indicates the 1/4 stability threshold.	109
6.3. Volume averaged vertical velocity evolution for cases A to C. (a) The exponential growth regime. (b) The long-time evolution.	114

6.4. Total vorticity in the x - z -plane for case A to C (see Table 6.2). The left column show cases A to C during saturation at approximately $\tilde{t} \approx 93$. (a) Case A. (c) Case B. (e) Case C. The right column show the same cases during the quasi-steady state at different times (for reference see Fig. 6.3). The dotted lines indicate the extent of the turbulent region of the saturated state as obtained from Equation (4.13). 116

6.5. The horizontally averaged and time averaged \bar{u}_x profiles are shown for cases A to H and O to U. In (a) the $\bar{u}_x(z)$ is displayed for cases A to C in (b) the $\bar{u}_x(z)$ for cases D to H are shown. 117

6.6. The total vorticity component perpendicular to the x - z -plane shortly after saturation. Dotted lines indicate L_{eff} . (a) case D. (b) case F. (c) case H where the red lines indicate the lower bound of the error for L_{eff} 120

6.7. The temperature fluctuations around the initial temperature profile shortly after saturation. (a) Case D. (b) Case F. (c) Case H. Note, the scale in (c) is of one order of magnitude greater, such that small scale disturbances at the middle are not visible. 121

6.8. The total vorticity component perpendicular to the x - z -plane. (a) case 3D-II at roughly $\tilde{t} \approx 200$. (b) case 3D-I at roughly $\tilde{t} \approx 120$ 127

6.9. The $\bar{u}_x(z)$ for the diffusive instability cases. 131

6.10. The vorticity component perpendicular to the x - z -plane, the vertical velocity w , and temperature fluctuations around the initial temperature profile for case Q long after saturation. (a) Vorticity. (b) Vertical velocity. (c) Temperature fluctuations. 132

7.1. A sketch of the scenario for potential tachocline dynamos, where the stages are explained in the text. Taken from Priest (2014). 143

7.2. Schematic illustration of the structure in different main-sequence stars. (a) Fully convective, low mass stars. (b) Solar-like stars with a deep convection zone. (c) Stars with two convection zones. (d) Massive stars with inner convection zones. 146

7.3. Magnetic energy with time together with and exponential curve fit.
a) Case 2a and case 2b, which have low Prandtl numbers. b) The two
large Prandtl number cases 2c and 2d. 151

7.4. Turbulent Reynolds numbers and typical length-scales with depth.
The vales are horizontally and time averaged during the saturated
regime for all three cases and different forcing methods. (a) $Re_t(z)$.
(b) $l_t(z)$ 152

7.5. Magnetic energy evolution for case 3b and case 3c. 153

7.6. Time averaged relative helicity, $\mathcal{H}(z)$, as defined in Equation (7.9)
for all cases. a) Helicity obtained for case 1 and for all three different
forcing methods is shown. b) Helicity for case 2 to case 4 is displayed. 154

7.7. Magnetic energy density evolution with time for large magnetic
Prandtl numbers of case 4. a) Case 4d with $\sigma_m = 10$. b) Case
4e. c) Case 4f. 155

7.8. Time evolution of B_{mean} for the cases 4d and 4e with time. 157

7.9. Time evolution of the horizontal magnetic field components $\langle B_x \rangle$ and
 $\langle B_y \rangle$ for the cases 4d and 4e with time. 157

7.10. $\Gamma(z)$ as a function of depth and time for case 4e. 158

D.1. Illustration of a sorting procedure for an array, which is distributed
on several cores. In this example z indicates the vertical coordinate. . 181

List of Tables

4.1. Comparing the linear eigenvalue-solver results with those from non-linear calculations during the linear phase. For case I the shear amplitude is $U_0 = 0.08$ and $1/L_u = 118$ such that $Ri = 8 \times 10^{-4}$. Taking $C_k = 8 \times 10^{-5}$ results in a $Pe \approx 8$. For case II $U_0 = 0.041$, $1/L_u = 20$ and $C_k = 1 \times 10^{-4}$ such that $Ri = 0.1$ and $Pe \approx 20$	71
5.1. Time intervals of the different dynamical stages.	93
6.1. Parameters for the investigated cases, where the resolution of the domain is given by N_x , N_y and N_z . The dynamical viscosity is $C_k\sigma$, where C_k is the thermal diffusivity and σ the Prandtl number. The temperature gradient is denoted as θ and the polytropic index is m . For the initial shear flow the shear amplitude is U_0 and the shear width is controlled by L_u	106
6.2. Comparing typical length-scales, turbulent Reynolds numbers and effective shear width L_{eff} for different transport coefficients. For cases A to H the initial Ri number is fixed to be 0.006, where $\theta = 1.9$, the polytropic index is $m = 1.6$, the shear amplitude $U_0 = 0.095$, and the shear width is $L_u = 0.016$. The effective shear width is calculated after saturation and \bar{Re}_t , \bar{Pe}_t , and \bar{l}_w are averaged in the turbulent region, which depends on the effective L_{eff} , and over a sufficiently long time interval.	112

6.3. For all cases $L_u = 0.016$ and $\sigma C_k = 1.0 \times 10^{-4}$. For cases I to K the temperature gradient is varied from $\theta = 0.85$ to $\theta = 6.5$. For cases L to N the Péclet number is varied, but $Ri = 0.006$. The effective shear width L_{eff} is calculated as described in Section 4.3. All turbulent quantities are averaged in time and over the turbulent region indicated by L_{eff} 113

6.4. For the diffusive instability cases O to U the temperature gradient, $\theta = 2.0$, and the polytropic index, $m = 3.0$, are fixed, but the initial Ri number changes from 0.4 for cases O to Q to 1.0 for case U. The effective shear width is calculated after saturation and \bar{Re}_t , \bar{Pe}_t , and \bar{l}_w are averaged in the region of the turbulence, depending on the effective L_{eff} 130

7.1. The values of various parameters for all cases considered together with the decay rates for each. For all cases the polytropic index is set to $m = 1.6$ and the dynamic viscosity $\mu = 5 \times 10^{-4}$. In part 1 calculations that were used in Chapter 5 with different forcing methods are studied. Part 2 shows low and moderate Péclet number cases used in Chapter 6. In part 3 a new case is set up. 150

Acknowledgements

The last years, during which I worked on my PhD research project, brought many positive changes to my life and I am very grateful for that. This would not have been possible without many people all over the world, their support, motivation and inspiration.

First and foremost I want to express my sincere gratitude to my supervisor Dr Lara Silvers. I appreciate all her contributions of time, ideas, and funding to make my PhD experience productive and stimulating. Her enthusiasm for research is contagious and motivated me, even during tough times in my PhD. I am also thankful for the excellent example she has provided as a successful woman in mathematics.

I would like to gratefully and sincerely thank Dr Benjamin Favier, who has been a truly dedicated mentor and collaborator, for his tremendous academic support and fruitful discussions. This research project would not have been possible without his permanent guidance and support.

I would also like to take this opportunity to thank my viva examiners Dr Oliver Kerr and Professor Steve Tobias for helpful comments and suggestions.

Very special thanks to all colleagues in the Department of Mathematics for their advice, collaborations and creating a pleasant working atmosphere. Additionally, I am very thankful for the friendship of all other PhD students in our office. Especially, I am indebted to Niamh and Laura for numerous discussions during our lunch breaks and their support.

Finally, and most importantly I would like to thank my family and my friends for all their love and encouragement. I thank my parents for their faith in me and for allowing me to pursue my dreams by means of moral and financial support. Special thanks to my best friends Mary and Javier, who are always there for me and support and encourage me.

Declaration

The candidate confirms that the work submitted is her own and that appropriate credit has been given where reference has been made to the work of others. The contents of this dissertation are original and have not been submitted in whole or in part for consideration for any other degree or qualification in this, or any other University. The candidate hereby declare that the University Librarian of City, University of London has the power to allow this thesis to be copied in whole or in part. This permission covers only single copies made for study purposes, subject to proper acknowledgement.

Abstract

Shear flows have a significant impact on the dynamics in various astrophysical objects, including accretion discs and stellar interiors. Due to observational limitations the complex dynamics in stellar interiors that result in turbulent motions, mixing processes, and magnetic field generation, are not entirely understood. It is therefore necessary to investigate the inevitable small-scale dynamics via numerical calculations. In particular a thin region with strong shear at the base of the convection zone in the Sun, the tachocline, is believed to play an important role in the Sun's interior dynamics and magnetic field generation. Velocity measurements suggest a stable tachocline. However, helioseismology can only provide large-scale time-averaged measurements, so small-scale turbulent motions can still be present. Therefore, studying the stability of shear flows and their non-linear evolution in a fully compressible polytropic atmosphere provides a fundamental understanding of potential motion in stellar interiors and is the main focus of this thesis.

To commence the investigations a linear stability analysis of a stratified system in a two-dimensional Cartesian geometry is performed to study the effect of compressibility and thermal diffusivity on the stability threshold. In addition, this first investigation provides a reference for subsequent non-linear calculations. Focusing on a local model of unstable shear flows, direct numerical calculations are used to first compare numerical forcing methods to sustain a shear flow against viscous dissipation; and then to study the effect of key parameters on the saturated quasi-steady regime. Finally, magnetic fields are included and the full set of MHD equations is solved to study a potential kinematic dynamo in shear-driven turbulence.

1. Introduction

The aspiration of mankind to understand nature has given rise to many scientific areas. One of them, astrophysics, is the study of celestial objects, such as planets, stars, and galaxies. A specific characteristic of astrophysics research is the method by which we obtain information on the object of interest: Since astrophysical objects are distant, the only way to measure their properties is to observe and investigate all types of radiation they emit. Therefore, detailed observations are difficult, even for our Sun (see Hansen and Kawaler, 1999a, and references therein). To enhance our understanding of these objects it is imperative to use analytical and numerical techniques in addition to observations. Using mathematical models requires appropriate assumptions to simplify the system in order to shed light on particular aspects. Therefore, numerical results have to be compared with available observations in order to be verified and to improve the current models. Before moving on to discuss numerical modelling in detail, it is crucial to gain a general picture of astrophysical objects.

Stars

Due to their fascinating appearance in the night sky, stars have been in the spotlight of research throughout history. When observing stars by the unaided eye, the first discovery is their different brightness levels. There are several reasons why some stars are brighter than others: The obvious reason is the distance between a particular star and the observer, as the flux density of the emitted radiation decreases with the inverse of the distance squared (Karttunen et al., 2007). However, a bright star far away might appear as bright as a dim star that is closer to the observer. Therefore, the absolute brightness of stars, called the absolute magnitude, is defined as the apparent magnitude at a distance of 10 parsecs (Karttunen et al., 2007) from the

star. Another quantity is the luminosity of a star, which is the total flux emitted. The luminosity remains constant with distance per definition, and so it is an intrinsic quantity of a star (Karttunen et al., 2007).

Taking a closer look reveals that stars have different colours, where one possible system of classification is made by distinguishing three colours. Here filters are used to obtain the magnitude of a star in the colours ranging from ultraviolet (U) to blue (B) and to visual (V). Depending on the difference of magnitude between U to B and B to V, stars are categorised into different spectral types (Karttunen et al., 2007). The spectral types range from very hot stars of type O over B, A, F, G and K to the coolest stars of type M. For example, yellow and red stars belong to the spectral types G-K-M. Our Sun is a G type star with the full classification, G2 V (Karttunen et al., 2007).

In the early 19th century a study of the relationship between the absolute magnitude of a star and its spectral type led to the well known Hertzsprung-Russell diagram (see Fig. 1.1).

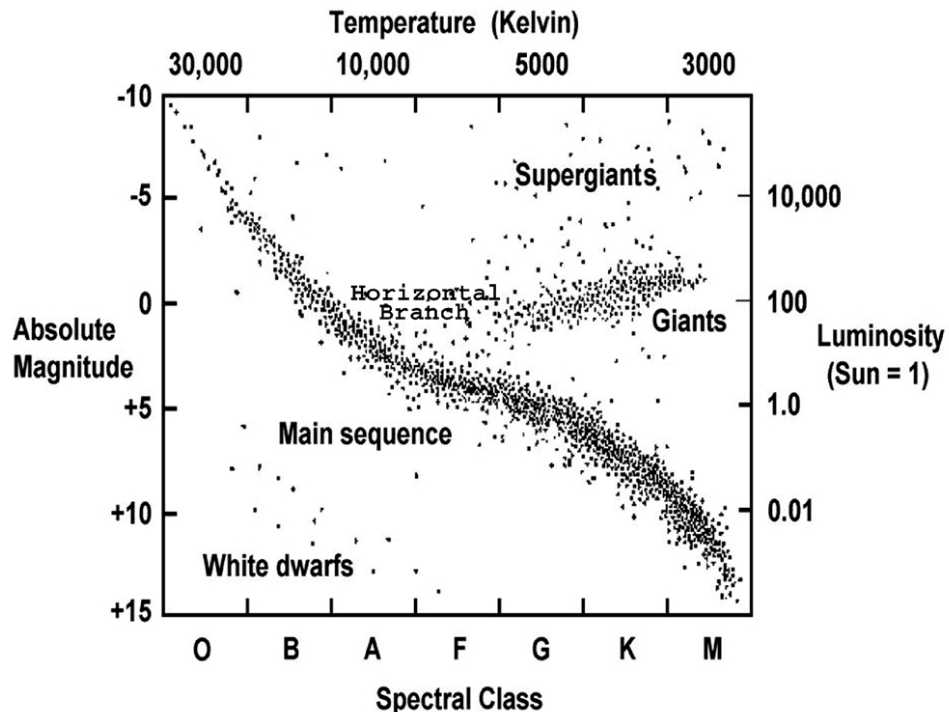


Figure 1.1.: The Hertzsprung-Russell diagram. Courtesy of NASA/CXC/SAO (2015).

Despite a potential uniform distribution in such a diagram, the investigations revealed that most stars are located on a diagonal curve, the so called main sequence (Karttunen et al., 2007). However, there are several other branches, as for example the horizontal branch, the red giants, the super-giants and the white dwarfs. The different branches correspond to different stages of stellar evolution, where not every star follows through the same stages (Karttunen et al., 2007). Dense regions represent evolution phases in which stars remain a long time. Since stars in the main sequence have similar interior structure and dynamics, our Sun, which is roughly at the middle of the main sequence, is a representative example of such stars.

Structure of the Sun

Our Sun has been a prominent object of investigations since 2000 B.C. (Priest, 2014). Nowadays, it is known that the Sun is a giant gas sphere with a complex underlying structure, which is divided into different layers, as illustrated in Fig. 1.2. The outer regions of the Sun are the corona, the chromosphere, and the photosphere.

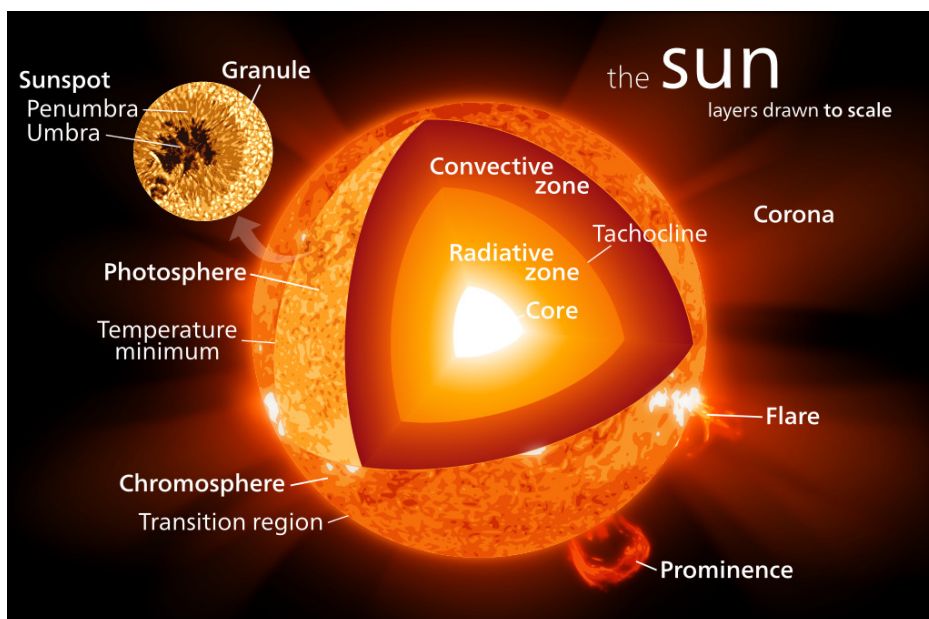


Figure 1.2.: Sun's structure. Illustration of stellar layers and phenomena occurring in the upper atmosphere. Taken from Kelvinsong (2012).

These regions are optically-thin layers (Sturrock, 1985), which means that radiation emitted in these regions can propagate into space, and so phenomena that occur there are observable on Earth. Therefore, many phenomena taking place in the solar atmosphere have been observed hundreds of years ago, for example, observations of

temporally appearing dark spots date back to approximately 350 B.C. (Priest, 2012). Such dark spots are regions of lower temperature than their surroundings and are called sunspots. The systematic investigations of sunspots started in 1610. At that time, Galileo and others began to use telescopes to record the number of sunspots (Hathaway, 2010), which eventually revealed a periodic behaviour of the sunspot activity. Much later, the emergence of sunspots was linked to underlying magnetic field evolution (Solanki, 2003), which demonstrates the complex interaction of solar processes. More comprehensive investigations started in the 19th century, where even the fine structure, called granulation (see Fig. 1.3), of the photosphere could be resolved by Langley (Priest, 2012). Such observations led to the discovery of abruptly occurring bright flashes, the so called solar flares. Solar flares, shown in Fig. 1.3, are often followed by bright, mostly loop shaped, gas patterns propagating outwards into the solar corona (Fletcher et al., 2011). These eruptions are solar prominences and are usually accompanied by coronal mass ejections (Schmieder et al., 2008). Nowadays, in order to investigate the composition of elements, densities and temperature in outer solar regions, various measurements using spectroscopic techniques are conducted (Appenzeller, 2012).

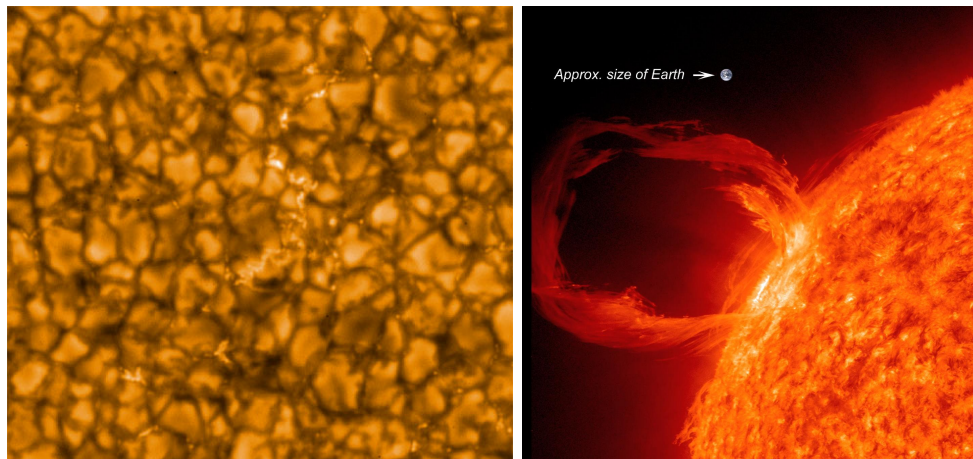


Figure 1.3.: On the left side: Solar granulation. Courtesy of JAXA/NASA/PPARC (2010). On the right side: Solar flare. Courtesy of NASA/SDO (2016).

Many solar phenomena have been studied intensively for centuries, and so our understanding of the Sun's structure and features has increased. This has been greatly assisted by high-resolution observation and satellite programmes over the last decades. However, there are still questions to be answered, especially regarding the inner re-

gions of the Sun, which are difficult to observe and are not entirely understood. The inner part of the Sun can be divided into the convection zone, the radiative zone, and the core. These regions obtained their names due to their energy transport properties: The convection zone is dominated by convective transport. The leading transport in the radiative zone is radiation and the core provides the energy source (D. H. Hathaway, 2015). Unlike the Sun's atmosphere, the convection zone, the radiative zone and the Sun's core are optically thick (Lopes, 2002). Therefore, electro-magnetic waves cannot escape this region, and optical observations are impossible. In order to obtain information of the structure and dynamics in these regions, measurements of acoustic wave propagation need to be used (Gough et al., 1996). This technique is called helioseismology. So far helioseismology can only provide time averaged measurements with rather low resolution (Christensen-Dalsgaard and Thompson, 2007).

However, these observations together with preceding theoretical conclusions allow one to draw the following picture: Beneath the solar surface the convection zone is located, where convectonal flows as well as turbulent motions are predominant. These dynamics reach down to the recently discovered tachocline (Kosovichev et al., 1997; Tobias, 2004), which separates the convection zone from the very distinct radiative zone. The radiative zone, which is stably stratified, rotates as a solid body, but above this region, in the convection zone, differential rotation is present. A region with strong differential rotation, the so-called tachocline, is needed to match the rotational dynamics of these two regions (Spiegel and Zahn, 1992; Goode et al., 1991). Global properties of the tachocline like the thickness and approximate location between $0.67 R_{\odot}$, where R_{\odot} is the solar radius, and $0.72 R_{\odot}$ were determined by helioseismic observations (see for example Kosovichev, 1996; Charbonneau et al., 1999; Arlt, 2009). However, approximations on the radial extent of the tachocline range from $0.019 R_{\odot}$ (Charbonneau et al., 1999) to $0.039 R_{\odot}$ (Elliott and Gough, 1999), which demonstrates the insufficient accuracy of measurements.

Magnetic Fields and Gas Dynamics

Due to the lack of detailed observations it remains difficult to obtain an extended picture of many processes in the Sun's interior. Therefore, understanding the in-

terior dynamics is one of the major problems in current solar research and one of high-priority, since the inner gas dynamics also play a crucial role in magnetic field generation (Hughes et al., 2007). In general, magnetic fields are generated as soon as there are electrically charged particles present and not at rest, which was established by the Ampère’s Law in 1825 (Jackson, 1975). As electrons have a magnetic dipole moment due to their spin, magnetic fields are present everywhere on sub-atomic scales (Dirac, 1958). However, such magnetic fields are randomly distributed. Therefore, to obtain magnetic fields that are structured on scales larger than sub-atomic scales, additional mechanisms are needed (Davidson, 2001). Despite the complex dynamics required to generate and sustain structured magnetic fields, they have been observed in most astrophysical objects, such as galaxies, stars and some planets on scales comparable to the size of the object (Kardashev, 1992). Solar magnetic fields were discovered in 1908 by Hale (Solanki, 2003). One of the successful ideas to explain these observations was by Sir Joseph Larmor (Ruzmaikin et al., 1988). His main statement, that magnetic fields are a general feature in large rotating astrophysical objects due to a dynamo process, initiated an extensive study of the interior dynamics in galaxies, stars and planets.

In this context, the strong shear flow in the tachocline region is believed to play a crucial role in the process of generating magnetic fields (see Parker, 1993; Silvers, 2008, and references therein). However, a consistent model is still absent, due to a lack of understanding of the small-scale and large-scale dynamics. Because of the absence of detailed observations in such regions, analytic and numerical techniques are required to shed light on the motions present. Therefore, the focus of this thesis is to exploit numerical calculations to study shear flows in stellar objects.

Shear flows

Shear flows, such as the one found in the solar interior, are present in various environments and so there have been a number of previous numerical investigations that examine shear flows in different contexts (Balbus and Hawley, 1991; Brandenburg et al., 1995; Hawley et al., 1999; Kitchatinov and Rüdiger, 2009). These have helped inform our approach to understanding the complex dynamics in stellar interiors. However, the earlier studies have not examined shear flows in appropriate

settings for us to understand the evolution of the shear flows inside the Sun. Therefore, we must start from a pure hydrodynamical system in our modelling to build up a comprehensive understanding, before including magnetic fields.

Previous studies of shear flows have shown that such flows can undergo what is known as the Kelvin-Helmholtz (KH) instability, which develops due to the conversion of the available kinetic energy of the shear flow into kinetic energy of the disturbances (see Drazin and Reid, 2004, Chap. 6). In addition to the KH instability, other instabilities, such as baroclinic instability (see Charney, 1947) or the Holmboe instability (Holmboe, 1962), can appear when flows are either rotating or stratified. For the study in this thesis the latter one is of greater interest for following reason: While the KH instability is suppressed by stratification, the more slowly growing Holmboe modes become dominant with increasing stratification (Peltier and Smyth, 1989).

To study any kind of instability, it is convenient to start by investigating the stability threshold of the system. For the extensively studied KH instability, the necessary criterion for stability requires the Richardson number to be greater than $1/4$ everywhere in the domain (Miles, 1961). This criterion was derived for a system with simplifying assumptions, where the fluid is incompressible, inviscid, and non-diffusive. However, dropping these simplifications may alter the stability criterion, such that in a system where thermal diffusion becomes important and acts on a smaller time-scale than buoyancy, the stability criterion requires a significant modification. Dudis (1974) and Zahn (1974) have shown that in such systems the product of the Richardson number with the Péclet number is the quantity that indicates stability. The effect of thermal diffusion on shear instabilities was only studied in the Boussinesq approximation by Jones (1977), Dudis (1974), and more recently by Lignières et al. (1999), such that it is not directly applicable to regions in stellar interiors, in which large pressure gradients have to be considered. In the solar tachocline neither large pressure gradients nor large Mach numbers have to be considered. However, no information on the properties of similar transition regions in other stars is available. Therefore, a more general approach is taken here. In the first part of the thesis a linear stability analysis is conducted to examine both the effect of high thermal diffusion and the effect of compressibility on the onset of shear flow instabilities in a

stably stratified polytropic atmosphere. While the main focus is on KH instabilities, the appearance and consequences of a Holmboe-like instability is investigated.

A linear stability analysis is not sufficient to understand the dynamics of shear flows such that three dimensional direct numerical calculations are required to investigate non-linear evolution. In the existing literature most numerical studies of the turbulence transition in shear flows take the approach of an unforced flow (Caulfield and Peltier, 2000; Smyth and Moum, 2000; Smyth and Winters, 2003), which results in a finite lifetime of an unstable mean state. However, the tachocline is not a transient feature such that physical mechanisms are present by which the flow is sustained. The resulting force acting on the flow is not known in detail. Thus investigations of astrophysical shear flows utilise different methods to reach a sustained flow.

In the context of stellar dynamics, global-scale calculations of stellar interior dynamics investigate the mechanism to maintain differential rotation by body forces resulting from viscous stresses, Reynold stresses and meridional circulation (Brun and Toomre, 2002; Miesch et al., 2008). Because in this work the investigations aim to model a local region of differential rotation in stellar interior, it is of twofold interest to choose a suitable method to maintain a target shear profile. First, the effect of different forcing methods on the evolution of turbulence can be investigated; and second, a comparison with results obtained by global-scale calculations can be drawn. Therefore, a comparative analysis of different forcing methods is the second part of this thesis. Finally, the last two parts of this thesis focus on the question of how modelling shear flows can help us to understand the complex dynamics and interaction of matter and magnetic fields in stellar interiors.

Outline

The thesis is structured as follows. In Chapter 2 the governing equations to model a localised region in stellar interior are derived. The first new research concerning the linear stability of fully compressible hydrodynamical systems is presented in Chapter 3. Moving on to non-linear calculations in Chapter 4 and Chapter 5, where different forcing methods are compared. The non-linear evolution of shear driven turbulence is studied in Chapter 6. Finally, the possibility of a kinematic dynamo driven by

shear induced turbulence is investigated in Chapter 7. A conclusion on possible shear flow instabilities in stellar interiors, their non-linear evolution, and their effect on the magnetic field evolution is drawn in Chapter 8.

2. Model

In search of a better understanding of dynamical processes in a particular system, it is necessary to formulate an appropriate model. In this chapter we start by reviewing some basic properties of solar-like stars in Section 2.1 in order to verify the choice of the basic state, the boundary conditions and geometry of the numerical domain. In Section 2.2 the set of governing equations for a pure hydrodynamical problem and its non-dimensional form is derived. For the magnetohydrodynamical problem, the principal assumptions of the induction equation and the complete set of differential equations are shown in Section 2.3. Finally, the numerical methods used to solve the set of differential equations are described in Section 2.4.

2.1. Stellar Properties

To numerically model stellar interior dynamics it is crucial to first examine stellar properties. In order to approximate the inner structure in real stars, static stellar models were considered, which obey the spherical symmetry of the system (Cox and Giuli, 1968). For this, two fundamental assumptions were made to model a stable homogeneous star. The first assumption is that mass changes with radius according to

$$\frac{dM(r)}{dr} = 4\pi r^2 \rho(r), \quad (2.1)$$

where $M(r)$ is the mass within the radius r , $\rho(r)$ the density. The second assumption is due to the requirement that the star is stable and so it needs to be in a hydrostatic equilibrium

$$\frac{dp(r)}{dr} = -\frac{GM(r)}{r^2} \rho(r) = -g(r)\rho(r), \quad (2.2)$$

where p is the pressure, G the gravitational constant and g the gravitational acceleration. To complete the set of differential equations a relation between the pressure

and the density needs to be considered. For most stars it is convenient to assume that the pressure depends only on the density such that a polytropic relation

$$P = K\rho^{1+1/m}, \quad (2.3)$$

where $m \in \mathbb{R}^+$ is the polytropic index and K is an arbitrary constant, can be assumed (Cox and Giuli, 1968). These equations form the earliest stellar models, where it is assumed that a star is a polytropic gas sphere with self gravity (Collins, 2003). After introducing dimensionless variables

$$\rho = \rho_c \theta^m, \quad P = P_c \theta^{m+1}, \quad r = \alpha \xi, \quad \alpha = \sqrt{\frac{m+1}{4\pi G} K \rho_c^{1/(m-1)}}, \quad (2.4)$$

where θ is the polytropic temperature, and combining Equations (2.1) - (2.3) the Lane-Emden equation can be derived,

$$\frac{1}{\xi^2} \frac{d}{d\xi} \left(\xi^2 \frac{d\theta}{d\xi} \right) = -\theta^m. \quad (2.5)$$

The order of the solutions for the Lane-Emden equation is determined by the polytropic index m , such that it can be distinguished between several cases. For $m = 0$, the solution corresponds to an incompressible sphere, where the density remains constant with the radius. In the range $1 \leq m \leq 1.5$ the solutions obtained represent a superadiabatic atmosphere that is unstable to convective motions, which is the case for the convection zone or fully convective stars (Cohen, 2009). For $m > 1.5$ the stratification is subadiabatic such that the atmosphere is stable against convection. A special case is $m = 3$, which corresponds to the Eddington approximation and for $m > 5$ the solutions cannot be used to model a star, because the radius of such a star becomes infinite.

The approach discussed above can be used to model white dwarfs, completely convective, or completely radiative stars, as well as massive stars and stellar envelopes. In solar like main-sequence stars the polytropic index will depend on the depth, such that additional differential equations are needed. However, here only a small portion of the stellar interior is considered, to understand the small-scale dynamics, and so a constant polytropic atmosphere is applicable. Understanding the inner structure,

and which layer of a star is modelled, is crucial in order to decide which type of basic state is required.

The substantial part of main-sequence stars is formed by the stellar core and the radiative zone, which exhibit the energy source of a star and where energy transport is due to radiative processes (Pradhan and Nahar, 2011). Above the radiative zone the stratification becomes super-adiabatic such that energy transport is predominately by convective motions. These two layers, the radiative zone and the convection zone, are separated by a thin region, the tachocline. This intermediate region is of particular interest, because it has a significant impact on magnetic field generation. Therefore, it is important to explore the known properties of this region.

Although, for other stars the location and properties of the tachocline are unknown, some information is available for the Sun, as helioseismology keeps constantly enhancing the measurement's accuracy. However, it is difficult to make assumptions about the precise shape of the shear flow, because the available measurements for the solar tachocline are not sufficient to resolve the velocity profile on small scales, such that only time averaged large-scale measurements can be provided (Christensen-Dalsgaard and Thompson, 2007). In the Sun, the tachocline overlaps with the base of the convection zone especially in regions of higher latitudes (Basu and Antia, 2001; Forgács-Dajka and Petrovay, 2002). The radiative envelope, located just beneath the tachocline, has an angular velocity $\Omega_0 = 2\pi \times 463$ nHz (Gough, 2007), i.e. assuming the top of the radiative envelope at $0.67R_\odot$ this results in a velocity of 1.36 kms⁻¹. The change of velocity across the tachocline was approximated to be $\Delta u \approx 50$ ms⁻¹ (Soward et al., 2005), such that taking the speed of sound at $0.7 R_\odot$ into account, the Mach number for the mean flow in the tachocline is about 0.005.

In order to understand the stability of the tachocline the Richardson number can be approximated from temperature and density profiles. The stratification changes from sub-adiabatic in the radiative envelope to super-adiabatic in the convection zone. Using Table 1.1 in Gough (2007) and considering a polytropic atmosphere, it is possible to calculate the polytropic index at $0.7R_\odot$ to be roughly 2.0, which corresponds to a strong stratification. Taking the buoyancy frequency and the change of the velocity over a height of $0.02 R_\odot$, the Richardson number is of order 10^2 at the

upper part of the tachocline, which suggests a stable shear flow. Furthermore, by taking the thermal diffusivity κ the Péclet number can be estimated to be of order 10^6 to 10^7 .

The transport coefficients are known to a greater accuracy throughout the solar interior. However, numerical calculations are incapable of reaching the correct order of magnitude of transport coefficients due to the numerical cost of performing at such low viscosity and thermal diffusivity. Therefore, it is necessary to verify the applicability of numerical calculations performed at different transport coefficients, respecting certain ratios. A more detailed discussion can be found in Chapter 6, where possible effects on the resulting dynamics are studied.

Setting up the model

Global-scale numerical calculations of stellar interior dynamics is one approach to investigate the mechanisms maintaining differential rotation (Brun and Toomre, 2002; Miesch et al., 2008). However, by using a global approach, such models cannot resolve a large range of length-scales in its entirety and have to rely on artificially large transport coefficients or subgrid-scale models. Therefore, numerical investigations using a local approach, where only a small fraction of the object is simulated, can help to provide a more detailed description of the region of interest. In this thesis, I focus on local dynamics in a Cartesian box. To model a small portion of stellar interiors it is necessary to assume a polytropic atmosphere as a basic state, where for the region of interest a stable stratification requires the polytropic index to be greater than 1.5. Although, in the Sun the tachocline can overlap with the overshoot region, the assumptions I make correspond to a shear region where the overshoot region is not included in the upper layers. Therefore, I consider boundaries that are impermeable and stress-free, because the exchange of matter can be neglected in the lower parts of the tachocline. In addition, such boundary conditions minimise effects that can affect the inner dynamics. The exact assumptions will be given in Subsection 2.2.2.

2.2. Hydrodynamics

A hydrodynamical description of the system involves the continuum hypothesis, which assumes a continuous medium (Wesseling, 2009), and is valid for stellar interiors. Furthermore, for the Navier-Stokes equations, which form a macroscopic hydrodynamic description, the hydrodynamical approximation has to be applicable. This is provided, if for any given time the system remains in a thermodynamic equilibrium, such that the relaxation time towards an equilibrium is less than the smallest time increment. If this condition is satisfied, hydrodynamical characteristics such as temperature and density can be defined. In the region of interest the gas constituents behave as if they are in a thermodynamic equilibrium (Hansen and Kawaler, 1999b), such that the following macroscopic description is valid.

The set of differential equations can be obtained by considering conservation laws. The first conservation law concerns the mass conservation. It states that the change of density within a certain volume dV is equal to the outflow through the surface, dS , for a closed system, i.e.

$$\frac{\partial}{\partial t} \left(\int_V \rho dV \right) = - \oint_S \rho \mathbf{u} \cdot \hat{\mathbf{n}} dS, \quad (2.6)$$

where ρ is the density, \mathbf{u} the velocity field and $\hat{\mathbf{n}}$ is the normal vector to the surface. The minus sign is convention due to the normal vector pointing outwards. Then using the divergence theorem the continuity equation takes the form

$$\frac{\partial \rho}{\partial t} = -\nabla \cdot (\rho \mathbf{u}). \quad (2.7)$$

The Navier-Stokes equation arises from the momentum conservation for a fluid parcel. The momentum change of a fluid parcel is equal to the sum of all forces acting on it. Then, the general form is given by

$$\rho \frac{D\mathbf{u}}{Dt} = \nabla \cdot \mathbf{o} + \mathbf{f}, \quad (2.8)$$

where $\frac{D}{Dt}$ is the total time derivative, \mathbf{o} is a symmetric tensor representing all surface stresses and \mathbf{f} takes into account body forces.

Making use of the continuity equation and rewriting the total derivative as the Lagrangian frame derivative leads to

$$\frac{\partial \rho \mathbf{u}}{\partial t} + \nabla \cdot (\rho \mathbf{u} \mathbf{u}) = \nabla \cdot \mathbf{o} + \mathbf{f}. \quad (2.9)$$

The stress tensor can be decomposed into the surface pressure and the viscous stresses, and the only body force considered is gravity, such that the Navier-Stokes equation becomes

$$\frac{\partial \rho \mathbf{u}}{\partial t} + \nabla \cdot (\rho \mathbf{u} \mathbf{u}) = -\nabla P + \mathbf{g} \rho + \mu \nabla \cdot \tau, \quad (2.10)$$

where P is the pressure, \mathbf{g} the gravity and τ the strain rate tensor. The dynamical viscosity is denoted by μ .

Finally, from energy conservation the heat equation (or temperature evolution equation) is derived, which is obtained by equating the total change of temperature, T , with all sinks and sources,

$$\rho \frac{\partial T}{\partial t} + \rho \mathbf{u} \cdot \nabla T = \underbrace{\gamma \kappa \nabla^2 T}_{\text{thermal diffusion}} + \underbrace{\frac{\mu(\gamma - 1)}{2} |\tau|^2}_{\text{viscous heating}} - \underbrace{\rho(\gamma - 1) T \nabla \cdot \mathbf{u}}_{\text{work by compression}}, \quad (2.11)$$

where κ is the thermal conductivity and $\gamma = c_p/c_v$ denotes the adiabatic index, which is the ratio of the heat capacities c_p at constant pressure, and c_v at constant volume. The thermal diffusion term was obtained by assuming a constant thermal conductivity throughout the domain. In this thesis the fluid is assumed to be an ideal gas, such that the equation of state is

$$P = R_{spec} \rho T, \quad (2.12)$$

where R_{spec} is the specific gas constant.

2.2.1. Non-dimensional Governing Equations

Throughout the research in this thesis a compressible fluid in a Cartesian domain with coordinates (x, y, z) of extent (L_x, L_y, d) is considered. The boundaries at $z = 0$

and $z = d$ are impermeable. The horizontal directions, x and y , are periodic (see Figure 2.1 for an illustration of the domain). The fluid is assumed to be an ideal gas

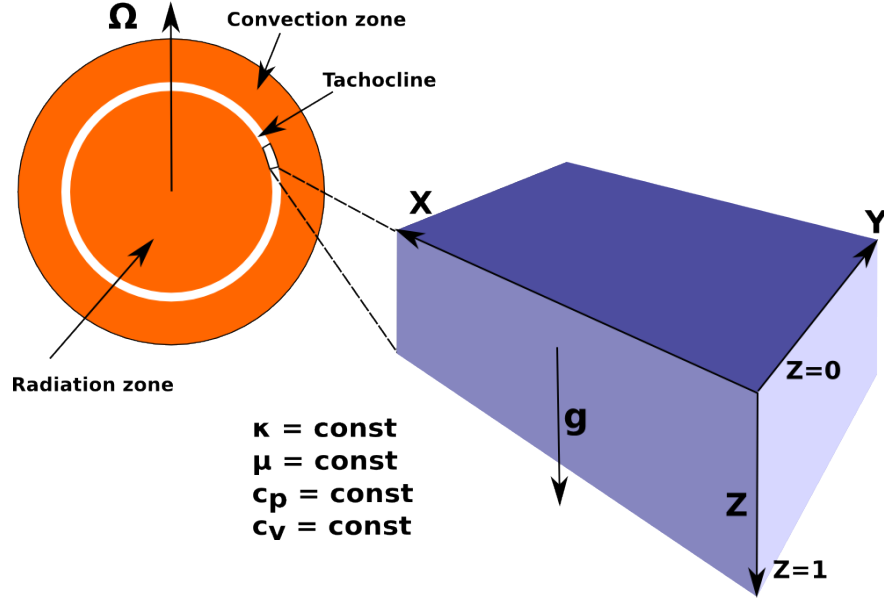


Figure 2.1.: Illustration of the local domain used for the model in correlation to the solar region that is subject to investigations.

with constant dynamic viscosity μ , constant thermal conductivity κ , constant heat capacities c_p at constant pressure, and c_v at constant volume. In order to obtain non-dimensional equations for the system under consideration, the fundamental unit of length is the domain depth d . Furthermore, fundamental units of temperature and density are set to be T_t and ρ_t , which correspond to the temperature and density at the top boundary, and results in the fundamental pressure $P_t = (c_p - c_v)\rho_t T_t$. The time is normalised by the sound crossing time, which is $\tilde{t} = d/[(c_p - c_v)T_t]^{1/2}$ for the chosen fundamental units. Then the equations, in non-dimensional form, are

$$\frac{\partial \rho}{\partial t} = -\nabla \cdot (\rho \mathbf{u}), \quad (2.13)$$

$$\frac{\partial \rho \mathbf{u}}{\partial t} = -\nabla P - \nabla \cdot (\rho \mathbf{u} \mathbf{u}) + \sigma C_k \left(\nabla^2 \mathbf{u} + \frac{1}{3} \nabla (\nabla \cdot \mathbf{u}) \right) - \rho \theta (m + 1) \hat{\mathbf{z}}, \quad (2.14)$$

$$\frac{\partial T}{\partial t} = \frac{C_k \sigma (\gamma - 1)}{2\rho} |\tau|^2 + \frac{\gamma C_k}{\rho} \nabla^2 T - \nabla \cdot (T \mathbf{u}) - (\gamma - 2) T \nabla \cdot \mathbf{u}, \quad (2.15)$$

where θ denotes the temperature gradient and m is the polytropic index. Due to the fundamental units the following non-dimensional numbers are used. The dimensionless Prandtl number, $\sigma = \mu c_p / \kappa$, is the ratio of viscosity to thermal conductivity and the thermal dissipation parameter is defined as $C_k = \kappa \tilde{t} / (\rho_0 c_p d^2)$, where the product

of both results in the non dimensional dynamical viscosity. Because a Newtonian fluid is considered, the strain rate tensor has the form

$$\tau_{ij} = \frac{\partial u_j}{\partial x_i} + \frac{\partial u_i}{\partial x_j} - \delta_{ij} \frac{2}{3} \frac{\partial u_k}{\partial x_k}. \quad (2.16)$$

2.2.2. Boundary Conditions and Background State

As discussed in Section 2.1 a polytropic relation between pressure and density has to be assumed, where the pressure is a function of density only i.e.

$$P(\rho) \propto \rho^{(1+\frac{1}{m})}, \quad (2.17)$$

where m is the polytropic index. Due to the Schwarzschild criterion the fluid is stable against convection if the inequality $m > 1/(\gamma - 1)$ holds, where the adiabatic index, γ , is equal to $5/3$. Then, the system is convectively stable for a polytropic index of $m > 1.5$. Only stable stratified atmospheres will be considered throughout this thesis.

Boundary conditions, at the top and bottom of the of the domain, are impermeable and stress-free velocity i.e.

$$u_z = \frac{\partial u_x}{\partial z} = \frac{\partial u_y}{\partial z} = 0 \quad \text{at} \quad z = 0 \quad \text{and} \quad z = 1 \quad (2.18)$$

and fixed temperature, which means:

$$T = 1 \quad \text{at} \quad z = 0 \quad \text{and} \quad T = 1 + \theta \quad \text{at} \quad z = 1. \quad (2.19)$$

To include thermal effects it is necessary to choose the background temperature in such a way, that it is a stationary solution of the heat equation or remains quasi-stationary on time-scales larger than the thermal diffusion time-scale. This results in a temperature and density profile of the form:

$$T(z) = T_t (1 + \theta z) \quad (2.20)$$

$$\rho(z) = \rho_t (1 + \theta z)^m. \quad (2.21)$$

Some background profiles for temperature and density are shown in Fig. 2.2.

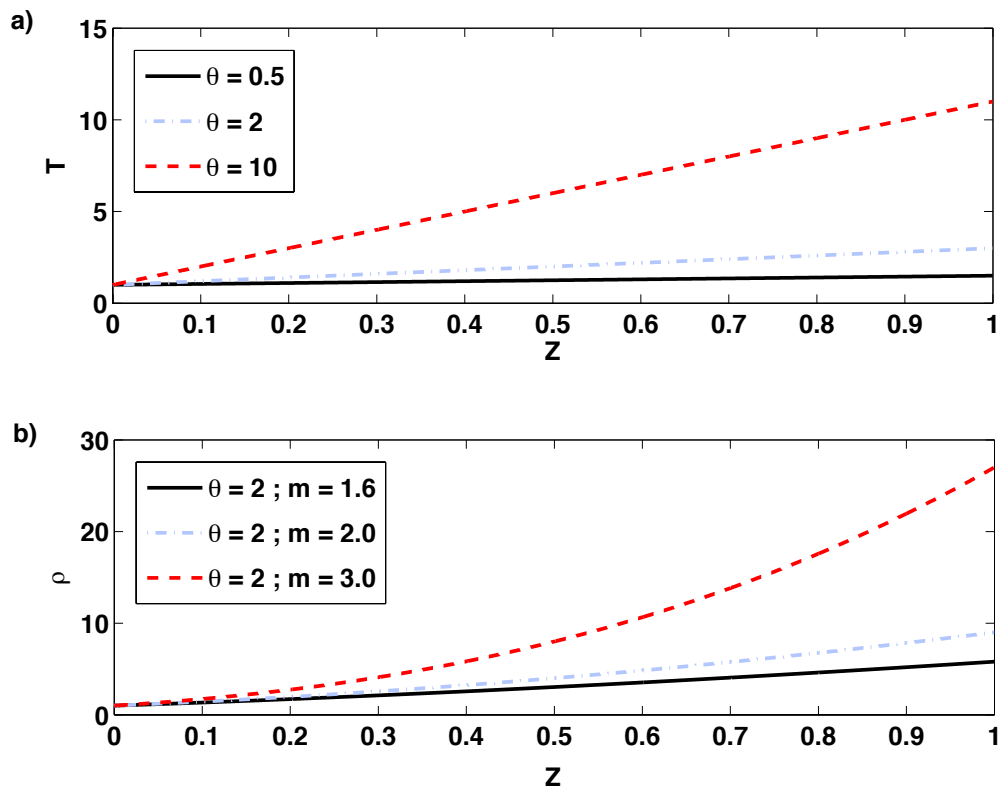


Figure 2.2.: Example background density and temperature profiles. a) Temperature profiles for different θ , that were used. b) Density profiles for $\theta = 2$ but three different polytropic indices m . For these indices m the atmosphere is stably stratified.

2.2.3. Important Approximations

Many investigations use approximations of the governing Equations (2.13) - (2.15), because solving the fully compressible equations is computationally expensive due to the small time-stepping, which is required to resolve the sound waves. Especially, when dealing with velocities much smaller than the speed of sound, the so-called Boussinesq approximation can be used (Boussinesq, 1903). For the Boussinesq approximation to be applicable in a system, any scale height has to be much greater than the vertical extent of the system (Spiegel and Veronis, 1960). Then, the approximated equations describe a system in which the density fluctuations result from

thermal effects rather than from pressure and in the momentum equations density fluctuations are neglected except their coupling to the gravitational term.

The Boussinesq approximation, which can be applied if the temperature variation and therefore the density variation is small over the region under consideration, is not valid for strongly stratified regions like those present in stellar interiors. Since the Boussinesq approximation will fail to describe many stratified environments there exist different alternative approaches. For example there are several anelastic models, which aim to filter out sound waves and predict a realistic behaviour of compressible fluids. Since sound waves are also important for energy transfer, it is not straight forward to find an approximation that filters sound waves, but remains energy conservative. Thus some anelastic models are not valid for any region and some of them do not respect the energy conservation (Brown et al., 2012). Some recent investigations focus on a methodical derivation of sound filtering models, which will *a priori* conserve all physical symmetries. However, in this work the fully compressible equations are considered in order to be able to model even systems with larger pressure gradients.

2.3. Magnetohydrodynamics

Stellar interiors consist of plasma. Therefore, the equations of magnetohydrodynamics (MHD) are required in order to fully model the dynamics. The set of MHD equations is similar to the set of differential equations derived for the pure hydrodynamical case in Section 2.2. However, additional terms that result from magnetic field coupling to matter need to be considered in the Navier-Stokes equation and temperature evolution equation. Furthermore, to describe the magnetic field evolution due to velocity fields and magnetic diffusion, the induction equation is needed.

To begin to obtain the full MHD equations, the induction equation is derived from the Maxwell equations, which are the fundamental equations of classical electrodynamics:

$$\nabla \cdot \mathbf{E} = 4\pi \varrho_e, \quad (2.22)$$

$$\nabla \cdot \mathbf{B} = 0, \quad (2.23)$$

$$\nabla \times \mathbf{E} = -\frac{1}{c} \partial_t \mathbf{B}, \quad (2.24)$$

$$\nabla \times \mathbf{B} = \frac{1}{c} (4\pi \mathbf{J} + \partial_t \mathbf{E}), \quad (2.25)$$

where \mathbf{E} is the electric field and \mathbf{B} is the magnetic field. The electrical charge density is denoted by ϱ_e , c is the speed of light and \mathbf{J} is the electrical current density. In addition to these equations, Ohm's Law has to be considered. It states that in a frame of reference that is at rest $\mathbf{J} = \sigma_0 \mathbf{E}$ holds, where σ_0 is the electrical conductivity. As here the frame of reference is moving with the fluid with a speed \mathbf{u} , it is necessary to perform a coordinate transformation under which the resulting electrical current remains unchanged. This description leads to the additional term $\mathbf{u} \times \mathbf{B}$, because the electric field transforms as $\mathbf{E} = \mathbf{E}_r - \mathbf{u} \times \mathbf{B}$, when the frame of reference is changed. Then Ohm's Law becomes

$$\mathbf{J} = \sigma_0 \left(\mathbf{E} + \frac{1}{c} \mathbf{u} \times \mathbf{B} \right). \quad (2.26)$$

In order to derive the induction equation, from the above equations, several assumptions are made. In general in plasmas the displacement current is neglected, because

the electric conductivity in a plasma is very high, such that no electrical potential is present on scales larger than the Debye length. This also follows from applying the magnetohydrodynamical approximation. Following the discussion in Kippenhahn and Möllenhoff (1975) to obtain the magnetohydrodynamical approximation a parameter α is introduced and only terms up to linear order in α are kept. Higher order terms are neglected. For that, the first assumption is that only non-relativistic velocities are considered. So if setting L as a typical length-scale and t_0 as the typical time-scale, the typical velocity $U_0 = L/t_0$ has to be much less than the speed of light c . This leads to the above mentioned parameter α ,

$$\frac{U_0}{c} = \frac{L/t_0}{c} = \alpha \ll 1.$$

Then, assuming that electric and magnetic fields do not change significantly on a typical time-scale and typical length-scale, the spatial and time derivatives can be approximated as follows

$$\begin{aligned} \frac{\partial \mathbf{E}}{\partial t} &\approx \frac{\mathbf{E}}{t_0} & \frac{\partial \mathbf{E}}{\partial x} &\approx \frac{\mathbf{E}}{L}, \\ \frac{\partial \mathbf{B}}{\partial t} &\approx \frac{\mathbf{B}}{t_0} & \frac{\partial \mathbf{B}}{\partial x} &\approx \frac{\mathbf{B}}{L}. \end{aligned}$$

With the above assumption, the third Maxwell Equation (2.24) requires that

$$\left| \frac{\mathbf{E}}{\mathbf{B}} \right| = \left| \frac{L/t_0}{c} \right| = \alpha \ll 1.$$

This is used to rewrite the fourth Maxwell Equation (2.25) as follows

$$\mathbf{B}/L = \frac{1}{c}4\pi\mathbf{J} + \frac{1}{c}\mathbf{E}/t_0. \quad (2.27)$$

This equation is rearranged as follows,

$$\mathbf{B} = \frac{L}{c}4\pi\mathbf{J} + \frac{L}{c}\frac{\alpha\mathbf{B}}{t_0} \quad \Rightarrow \quad \mathbf{B} = \frac{L}{c}4\pi\mathbf{J} + \alpha^2\mathbf{B}, \quad (2.28)$$

in order to obtain an expression for the magnetic field. The last term on the right-hand side is negligible, as it is of second order in α . It can be seen that all terms in

Equation (2.26) are of the same order and therefore both terms on the right-hand side remain. At this point it is straight forward to rewrite the third and fourth Maxwell equations together with the Ohm's Law to obtain

$$\partial_t \mathbf{B} = \nabla \times (\mathbf{u} \times \mathbf{B}) - \nabla \times \left(\frac{c^2}{4\pi\sigma_0} \nabla \times \mathbf{B} \right), \quad (2.29)$$

where the pre-factor $c^2/(4\pi\sigma_0) = \eta$, which is the magnetic diffusivity. In this particular case, the magnetic diffusivity is assumed to remain constant throughout the domain, such that using the vector identity $\nabla \times (\nabla \times \mathbf{B}) = \nabla(\nabla \cdot \mathbf{B}) - \nabla^2 \mathbf{B}$ the induction equation becomes

$$\partial_t \mathbf{B} = \nabla \times (\mathbf{u} \times \mathbf{B}) + \eta \nabla^2 \mathbf{B}. \quad (2.30)$$

The first term on the right-hand side corresponds to the response of the magnetic field to plasma motion and the second term describes the diffusion of the magnetic field.

Having the MHD approximation and the Maxwell equations in mind, it is possible to write down the Navier-Stokes equation that become of the form

$$\frac{\partial \rho \mathbf{u}}{\partial t} + \nabla \cdot (\rho \mathbf{u} \mathbf{u}) = -\nabla P + \mu \nabla \cdot \tau + \mathbf{g} \rho + \frac{1}{\mu_0} (\nabla \times \mathbf{B}) \times \mathbf{B}$$

where μ_0 is the vacuum permeability and the last term comes from the Lorentz force $\mathbf{F}_{\text{Lorentz}} = \varrho_e (\mathbf{E} + \mathbf{u} \times \mathbf{B})$. Here the first term in the Lorentz force is negligible due to the MHD approximation and the second term was rewritten by using the fourth Maxwell Equation (2.25).

For the temperature evolution equation, an energy loss has to be considered due to ohmic dissipation, which is represented as an additional term

$$\rho \frac{\partial T}{\partial t} + \rho \mathbf{u} \cdot \nabla T = \gamma \kappa \nabla^2 T + \frac{\mu(\gamma - 1)}{2} |\tau|^2 - \rho(\gamma - 1) T \nabla \cdot \mathbf{u} + \underbrace{(\gamma - 1) \eta |\mathbf{J}|^2}_{\text{ohmic dissipation}}, \quad (2.31)$$

all other terms are as denoted in Equation (2.11).

2.3.1. Non-dimensional MHD Equations

Using the same fundamental units as used for a pure hydrodynamical system in the previous section the non-dimensional MHD equations are obtained. The resulting equations are (Matthews et al., 1995):

$$\frac{\partial \rho}{\partial t} = -\nabla \cdot (\rho \mathbf{u}) \quad (2.32)$$

$$\frac{\partial \rho \mathbf{u}}{\partial t} = -\nabla P^* - \nabla \cdot (\rho \mathbf{u} \mathbf{u} - f \mathbf{B} \mathbf{B}) - \rho \mathbf{g} + \sigma C_k \left(\nabla^2 \mathbf{u} + \frac{1}{3} \nabla (\nabla \cdot \mathbf{u}) \right) \quad (2.33)$$

$$\begin{aligned} \frac{\partial T}{\partial t} = & \frac{\gamma C_k}{\rho} \nabla^2 T - \nabla \cdot (T \mathbf{u}) - (\gamma - 2) T \nabla \cdot \mathbf{u} \\ & + \frac{C_k (\gamma - 1)}{\rho} \left(\frac{\sigma}{2} |\boldsymbol{\tau}|^2 + f \xi |\mathbf{J}|^2 \right), \end{aligned} \quad (2.34)$$

$$\frac{\partial \mathbf{B}}{\partial t} = \nabla \cdot (\mathbf{B} \mathbf{u} - \mathbf{u} \mathbf{B}) + \xi C_k \nabla^2 \mathbf{B} \quad (2.35)$$

$$\nabla \cdot \mathbf{B} = 0, \quad (2.36)$$

where the total pressure $P^* = \rho T + f |\mathbf{B}|^2 / 2$ includes the magnetic pressure. Here, $f = |\mathbf{B}|^2 / \mu_0 P_t$ gives the ratio of the magnetic pressure to the fundamental unit pressure. Note, that only for calculations with $f \neq 0$ the magnetic field is normalised by the magnitude of the background magnetic field. Like in the previous section, $C_k = \kappa \tilde{t} / (\rho_0 c_p d^2)$ is the thermal dissipation parameter, $\sigma = \nu / C_k$ is the Prandtl number and one additional non-dimensional parameter is introduced, the inverse Roberts number $\xi = \eta c_p \rho_t / \kappa$. The inverse Roberts number represents the ratio of the Prandtl number to the magnetic Prandtl number $\sigma_M = \rho_0 \mu / \eta$. Like in the pure hydrodynamic case, the strain rate tensor has the form as in Equation (2.16). In addition the magnetic field has to remain divergence free due to the non-existence of magnetic monopoles and therefore Equation (2.36) has to hold.

2.3.2. Boundary Conditions and Background State

The boundary conditions and resulting background profiles for the density and temperature are the same as defined previously in Subsection 2.2.2, where the background temperature and density profiles are given in Equation (2.20) and Equation (2.21) respectively.

For the magnetic field there exist two possible boundary conditions: One possibility, the so called pseudo-vacuum (Favier and Proctor, 2013; Jackson et al., 2014), assumes the magnetic field to be normal to the boundary. Here the boundary conditions read

$$B_x = B_y = \partial_z B_z = 0 \quad \text{at} \quad z = 0 \quad \text{and} \quad z = 1. \quad (2.37)$$

For the second possibility the magnetic field is tangential to the boundary, such that

$$B_z = \partial_z B_x = \partial_z B_y = 0 \quad \text{at} \quad z = 0 \quad \text{and} \quad z = 1. \quad (2.38)$$

This is also called a perfect electrical conductor (Favier and Proctor, 2013).

2.4. Numerical Methods

One major issue solving Navier-Stokes or MHD equations numerically is due to the demand of resolution of a rapidly increasing instantaneous range of scales with greater Reynolds numbers. The existing methods to solve the set of equations numerically can be classified into three categories; direct numerical simulations (DNS), large eddy simulations (LES) or Reynolds-averaged Navier-Stokes simulations (RANS) (Miki, 2008). DNS provide the most accurate approach due to their theoretical ability to resolve all spatial and temporal scales. In practice, DNS solves a reasonable subset of scales that ensure accuracy but to keep the computational cost low. The latter two methods come with approximations: The RANS solve for a statistical evolution of the quantities, where each quantity is decomposed into a mean value and a fluctuating part (Durbin and Reif, 2010). The LES employ filter functions to model a certain range of small-scales, but directly solves large-scales (Garnier et al., 2009). Therefore, DNS are suitable for addressing fundamental research questions that require high accuracy, as for example needed in turbulent flows.

2.4.1. Non-linear DNS Calculations

To solve the set of differential equations derived in Section 2.2 and Section 2.3 numerically a direct numerical method (DNS) will be used. For that a finite-

difference/pseudo-spectral code is exploited, where a description can be found in Matthews et al. (1995). This code was further developed, optimised and used over the last two decades (see for example Matthews et al., 1995; Silvers et al., 2009a; Favier and Bushby, 2012, 2013, and references therein).

Since the computational domain that I will consider is a Cartesian box with impermeable walls at the top and bottom and periodic boundary conditions in x - and y -directions, the following numerical methods to calculate spatial and time derivatives are used.

Vertical Derivatives

The derivatives in the vertical direction are obtained by using an explicit fourth-order finite-difference scheme. The finite difference method (FDM) is the oldest method and dates back to 1768, when it was applied by Euler (Hirsch, 2007a). For such a method the conservative form of the differential form of the equations is used. The basic idea behind this method is to use the definition of the derivative

$$\frac{\partial f(x)}{\partial x} = \lim_{\Delta x \rightarrow 0} \frac{f(x + \Delta x) - f(x)}{\Delta x} \quad (2.39)$$

together with the Taylor expansion

$$\begin{aligned} f(x + \Delta x) = & f(x) + \Delta x \frac{\partial f(x)}{\partial x} + \frac{\Delta x^2}{2} \frac{\partial^2 f(x)}{\partial x^2} + \frac{\Delta x^3}{3!} \frac{\partial^3 f(x)}{\partial x^3} + \dots \quad (2.40) \\ & + \frac{\Delta x^{n-1}}{(n-1)!} \frac{\partial^{n-1} f(x)}{\partial x^{n-1}} + \mathcal{O}(\Delta x^n), \end{aligned}$$

which is expanded around $f(x)$.

Assuming an uniformly discretised grid and rewriting Equation (2.40) the first derivative at the point i is

$$f_i^{(1)} = \left(\frac{\partial f}{\partial x} \right)_i = \frac{f_{i+1} - f_i}{\Delta x} - \underbrace{\frac{\Delta x}{2} f_i^{(2)}}_{\text{truncation error}} - \mathcal{O}(\Delta x^2), \quad (2.41)$$

where $f_i^{(m)}$ denotes the m^{th} derivative with respect to x and the subscript $i+1$ that it is at the point $i+1$ on the mesh. As can be seen the formula includes the point

itself and one neighbouring point to its right. Furthermore, the highest order in the truncation error is of order one. Since the accuracy order depends on the power of the truncation error, Equation (2.41) is the first order forward difference formula. It is also possible to derive the backward difference scheme and a centred formula. As an example calculation, the centred formula can be obtained by taking f_{i+1} and f_{i-1} and subtracting them from each other:

$$f_{i+1} - f_{i-1} = 2\Delta x f^{(1)} + \frac{2\Delta x^3}{3!} f^{(3)} + \frac{2\Delta x^5}{5!} f^{(5)} + \dots + \frac{2\Delta x^{2n+1}}{(2n+1)!} f^{(2n+1)} + \dots, \quad (2.42)$$

Rearranging this equation, the general centred finite difference approximation becomes

$$\frac{f_{i+1} - f_{i-1}}{2\Delta x} = f^{(1)} + \frac{\Delta x^2}{3!} f^{(3)} + \frac{\Delta x^4}{5!} f^{(5)} + \dots + \frac{\Delta x^{2n}}{(2n+1)!} f^{(2n+1)} + \dots \quad (2.43)$$

For example, to get the second order centred scheme, Equation (2.43) is truncated after the first term on the right-hand side. For the fourth order it is necessary to incorporate two more points. This is achieved by deriving the formula for f_{i+2} and f_{i-2} , then getting rid of the second order error term one obtains:

$$\frac{8(f_{i+1} - f_{i-1}) - (f_{i+2} - f_{i-2})}{12\Delta x} = f_i^{(1)} - \mathcal{O}(\Delta x^4). \quad (2.44)$$

For the non-linear calculations in this thesis this scheme is used for the interior points, whereas for the points at the boundaries forward or backward schemes are applied. Alternatively, it is also possible to introduce so-called ghost points that extend the grid size when calculating derivatives at the boundaries of the domain and keep the centred scheme.

The method of finite differences is not the only numerical method that can be used. There exist several methods to obtain solutions for partial differential equations, which can be divided into three classes. However, other methods, the finite volume method (FVM) and the finite element method (FEM) are applied to the integral form of the conservation law (Hirsch, 2007b). Due to the more general approach of these two methods, they can be more beneficial if either the problem poses Neumann boundary conditions, or discontinuous sources are present, or if the problem

involves complex geometries, which is not the case here. The advantage of these two methods is that they are more easily applicable to arbitrary meshes, e.g. structured and unstructured, but the numerical implementations are more complex. For uniform grids in a Cartesian geometry as used for the problem at hand, the FDM and FVM lead to the same difference equations (Hirsch, 2007b). Therefore, it is more convenient to exploit FDM to calculate the derivatives in the vertical direction.

Horizontal Derivatives

Taking advantage of periodicity of the domain in both horizontal directions, a pseudospectral method using fast Fourier transforms can be employed to calculate the spatial derivatives. Using spectral methods it is possible to obtain more accurate solutions than by using finite-difference methods with the same resolution (Canuto et al., 1988). The name pseudospectral was given by Orszag (1971) and indicates that the spectral method approximates the function not by the true spectral Galerkin method (Canuto et al., 2006), and the fact that the functions are discretised on a grid (Shizgal, 2015).

To demonstrate the general approach of spectral differentiation following the online lecture notes (Yu, 2015), the first formula for the first derivative of a periodic function $f(x)$ with period L is derived. Having discretised the function $f(x)$ into N samples $f_n = f(nL/N)$, which are defined on $n = 0, 1, \dots, N - 1$. Rewriting f_n in the form

$$f_n = \sum_{k=0}^{N-1} Y_k e^{i2\pi kn/N},$$

where the coefficients Y_k can be found by using the discrete Fourier transform (DFT)

$$Y_k = \frac{1}{N} \sum_{n=0}^{N-1} f_n e^{-i2\pi kn/N}. \quad (2.45)$$

Then, a derivative operator d/dx in x direction is just a multiplication operation in the k space. Using a fast Fourier transform algorithm enables one to perform forward and backwards Fourier transformations in operations of order $N \log N$. Therefore, this method provides a convenient way of computing derivatives. However, its resulting solutions are ambiguous due to the fact that the terms $Y_k e^{i2\pi kn/N}$ and

$Y_k e^{i2\pi(k+mN)n/N}$ will give the same result on a discretised grid with N samples. Here the alternative solutions have m times more oscillations between the sample points and therefore lead to significantly different derivatives (Yu, 2015; Canuto et al., 2006). This phenomena is called aliasing (see for example Hou and Li, 2007). In order to find a way around this ambiguity it needs additional criteria to find de-aliased solutions. There are several possibilities to do so. One solution is to restrict the possible frequencies to $|k + m_k N| \leq N/2$ or equivalently to minimise the first derivative.

When minimising the mean-square slope (detailed derivation can be found in Yu, 2015), minima are found for $m_k = 0$ if $0 \leq k < N/2$ and for $m_k = -1$ if $N/2 < k < N$. However, for $k = N/2$, which is also called the Nyquist frequency, and for even N non-unique solutions exist. Following the procedure in Yu (2015), the ‘unique trigonometric interpolation’ that minimises the oscillations between the sample points has the form:

$$f(x) = F_0 + \sum_{0 < k < N/2} (F_k e^{i2\pi kx/L} + F_{N-k} e^{-i2\pi kx/L}) + F_{N/2} \cos(\pi N x/L). \quad (2.46)$$

Note, calculating derivatives in the frequency space corresponds to a multiplication, where caution is required due to different solutions for the third term in (2.46) for even and odd N . The first derivative can be obtained by applying the derivative operator $\partial/\partial x$ to Equation (2.46). However, the second derivative must not be obtained by performing the derivation twice onto Equation (2.46), but by multiplying the F_k term by $-(2\pi k/L)^2$, the F_{N-k} term by the corresponding $-(2\pi(k-N)/L)^2$, and the $F_{N/2}$ by $-(\pi N/L)^2$. Then any odd derivative is obtained in a similar way as the first derivative and any even derivative in a similar way as the second derivative. It becomes evident that the last term, also called the ‘Nyquist term’, only contributes to even derivatives. In the numerical approach taken in this work, the de-aliasing is obtained by introducing a more restricting cut off at one third of the possible frequencies $(N/2)/3$ to ensure more accurate calculations. Finally, there exist other methods of de-aliasing, where a discussion can be found in Canuto et al. (2006).

Time-Stepping

After calculating all spatial derivatives a third-order Adams-Bashforth scheme, an explicit method, is used to evolve the equations in time. The choice of time-step length is restricted by stability constraints relating to the diffusion time and the wave travel time over a mesh interval. These two limits were found to be similar in magnitude (Matthews et al., 1995).

There exist several methods to evolve a system in time, which can be divided into explicit and implicit time-stepping methods. Explicit methods use the past state and the current state of the function to find the future state. Therefore, explicit methods are easy to implement, but require small time-steps for certain problems (Kuzmin, 2015). On the contrary, implicit methods incorporate an approximation of the later state to find the later state by solving an additional equation. So implicit methods require additional calculations that are difficult to implement, and are insufficiently accurate for transient problems (Kuzmin, 2015).

Apart from the classification of explicit and implicit methods there exist several numerical approaches for time-stepping, for example the Runge-Kutta method, Leapfrog method, and Adams methods. Runge-Kutta methods refer to the single-step methods (Butcher, 2008), but have multiple stages per step. The Leapfrog and Adams method are multi-step methods, where the past solutions are considered to evaluate the future solution. Although Runge-Kutta methods are the most popular methods, multi-step methods are more suitable for the code used here. All methods are generalisations of the Euler method, which was formulated as follows (Butcher, 2008). Consider the initial value problem:

$$s(t_0, x) = s_0(x), \quad \frac{\partial s(t, x)}{\partial t} \Big|_{t=t_0} = s_0^{(1)}(x). \quad (2.47)$$

Using the Euler method in order to find an approximation function $f(t, x)$ for the function $s(t, x)$ at a later time $t_0 + h$, the formula is given by

$$s(t_0 + h, x) \approx f(t_0 + h, x) = f(t_0, x) + hf_0^{(1)}(x). \quad (2.48)$$

In the numerical approach taken here, the time-step size depends on the diffusive times involved in the problem, such that time-steps are evaluated and adopted during run-time. Therefore, it is more convenient to use a multi-step method like the third-order Adams-Bashforth (AB) scheme. This method includes the time derivatives of the two previous time points. This means that f_{n+1} is evaluated in terms of f_n , $f_n^{(1)}$, $f_{n-1}^{(1)}$ and $f_{n-2}^{(1)}$, where the subscript n denotes the time point. Note, that when the numerical calculation is started no previous time points exist, so the first iteration uses the first-order AB method, the second uses the second order, and finally the third-order AB method is used for all following iterations. The lack of accuracy in the first time-steps is not important, because the problem considered does not crucially depend on the initial conditions. This has been checked using two-dimensional calculations that were started from different random perturbations. The resulting global and statistical quantities remained the same for different runs.

To illustrate how the Euler method has to be generalised to obtain higher order AB schemes, the second-order formula is derived: Consider the same initial value problem as in Equation (2.47), then expand Equation (2.48) up to terms including $f_{n-1}^{(1)}$:

$$f_{n+1} = f_n + \alpha_0 f_n^{(1)} + \alpha_1 f_{n-1}^{(1)}. \quad (2.49)$$

To find the Adams weights, α_0 and α_1 , the fundamental idea is to integrate $f^{(1)}$ from t_n to t_{n+1} and approximate the derivative $f^{(1)}$ by a polynomial of degree m (Duraishwami, 2010). The coefficients of the polynomial can be found from the $m + 1$ previously calculated points. Therefore, for the second-order AB formula, it is necessary to consider a polynomial of degree one, i.e. $P(t) = At + B$. Using the two points at n and $n - 1$, the following set of equations is obtained

$$At_n + B = f_n^{(1)}, \quad At_{n-1} + B = f_{n-1}^{(1)}. \quad (2.50)$$

Solving for the coefficients A and B , one gets

$$A = \left(f_n^{(1)} - f_{n-1}^{(1)} \right) / h_1, \quad B = \left(t_n f_{n-1}^{(1)} - t_{n-1} f_n^{(1)} \right) / h_1, \quad (2.51)$$

where $h_1 = t_n - t_{n-1}$. Note, the time-steps are not equidistant in the calculations used in this thesis. Then, integration of the polynomial gives

$$\begin{aligned} f_{n+1} - f_n &= \frac{1}{2}A(t_{n+1}^2 - t_n^2) + B(t_{n+1} - t_n) \\ &= f_n^{(1)} \left(\frac{(t_{n+1}^2 - t_n^2)}{2h_1} - \frac{h_0 t_{n-1}}{h_1} \right) - f_{n-1}^{(1)} \left(\frac{(t_{n+1}^2 - t_n^2)}{2h_1} - \frac{h_0 t_n}{h_1} \right), \end{aligned} \quad (2.52)$$

where $h_0 = t_{n+1} - t_n$. After rearranging one gets

$$f_{n+1} = f_n + f_n^{(1)} \left(h_0 + \frac{h_0^2}{h_1} \right) - \frac{h_0^2}{h_1} f_{n-1}^{(1)}. \quad (2.53)$$

Then, the coefficients for the second-order AB formula, see Equation (2.49), are

$$\alpha_0 = h_0 \left(1 + \frac{h_0}{2h_1} \right), \quad \alpha_1 = -\frac{h_0^2}{2h_1}. \quad (2.54)$$

In a similar way the coefficients for the third-order AB formula with non-uniform time-steps can be obtained

$$f_{n+1} = f_n + \alpha_0 f_n^{(1)} + \alpha_1 f_{n-1}^{(1)} + \alpha_2 f_{n-2}^{(1)} \quad (2.55)$$

with

$$\begin{aligned} \alpha_0 &= h_0 + \frac{h_0^2(h_1 + h_2)}{2h_1h_2} + \frac{h_0}{3h_1h_2}, \\ \alpha_1 &= \frac{h_0^2h_2}{2h_1(h_1 - h_2)} + \frac{h_0^3}{3h_1(h_1 - h_2)}, \\ \alpha_2 &= -\frac{h_0^2h_1}{2h_2(h_1 - h_2)} - \frac{h_0^3}{3h_2(h_1 - h_2)}, \end{aligned} \quad (2.56)$$

where the additional time-interval $h_2 = t_n - t_{n-2}$ was introduced.

Possible Numerical Inaccuracies

When using direct numerical calculations to solve the system numerically over considerable iterations, an issue concerning the momentum conservation might appear, which is specific to the choice of stress-free boundary conditions (see discussion in Jones et al., 2011). The equations for conservation of mass, momentum and mag-

netic field in this model are in conservative form. This is required to conserve the mass, momentum, and the divergence of the magnetic field up to machine precision. Despite the fact that Equation (2.14) together with the boundary conditions in Equation (2.18) conserves the momentum, a cumulative effect of truncation errors at each time-step might lead to a non-physical change in momentum when integrating over a vast number of time-steps. Both momentum and mass have been checked and are indeed conserved for all the calculations presented in this thesis.

3. Pure Hydrodynamic Shear Flow Instabilities

At the base of the solar convection zone there is a thin region of radial shear called the tachocline (Kosovichev et al., 1997; Tobias, 2004), which is believed to play a crucial role in the solar dynamo (see Silvers, 2008, and references therein). Velocity measurements suggest that the tachocline region is hydrodynamically stable against vertical shear flow (Miesch, 2007). However, helioseismology is restricted to large-scale time averaged measurements (Christensen-Dalsgaard and Thompson, 2007) and so turbulent motions can be still present on small length-scales and time-scales. Thus it is very plausible for the tachocline to appear as stable, using current helioseismology techniques, but actually be hydrodynamically or magnetohydrodynamically unstable.

Schatzman et al. (2000) have shown that shear turbulence can appear in a narrow part of the tachocline, although it is widely assumed that the tachocline is stable (see Tobias, 2004). An unstable tachocline would be significantly different in their dynamical interactions from a stable region. Therefore, in order to understand the role of this region, for example in the solar dynamo, it is essential to understand unstable shear flows in a polytropic atmosphere.

Before considering the full magnetohydrodynamical problem, a pure hydrodynamical system is investigated. This first study provides a reference system, which can help to understand systems when magnetic fields are involved. First, a brief overview of known results on shear flow instabilities will be given in Section 3.1. Then, I move on to introduce the linear stability analysis of the fully compressible stratified system in Section 3.2, which is a new approach to investigate the stability of shear flows

in polytropic atmospheres. The results of the stability analysis will be presented in Section 3.3, followed by a discussion in Section 3.4.

3.1. Shear Flow Instabilities

Shear flows occur in a wide variety of natural settings as for example in oceanic flows, planetary atmospheres, stars and galactic discs (see for example Sundberg et al., 2010; Itsweire et al., 1993; Hawley et al., 1999; Kitchatinov and Rüdiger, 2009). Therefore, there have been a number of previous investigations that examine shear flows in different contexts that can help inform the approach to the examination of shear flows in stars (Balbus and Hawley, 1991; Brandenburg et al., 1995; Hawley et al., 1999; Kitchatinov and Rüdiger, 2009). While studying flows in general there exist many mechanisms of instability. Generally instability may occur whenever the equilibrium of forces acting on the fluid is disturbed (Paterson, 1983; Drazin and Reid, 2004). Before discussing shear flow instabilities in more detail in Section 3.2, it is convenient to introduce the concept of stability and some well established results.

3.1.1. Concept of Stability

To give a general understanding of the concept of stability the equilibrium state is considered to be the base state of the system, which is defined as follows (Drazin and Reid, 2004; Chen and Huang, 2015).

Definition 1. *A state \mathbf{x}_e is called equilibrium state or equilibrium point of the system if the system remains in this point, \mathbf{x}_e , for all future times, t .*

Perturbing the base state by small disturbances may lead to either a decay of the disturbances, a growth of the disturbances or the initial disturbances will persist. A system in which small perturbations will decay away is called a stable system, whereas in an unstable system the initial perturbations will grow. Mathematically the concept of stability was formulated by Liapounov. A definition in the sense of Liapounov can be found in Chapter I in Drazin and Reid (2004) as follows:

Definition 2. *The equilibrium state \mathbf{x}_e is stable, if for any $\epsilon > 0 \quad \exists \quad \delta > 0$ such that if $\|\mathbf{x}(t = 0) - \mathbf{x}_e(t = 0)\| < \delta$ then $\|\mathbf{x}(t) - \mathbf{x}_e(t)\| < \epsilon \quad \forall \quad t \geq 0$.*

Having this definition in mind, it is possible to study the linear stability of a given system. This is achieved by decomposing all quantities into their background part and a small perturbation, i.e. $f(\mathbf{x}, t) = f_e(\mathbf{x}) + \delta f(\mathbf{x}, t)$, where f_e is the equilibrium solution for the governing equations. Using this decomposition a set of equations that does not include higher order perturbation terms can be derived (for the problem at hand I will derive these equations below in Subsection 3.2.2). By solving the linearised equations it can be concluded if a system is stable, i.e. the solution for the perturbations is a decaying function with time, or unstable, i.e. the solution is a growing function.

Dimensionless Numbers

In general to check for linear stability of a particular system, the set of linearised equations needs to be derived, a basic state found and then the solutions for the perturbations calculated. Since it is tedious to go through this procedure every time when a certain parameter of the system is changed, it is convenient to seek for dimensionless parameters that provide a good estimate of the stability of the system. This means stability criteria that separates stable from unstable systems.

To give a reasonable definition in terms of parameters for such a critical point it is necessary to understand what physical mechanism cause the instability. Generally, a system becomes unstable if the equilibrium between external forces, inertia and viscous stresses acting on the fluid is absent (Paterson, 1983; Drazin and Reid, 2004). Therefore, dimensionless numbers which can give a measure of the ratio between a stabilising and a destabilising mechanism are usually introduced to characterize systems. An illustrative example is the Rayleigh number Ra , which is used to characterize systems where the fluid is at rest and the bottom has a higher temperature than the top, i.e. a steep temperature gradient exists. In such a system the buoyancy force acts destabilising and diffusive forces counteract, therefore Ra is a ratio of these forces (Chandrasekhar, 1961).

For parallel shear flows in systems with a density change, the Richardson number, Ri , is such a characterizing number. It gives the ratio of the stabilising effect of gravitational force to the destabilisation caused by the shear profile (Chandrasekhar,

1961; Drazin and Reid, 2004). A derivation of the Richardson number criterion is shown further below.

3.1.2. Important Theorem's

Inflexion Point Theorem

In the past it was not always possible to use numerical approximations to solve the set of equations describing a hydrodynamical problem. Therefore, simplifying assumptions were made to reduce the complexity of the system to find analytical solutions. So many different configurations of shear flows have been investigated in the past, where the fluid was assumed to be non-diffusive and with constant density (Paterson, 1983). For such systems different continuous velocity profiles, as shown in Fig. 3.1, were studied in detail by Helmholtz (1868), Kelvin (1871) and Rayleigh (1880) (Drazin and Reid, 2004). These investigations revealed a crucial result on the role of an inflexion point in the velocity profile:

Theorem 3.1.1. (Rayleigh's Theorem) *A necessary condition for instability is that the basic velocity profile should have an inflexion point.*

According to the Rayleigh's Theorem an inviscid flow with a velocity profile as shown in Fig. 3.1 (a) would be stable, but a shear profile of the form as Fig. 3.1 (b) would be unstable.

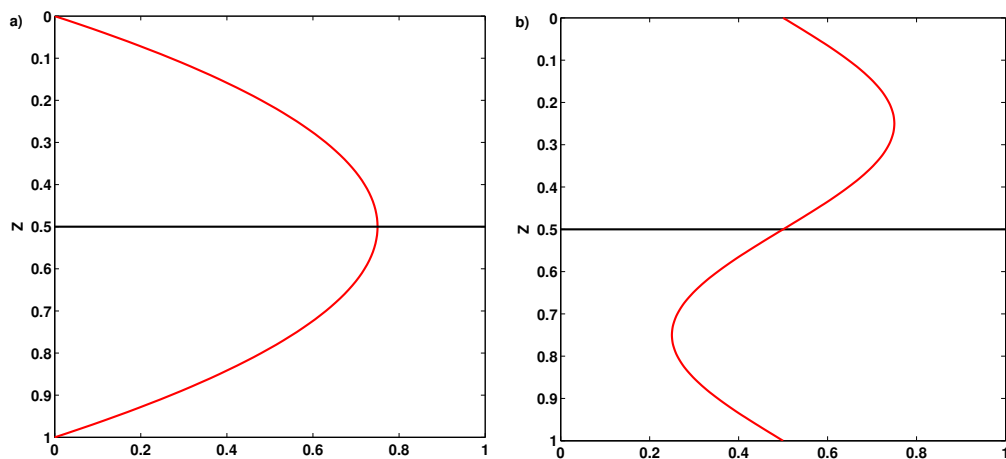


Figure 3.1.: The velocity profiles considered by Reynolds (1883). (a) Velocity profile without an inflection point. (b) Velocity profile with an inflection point.

A detailed derivation of this result can be found in Drazin and Reid (2004). Note, this is not a necessary criterion for a system with an interface of different densities as will be discussed in more detail further below.

Squire's Theorem

Another useful theorem is the Squire's Theorem (Squire, 1933; Drazin and Reid, 2004), which states that the set of linearised equations can be simplified to a two-dimensional problem without losing any information on the stability of the three-dimensional system if a Squire's transformation can be applied.

Theorem 3.1.2. Squire's Theorem on inviscid fluid (Squire, 1933): *To each unstable three-dimensional disturbance there corresponds a more unstable two-dimensional one.*

In order to prove the validity of this theorem, generally it is sufficient to find a coordinate transformation, such that given the solution for three dimensional problem, the solution for the two-dimensional problem will have a greater temporal growth rate.

In order to show an example the following three-dimensional simplified linearised set of equations is considered (Drazin and Reid, 2004):

$$ik_x(U_0 - \zeta)\hat{u} + \frac{dU_0}{dz}\hat{w} = -ik_x\hat{P}, \quad (3.1)$$

$$ik_x(U_0 - \zeta)\hat{v} = -ik_y\hat{P}, \quad (3.2)$$

$$ik_x(U_0 - \zeta)\hat{w} = -i\frac{d\hat{P}}{dz}, \quad (3.3)$$

$$i(k_x\hat{u} + k_y\hat{v}) + \frac{d\hat{w}}{dz} = 0, \quad (3.4)$$

which was derived from the Euler equation together with the incompressible condition by assuming that the velocity \mathbf{u} and the pressure P can be decomposed into a background part and small perturbations. The perturbations are assumed to be proportional to $\hat{P}(\mathbf{x}, t) = \hat{P}(z) \exp i(k_x x + k_y y - k_x \zeta t)$. Inserting this into the Euler equation and considering only terms that are first order in perturbations, the

Equations (3.2) - (3.4) are obtained. For the Squire's transformation, the following coordinate transformation can be used:

$$\tilde{k} = \sqrt{k_x^2 + k_y^2}, \quad \tilde{k}\tilde{u} = k_x\hat{u} + k_y\hat{v}, \quad \frac{\tilde{P}}{\tilde{k}_x} = \frac{\hat{P}}{k_x}, \quad \tilde{w} = \hat{w}, \quad \tilde{\zeta} = \zeta. \quad (3.5)$$

This coordinate transformation reduces the three dimensional set of equations to a two dimensional one:

$$\begin{aligned} i\tilde{k} \left(U_0 - \tilde{\zeta} \right) \tilde{u} + \frac{dU_0}{dz} \tilde{w} &= -i\tilde{k}\tilde{P} \\ i\tilde{k} \left(U_0 - \tilde{\zeta} \right) \tilde{w} &= -i\frac{d\tilde{P}}{dz} \\ i\tilde{k}\hat{u} + \frac{d\tilde{w}}{dz} &= 0, \end{aligned} \quad (3.6)$$

which becomes obvious, if setting both k_y and \hat{v} to zero in the Equations (3.2) - (3.4). In order to prove Squire's Theorem consider one solution to the three-dimension equations to be $\zeta = f(k_x)$, where $k_y = 0$ and $\hat{v} = 0$. Then, the solution of the two-dimensional problem formulated in (3.6) is $\tilde{\zeta} = f(\tilde{k})$. Using the Squire's transformation one gets the corresponding solution for the three-dimensional set of equations as $\zeta = f(\sqrt{k_x^2 + k_y^2})$. Therefore, to each disturbance in three dimensions with a growth rate $k_x\zeta_i$ there exist a two-dimensional disturbance that has the growth rate $\tilde{k}\tilde{\zeta}_i$. The growth rate of the two-dimensional disturbance is greater, because $\tilde{k} > k_x$ if $k_y \neq 0$.

3.1.3. Shear Flow Instabilities in Stratified Systems

The Kelvin-Helmholtz Instability

For a fluid that is heterogeneous (or stratified) and where the layers are in a relative motion to each other, the Kelvin-Helmholtz (KH) instability is a typical instability to occur (Miles, 1961). The simplest configuration where a KH instability appears is if one considers a horizontal superposition of two fluid layers with steady parallel flows of different velocities and densities as shown in Fig. 3.2 (a). For a continuously varying velocity profile as for example shown in Fig. 3.2 (b), a dimensionless number, the Richardson number, can be defined that provides information on the stability of the system (a detailed discussion can be found in Chandrasekhar, 1961).

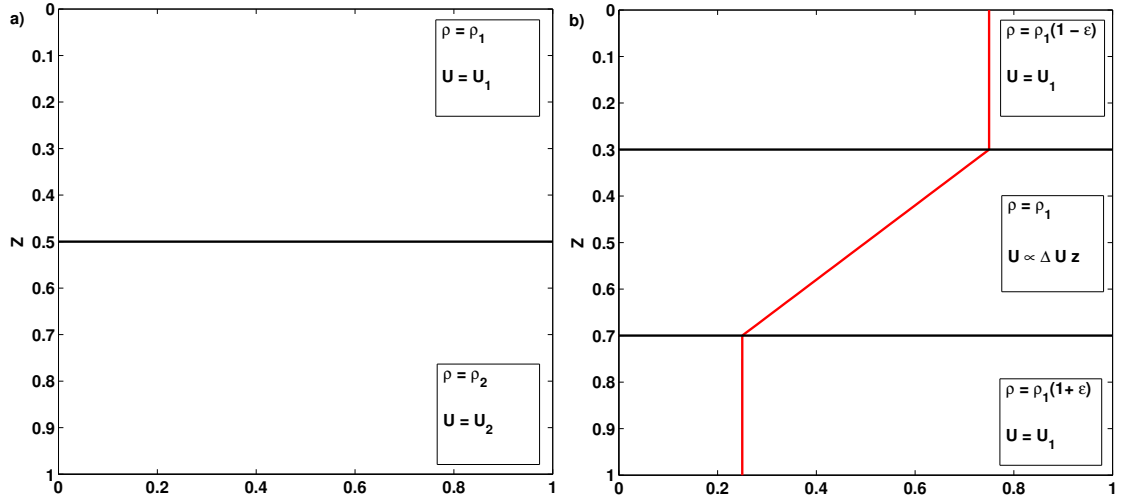


Figure 3.2.: Simple systems for a KH instability. (a) An interface with different density and velocity at the top layer and bottom layer is shown. (b) A three layered system, where the middle layer has a continuously changing velocity and density ρ_1 . The top layer has a constant velocity U_1 with a lower density and the bottom layer has a constant velocity U_2 .

The mechanism by which an instability in such a simple system can occur is due to the conversion of the kinetic energy of the global shear flow into kinetic energy of disturbances. If the kinetic energy of the disturbances is sufficient to overcome the potential energy required for the corresponding fluid parcel to rise, the system becomes unstable. Therefore, a simple criterion for stability can be derived as follows: Consider two fluid parcels of the same extent at two different heights z_0 and $z_0 + \delta z$, where it is assumed that the difference in heights δz is infinitesimally small. Furthermore, parcel one at z_0 has a density ρ_0 and parcel two has a density $\rho_0 + \delta \rho$. The initial velocities for parcel one and parcel two are U_0 and $U_0 + \delta U$, where $\delta U = (dU/dz)\delta z$, respectively. By interchanging these two parcels the work, W , per unit volume $W = -g\delta\bar{\rho}\delta z$, where $\delta\bar{\rho} = (d\bar{\rho}/dz)\delta z$, has to be done. The kinetic energy, E_{kin} , per unit volume that is gained can be calculated as the difference of the kinetic energy of the fluid parcels at their initial positions and velocities and the kinetic energy of the fluid parcels at their final positions and velocities. Assuming that the horizontal change in position is infinitesimally small and the momentum

conserved, parcel one (initially at z_0) will change its velocity to $U_0 + s\delta U$ and parcel two will have the velocity $U_0 + (1-s)\delta U$. Therefore, the kinetic energy difference is

$$\delta E_{kin} = s(1-s)\bar{\rho}(\delta U)^2 + sU_0\delta U\delta\bar{\rho} \quad (3.7)$$

An instability can only occur if the work done by the kinetic energy due to the relative motion of the layers cannot be balanced by the gravitational acceleration. Therefore, by requiring $W \leq \delta E_{kin}$ a necessary condition for instability is derived:

$$-g\frac{d\bar{\rho}}{dz} \leq s(1-s)\bar{\rho}\left(\frac{dU_0}{dz}\right)^2 + sU_0\frac{dU_0}{dz}\frac{d\bar{\rho}}{dz} \leq \frac{1}{4}\bar{\rho}\left(\frac{dU_0}{dz}\right)^2 + sU_0\frac{dU_0}{dz}\frac{d\bar{\rho}}{dz}, \quad (3.8)$$

where the second inequality becomes an equality for $s = 1/2$. Since this is an upper bound on a necessary criterion, it is possible to decrease the right-hand side further by considering only the first term. This leads to

$$-g\frac{d\bar{\rho}/dz}{\bar{\rho}(dU_0/dz)^2} \leq \frac{1}{4}, \quad (3.9)$$

where the left-hand side is a non-dimensional expression, called Richardson number, Ri , after Richardson who applied this argument to turbulence. Therefore, a necessary criterion for stability requires the Richardson number to be greater than $1/4$ everywhere in the domain (Miles, 1961). However, this criterion is valid for inviscid fluids and under the assumption that the inertial effects of density variation can be neglected.

Since in this work stratified systems are considered and the Boussinesq approximation does not apply the general definition of the Brunt-Väisälä frequency given by

$$N^2(z) = \frac{g}{\tilde{T}} \frac{\partial \tilde{T}}{\partial z}, \quad (3.10)$$

where $\tilde{T} = TP^{1/\gamma-1}$, the potential temperature, needs to be used. Then, by using the polytropic relation and the initial temperature profile given in Equation (2.20) the Brunt-Väisälä frequency becomes

$$N^2(z) = g \left(T^{-1/\gamma} \frac{\partial T^{1/\gamma}}{\partial z} + \rho^{1-1/\gamma} \frac{\partial \rho^{1/\gamma-1}}{\partial z} \right) = g \left(\frac{1}{\gamma T} \frac{\partial T}{\partial z} + \left(\frac{1}{\gamma} - 1 \right) \frac{1}{\rho} \frac{\partial \rho}{\partial z} \right). \quad (3.11)$$

Inserting the background temperature profile and density profile, as can be found in Equations (2.20) - (2.21), the initial Brunt-Väisälä frequency becomes

$$N^2(z) = \frac{g\theta}{1+z\theta} \left(\frac{1+m}{\gamma} - m \right) \quad (3.12)$$

and the minimal local Richardson number for stratified systems is defined as

$$Ri_{min} = \min_{0 \leq z \leq 1} \left(N(z)^2 / \left(\frac{\partial u_0(z)}{\partial z} \right)^2 \right). \quad (3.13)$$

Holmboe Instability

Another more exotic instability was found in stratified systems with symmetric background profiles, i.e. the velocity profile and stratification are line symmetric along a horizontal interface. This instability was first investigated by Holmboe and so it is called the Holmboe instability (Holmboe, 1962). The Holmboe instability results from interacting waves, that propagate in opposite directions (Baines and Mitsudera, 1994). The Holmboe instability differs from the KH instability in several ways (see the review article by Peltier and Caulfield, 2003). First, the KH instability is stationary in a frame of reference, but the Holmboe instability has counter propagating unstable modes, which both have the same growth rate. One mode occupies the upper plane and the other the lower plane, such that a superposition of both solutions form a standing wave solution. Second, the Holmboe instability is favoured in stable stratified atmospheres and can dominate the Kelvin-Helmholtz instability when the stratification is increased, such that a KH instability disappears due to the Richardson criterion (Peltier and Smyth, 1989).

3.2. Considering Complex Shear Flows

General investigations of shear flows in the past considered simplified systems, i.e. non-diffusive fluids or incompressible fluids by using the Boussinesq approximation. However, viscous and thermal dissipation affect both the linear stability and the non-linear evolution of a shear flow. Dropping those simplifications may alter the stability criterion such that in a system where thermal diffusion becomes important and acts on a smaller time-scale than buoyancy the stability criterion requires a

significant modification. Dudis (1974) and Zahn (1974) have shown that in such systems the product of the Richardson number with the Péclet number is the quantity that indicates stability. The effect of thermal diffusion on shear instabilities was only studied in the Boussinesq approximation by Jones (1977), Dudis (1974) and more recently by Lignières et al. (1999), such that it is not directly applicable for stellar interiors regions in which large pressure gradients have to be considered. While Miczek (2013) considers a fully compressible fluid in an adiabatic atmosphere, the effect of varying all, especially thermal, transport coefficients was not studied. Therefore, this study does not capture all relevant effects present in all regions of stellar interiors.

Although, considerable work has been undertaken to examine shear flows in a variety of different contexts, no work to examine fully compressible shear flows in a polytropic atmosphere has been carried out and thus I will conduct this research. In the following subsections I will discuss the choice for the background shear flow profile, I will derive the set of linearised equations for our particular system, and discuss how they are solved. Then, in the Section 3.3 results for differently stratified systems will be presented.

3.2.1. Shear Flow Profile

Since one is interested in investigating a shear flow, it is necessary to consider an initial background velocity, which satisfies the purpose and the boundary conditions. Previous studies of astrophysical flows looked at an assortment of different velocity profiles, depending on the problem and choice of boundary conditions. In the case of Keplerian motion, which is investigated in the context of accretion discs, usually a linear velocity profile is assumed (e.g. Brandenburg et al., 1995; Hawley et al., 1999; Dubrulle et al., 2005; Silvers, 2008). This type of shear profile does not require an external force to balance viscous dissipation and instead the velocity is incorporated via a shearing-box approach (Goldreich and Lynden-Bell, 1965; Narayan et al., 1987), where the velocity is instantaneously present. In contrast, some investigations of stellar shear flows have used polynomial functions, as for example in Tobias and Hughes (2004) and Cline et al. (2003a), while other investigations have utilized trigonometric functions to model the velocity field (see,

for example, Hughes and Proctor, 2013; Cline et al., 2003b). Such velocity profiles have a non-vanishing gradient at the boundaries. In order to minimise the effect of the boundaries on the shear layer a hyperbolic tangent profile can be used (see for example Brüggem and Hillebrandt, 2001; Hughes and Tobias, 2001; Vasil and Brummell, 2008). In addition, hyperbolic tangent profiles are commonly used in classical studies of Kelvin-Helmholtz instability and turbulence. Therefore, here the background velocity profile takes the form

$$u(z) = U_0 \tanh\left(\frac{z - 0.5}{L_u}\right) \quad (3.14)$$

with a shear amplitude U_0 and a scaling factor $1/L_u$ that controls the width of the shear profile, see Fig. 3.3 for example profiles. The boundary conditions introduced

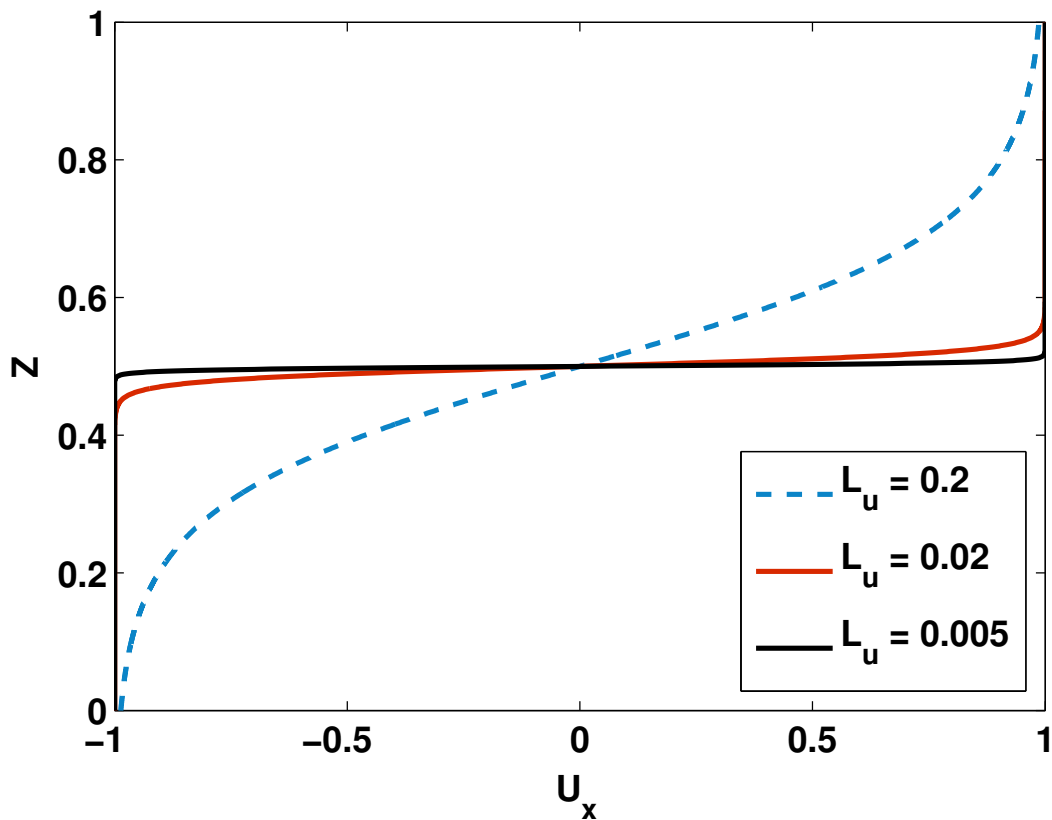


Figure 3.3.: Example background shear flow profiles for three different L_u . Shear flow profiles with very small and very large characteristic length L_u for comparison.

in Equation (2.18) and Equation (2.19) restrict our shear profile to values of L_u , which will result in a small enough value of the z -derivative at the boundaries. For the initial static state the temperature and density profiles are taken as in

Equation (2.20) and Equation (2.21), respectively. Then, the equilibrium state is characterized by $\mathbf{u}_0(z) = (u(z), 0, 0)^T$, $T_0(z)$, $P_0(z)$ and $\rho_0(z)$. The local Richardson number, defined in Equation (3.13), for such systems becomes

$$Ri_{min} = \min_{0 \leq z \leq 1} \left(\frac{\theta^2 L_u^2 (m+1) \left(\frac{m+1}{\gamma} - m \right)}{(1 + \theta z) (U_0 - u_0(z)^2/U_0)^2} \right), \quad (3.15)$$

where the derivative of the background velocity profile, defined in Equation (3.14), with respect to z corresponds to a local turnover rate of the shear. For most cases the minimum Ri value is at $z = 0.5$, but for some parameter choices with large temperature gradient, θ , and broad shear width the minimum is shifted towards greater z .

3.2.2. Linear Stability Analysis

The best starting point to study a system is to start by investigating its linear stability. This is achieved by linearising the governing equations (see Section 2.2.1, Equations (2.13) - (2.15)), finding the initial basic state and studying the linear perturbation evolution in time. For systems, where any diffusive processes are considered a static initial state can not be defined. Therefore, it is necessary to consider a basic state for which the typical diffusive time-scales are much greater than the time that is required to develop the linear instability. Performing a stability analysis with such quasi-static initial states requires an *a posteriori* verification.

In a diffusive system there are a number of different time-scales for the system including the time-scale associated with the shear dynamics $t_S = L_u/(U_0)$, the time-scale for buoyancy $t_B = 1/N(z)$, where $N(z)^2$ is the Brunt-Väisälä frequency defined in Equation (3.10), and the time-scale for thermal diffusion $t_k = L_u^2/C_k$. In this thesis, the focus is on the regime where the viscous time-scale, $t_\mu = L_u^2/\mu$, is much larger than any other time-scales. This allows us to neglect viscous heating, which corresponds to the first term on the right-hand side in Equation (2.15). In addition, the shear flow given by Equation (3.14) is in equilibrium only if t_μ is much larger than the instability time-scale, which is verified *a posteriori*. When t_μ

becomes comparable with other relevant time-scales, the background shear flow is not in equilibrium and the analysis would be inappropriate for this case.

Formulation of the Eigenvalue Problem

In order to derive the linearised equations each quantity that appears in the governing Equations (2.13) - (2.15) is perturbed such that $f = f_0 + \delta f$ and

$$\delta f(x, y, z, t) = \tilde{f}(z) \exp(ikx + ily + \zeta t), \quad (3.16)$$

where $k \in \mathbb{R}$ and $l \in \mathbb{R}$ are the horizontal wave numbers, and $\zeta = \zeta_r + i\zeta_i \in \mathbb{C}$, where ζ_r gives the growth rate of the linear instability. Then, for the stability analysis of a shear flow in x -direction, where the basic state depends only on the vertical direction the equilibrium state is characterized by $\mathbf{u}_0(z)$, $T_0(z)$, $P_0(z)$ and $\rho_0(z)$, the linear perturbations can be expanded around that equilibrium state as follow

$$\mathbf{u} = \mathbf{u}_0 + \delta\mathbf{u}, \quad T = T_0 + \delta T, \quad \rho = \rho_0 + \delta\rho, \quad P = P_0 + \delta P. \quad (3.17)$$

In order to keep the notation simple, the velocity perturbations are denoted by $\delta\mathbf{u} = (u, v, w)^T$ and the initial velocity $\mathbf{u}_0 = (U_0(z), 0, 0)$, where it was assumed that only a horizontal component is present. Inserting this decomposition back into the governing Equations (2.13) - (2.15) and keeping only terms that are of linear order in perturbations lead to a set of linearised coupled set of equations. The continuity equation becomes

$$\zeta\delta\rho = -(iku + ilv)\rho_0 - \frac{\partial}{\partial z}(w\rho_0) - ik\delta\rho U_0. \quad (3.18)$$

The three components of the Navier-Stokes equation in linearised form are

$$\begin{aligned} \zeta\rho_0 u = & -ik(\rho_0\delta T + T_0\delta\rho) - \rho_0 w \frac{\partial U_0}{\partial z} - ik\rho_0 U_0 u \\ & + \sigma C_k \left(-\frac{4}{3}k^2 u - l^2 u + \frac{\partial^2 u}{\partial z^2} - kl\frac{1}{3}v + ik\frac{1}{3}\frac{\partial w}{\partial z} \right), \end{aligned} \quad (3.19)$$

$$\begin{aligned} \zeta \rho_0 v = & -il(\rho_0 \delta T + T_0 \delta \rho) - ik \rho_0 U_0 v \\ & + \sigma C_k \left(-k^2 v - \frac{4}{3} l^2 v + \frac{\partial^2 v}{\partial z^2} - kl \frac{1}{3} u + \frac{1}{3} il \frac{\partial w}{\partial z} \right), \end{aligned} \quad (3.20)$$

$$\begin{aligned} \zeta \rho_0 w = & -\frac{\partial}{\partial z} (\rho_0 \delta T + T_0 \delta \rho) - ik \rho_0 U_0 w + \delta \rho \theta (m+1) \\ & + \sigma C_k \left(-k^2 w - l^2 w + \frac{4}{3} \frac{\partial^2 w}{\partial z^2} + ik \frac{1}{3} \frac{\partial u}{\partial z} + il \frac{1}{3} \frac{\partial v}{\partial z} \right), \end{aligned} \quad (3.21)$$

and the linear heat equation is

$$\begin{aligned} \zeta \delta T = & \frac{C_k \gamma}{\rho_0} \left(\frac{\partial^2 \delta T}{\partial z^2} - k^2 \delta T - l^2 \delta T \right) - (\gamma - 1) T_0 \left(ik u + il v + \frac{\partial w}{\partial z} \right) \\ & - ik U_0 \delta T - w \frac{\partial T_0}{\partial z}. \end{aligned} \quad (3.22)$$

A more general and detailed derivation, where the basic flow can have components in both horizontal direction can be found in Appendix A.2.

Note, the equations for the perturbed quantities that are obtained do not inherit the same symmetry properties as the well known Taylor-Goldstein equation (e.g. Miles, 1961), where taking the complex conjugate of the eigenfunction and eigenvalue leads to the same equation. This symmetry is broken in this set of equations, because there are still terms linear in k and l . Therefore, for this eigenvalue problem there do not necessarily exist two complex conjugated solutions where one is decaying and one is a growing solution.

In order to simplify the computation it is convenient to use the Squire's theorem (see Theorem 3.1.2), which was formulated for an inviscid fluid, but can be used for a viscous fluid as well, if the corresponding Squire transformation exist. Then, to simplify the three-dimensional problem to a corresponding two-dimensional one, I found a Squire transformation for the initial set of equations. The transformation can be written as:

$$\begin{aligned} \tilde{k}^2 &= k^2 + l^2 & \tilde{k} \delta \tilde{u} &= k \delta u + l \delta v & \delta \tilde{w} &= \delta w \\ \tilde{U}_0 &= U_0 & \tilde{c} &= c & \tilde{\theta} (\tilde{m} + 1) &= \frac{\tilde{k}^2}{k^2} \theta (m + 1) \\ \delta \tilde{T} &= \frac{\tilde{k}}{k} \delta T & \tilde{T}_0 &= \frac{\tilde{k}^2}{k^2} T_0 \\ \tilde{\rho}_0 &= \frac{k}{\tilde{k}} \frac{\tilde{C}_k}{C_k} \rho_0 & \delta \tilde{\rho} &= \frac{k}{\tilde{k}} \frac{\tilde{\rho}_0}{\rho_0} \delta \rho \end{aligned} \quad (3.23)$$

In the linearised equations $\zeta = kc$, such that $\tilde{\zeta} = \tilde{k}\zeta/k$. Note, I have also checked numerically that indeed for a certain wave number k the growth rate ζ_r decreases with increasing l , one could have set $l = 0$ and $v = 0$ without loss of generality for the following calculations. To show how the three-dimensional set of equations transforms under the Squire's transformation, a detailed calculations is presented in the following. Inserting the transformation into the continuity equation leads to

$$\begin{aligned} \frac{k}{\tilde{k}} \tilde{\zeta} \frac{\tilde{k}\rho_0}{k\tilde{\rho}_0} \delta\tilde{\rho} &= -i(\tilde{k}\tilde{u}) \frac{\tilde{k}C_k}{k\tilde{C}_k} \tilde{\rho}_0 - \frac{\tilde{k}C_k}{k\tilde{C}_k} \frac{\partial}{\partial z} (\tilde{w}\tilde{\rho}_0) - ik \frac{\tilde{k}\rho_0}{k\tilde{\rho}_0} \delta\tilde{\rho}\tilde{U}_0 \\ \frac{\rho_0}{\tilde{\rho}_0} \tilde{\zeta} \delta\tilde{\rho} &= -i(\tilde{k}\tilde{u}) \underbrace{\frac{\tilde{k}C_k}{k\tilde{C}_k}}_{=\rho_0/\tilde{\rho}_0} \tilde{\rho}_0 - \underbrace{\frac{\tilde{k}C_k}{k\tilde{C}_k}}_{=\rho_0/\tilde{\rho}_0} \frac{\partial}{\partial z} (\tilde{w}\tilde{\rho}_0) - ik \frac{\rho_0}{\tilde{\rho}_0} \delta\tilde{\rho}\tilde{U}_0 \\ \tilde{\zeta} \delta\tilde{\rho} &= -i(\tilde{k}\tilde{u})\tilde{\rho}_0 - \frac{\partial}{\partial z} (\tilde{w}\tilde{\rho}_0) - ik\delta\tilde{\rho}\tilde{U}_0 \end{aligned} \quad (3.24)$$

For the next equation it is necessary to multiply Equation (3.19) by k and Equation (3.20) by l and add them up to get

$$\begin{aligned} k\zeta\rho_0u + l\zeta\rho_0v &= -i(k^2 + l^2) (\rho_0\delta T + T_0\delta\rho) - k\rho_0w \frac{\partial U_0}{\partial z} - ik\rho_0U_0 (ku + lv) \\ &\quad + \sigma C_k \left(-\frac{4}{3}k^3u - kl^2u + k \frac{\partial^2 u}{\partial z^2} - k^2l \frac{1}{3}v + ik^2 \frac{1}{3} \frac{\partial w}{\partial z} \right) \\ &\quad + \sigma C_k \left(-lk^2v - \frac{4}{3}l^3v + l \frac{\partial^2 v}{\partial z^2} - kl^2 \frac{1}{3}u + \frac{1}{3}il^2 \frac{\partial w}{\partial z} \right) \\ \frac{k}{\tilde{k}} \tilde{\zeta} \frac{\tilde{k}C_k}{k\tilde{C}_k} \tilde{\rho}_0 \tilde{k}\tilde{u} &= -i\tilde{k} \left(\frac{\tilde{k}C_k}{k\tilde{C}_k} \tilde{\rho}_0 \frac{k}{\tilde{k}} \delta\tilde{T} + \frac{k^2}{\tilde{k}^2} \tilde{T}_0 \frac{\tilde{k}\rho_0}{k\tilde{\rho}_0} \delta\tilde{\rho} \right) - k \frac{\tilde{k}C_k}{k\tilde{C}_k} \tilde{\rho}_0 \tilde{w} \frac{\partial \tilde{U}_0}{\partial z} - ik \frac{\tilde{k}C_k}{k\tilde{C}_k} \tilde{\rho}_0 \tilde{U}_0 \tilde{k}\tilde{u} \\ &\quad + \sigma C_k \left(-\frac{4}{3} (k^3u + kl^2u + k^2lu + l^3v) + \tilde{k} \frac{\partial \tilde{u}}{\partial z} + ik^2 \frac{1}{3} \frac{\partial \tilde{w}}{\partial z} \right) \\ \frac{\tilde{k}C_k}{\tilde{C}_k} \tilde{\zeta} \tilde{\rho}_0 \tilde{u} &= -i \frac{\tilde{k}C_k}{\tilde{C}_k} \left(\tilde{\rho}_0 \delta\tilde{T} + \tilde{T}_0 \delta\tilde{\rho} \right) - \frac{\tilde{k}C_k}{\tilde{C}_k} \tilde{\rho}_0 \tilde{w} \frac{\partial \tilde{U}_0}{\partial z} - i \frac{\tilde{k}C_k}{\tilde{C}_k} \tilde{\rho}_0 \tilde{U}_0 \tilde{k}\tilde{u} \\ &\quad + \sigma C_k \tilde{k} \left(-\frac{4}{3} \tilde{k}^2 \tilde{u} + \frac{\partial \tilde{u}}{\partial z} + ik \frac{1}{3} \frac{\partial \tilde{w}}{\partial z} \right) \\ \tilde{\zeta} \tilde{\rho}_0 \tilde{u} &= -i \left(\tilde{\rho}_0 \delta\tilde{T} + \tilde{T}_0 \delta\tilde{\rho} \right) - \tilde{\rho}_0 \tilde{w} \frac{\partial \tilde{U}_0}{\partial z} - ik \tilde{\rho}_0 \tilde{U}_0 \tilde{u} \\ &\quad + \sigma \tilde{C}_k \left(-\frac{4}{3} \tilde{k}^2 \tilde{u} + \frac{\partial \tilde{u}}{\partial z} + ik \frac{1}{3} \frac{\partial \tilde{w}}{\partial z} \right) \end{aligned} \quad (3.25)$$

Then the third Navier-Stokes equation using the transformation in Equation (3.23) becomes:

$$\begin{aligned}
 \frac{k}{\tilde{k}} \frac{\tilde{k} C_k}{\tilde{C}_k} \tilde{\rho}_0 \tilde{w} &= - \frac{\partial}{\partial z} \left(\frac{\tilde{k} C_k}{\tilde{C}_k} \tilde{\rho}_0 \frac{k}{\tilde{k}} \delta \tilde{T} + \frac{k^2}{\tilde{k}^2} \tilde{T}_0 \frac{\tilde{k} \rho_0}{k \tilde{\rho}_0} \delta \tilde{\rho} \right) - ik \frac{\tilde{k} C_k}{\tilde{C}_k} \tilde{\rho}_0 \tilde{U}_0 \tilde{w} + \frac{\tilde{k} \rho_0}{k \tilde{\rho}_0} \delta \tilde{\rho} \frac{k^2}{\tilde{k}^2} \tilde{\theta} (\tilde{m} + 1) \\
 &\quad + \sigma C_k \left(- (\tilde{k}^2 - l^2) \tilde{w} - l^2 \tilde{w} + \frac{4}{3} \frac{\partial^2 \tilde{w}}{\partial z^2} + i \frac{1}{3} \frac{\partial}{\partial z} (uk + il) \right) \\
 \tilde{\zeta} \frac{C_k}{\tilde{C}_k} \tilde{\rho}_0 \tilde{w} &= - \frac{\partial}{\partial z} \left(\frac{C_k}{\tilde{C}_k} \tilde{\rho}_0 \delta \tilde{T} + \frac{k \rho_0}{\tilde{k} \tilde{\rho}_0} \tilde{T}_0 \delta \tilde{\rho} \right) - i \tilde{k} \frac{C_k}{\tilde{C}_k} \tilde{\rho}_0 \tilde{U}_0 \tilde{w} + \underbrace{\frac{k \rho_0}{\tilde{k} \tilde{\rho}_0}}_{=C_k/\tilde{C}_k} \delta \tilde{\rho} \tilde{\theta} (\tilde{m} + 1) \\
 &\quad + \sigma C_k \left(-\tilde{k}^2 \tilde{w} + \frac{4}{3} \frac{\partial^2 \tilde{w}}{\partial z^2} + i \tilde{k} \frac{1}{3} \frac{\partial \tilde{w}}{\partial z} \right) \\
 \tilde{\zeta} \tilde{\rho}_0 \tilde{w} &= - \frac{\partial}{\partial z} \left(\tilde{\rho}_0 \delta \tilde{T} + \tilde{T}_0 \delta \tilde{\rho} \right) - i \tilde{k} \tilde{\rho}_0 \tilde{U}_0 \tilde{w} + \delta \tilde{\rho} \tilde{\theta} (\tilde{m} + 1) \\
 &\quad + \sigma \tilde{C}_k \left(-\tilde{k}^2 \tilde{w} + \frac{4}{3} \frac{\partial^2 \tilde{w}}{\partial z^2} + i \tilde{k} \frac{1}{3} \frac{\partial \tilde{w}}{\partial z} \right)
 \end{aligned} \tag{3.26}$$

Finally, the temperature evolution equation becomes

$$\begin{aligned}
 \frac{k}{\tilde{k}} \frac{\tilde{k} C_k}{\tilde{C}_k} \delta \tilde{T} &= \frac{k \tilde{C}_k C_k \gamma}{\tilde{k} C_k \tilde{\rho}_0} \left(\frac{k}{\tilde{k}} \frac{\partial^2 \delta \tilde{T}}{\partial z^2} - \tilde{k}^2 \frac{k}{\tilde{k}} \delta \tilde{T} \right) - (\gamma - 1) \frac{k^2}{\tilde{k}^2} \tilde{T}_0 \left(i \tilde{k} \tilde{u} + \frac{\partial \tilde{w}}{\partial z} \right) \\
 &\quad - ik \tilde{U}_0 \frac{k}{\tilde{k}} \delta \tilde{T} - \tilde{w} \frac{k^2}{\tilde{k}^2} \frac{\partial \tilde{T}_0}{\partial z} \\
 \frac{k^2}{\tilde{k}^2} \tilde{\zeta} \delta \tilde{T} &= \frac{k^2 \tilde{C}_k \gamma}{\tilde{k}^2 \tilde{\rho}_0} \left(\frac{\partial^2 \delta \tilde{T}}{\partial z^2} - \tilde{k}^2 \delta \tilde{T} \right) - (\gamma - 1) \frac{k^2}{\tilde{k}^2} \tilde{T}_0 \left(i \tilde{k} \tilde{u} + \frac{\partial \tilde{w}}{\partial z} \right) \\
 &\quad - i \frac{k^2}{\tilde{k}} \tilde{U}_0 \delta \tilde{T} - \frac{k^2}{\tilde{k}^2} \tilde{w} \frac{\partial \tilde{T}_0}{\partial z} \\
 \tilde{\zeta} \delta \tilde{T} &= \frac{\tilde{C}_k \gamma}{\tilde{\rho}_0} \left(\frac{\partial^2 \delta \tilde{T}}{\partial z^2} - \tilde{k}^2 \delta \tilde{T} \right) - (\gamma - 1) \tilde{T}_0 \left(i \tilde{k} \tilde{u} + \frac{\partial \tilde{w}}{\partial z} \right) - i \tilde{k} \tilde{U}_0 \delta \tilde{T} - \tilde{w} \frac{\partial \tilde{T}_0}{\partial z}
 \end{aligned} \tag{3.27}$$

For simplicity, I will drop the tilde for all quantities and summarise the linearised equations.

Having applied the Squire's transformation formulated in Equation (3.23), the two-dimensional linearised coupled set of equations reads:

$$\zeta \delta \rho = -iku\rho_0 - \frac{\partial}{\partial z}(w\rho_0) - ik\delta\rho U_0 \quad (3.28)$$

$$\begin{aligned} \zeta \rho_0 u &= -ik(\rho_0 \delta T + T_0 \delta \rho) - \rho_0 w \frac{\partial U_0}{\partial z} - ik\rho_0 u U_0 \\ &\quad - C_k \sigma \left(\frac{4}{3} k^2 u - \frac{\partial^2 u}{\partial z^2} - \frac{1}{3} ik \frac{\partial w}{\partial z} \right) \end{aligned} \quad (3.29)$$

$$\begin{aligned} \zeta \rho_0 w &= -\frac{\partial}{\partial z}(\rho_0 \delta T + T_0 \delta \rho) - ikU_0 \rho_0 w + \theta(m+1)\delta\rho \\ &\quad - C_k \sigma \left(k^2 w - \frac{4}{3} \frac{\partial^2 w}{\partial z^2} - \frac{1}{3} \frac{\partial}{\partial z}(iku) \right) \end{aligned} \quad (3.30)$$

$$\begin{aligned} \zeta \delta T &= \frac{C_k \gamma}{\rho_0} \left(\frac{\partial^2 \delta T}{\partial z^2} - k^2 \delta T \right) - ikU_0 \delta T \\ &\quad - (\gamma - 1) T_0 \left(iku + \frac{\partial w}{\partial z} \right) - w \frac{\partial T_0}{\partial z} \end{aligned} \quad (3.31)$$

The boundary conditions are the same as for the non-linear set of equations, defined in Equations (2.18) - (2.19) but for two-dimensions. A similar set of equations was derived for a MHD problem by Tobias and Hughes (2004). The system is characterized by six parameters m , θ , σ , C_k , M and L_u .

Eigenvalue Problem Solver

Equations (3.29) - (3.31) are numerically solved on a one dimensional grid in z -direction that is discretised uniformly, this method is adapted from the method used by Favier et al. (2012). Recasting the set of differential equations into the form

$$\zeta \mathbf{f} = A \mathbf{f}, \quad (3.32)$$

where the matrix A contains the finite difference coefficients applied to the discretised eigenfunctions $\mathbf{f} = (\delta\rho, u, v, w, \delta T)^T$, reduces the problem to a matrix equation. For the computation of the relevant coefficients in A , a central fourth-order finite differences scheme was used. To find the eigenvalues and vectors the Schur factorization is used (Anderson et al., 1999). Having solved the eigenvalue problem numerically leads to several solutions. Therefore, I seek for solutions that satisfy the following two conditions: The eigenvector w needs to vanish at the boundaries,

and real part of the eigenvalue ζ has to be the largest eigenvalue. Because the ultimate aim is to undertake non-linear simulations with a pseudo-spectral code and viscosity will be mandatory in that case, most calculations will consider a viscous fluid.

3.3. Results

In this section I will focus on a number of key areas of interest. First, the change of the stability threshold while the Mach number is varied will be presented, which correspond to a continuous transition between an incompressible to a compressible fluid. The effect of compressibility is separately investigated in a weakly thermally stratified and a strongly thermally stratified atmosphere in Section 3.3.1. Later in Section 3.3.2, the growth rates of the linear shear instability together with the critical Ri for different Péclet numbers are compared and the effect on the stability against buoyancy is discussed. In Section 3.3.3 the effect of different polytropic indices on the instability is addressed and the possibility of a Holmboe like instability is investigated in Section 3.3.4.

3.3.1. The Effect of Varying the Mach Number on the Instability Threshold

As the Richardson criterion is based on simple energetic arguments and does not take compressibility into account, clarification is needed to determine whether compressibility affects the stability of a shear flow. Therefore, in this section I focus on the stability threshold for different Mach numbers in a stably stratified fluid with $m = 1.6$, where the Mach number, M , will be given as

$$M = \frac{U_0}{\sqrt{(1 + 0.5\theta)}}. \quad (3.33)$$

This form of M arises because of the particular non-dimensionalisation used in Section 2.2. Velocity is given in units of the speed of sound that is computed at the top of the domain. However, the temperature changes across the domain and so

does the speed of sound. As the inflexion point of the shear flow is at $z = 0.5$ it is necessary to compute the actual Mach number at $z = 0.5$.

According to Schochet (1994) and Guillard and Murrone (2004) the solutions of the compressible Euler equations reduce to the solutions of the incompressible Euler equations in the low Mach number limit. Thus, varying of the Mach number allows to investigate the validity of the Richardson criterion for low to moderate Mach numbers ($0.02 < M < 0.15$).

To find the critical Richardson number, Ri , the eigenvalue problem formulated in Equation (3.32) for a small Ri is solved, while varying the wave numbers, k , between 0 and $1/L_u$ to find the most unstable mode k_{max} . For large, but finite, Reynolds numbers the system is assumed to be stable if the growth rate, ζ , is less or equal to zero for all wave numbers or the time-scale for the instability, $t_\zeta = 1/\zeta$, compared to the viscous time-scale, t_μ , is of the same order.

I perform a detailed survey for $\theta = 2$, a weakly stratified atmosphere, and for $\theta = 10$, a strongly stratified atmosphere. In this investigation the Prandtl number is $\sigma = 1.0$ and the thermal diffusivity is $C_k = 10^{-6}$. In Fig. 3.4 the critical Richardson numbers found in this study for different Mach numbers are shown. It reveals that the critical Richardson number decreases for Mach numbers greater than 0.08. Whereas for very small Mach numbers the critical Richardson number does not significantly deviate from the well known $1/4$ threshold for stability. In the case of a weakly stratified atmosphere the critical Richardson number decreases rapidly below $Ri = 0.1$ for $M \approx 0.14$. In a strongly stratified fluid a qualitatively same behaviour as for the weakly stratified case is found, but the critical Richardson number does not drop below $Ri = 0.2$ for $M \approx 0.14$. The shift of the stability threshold, for both cases, towards smaller Richardson number for moderate Mach number indicates a stabilising effect of compressibility on the KH instability.

The stabilising effect for Mach numbers greater than 0.08, found in this investigation, can be explained as follows. The Richardson criterion uses simple energetic arguments, where two neighbouring fluid parcels are exchanged. The density of these parcels remains constant for an incompressible fluid such that only the change in velocity at different height changes the kinetic energy, ΔE_{kin} , and the potential energy,

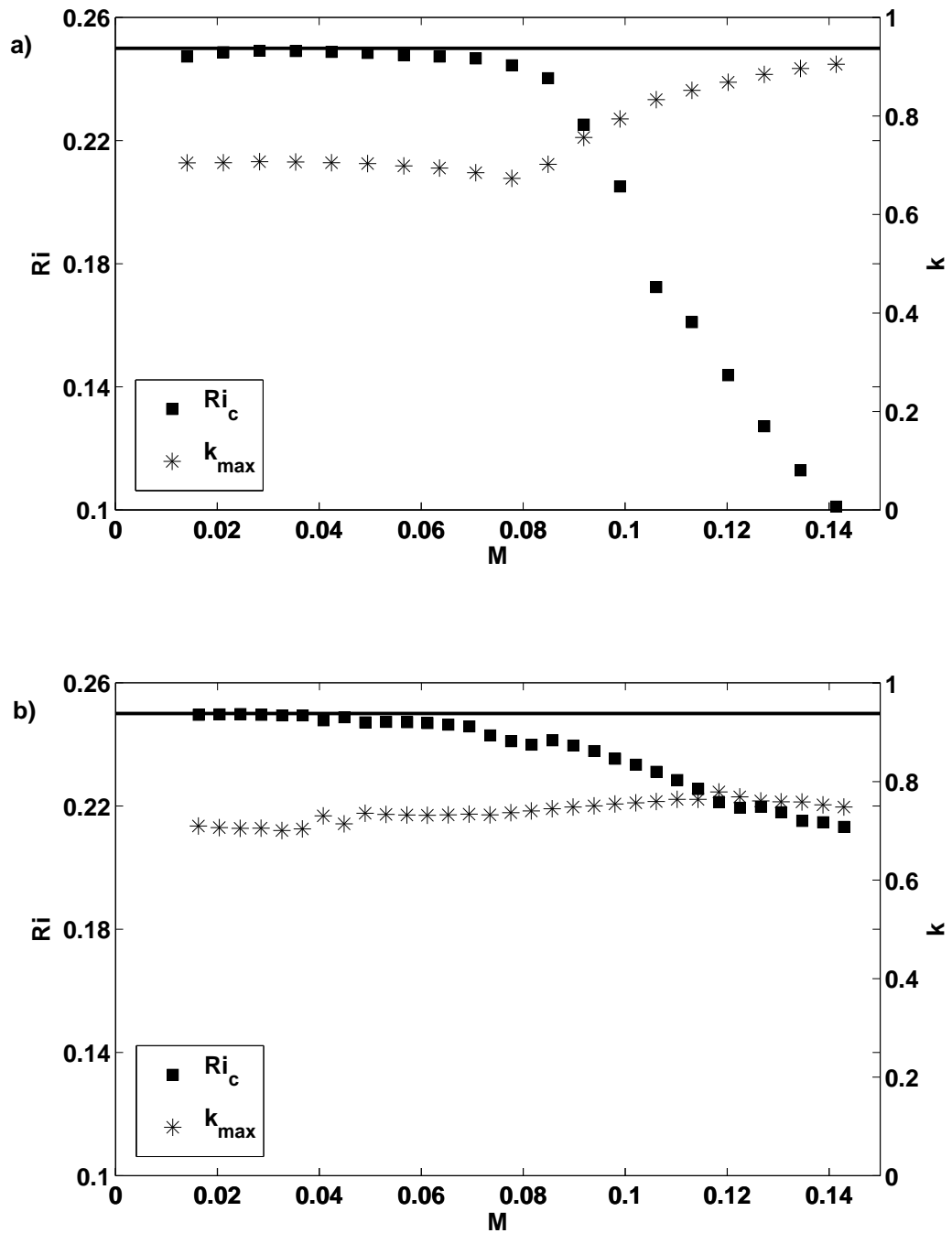


Figure 3.4.: Critical Richardson number in a viscous fluid with $\mu = 10^{-6}$ for different Mach numbers, M . The corresponding wave numbers k_{max} of the most unstable mode at the onset of instability are plotted, and the wave number is normalised by the inverse of the characteristic length $1/L_u$. The horizontal line in both plots corresponds to $Ri = 0.25$. (a) Weakly stratified atmosphere with $\theta = 2$. (b) Strongly stratified atmosphere, $\theta = 10$.

ΔE_{pot} , of the fluid parcel. While for a compressible fluid the density will decrease to a certain amount when a fluid parcel is moved up, such that a part of the kinetic energy is converted by the process of expansion. Then, the generated sound waves are an efficient way to transport energy away from the disturbances. Such that the disturbances lose more energy by sound waves rather than just diffusion. Therefore, to reach the instability threshold more kinetic energy is needed. Thus in the limit of an ideally compressible fluid, where a fluid parcel responds instantaneously to its surrounding conditions, the system would be always stable. Note, it was shown by Blumen (1970) that for a parallel shear flow in an inviscid fully compressible fluid without gravity the growth rate becomes zero in the limit of $M \rightarrow 1$.

Comparing the slopes found for the critical Richardson numbers with different Mach numbers in Fig. 3.4 (a) and Fig. 3.4 (b) a significant difference is present. The critical Richardson number drops faster for a weaker stratified system with $\theta = 2$ than for a very strong stratified system. In order to understand the origin of the complex effect of stratification, the eigenfunctions are investigated. In Fig. 3.5 eigenfunctions for two different θ are displayed. It reveals that the eigenfunctions found for a fixed M and L_u are asymmetric and the asymmetry changes with stratification. It can be seen that the eigenfunction for the temperature perturbation for $\theta = 10$, in Fig. 3.5 (b), is not symmetric around $z = 0.5$ and reaches greater absolute values in the middle of the domain while for $\theta = 2$ in Fig. 3.5 (e), it is almost symmetric. As changing θ from 2 to 10 leads to significantly greater Ri , I find that the eigenfunction for the vertical velocity w develops a local maximum for decreasing Ri number. The asymmetry becomes present closer to the boundaries for the eigenfunction of w .

This asymmetry can be explained by the background profiles. For example, different temperature gradients have a non-trivial effect on the effective Mach number throughout the domain. For weak thermal stratification M remains almost constant whereas in a strongly stratified atmosphere it changes according to

$$M(z) = \frac{u(z)}{\sqrt{1 + \theta z}}.$$

This asymmetry has impact on the observed deviation between the change of the critical Richardson number for $\theta = 2$ and $\theta = 10$. In fact, in a stratified atmosphere

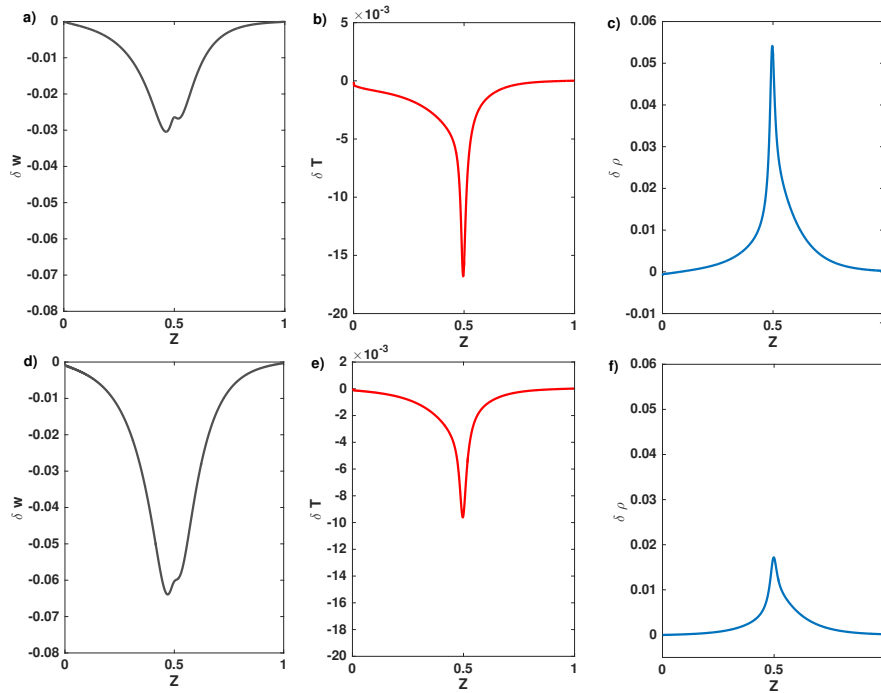


Figure 3.5.: Eigenfunctions for a fixed $M = 0.1$ and a fixed characteristic length-scale $L_u = 0.05$ are found for two different θ , where $\theta = 10$ for top plots a, b, c and $\theta = 2$ for the plots d, e, f. In both cases the eigenfunctions for δw , δT and $\delta \rho$ for the most unstable mode are shown.

exchanged fluid parcels, where one is shifted downwards from the middle plane $z = 0.5$ and the other upwards, move at the same speed in opposite directions, but have different Mach numbers. With an increasing temperature gradient the effective Mach number in the lower half of the domain has a steeper drop such that the stabilising effect of compressibility vanishes. Therefore, the stabilising effect of larger Mach number in a strongly stratified atmosphere is weaker.

3.3.2. Small Péclet Number Regime

So far the effect of thermal diffusion on the stability of a shear flow has been investigated in the Boussinesq approximation (Jones, 1977; Dudis, 1974; Lignières et al., 1999). In order to understand how compressibility and stratification affect previous results, in the following the impact of thermal diffusion in a stably stratified fluid is investigated. For this purpose a non-dimensional number can be introduced, the Péclet number. The Péclet number is given as

$$Pe = \frac{U_0 L_u}{C_k}, \quad (3.34)$$

where L_u is the characteristic length of the shear width and U_0 corresponds to the Mach number at the top of the domain as the velocity is normalised with respect to the speed of sound. The Péclet number is associated with the ratio of advective transport to thermal diffusion. Note, that due to the definition of U_0 and L_u in Equation (3.14) a factor of 4 is formally needed to be consistent with the mostly used definitions. As often the Péclet number is defined as $Pe = \Delta U l / C_k$, where ΔU is the velocity change across a certain layer and l is a typical length. However, since the Péclet number is not exactly defined and only the order of this non-dimensional number gives a meaningful characterisation of the system, the pre-factor of four is dropped in this thesis.

Varying the Péclet number in a compressible fluid stresses the results found by Lignières et al. (1999), where a higher thermal diffusion destabilises the system as it effectively weakens the stable stratification, i.e. the system becomes more unstable against buoyancy. Therefore, thermal diffusion becomes important in a system where $t_k < t_B$, such that buoyancy is much slower than thermal diffusion. As t_B has to be smaller than the system's dynamic time-scale t_S , the Péclet number has to become smaller than unity, to satisfy this requirement.

In Fig. 3.6 the growth rates for different Péclet numbers in a compressible and a weakly compressible fluid are illustrated. Comparing instability growth rates for a setup with $Pe < 1$ and $Pe > 1$ shows that ζ increases with decreasing Pe , where a significant jump can be observed when Pe becomes smaller than unity. It is found that the overall growth rate is smaller for a shear flow with $M = 0.09$,

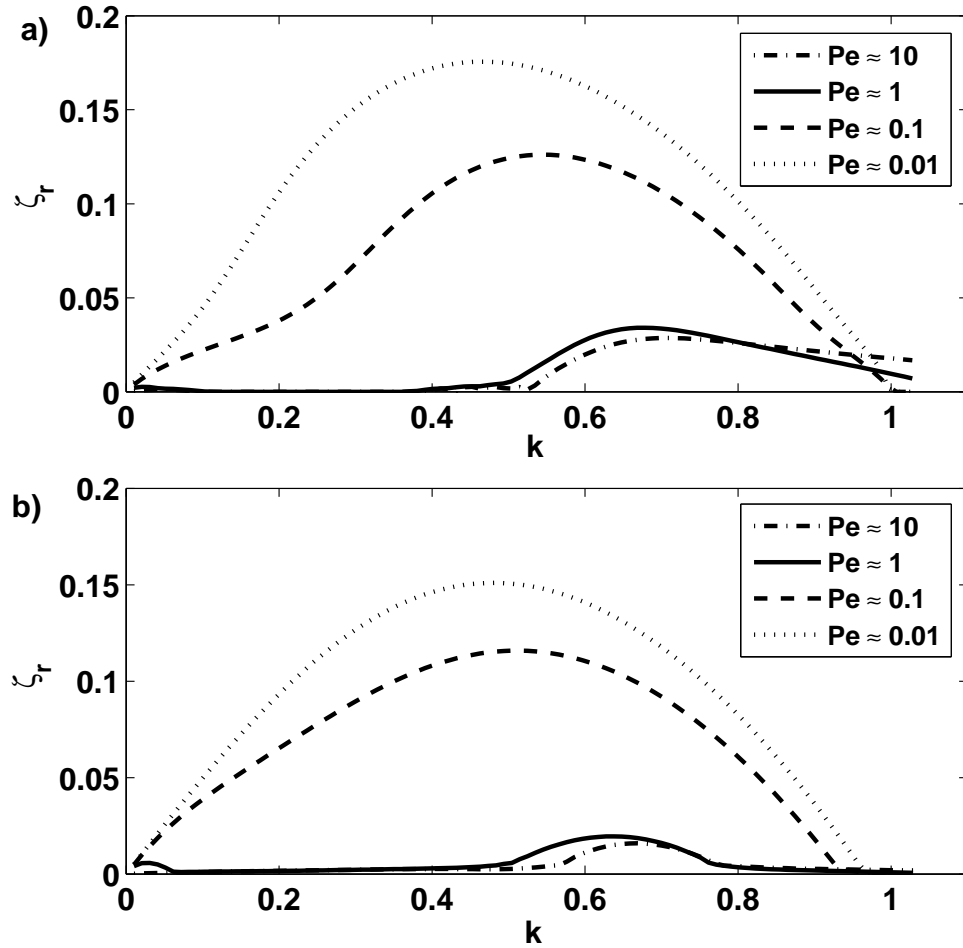


Figure 3.6.: Both plots show the growth rates ζ in a weakly thermally stratified atmosphere with $\theta = 0.5$ for a Richardson number of $Ri = 0.22$. (a) the fluid is compressible with $M = 0.09$. (b) $M = 0.009$, which corresponds to a incompressible fluid. The Péclet number is varied among three orders of magnitude.

this demonstrates a stabilising effect of moderate Mach numbers as discussed in Section 3.3.1. However, an increase in the instability growth rate does not necessarily indicate a shift of the stability threshold to greater Richardson numbers.

Focusing on the stability threshold it is necessary to seek for the critical Richardson numbers in different Péclet number regimes. Previous studies assumed an inviscid fluid to simplify the problem and to avoid the issue of the initial state being actually not an equilibrium state. Here, it is more convenient to include viscosity as it is numerically easier to obtain results for the limit of small viscosity than for an inviscid fluid. For a shear flow the onset of instability does not change for small enough k , if large enough Reynolds numbers are considered. However, including viscosity may have non-trivial effects on the stability if the fluid has large thermal diffusivity (see Jones, 1977). Jones (1977) derived a criterion for instability at long wave length of the form $kPeRi < 0.086$ in an inviscid fluid. For a viscous fluid it can be rewritten as $k\sigma ReRi < 0.086$ such that for reasonably small wave numbers, the system can be still unstable if the Reynolds number is not sufficiently large. It can be seen when investigating Equation (3.29) and Equation (3.30), where the part of the viscous term that is not proportional to the wave number starts to dominate in the limit of small wave numbers. For Equation (3.29) it is the term proportional to $\partial^2 u / \partial z^2$ and for Equation (3.30) it is the term proportional to $\partial^2 w / \partial z^2$. These additional terms lead to a destabilisation of the system for small wave numbers. Therefore, for small wave numbers the viscous term becomes relatively more important for the dynamic of the system. To make sure that the results obtained correspond to a regime where viscosity does not affect the stability threshold, several computations were repeated with a smaller viscosity and a greater viscosity than used in the actual computations.

In Fig. 3.7 curves of marginal stability for four different Péclet numbers in a polytropic atmosphere are displayed for $\theta = 0.5$ and $\theta = 2.0$. As expected the domain for an unstable shear flow increases as the Péclet number is decreased. It shows that not only the growth rate of the instability is altered but indeed the stability threshold changes for small Péclet numbers. The critical Richardson numbers for $Pe \leq 1$ reveal a destabilisation for small k . Lignières et al. (1999) explained this behaviour by the effect of the anisotropy of the buoyancy force. The stabilising effect

of stratification becomes inefficient for predominant horizontal motion compared to the thermal diffusion. Indeed, by computing the ratio of the vertical to horizontal kinetic energy of the unstable mode for a certain k i.e.

$$\frac{E_w}{E_u} = \frac{\int_0^1 w_k(z)^2 dz}{\int_0^1 u_k(z)^2 dz}, \quad (3.35)$$

where $w_k(z)$ and $u_k(z)$ are the eigenfunctions for the vertical and horizontal velocity disturbances at a certain k respectively, it is possible to investigate the nature of the instability. Comparing this ratio for a mode with $k = 0.1$ and $k = 0.7$ for $Pe = 0.1$, it turns out that the ratio for the larger k -mode is of one to two orders of magnitude greater than for the small k -mode. For a representative case with $Pe = 0.1$ and $Ri = 0.2$, the energy in the vertical motion is $E_w = 4.4 \times 10^{-9}$ for $k = 0.1$ and $E_w = 4.0 \times 10^{-14}$ for $k = 0.75$, whereas for the horizontal motion $E_u = 7.7 \times 10^{-5}$ for $k = 0.1$ and $E_u = 6.2 \times 10^{-11}$ for $k = 0.75$. Thus the horizontal motion associated with larger wave lengths in horizontal direction is predominant at very small k .

The results carried out for a greater temperature gradient, $\theta = 2$ shown in Fig. 3.7 (b), reveal a qualitatively different behaviour for small Péclet numbers than it is the case for $\theta = 0.5$ shown in Fig. 3.7 (a). The $\theta = 0.5$ case has overall greater critical Richardson numbers, but has a gradual increase towards a smaller critical Richardson number in the small k limit. This indicates a more efficient destabilisation for most of the wave number and a less efficient destabilisation for small k .

Looking again at the ratio of kinetic energy in vertical and horizontal motions reveals that for lower θ the ratio of vertical motions to horizontal motions remains significantly smaller than for the higher stratification $\theta = 2$, which indicates that buoyancy force is more efficient in a strongly stratified atmosphere against the destabilising effect of thermal diffusion. A weakly stratified atmosphere can be destabilised quicker by thermal diffusion.

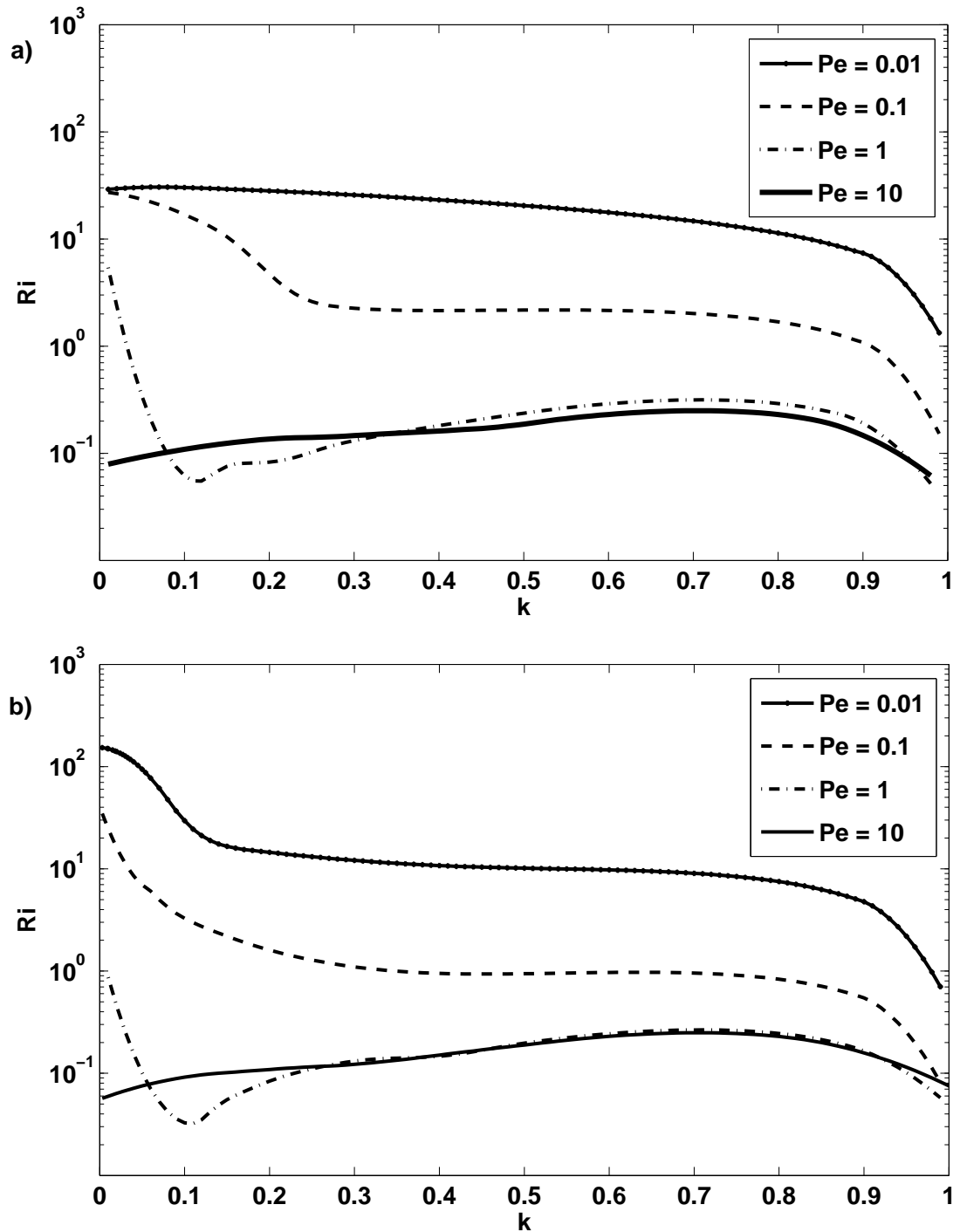


Figure 3.7.: Plots of critical Richardson numbers for all k in a viscous fluid with a Mach number, $M = 0.009$, a) $\theta = 0.5$ and b) $\theta = 2.0$ and viscosity $\nu = 1 \times 10^{-7}$. The Péclet number is varied from 10 to 0.01.

3.3.3. Effect of the Distance to the Onset of Convection on the Instability

The destabilising mechanism of thermal diffusion can be traced back to the fact that thermal diffusion weakens the stable stratification against buoyancy. To investigate if, and how, this effect changes if the system is further away from the onset of convection the polytropic index is varied between 1.6, which is close to the threshold, and 2.07 which is far from the onset of convection. In Fig. 3.8 (a) the growth rate, ζ , is plotted for different polytropic indices while the Richardson number was fixed to the value $Ri = 0.22$ and the Péclet number is unity.

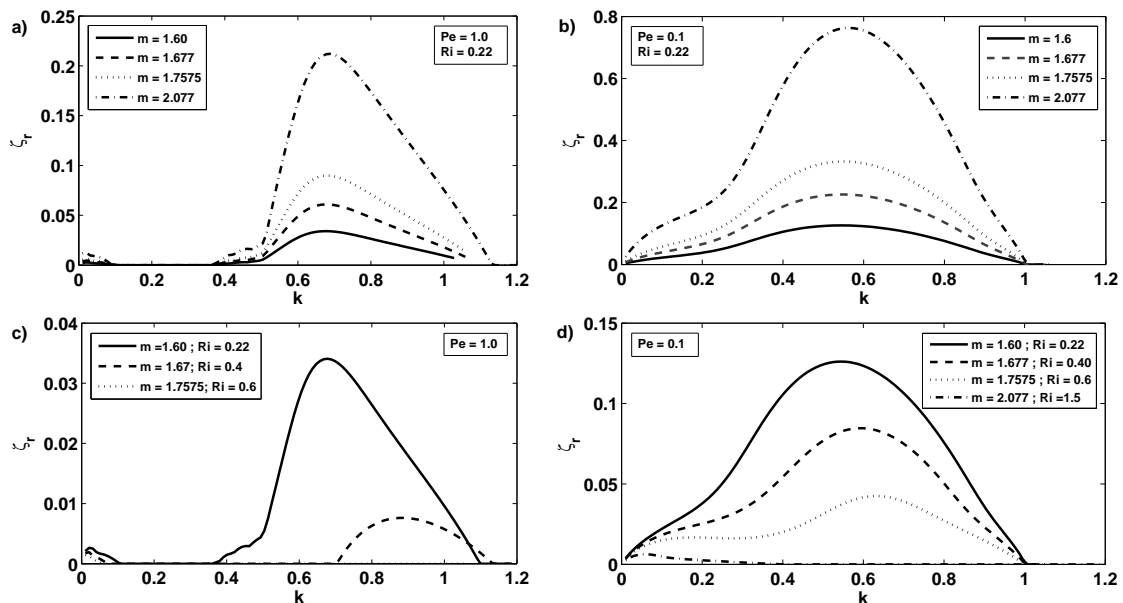


Figure 3.8.: Growth rate of the instability for a viscous fluid with $\theta = 2.0$ and a Mach number of order 10^{-2} . In (a) and (c) the Péclet number is $Pe = 1$. In (b) and (d) $Pe = 0.1$. Ri is varied in (a) and (b), but $Ri = 0.22$ for the top plots (c) and (d).

The growth rate is given in units of inverse sound crossing time, \tilde{t} , such that a rescaling is necessary while the Mach number is adjusted to fix Ri . The same is done for a Péclet number of 0.1 in Fig. 3.8 (b) where the same tendency of an increasing growth rate with increasing polytropic index is observed. To exclude that this behaviour is due to the effect of thermal diffusion the growth rate for two different m is computed for a fixed Ri smaller than $1/4$ for much greater Pe than

unity, where the same tendency is found. However, the critical Ri for increasing m increases. Therefore, a system with larger polytropic index, m , is less stable such that for the same Ri the system with a larger m is further away from the stability threshold and has a larger growth rate. Non-linear direct numerical computations of two cases approved the results obtained with the linear EV solver. For this purpose Equations (2.13) - (2.15) were solved by using a hybrid finite-difference/pseudo-spectral code (see for example Matthews et al., 1995; Silvers et al., 2009a,b, and references therein).

While increasing the polytropic index requires a greater shear flow amplitude to obtain the same value for the Richardson number, the kinetic energy of the shear flow is increased as it is proportional to both parameters. Consequently, as soon as the system can overcome the stabilising effect of density stratification the instability has more available kinetic energy from which it can grow more rapidly.

In the two plots at the bottom of Fig. 3.8 the growth rate for different polytropic indices is shown while all other parameter are fixed. The solid lines in Fig. 3.8 (c) and Fig. 3.8 (d) correspond to the solid lines in Fig. 3.8 (a) and Fig. 3.8 (b) respectively. As expected the instability growth rate decreases with increasing density stratification and greater Ri . While for a Péclet number of unity the instability shuts down rapidly, which is displayed in Fig. 3.8 (c), for $Pe < 1$ the same behaviour is observed but the instability for greater m is still present for small wave numbers. As discussed in Section 3.3.2 this is explained by the anisotropy of the buoyancy force.

3.3.4. Subdominant Shear Instability

For certain configurations, where the shear width is sufficiently small, the velocity profile is similar to two counter flows. Investigating the growth rate for different wave numbers, a typical case is shown in Fig. 3.9 (a), reveals that there are two arches present. In order to study the nature of these two instabilities I look at the eigenfunctions present in the two arches. For unstable modes with k corresponding to the smaller arch, one eigenfunction of the vertical velocity is displayed in Fig. 3.9 (b).

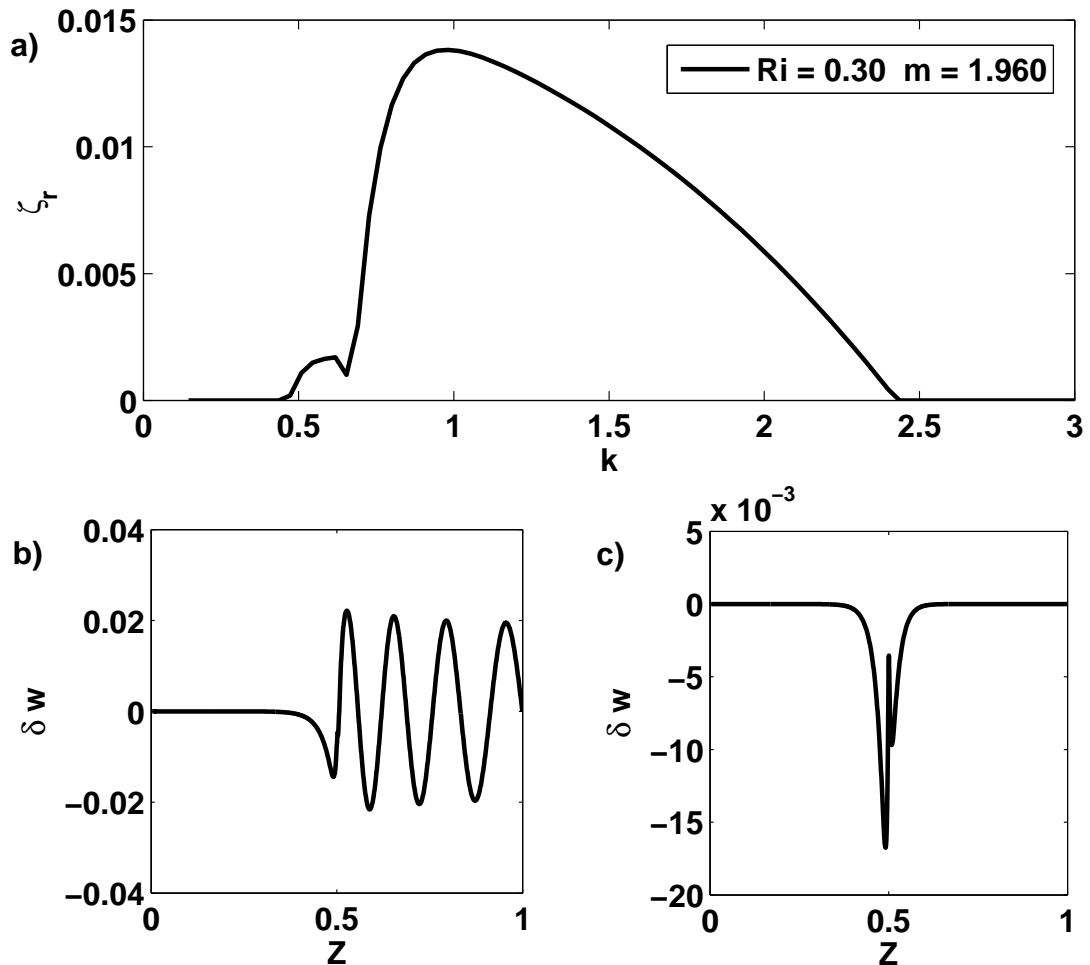


Figure 3.9.: Characteristics of instabilities for a viscous fluid with $\theta = 1.0$, Péclet number of order 10^3 and $Ri = 0.3$. (a) Growth rates. (b) Eigenfunction found for the vertical velocity w in the small arch. (c) Eigenfunction for the vertical velocity w in the large arch.

It shows an eigenfunction that is propagating in the lower half plane, the corresponding mode with the opposite phase velocity shows the oscillations in the upper half plane. Such eigenfunctions exhibit all properties of the Holmboe instability, where two counter propagating modes, one in the upper and one in the lower half plane, are present. Therefore, I conclude that for a stable stratification and Péclet numbers much greater than unity a Holmboe like instability can occur.

The second arch has greater growth rates and appears at greater k . The corresponding eigenfunction for the vertical velocity of these modes is shown in Fig. 3.9 (c). It reveals that the instability is localised at the center of the shear flow, which corre-

sponds to the KH instability, where only one unstable mode is present for a certain wave number and its phase velocity corresponds to the mean flow velocity. Investigating all possible eigenfunctions at the overlap region between the two arches, reveals that Holmboe modes are present but have a smaller growth rate as the KH instability or *vice versa*.

The observed Holmboe like instability only appears for large Péclet numbers while for small Pe the range for the KH instability is enlarged to smaller wave numbers, such that even in the presence of the Holmboe like instability the KH instability for the same wave numbers dominates. This can be seen in Fig. 3.8 (a) and Fig. 3.8 (b), where the small arch present in (a) for $Pe = 1$ is dominated by the KH instability in (b) for $Pe = 0.1$.

To make sure that those modes are physical and not a numerical artifact I checked that they remain for a system where an inviscid non-diffusive incompressible fluid is assumed. In a second check, the discretisation step sizes in z direction are changed from a uniform to a weighted distribution, which has the consequence that the matrix changes. With both approaches a second instability, with the same properties, was found at slightly smaller wave numbers than the KH instability. Using non-linear calculations both instabilities are found during the linear growth regime with similar growth rates and eigenfunctions as predicted by the EV-solver.

3.4. Conclusions

Shear flow instabilities, which may lead to turbulent motions, are important for the understanding of the dynamics in stellar interiors. Using linear stability analysis the onset of shear flow instabilities in a compressible polytropic atmosphere was investigated, where a detailed analysis of the effect of moderate Mach numbers, small Péclet numbers and different polytropic indices was carried out separately.

For a flow of moderate Mach numbers a stabilising effect that results in a smaller critical Richardson number was found, such that for some small Richardson numbers the shear flow remains stable. This effect becomes significant for Mach number

greater than 0.1. However, the stabilising is weaker for strongly stratified atmospheres.

For fluids with high thermal diffusivity, where the Péclet number drops below unity, a destabilisation of the system can be shown. These results are in agreement with Lignières et al. (1999), where the regime of small Péclet numbers were examined in a Boussinesq fluid. A significantly greater growth rate was found for highly diffusive fluids as well as greater critical Richardson numbers for $Pe < 1$ compared to systems with large Péclet numbers. Steeper temperature gradients lead to an overall stabilisation for small Péclet numbers.

An interesting result is that of the possibility of Holmboe like instabilities present in polytropic atmospheres. This instability is dominated by the KH instability for small Péclet numbers, but is clearly present for large Péclet numbers. While no setup was found where the Holmboe like instability dominates the KH instability it may be found in future investigations.

Studying more complex systems, which include key properties of stars, by means of a linear stability analysis provides a powerful tool to investigate their linear behaviour. However, the vertical length-scale for which these shear flows can become unstable is far below the resolution of helioseismological techniques and as the perturbation's amplitude can be finite in the tachocline (see Michaud and Zahn, 1998) the assumption of infinitesimal perturbations made in the stability analysis might lead to different results. To clarify the second issue it is necessary to investigate the stability properties of such flows by means of direct numerical computations, where the initial state is perturbed by perturbations with a finite amplitude. In addition to finite amplitude effects, the non-linear behaviour of unstable shear flows after a saturation is crucially important for the understanding of mixing in stellar interiors regardless of the nature of the initial instability.

4. Non-linear Calculations: Forcing Methods Part I

Most local numerical studies of the turbulence transition in shear flows take the approach of an unforced flow (Caulfield and Peltier, 2000; Smyth and Moum, 2000; Smyth and Winters, 2003), which results in a finite lifetime of an initially unstable background state due to its inevitable viscous decay. However, astrophysical shear flows can be either transient features or be sustained over very long time-scales (Mahajan and Rogava, 1999; Rogava et al., 2000), where the physical mechanism maintaining the shear flow is usually unknown (Leprovost and Kim, 2008; Paternò, 2010). Incorporating a forcing into the numerical model has therefore two roles first to sustain the initial state, for which a linear stability analysis can be carried out, and second to model the unknown physical processes responsible for the resulting flow in an astrophysical system. A variety of classical studies of shear driven turbulence exploit a method where a decoupled background shear flow is present (for example used by Holt et al., 1992; Jacobitz et al., 1997; Barker et al., 2012). This method requires a change of variables to incorporate a mean shear profile and does not allow for a back-reaction of the actual flow on the forcing.

Investigations of astrophysical shear flows have commonly exploited different methods to provide a sustained flow. For example in Miesch (2003), Vasil and Brummell (2008), and Silvers et al. (2009b) a method to balance viscous dissipation by introducing an external force proportional to the viscous term is utilized. Another option that has been selected is the relaxation method (e.g. Prat and Lignières, 2013), which incorporates an external force proportional to the difference between the actual velocity profile and the target shear profile.

The aim in the following two chapters is to compare different forcing methods to find an appropriate method for our purpose. For simplicity the investigations are divided into two parts, where first the linear growth phase of a shear instability for different forcing methods will be compared in this chapter. Subsequently in the next chapter, the non-linear regime will be investigated in full detail.

For the first part of the study it is sufficient to use two-dimensional calculations as in that case the linear growth of the KH instability should not significantly differ from a three-dimensional evolution. After the secondary instability starts to develop, which happens when the KH instability saturates, it becomes necessary to consider a three-dimensional setup, which is done in Chapter 5.

In Section 4.1 the different forcing methods are introduced in detail. I compare the linear growth of a KH instability for all forcing methods in Section 4.2, where the focus is on the growth rate, the wave number of the most unstable mode and form of the eigenfunctions. In addition, the results are compared to results obtained by linear stability analysis, which was used previously to investigate the behaviour of the KH instability for different parameter regimes (see Chapter 3).

4.1. Forcing methods

Four different methods to sustain an initial shear flow are compared, I will distinguish between methods that are static, i.e. the force term does not change throughout the calculation, and dynamic forcing methods that might vary depending on the current flow. Furthermore, methods with a force applied to a localised region have a local force, whereas the force term applies on the whole domain for global forcing methods. Our main goal is to find a forcing method that does not significantly alter the characteristics of the linear phase of the evolution, but allows to reach a quasi-steady non-linear state.

Viscous Method

In order to balance the viscous dissipation associated with the initial shear flow profile given by Equation (3.14) the force

$$\mathbf{F} = -\sigma C_k \nabla^2 \mathbf{U}_0 \quad (4.1)$$

is added to the RHS of Equation (2.14). By applying this viscous forcing the initial state given by Equation (2.20), Equation (2.21) and Equation (3.14) is in equilibrium provided that viscous heating is neglected. This method has been broadly applied in forced shear flows to model the dynamics of the solar tachocline (e.g. Miesch, 2003; Silvers et al., 2009b). Note that this method only balances for the viscous diffusion of momentum associated with the target profile and does not depend on the actual non-linear solution. In that sense, the forcing can be considered to be local and static.

Perturbation Method

The second method, the perturbation method, was previously used by Holt et al. (1992); Jacobitz et al. (1997); Barker et al. (2012). For this method a slightly different set of differential equations is solved. A decomposition of the velocity, $\mathbf{u} = \mathbf{U}_0 + \tilde{\mathbf{u}}$ into a background shear flow, \mathbf{U}_0 , and the deviation from the background profile $\tilde{\mathbf{u}}$ enables the maintenance of a shear flow that is independent of the unstable perturbations. Note, the background velocity profile U_0 has to be time independent and divergence free. Thus, inserting the above decomposition into the momentum Equation (2.14) the following is obtained

$$\begin{aligned} \rho \frac{\partial}{\partial t} (\tilde{\mathbf{u}} + \mathbf{U}_0) &= -\nabla p + \theta(m+1)\rho \hat{\mathbf{z}} - \rho (\tilde{\mathbf{u}} + \mathbf{U}_0) \cdot \nabla (\tilde{\mathbf{u}} + \mathbf{U}_0) \\ &\quad + \sigma C_k \left[\nabla^2 (\tilde{\mathbf{u}} + \mathbf{U}_0) + \frac{1}{3} \nabla \nabla \cdot (\tilde{\mathbf{u}} + \mathbf{U}_0) \right], \end{aligned} \quad (4.2)$$

since it is assumed that the background profile does not vary with time and in the flow direction, the time derivative of \mathbf{U}_0 and the term $\mathbf{U}_0 \cdot \nabla \mathbf{U}_0$ vanish. In order to

ensure that the background velocity is not dissipated by viscosity the viscous term associated with it is dropped. The equation takes the form

$$\begin{aligned} \rho \frac{\partial \tilde{\mathbf{u}}}{\partial t} = & -\nabla p + \theta(m+1)\rho \hat{\mathbf{z}} - \rho \tilde{\mathbf{u}} \cdot \nabla \mathbf{U}_0 - \rho \mathbf{U}_0 \cdot \nabla \tilde{\mathbf{u}} \\ & + \sigma C_k \left(\nabla^2 \tilde{\mathbf{u}} + \frac{1}{3} \nabla (\nabla \cdot \tilde{\mathbf{u}}) \right), \end{aligned} \quad (4.3)$$

such that effectively the differential equation for the velocity perturbations only is solved. Here, the velocity perturbations, $\tilde{\mathbf{u}}$, are initially zero, but the background velocity is incorporated through the two advective terms involving \mathbf{U}_0 . By the same procedure the Equation (2.13) and Equation (2.15) become:

$$\frac{\partial \rho}{\partial t} = -\nabla \cdot (\rho \tilde{\mathbf{u}}) - \mathbf{U}_0 \cdot \nabla \rho \quad (4.4)$$

$$\begin{aligned} \frac{\partial T}{\partial t} = & \frac{C_k \sigma (\gamma - 1)}{2\rho} |\tau|^2 + \frac{C_k \sigma (\gamma - 1)}{2\rho} \frac{\partial^2 \mathbf{U}_0}{\partial z^2} + \frac{\gamma C_k}{\rho} \nabla^2 T \\ & - \nabla \cdot (T \tilde{\mathbf{u}}) - (\gamma - 2) T \nabla \cdot \tilde{\mathbf{u}} - \mathbf{U}_0 \cdot \nabla T, \end{aligned} \quad (4.5)$$

where the effect of the background velocity, \mathbf{U}_0 , on the density and temperature is taken into account. Mathematically, the equations for $\mathbf{U}_0 + \tilde{\mathbf{u}}$ are the same as for \mathbf{u} in the viscous method. Therefore, both methods should give the same solutions, even if the approach and numerical implementation are significantly different.

Average Relaxation Method

In this relaxation method, an external force ensures that the flow relaxes towards the initial profile on an arbitrary time-scale τ_0 . Any quantity \bar{f} is defined as

$$\bar{f}(z) = \frac{1}{N_x N_y} \sum_{i=1}^{N_x} \sum_{j=1}^{N_y} f(i, j, z), \quad (4.6)$$

where the overbar denotes that the quantity f is horizontally averaged, and N_x and N_y are the resolutions in x -direction and in y -direction respectively. The force for the relaxation method in the momentum equation depends on the horizontally averaged velocity $\bar{u}_x(z)$ and is given by

$$\mathbf{F} = \frac{\rho}{\tau_0} (\mathbf{U}_0 - \bar{u}_x(z) \hat{\mathbf{e}}_x), \quad (4.7)$$

where $\hat{\mathbf{e}}_x$ is the unit vector in x -direction. The forcing is applied continuously with time rather than at particular time-steps. Therefore, the relaxation time controls the strength of the forcing term. For this method it is crucial to ensure that the forcing is aligned with the flow direction and does not depend on the velocity variation along this horizontal direction, which would otherwise correspond to a local small-scale force as described further below. The relaxation method was used by Prat and Lignières (2013) to model shear driven turbulence and provides the advantage of an adjustable back-reaction on the actual mean flow. It is a global forcing (due to the averaged operator) and a dynamical forcing, because it depends on the actual flow.

Local Relaxation Method

For the local relaxation method a local force

$$\mathbf{F} = \rho (\mathbf{U}_0 - \mathbf{u}) / \tau_0 \quad (4.8)$$

operates to push the flow towards a target profile \mathbf{U}_0 where the relaxation time, τ_0 , indicates how fast the response to a velocity change is. The force strength varies with the direction of forcing and depends on the actual velocity profile. Therefore, it corresponds to a dynamical small-scale force. This method was applied, for example, to study the interaction between penetrative convection and shear flows (Guerrero and Käpylä, 2011). Although this method provides a forcing that depends on the evolution of the velocity field it suppresses any deviation from the target flow.

4.2. Exponential Growth Regime

I begin by comparing the forcing methods introduced in Section 4.1 during the exponential growth regime of a shear flow instability. Since the initial linear phase of shear flow instabilities is purely two-dimensional, which is justified by the Squire's theorem (Squire, 1933), the focus here is on calculations in a two-dimensional domain, which has a spatial resolution of $N_x = 512$ and $N_z = 480$. In order to obtain a two-dimensional setup the three-dimensional differential Equations (2.13) - (2.15) are used, but I neglect the spatial variations in the horizontal y -direction. Furthermore the velocity component along the y -direction is assumed to be zero. All

non-linear calculations in this thesis are initialized by adding a small random temperature perturbation to the equilibrium state defined in Equations (2.20) - (2.21) including the additional shear flow given by Equation (3.14).

The stability of a shear flow in a stratified atmosphere is characterized by the non-dimensional Richardson number, Ri defined in Equation (3.15). Therefore, in order to investigate the exponential growth of shear instabilities in this chapter only shear flows with a Richardson number less than $1/4$ at a point in the domain are considered. Shear instabilities triggered by thermal diffusion for which larger values of Ri can be used (Dudis, 1974; Zahn, 1974; Lignières et al., 1999) are not considered in this chapter. Because the $1/4$ criterion is a necessary, but not sufficient, requirement for instability I also solve the corresponding linear stability problem without additional forcing terms based on the approach used in Chapter 3 in addition to conducting the non-linear calculations. For simplicity, the Prandtl number is fixed to be unity whereas the dimensionless thermal diffusivity C_k is varied from 10^{-4} to 10^{-5} . Taking the previous linear study in Chapter 3 into account, the parameters satisfy the following requirements: To ensure a stable stratification the polytropic index is set to be $m = 1.6$, the amplitude U_0 of the shear flow is chosen such that the Mach number in the middle of the domain remains less than 0.08, which avoids additional stabilisation by compressible effects. Furthermore, the initial Péclet number, which was defined in Equation (3.34), is taken to be much greater than unity to avoid a destabilising effect caused by thermal diffusion.

Here, I compare two linearly unstable cases with distinct behaviour when no external forcing is included. An unforced case will decay if the instability grows on a larger time-scale than the viscous dissipation time-scale. Therefore, two different cases corresponding to two different minimum Ri values are considered. In case I, a very small value of $Ri = 8 \times 10^{-4}$ is chosen, such that the system is unstable even without external forcing. Case II has a greater $Ri = 0.1$ and greater C_k so that the system is unstable only if an external forcing is introduced. Without forcing, the initial shear flow diffuses quickly such that the Richardson number increases rapidly above $1/4$ and no shear instability can be sustained. By considering these two different cases, I investigate how the forcing method used affects the development of a shear instability during the exponential growth phase. Unforced calculations provide a

reference for the system's evolution without any external forces. All parameters for case I and case II, the resulting linear growth rates, and the wave number for the most unstable mode for each method are summarised in Table 4.1 using both an eigenvalue solver and direct numerical calculations of unforced and forced cases.

Table 4.1.: Comparing the linear eigenvalue-solver results with those from non-linear calculations during the linear phase. For case I the shear amplitude is $U_0 = 0.08$ and $1/L_u = 118$ such that $Ri = 8 \times 10^{-4}$. Taking $C_k = 8 \times 10^{-5}$ results in a $Pe \approx 8$. For case II $U_0 = 0.041$, $1/L_u = 20$ and $C_k = 1 \times 10^{-4}$ such that $Ri = 0.1$ and $Pe \approx 20$.

Method:	ζ_r	k_{max}	$2/L_{eff}$
Case I:			
EV-solver	$(119 \pm 0.5) \times 10^{-2}$	42.5 ± 1	118
unforced	$(30 \pm 1) \times 10^{-2}$	14.1 ± 1.6	51 ± 2
viscous method	$(110 \pm 5) \times 10^{-2}$	33.0 ± 1.6	105 ± 5
perturbation method	$(110 \pm 5) \times 10^{-2}$	33.0 ± 1.6	106 ± 6
averaged relaxation, $\tau_0 = 10$	$(45 \pm 3) \times 10^{-2}$	14.1 ± 1.6	37 ± 2
averaged relaxation, $\tau_0 = 1.0$	$(80 \pm 3) \times 10^{-2}$	31.4 ± 1.6	73 ± 3
averaged relaxation, $\tau_0 = 0.1$	$(105 \pm 5) \times 10^{-2}$	33.0 ± 1.6	105 ± 5
averaged relaxation, $\tau_0 = 0.01$	$(110 \pm 5) \times 10^{-2}$	33.0 ± 1.6	104 ± 3
local relaxation, $\tau_0 = 10$	$(34 \pm 2) \times 10^{-2}$	14.1 ± 1.6	36 ± 3
local relaxation, $\tau_0 = 2.5$	$(27 \pm 1) \times 10^{-2}$	22.0 ± 1.6	57 ± 2
local relaxation, $\tau_0 = 1.0$	$(30 \pm 3) \times 10^{-3}$	15.7 ± 1.6	74 ± 2
local relaxation, $\tau_0 = 0.1$	$(8 \pm 1) \times 10^{-3}$	7.9 ± 1.6	105 ± 4
Case II:			
EV-solver	$(53 \pm 0.5) \times 10^{-3}$	10.6 ± 0.1	20
unforced	-0.01	not applicable	not applicable
viscous method	$(47 \pm 8) \times 10^{-3}$	9.4 ± 1.6	19 ± 1
perturbation method	$(47 \pm 8) \times 10^{-3}$	9.4 ± 1.6	19 ± 1
averaged relaxation, $\tau_0 = 0.01$	$(48 \pm 8) \times 10^{-3}$	9.4 ± 1.6	19.8 ± 0.3

4.3. Results

In order to analyse the exponential growth regime of the shear flow instabilities the growth rate, ζ_r , the wave number of the most unstable mode, k_{max} , and the effective shear width just at the beginning of the exponential growth is calculated. The growth rates for the non-linear calculations are obtained by calculating

$$\zeta_r = \frac{d \ln \langle w \rangle}{dt} = \frac{1}{\langle w \rangle} \frac{d \langle w \rangle}{dt}, \quad (4.9)$$

where the angle brackets denotes that any quantity f is volume averaged as follows

$$\langle f \rangle = \frac{1}{N_x N_z} \sum_{i=1}^{N_x} \sum_{j=1}^{N_z} \sqrt{f(i, j)^2}. \quad (4.10)$$

In order to find the most unstable wave number, which corresponds to the wave number with the most energy, the kinetic energy spectrum is calculated as

$$E(k_x) = \frac{1}{4} \sum_{k_x=1}^{k_{max}} \sum_{z=1}^{N_z} \hat{\mathbf{u}}(k_x, z) \hat{\rho} \hat{\mathbf{u}}^*(k_x, z) + \hat{\rho} \hat{\mathbf{u}}(k_x, z) \hat{\mathbf{u}}^*(k_x, z), \quad (4.11)$$

where $k_{max} = (N_x/3 + 1)$, the hat symbol denotes the Fourier transform of the corresponding quantity and the star symbol denotes the complex conjugate. In addition, to estimate the shear width during the exponential regime an effective shear width, L_{eff} , is needed. For that the horizontally averaged velocity in x -direction is calculated as

$$\bar{u}_x(z) = \frac{1}{N_x} \sum_{i=1}^{N_x} u_x(i, z), \quad (4.12)$$

where the overbar denotes that the quantity u_x is horizontally averaged, and N_x is the resolutions in x -direction. Taking the horizontally averaged velocity profile an effective shear width L_{eff} can be obtained, by fitting to the function

$$f(z) = U_{eff} \tanh \left(\frac{2}{L_{eff}} (z - 0.5) \right). \quad (4.13)$$

To compare the shear profile that triggers the shear flow instability with the initial shear profile, the effective scaling factor $2/L_{eff}$ is calculated shortly after the instability starts to grow. The obtained values for different forcing methods are

summarised in Table 4.1. Note, that a pre-factor of two in Equation (4.13) is introduced for later calculations in Section 6.2, where not only the scaling factor is compared, but the actual effective shear width L_{eff} .

Growth rates and most unstable modes

The growth rates, ζ_r , and the wave number for the most unstable mode, k_{max} , are summarised in Table 4.1. For the viscous forcing, the perturbation method and the averaged relaxation method with $\tau_0 = 0.01$ the growth rate $\zeta_r = 1.1$ remains identical for case I. For case II the growth rate for these forcing methods is almost identical $\zeta_r = 4.7 \times 10^{-2}$, where a small difference occurs for the averaged relaxation method $\zeta_r = 4.8 \times 10^{-2}$. The growth rates achieved by these methods in case II correspond to the growth rate calculated by using the EV-solver with a 12% relative error when taking the growth rate from the EV-solver, which is $\zeta_r = 5.3 \times 10^{-2}$, as reference. For case I, where the growth rate from the linear analysis is $\zeta_r = 1.19$, this error is 8%. On the contrary the local relaxation method in case I shows growth rates at least on order of magnitude smaller than predicted by the EV-solver. Moreover, an opposite trend, where the growth rate decreases with decreasing relaxation time, τ_0 , is present.

The most unstable mode obtained in non-linear calculations is the same for the viscous- and the perturbation method, where for case I it is $k_{max} = 33$ and for case II it is $k_{max} = 9.4$. The most unstable wave number obtained by DNS is always slightly smaller than the one obtained from the EV-solver, and more so for case I, where it is $k_{max} = 42.5$, than for case II, where it is $k_{max} = 10.6$. This is due to a thinner shear width in case I, which is more affected by viscous dissipation, such that the instability is triggered when the shear profile is significantly broader. Therefore, k_{max} deviates for case I more than for case II, where the initial shear width is broader. For the local relaxation method k_{max} shows the opposite behaviour and differs significantly from the predicted k_{max} by the linear stability analysis. For case II no results were obtained by using the local relaxation method, because for $\tau_0 \leq 1$ as well as for $\tau_0 > 1$ the system remained stable and the initial perturbations decay. Therefore, a more detailed investigation of the effect of this forcing method is discussed further below.

Volume averaged vertical velocity and visualisation

For both relaxation methods the relaxation time, τ_0 , is varied in order to investigate the effect of differently quick responses to a change of the velocity field. For a qualitative study of the shear instability present the vertical velocity is displayed in Fig. 4.1 for selected forcing methods: For the average relaxation method the instability appears always in the middle of the domain and is visually similar to the instability observed by using either the viscous method or the perturbations method. Note, that only the viscous method is displayed, because the visualisation for the perturbation method shows exactly the same pattern. Comparing Fig. 4.1 (b) and Fig. 4.1 (c) shows a decrease of the length of the KH billows when the relaxation time for the averaged relaxation method is decreased. The obtained length of the KH billows in the case with the shorter relaxation time is similar to the length obtained by using the viscous method in Fig. 4.1 (a).

Now the attention is drawn onto the effect of varying the relaxation time-scale τ_0 in the averaged relaxation method. The instability develops always in the middle of the domain and is visually similar to the instability observed by using either the viscous- or the perturbation method, as can be seen in Fig. 4.1 (b) and Fig. 4.1 (c). The evolution of $\langle w \rangle$, for different τ_0 parameters, for case I and case II is shown in Fig. 4.2 and the growth rates of these runs are summarised in Table 4.1. For all cases the onset of the instability is insensitive to the chosen relaxation time-scale τ_0 , but the growth rate decreases with increasing τ_0 . This is expected since a smaller τ_0 implies a larger restoring force as soon as the averaged velocity profile differs from the target Equation (3.14). Therefore, for increasing relaxation times the viscous dissipation might be unbalanced such that the initial state changes before an instability is triggered. The relaxation method leads either to the same instability or sustains an instability triggered by a smoother velocity profile, when the relaxation time τ_0 is increased. To put τ_0 in relation with typical dynamical times the initial turnover time of the shear flow, $t_s = L_u/U_0$, is calculated, which is $t_s \approx 0.1$ for case I and $t_s \approx 1.2$ for case II. Furthermore, the initial viscous time-scale, $t_\mu = L_u^2/\mu$, that accounts for the time on which the initially shear width is dissipated, gives another reference time.

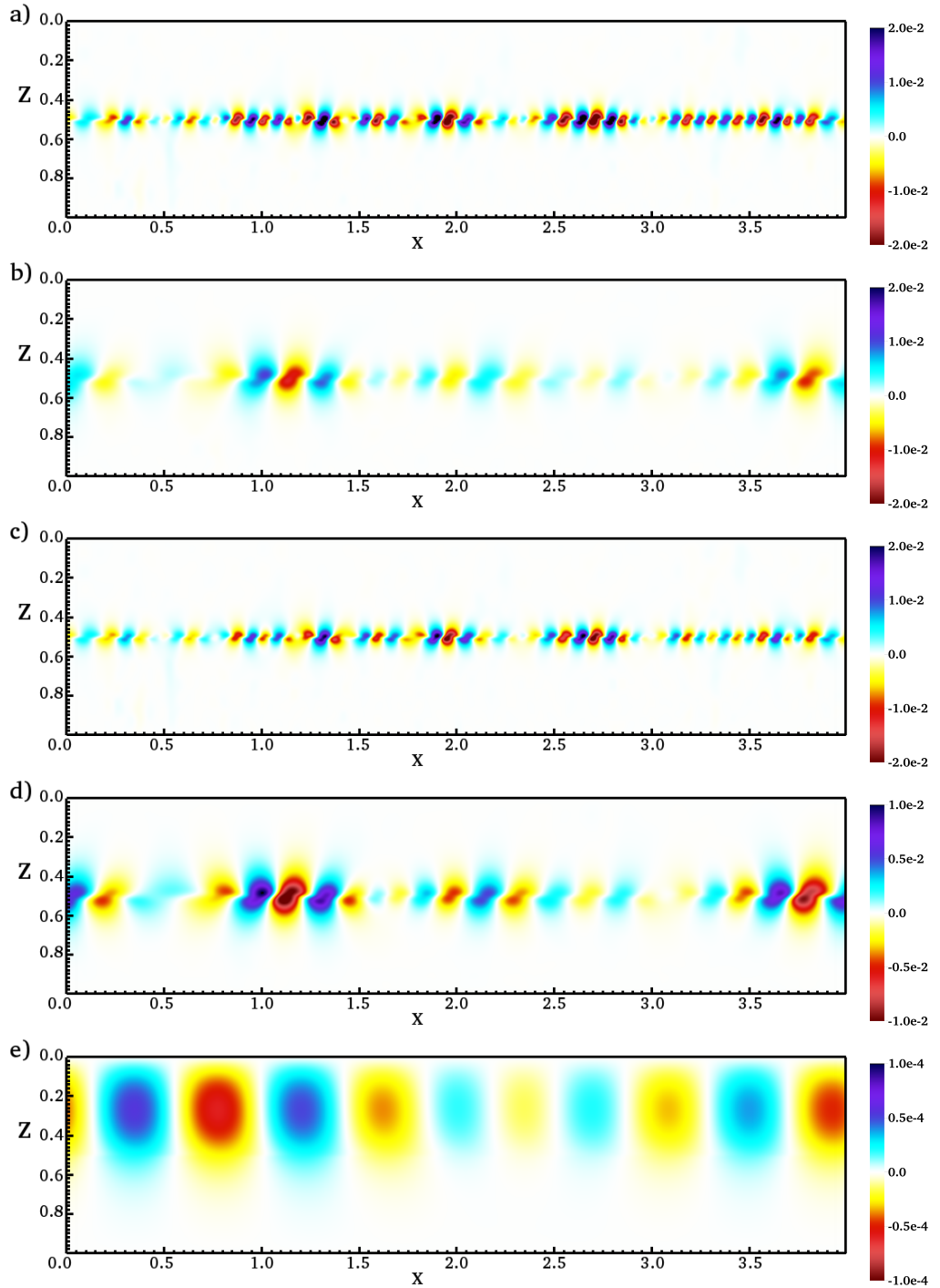


Figure 4.1.: Vertical velocity perturbations for different forcing methods just at the end of the exponential growth regime. (a) The viscous method. (b) The averaged relaxation method with $\tau_0 = 10$. (c) The averaged relaxation method with $\tau_0 = 0.1$. (d) The local relaxation method with $\tau_0 = 10$ and in (e) with $\tau_0 = 0.1$.

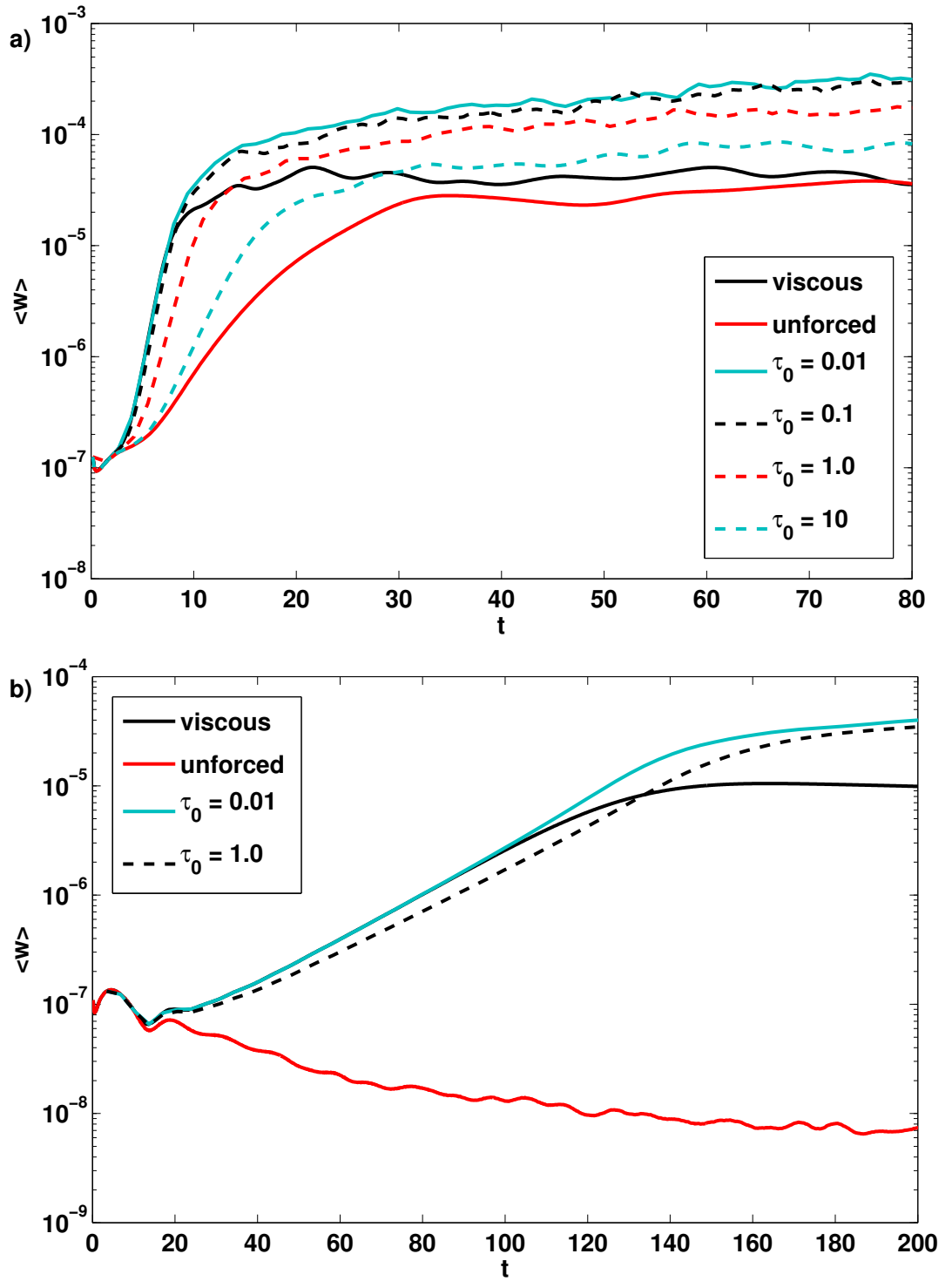


Figure 4.2.: The time evolution of the volume averaged vertical velocity, as defined in Equation (4.10), for the two-dimensional calculations for case I in (a) and for case II in (b). Different τ_0 parameters for the relaxation method are used and compared to the viscous method and unforced calculations. The vertical velocity is displayed in logarithmic scale and t is given sound-crossing time.

For case I the viscous time-scale is $t_\mu = 0.9$ and for case II it is $t_\mu = 25$. Note, that both time-scales represent initial time-scales given by the initial configuration and will change with time as the system evolves, especially in the saturated regime these times might be significantly different from the initial values. So that a relaxation time greater than both the viscous and dynamical time-scale corresponds to a very weak back-reaction of the forcing to the change of the averaged velocity. Note that $\tau_0 < 1$ means that the response is quicker than a sound crossing time which is unlikely to occur in physical system. By varying the relaxation time, τ_0 , it is investigated how to choose an appropriate τ_0 with respect to the initial time-scales in order to recover the linear instability dictated by the initial state and at the same time a saturated regime that evolves towards a quasi-static state.

For the local relaxation method a significantly different instability is triggered for cases with $\tau_0 \leq 1$ as displayed in Fig. 4.1 (e). The instability manifests in the upper half plane of the box and has a regular pattern. However, for $\tau_0 > 1$ the KH instability is recovered. This can be explained by the form of the force. Since the local relaxation method suppresses any deviation from the initial shear flow profile, the system remains stable for fast forcing, i.e. $\tau_0 \leq 1$. Then, at very large time, a non-physical instability is triggered. This is also reflected in the observed dynamics for the local relaxation method displayed in Fig. 4.3. The time evolution of $\langle w \rangle$ significantly differs to the one using the averaged relaxation method in Fig. 4.2. Fig. 4.3 shows that for $\tau_0 = 1.0$ and $\tau_0 = 0.1$ an instability starts at different times, where for $\tau_0 = 0.1$ the starting-time is much later. The difference is of three order of magnitude compared to all other forcing methods. In cases with greater relaxation times, the forcing is insufficient and therefore the KH instability overcomes the forcing. Therefore, the growth rate increases for increasing relaxation times, as can be seen in Table 4.1. Since in case I the flow is unstable even without forcing, the expected KH instability can occur if τ_0 much greater than unity when using the local method. Therefore, for the second case the KH instability will be suppressed even for large τ_0 and so no results for case II were obtained as mentioned above.

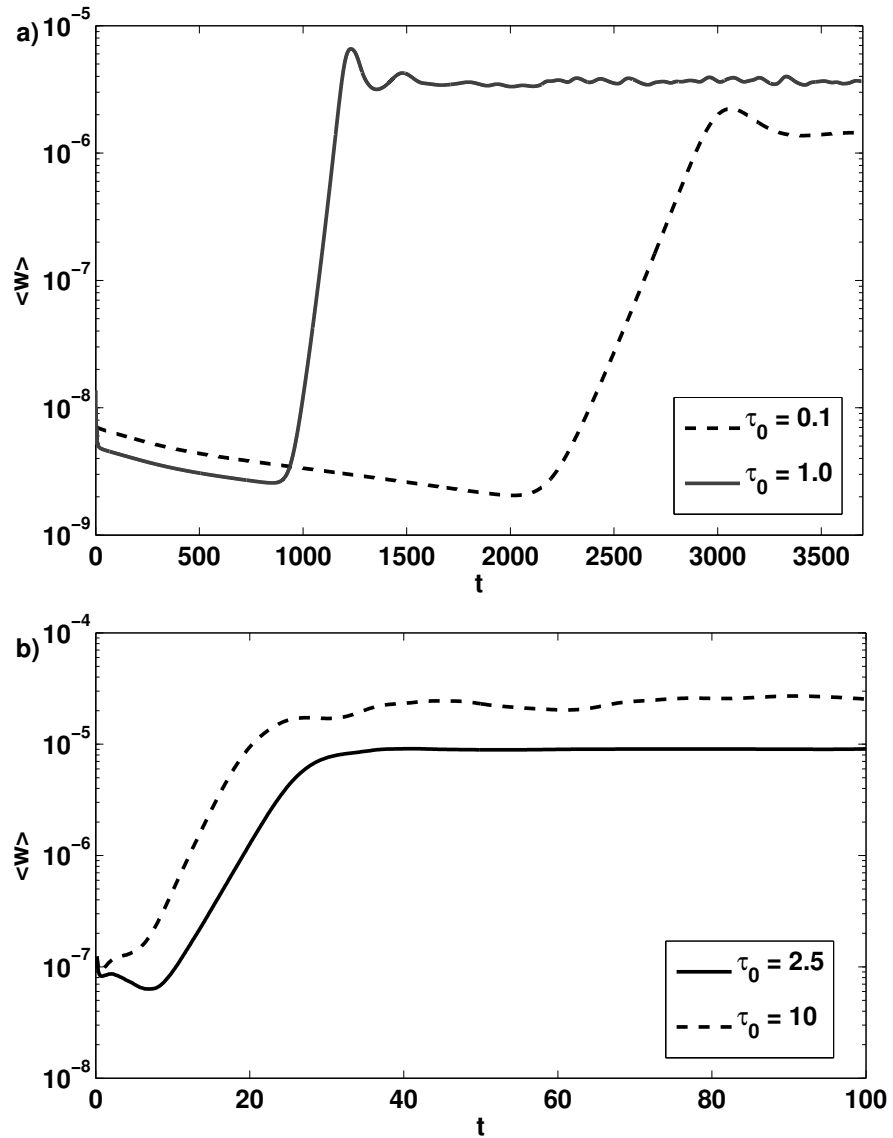


Figure 4.3.: The time evolution of the volume averaged vertical velocity for case I with the local relaxation method. (a) Cases with $\tau_0 \leq 1$. (b) Cases with $\tau_0 > 1$. The vertical velocity is displayed in logarithmic scale and t is given sound-crossing time.

4.4. Conclusion

Some of the difficulties of modelling shear flows in stellar interiors are due to the fact that the underlying physical mechanisms that generate and sustain the shear flow are not known (Gough and McIntyre, 1998; Vasil and Brummell, 2009). Therefore, it is not understood what form the force that needs to be applied has. In this chapter I investigated the effect of different forcing methods, which have been widely used, to clarify which method is most suitable when investigating shear flows like the one in the tachocline. Having compared the evolution of the exponential growth phase of a shear instability for different forcing methods by using non-linear calculations I conclude the following. Viscous forcing prevents the shear profile from being smoothed out by the viscosity and so a KH instability is obtained. This method only affects the flow on a viscous time-scale, which is not relevant to the turbulent regime that is considered further below. The forcing is static, i.e. the form of the force does neither depend on the actual velocity of the system nor on the time. Furthermore, this forcing drives the system close to the middle plane, but very little force is applied to the outer part of the domain. As expected the numerical calculations using the viscous method and perturbation method lead to exactly the same results, because both methods are mathematically equivalent. Note however that the computational cost is slightly greater when using the perturbation method. Therefore, the perturbation method will be discarded in the following comparison in Chapter 5.

The average relaxation method results in a similar evolution as obtained by the viscous forcing with the additional possibility to adjust the time-scale on which the force responds to changes in the actual flow. The forcing acts on large global-scales and has a uniform strength along the forcing direction. Depending on the relaxation time, τ_0 , either the instability dictated by the initial state is triggered or a slightly different shear flow instability is triggered. The later one occurs due to the smoother velocity profile than initial set. Finally, the local relaxation forcing suppresses any instability and can lead to non-physical behaviour. Therefore, this forcing should be avoided and it does not suit to sustain a shear flow.

5. Non-linear Evolution: Forcing Methods Part II

Having analysed the linear phase during which the KH instability exponentially grows in two dimensions, the next question to address is what occurs after the instability starts to saturate. A shear instability can lead to a turbulent regime after initiating a secondary instability that develops in the third dimension (see for example Peltier and Caulfield, 2003). These secondary instabilities lead to a turbulent collapse of horizontal vortices that are suppressed in a two-dimensional setup as discussed by Scinocca (1995). And so a three-dimensional domain is crucial to study the non-linear evolution of a stratified shear flow (Thorpe, 1987). Therefore, to capture the effect of different forcing methods on the entire dynamics I use fully three-dimensional calculations in this chapter.

As discussed in Chapter 4, the viscous method and the perturbation method are equivalent. After checking that the calculations are indeed the same when using the perturbation method, in the following, only results obtained by using the viscous method are shown in this chapter for brevity. So in this chapter I will compare the non-linear dynamics obtained by using the viscous method and the relaxation method. Furthermore, the effect of varying τ_0 in the relaxation method, and how does it compare with the viscous method will be discussed.

In order to analyse the non-linear dynamics quantitatively, several global quantities will be calculated. For this purpose different energy budgets, which are introduced in Section 5.1, are tracked separately during the non-linear calculations. Then, the results of the different methods are presented in Section 5.2, where I start the qualitative analysis by comparing vorticity and vertical velocity snap-shots during the steady state in Subsection 5.2.1. In Section 5.2 I will then move to look at the

quantitative comparison using horizontally averaged profiles of the characteristic quantities and energy budgets. Finally, in Section 5.3 the differences of the forcing methods will be discussed and a conclusion will be given.

5.1. Theoretical Framework for Energy Budgets

To get a comprehensive insight on the processes involved when a linear shear flow instability saturates, it is useful to track the evolution of the standard forms of energy during the transition phase and beyond. Following the same procedure, as used in Landau and Lifshitz (1987) and Griffies (2004), the total energy is decomposed into the kinetic energy, E_{kin} , internal energy, I , and gravitational potential energy, E_{pot} . For our specific non-dimensionalisation these three energies are given as

$$E_{kin} = \frac{1}{2} \int_V \rho \mathbf{u}^2 dV, \quad (5.1)$$

$$I = c_v \int_V T \rho dV, \quad (5.2)$$

$$E_{pot} = -\theta(m+1) \int_V \rho z dV, \quad (5.3)$$

where the volume integral is taken over the whole domain and the internal energy for an ideal gas is considered. However, following the energy forms separately does not allow a detailed analysis of the flow evolution, because several physical mechanisms are responsible for a change in the kinetic, potential and internal energy budgets. Therefore, it is useful to calculate the changes in the kinetic energy, the total gravitational potential energy and the internal energy throughout the flow evolution. Furthermore, it is possible to separate the changes in the energies according to different physical processes that lead to the change. This enables a more detailed insight into the energy budgets.

To derive the time evolution of the energy budgets the Equations (2.13) - (2.15) are used. The time derivative of the kinetic energy becomes

$$\frac{\partial E_{kin}}{\partial t} = \frac{\partial}{\partial t} \left(\frac{1}{2} \int_V \mathbf{u} \cdot \mathbf{u} \rho dV \right). \quad (5.4)$$

Using the momentum Equation (2.14), the right-hand side of this equation can be divided into different contributions:

$$\begin{aligned}
\frac{1}{2} \frac{\partial}{\partial t} \int_V \mathbf{u} \cdot \mathbf{u} \rho dV &= \underbrace{\sigma C_k \oint_S \tau \cdot \mathbf{u} \cdot \hat{\mathbf{n}} dS}_{=0} - \underbrace{\sigma C_k \int_V \tau_{ij} \frac{\partial u_i}{\partial x_j} dV}_{\varepsilon} - \underbrace{\int_V \mathbf{u} \cdot \nabla p dV}_{\mathcal{H}_p} \quad (5.5) \\
&\quad - \underbrace{\frac{1}{2} \oint_S |\mathbf{u}|^2 \rho \mathbf{u} \cdot \hat{\mathbf{n}} dS}_{\mathcal{H}_a} + \underbrace{\int_V \theta(m+1) \rho w dV}_{\mathcal{H}_\rho} + \underbrace{\int_V \mathbf{u} \cdot \mathbf{F} dV}_W \\
&= -\varepsilon - \mathcal{H}_p - \mathcal{H}_a + \mathcal{H}_\rho + W,
\end{aligned}$$

where S denotes the volume surface, ε is the positive viscous dissipation rate, \mathcal{H}_a is the change rate due to advection, \mathcal{H}_p is the rate of work done by expansion and contraction, \mathcal{H}_ρ denotes the exchange rate with the potential energy due to density flux and W is the work done by external forcing. For a more detailed derivation of the separate contributions see Appendix C.

For the rate of change of the internal energy one gets

$$\frac{\partial}{\partial t} I = \frac{\partial}{\partial t} \left(c_v \int_V T \rho dV \right). \quad (5.6)$$

Using the temperature evolution Equation (2.15) the RHS can be rewritten as

$$\begin{aligned}
c_v \frac{\partial}{\partial t} \int_V T \rho dV &= \underbrace{c_v \oint_S \gamma C_k \nabla T dS}_{\Phi_{temp}} + c_v (\gamma - 1) \underbrace{\int_V \mathbf{u} \cdot \nabla p dV}_{\mathcal{H}_p} + c_v \underbrace{\int_V \rho q dV}_{\varepsilon} \quad (5.7) \\
&= \Phi_{temp} + \mathcal{H}_p + \varepsilon,
\end{aligned}$$

where $q = C_k \sigma (\gamma - 1) |\tau|^2 / 2\rho$ such that ε is due to viscous heating, and has the same form as the viscous dissipation rate in Equation (5.5), but with an opposite sign. Φ_{temp} corresponds to heat loss or gain at the surface, S .

In the standard form, the changes in the gravitational potential energy are only due to the exchange of density flux as can be seen by taking the time derivative

$$\begin{aligned} \frac{\partial}{\partial t} E_{pot} &= \frac{\partial}{\partial t} \left(- \int_V \theta(m+1) \rho z dV \right) \\ &= \underbrace{\theta(m+1) \oint_S z \rho \mathbf{u} \cdot \hat{\mathbf{n}} dS}_{=0} - \underbrace{\theta(m+1) \int_V \rho w dV}_{\mathcal{H}_\rho} = -\mathcal{H}_\rho. \end{aligned} \quad (5.8)$$

Summing Equations (5.5) - (5.8) yields the total energy change of the system

$$\frac{\partial}{\partial t} (E_{kin} + E_{pot} + I) = W + \Phi_{temp} - \mathcal{H}_a, \quad (5.9)$$

which is only due to external forces, heat loss or gain at the surfaces, and advection. Note, that \mathcal{H}_a is negligible in the case considered here because the system is closed and mass is conserved. It can be seen that viscous dissipation, ε , density flux, \mathcal{H}_ρ , and work done by expansion and contraction, \mathcal{H}_p are exchanged between the kinetic energy and the potential energies.

Using the standard decomposition of energies it remains impossible to distinguish between reversible and irreversible energy exchange between these three energy budgets (see for example Peltier and Caulfield, 2003). In order to resolve this issue Winters et al. (1995) introduced a method to analyse the mixing behaviour of a turbulent flow, which can be used to track reversible and irreversible changes of different potential energies. This framework was further extended to compressible fluids by Tailleux (2013). For this method the gravitational potential energy of the system, defined in Equation (5.3), is decomposed into two parts. One part is the so-called background potential energy defined as

$$E_{back} = -\theta(m+1) \int_V \rho_\star z dV, \quad (5.10)$$

where the ρ_\star is the adiabatically redistributed density. This definition can be used for a compressible fluid. Another part is the available potential energy

$$E_{avail} = -\theta(m+1) \int_V (\rho - \rho_\star) z dV, \quad (5.11)$$

which corresponds to the difference between the actual potential energy E_{pot} and E_{back} . The available potential energy can be transformed into other types of energies, whereas the background energy can not be accessed and transformed in other types of energies. Therefore, the background potential energy can be interpreted as the part of the total gravitational potential energy that corresponds to the lowest energy level that can be reached if the system is adiabatically redistributed. While a system is evolving the background potential energy can be only changed by irreversible processes. In numerical calculations that I will discuss in this chapter, the background potential energy is obtained by taking the actual density distribution and sorting it in an ascending order, such that the highest density is at the bottom of the domain. A more detailed discussion of the numerical parallel sorting procedure is provided in Appendix D. In a similar procedure the internal energy can be decomposed into a background internal energy budget and an available internal energy budget, for a more detailed discussion see Tailleux (2013). However, for the purpose here it is sufficient to analyse only the budgets for the gravitational potential energy in order to understand the mixing behaviour of the system.

5.2. Results for the Non-linear Phase

In order to avoid confinement effects associated with the upper and lower boundaries, I consider a temperature gradient $\theta = 5$. In this case the instability is more likely to remain confined in a narrow central region as to minimize the importance of the particular choice of boundaries. The polytropic index, $m = 1.6$, is kept the same as in Chapter 4 to ensure a stable stratification. A parameter search was conducted to find combinations of the other parameters that lead to a finite spread of the unstable region. The dynamical viscosity is taken of order 10^{-4} and the Prandtl number, $\sigma = 0.1$, because low Prandtl number flows are more relevant for stellar interiors. The shear flow amplitude is set to $U_0 = 0.2$ and the shear width is taken as $1/L_u = 80$ such that $Ri_{min} = 0.003$. Then, the initial $Pe = 0.5$ and the initial Reynolds number, $Re(z) = \rho(z)U_0L_u/\mu$, at the top is $Re(0) = 5$, whereas at the bottom of the domain $Re(1) \approx 88$. To ensure that all scales remain well resolved (which I checked by investigating the energy spectrum), the spatial resolution of the

numerical domain is $N_x = 256$, $N_y = 256$ and $N_z = 360$. In Fig. 5.1 the volume averaged vertical velocity $\langle w \rangle$ with time for the three-dimensional calculations is shown to illustrate the different stages of the shear flow evolution. For example, for the case where the viscous method is used, the system starts to saturate after roughly five sound crossing times and reaches a statistically steady state after about 25 sound crossing times.

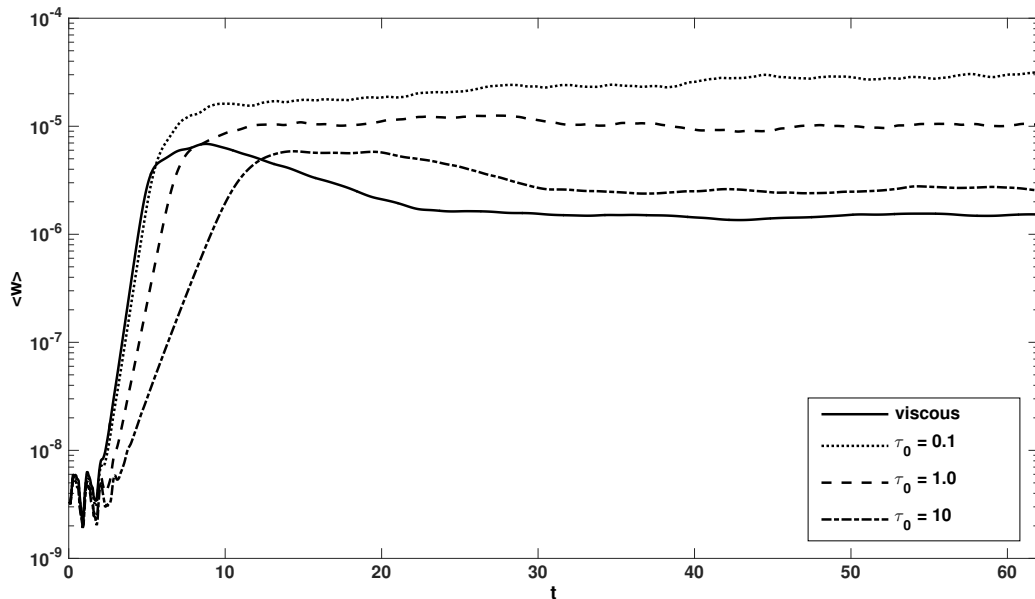


Figure 5.1.: The time evolution of the volume averaged vertical velocity, similar to the definition in Equation (4.10) but for three-dimensional calculations. Different τ_0 parameters for the relaxation method are used and compared to the viscous method. The vertical velocity is displayed in logarithmic scale and t is given sound-crossing time.

5.2.1. Visualisation

In order to compare the flow evolution a visualisation of the vorticity at two different stages, which can be identified from the $\langle w \rangle$ evolution shown in Fig. 5.1, during the non-linear saturation is shown in Fig. 5.2. The first stage is the exponential growth phase, during which all forcing methods show a similar evolution, where the layer with non-zero vorticity spreads vertically. For the viscous forcing and the relaxation method with $\tau_0 \ll 1$, this layer remains significantly smaller than for calculations where the relaxation method with τ_0 close to unity is used. Note, the initial viscous time-scale in this system is $t_\mu \approx 1.5$.

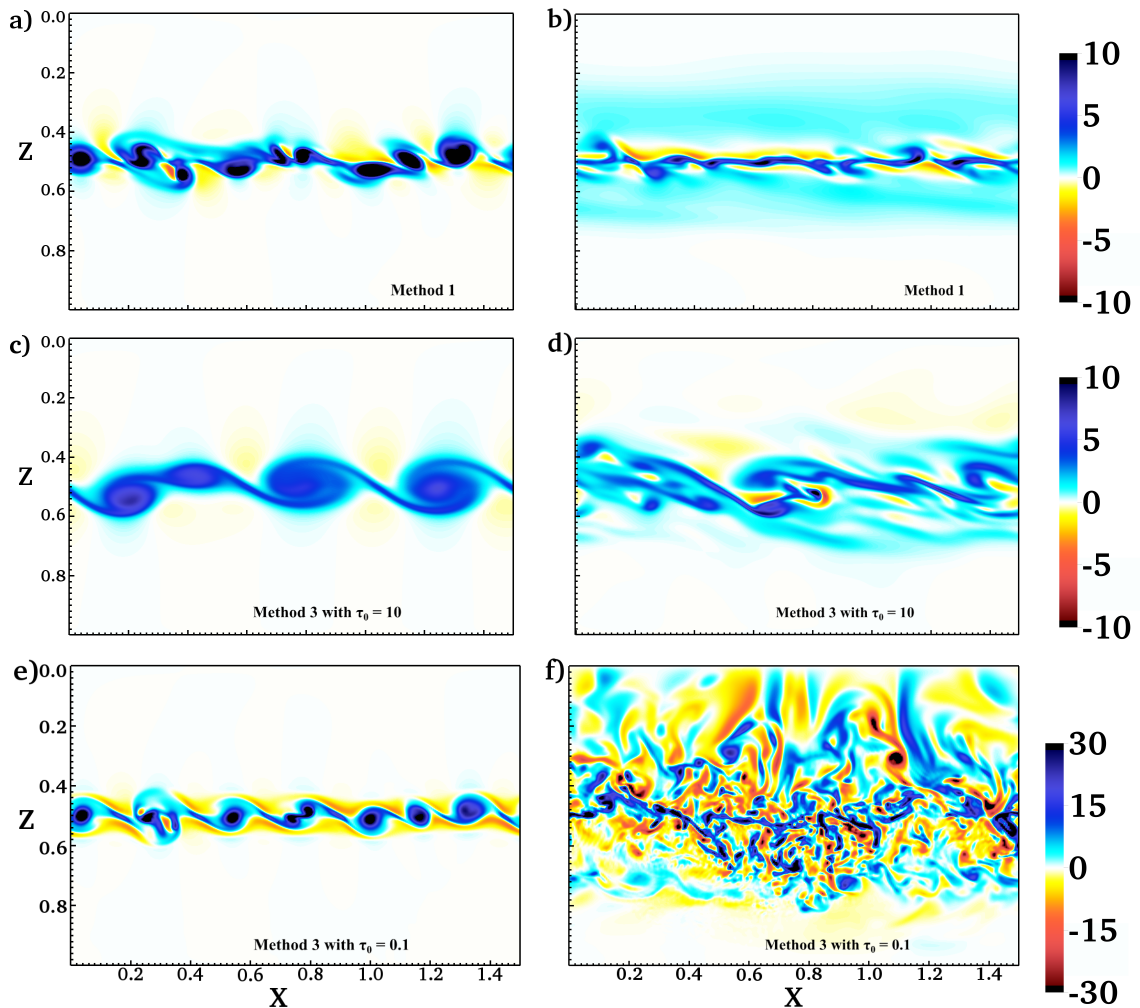


Figure 5.2.: The vorticity component perpendicular to the x - z -plane for different forcing methods at two different stages during the time evolution. The plots at the top (a) and (b) show snapshots of two different times for the viscous method, where (a) is at $\tilde{t} = 7.2$ and (b) at $\tilde{t} = 40$. The middle row (c) and (d) show the relaxation method with $\tau_0 = 10$ at $\tilde{t} = 6.8$ and $\tilde{t} = 40$, respectively. In (e) and (f) the relaxation method with $\tau_0 = 0.1$ was used, where $\tilde{t} = 12.3$ in (e) and $\tilde{t} = 38$ in (f).

The second stage I define to be at a point when the instability starts to saturate and the fluid parcels overturn, and the third stage I take to be sufficiently long after the system saturated. In Fig. 5.2 the vorticity component perpendicular to the x - z -plane for the viscous forcing, the relaxation method with $\tau_0 = 0.1$ and $\tau_0 = 10$ for the second and third stage are plotted in the x - z -plane at $y=0.8$. In Fig. 5.2 (a), Fig. 5.2 (c) and Fig. 5.2 (e) it can be seen that the dynamics for the second stage differ between the different forcing methods. In Fig. 5.2 (a) small patches of strong positive vorticity are merging together into each other along a thin horizontal layer and a few small negative vorticity patches are present. In comparison, when using

the relaxation method with $\tau_0 = 10$, see Fig. 5.2 (c), large billows of smaller positive vorticity occupy a horizontal layer, which is more extended in the vertical direction. This can be explained by the smoother shear width, which is a consequence of the slow back-reaction of the forcing. Analysing the differences in Fig. 5.2 (a) and Fig. 5.2 (e) the vorticity amplitude drastically changes, as can be seen by comparing the different colour scales. Using a smaller τ_0 leads to a greater vorticity amplitude than achieved by the viscous method, while the spread of the instability remains similar.

The third stage for the different methods is several sound crossing times after saturation, where the flow is evolving towards a quasi-steady state. Comparing Fig. 5.2 (b), where the viscous method is used, with Fig. 5.2 (d), and Fig. 5.2 (e), where the relaxation method with $\tau_0 = 10$ and $\tau_0 = 0.1$ are used, the main differences are the vertical extent of the overturning region and the amplitude of the vorticity. When comparing Fig. 5.2 (b) and Fig. 5.2 (d) it becomes evident that using a larger $\tau_0 = 10$ leads to a similar situation as for the viscous method. In Fig. 5.2 (b) the layer is thin and shows elongated regions of strong positive vorticity, whereas in Fig. 5.2 (d) the region is significantly extended with small patches of strong positive and negative vorticity. A few larger regions are present further away from the middle of the domain. For the relaxation method with $\tau_0 = 0.1$ a drastically different behaviour is observed, see Fig. 5.2 (f), where the vorticity amplitude is much greater and the region where overturning is present is taking up almost the entire domain. In addition, much more small-scale turbulence occurs around $z = 0.5$. This can be explained by the form of the forcing used: The viscous method acts with a force, that is confined in a narrow region around the middle of the domain such that outside of this region no additional forcing affects the dynamics. Therefore, the instability can develop freely further away from $z = 0.5$. On the contrary, the relaxation method drives the fluid towards the target profile at every height in the domain, such that the turbulent dynamics are affected by the forcing everywhere in the domain. This supports additional spread of the shear instability and triggers more turbulent motions. It is worth mentioning that for the relaxation method with $\tau_0 = 0.1$ convective motion is present in the upper half of the domain due to strong viscous heating. This is checked by calculating the Brunt-Väisälä frequency (Lord Rayleigh, 1883; Väisälä,

1925; Brunt, 1927) as defined in Equation (3.10), but by using horizontally averaged density and temperature profiles for different times. After the system has saturated the Brunt-Väisälä frequency becomes negative in the upper layers. This dynamics will not be further discussed, as it is the result of the artificially low value of τ_0 used in that case. Furthermore, it is expected that this unrealistic instability will disappear at lower Prandtl numbers, but it has not been shown here due to numerical limitations.

Fig. 5.3 shows contour plots of the vertical velocity in three dimensions at approximately 40 sound-crossing times, which is well after the non-linear saturation. For the viscous method the patches of downwards and upwards motion form an alternating pattern along the x -direction, where regions of the same velocity are arranged in small tubes that are extended along the y -direction, see Fig. 5.3 (a). Such a pattern is not present in Fig. 5.3 (b), where the relaxation method with $\tau_0 = 10$ is used. Here, the regions of the same velocity form larger patches that are extended along the x -direction and changes sign along the y -direction. Such behaviour indicates that a secondary instability, which forms overturning billows along the y -direction, is more dominating when the relaxation method with larger values of τ_0 is used. For the relaxation method with $\tau_0 = 0.1$, displayed in Fig. 5.3 (c), the artificially strong forcing leads to an intense forward energy cascade and associated small-scale turbulent motions in the middle of the layer, which is identified in the energy spectrum. The large-scale structures observed in the upper part of the domain are convective cells resulting from the large central viscous heating.

When looking at the time evolution for the viscous method and the relaxation method with $\tau_0 = 0.1$, where snapshots for both cases are displayed in Fig. 5.2, a significant difference in the amplitude of the vorticity can be noticed. For the viscous method the amplitude increases towards a peak during the saturation, shown in Fig. 5.2 (a), and starts to decrease afterwards. On the other hand, for the relaxation method the amplitude of the vorticity constantly increases and reaches a maximum after saturation, see Fig. 5.2 (b) and Fig. 5.2 (f). This might be explained by the form of the forcing as follows: Because the relaxation method adjusts the magnitude of the force according to the mean flow, the strength of the force increases constantly and lead to more overturning with time. Whereas when using the viscous method,

the force remains constant, such that the overturning settles down after saturation. However, in order to check if this is indeed the case a more detailed analysis on the work done by the force and the total viscous dissipation is required, which is carried out in Subsection 5.2.3.

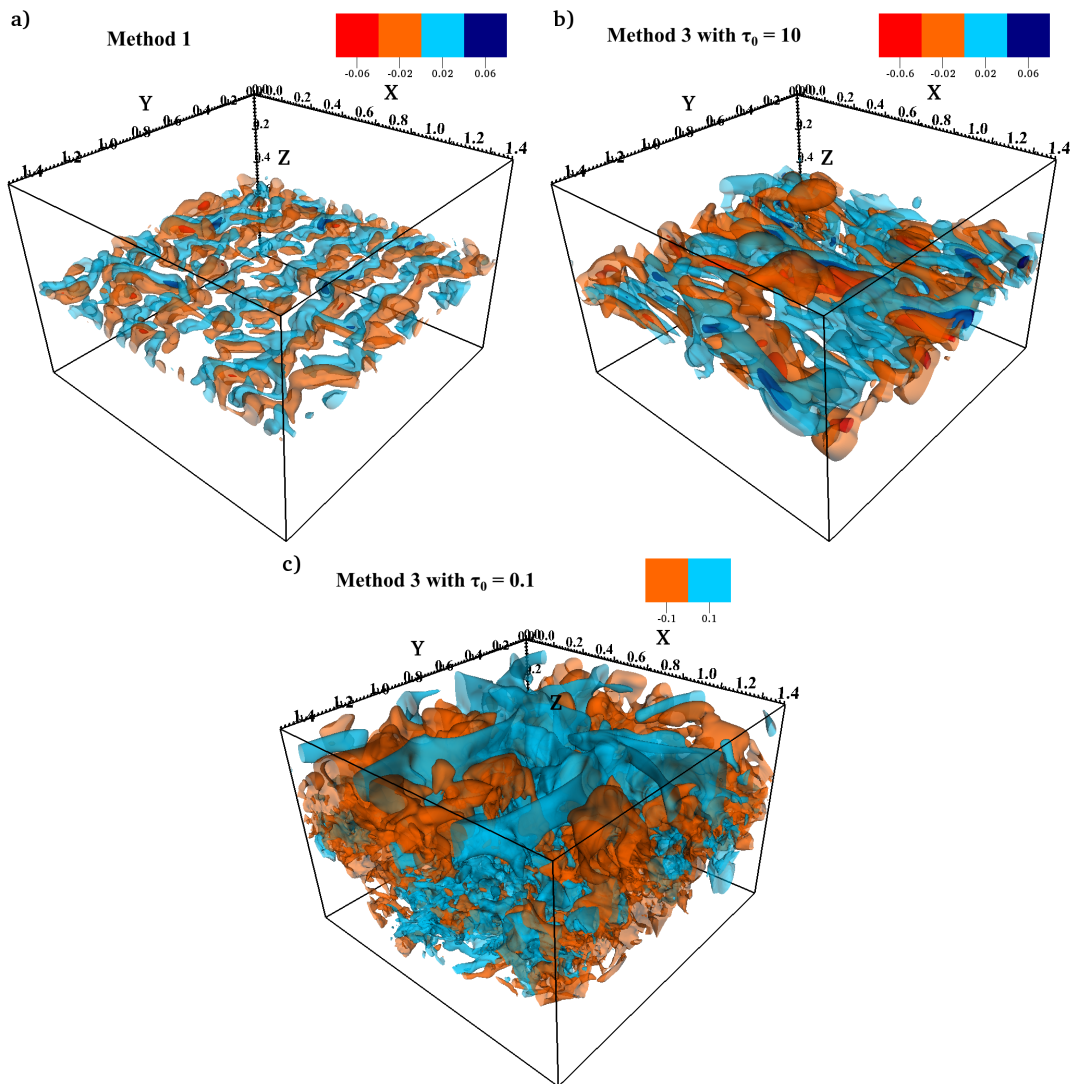


Figure 5.3.: The vertical velocity component, w , for different forcing methods after saturation. (a) Viscous method at $\tilde{t} \approx 40$. (b) Averaged relaxation method with $\tau_0 = 10$ at $\tilde{t} \approx 40$. (c) Averaged relaxation method with $\tau_0 = 0.1$ at $\tilde{t} \approx 38$.

Having compared the non-linear evolution for different forcing methods qualitatively the following can be concluded. The viscous method and the relaxation method with τ_0 of the same order as the viscous time-scale t_μ or larger result in similar, but still

distinct, evolutions. Using a relaxation time $\tau_0 \ll t_\mu$, but still greater than the dynamic time-scale $t_s \approx 0.06$, leads to a very different non-linear dynamics with much mixing and possible non-physical behaviour leading to convection. Therefore, for the saturated regime, the initial viscous time-scale, here $t_\mu \approx 1.5$, gives a reference time for the choice of τ_0 . Therefore, the case with $\tau_0 = 0.1$ will be excluded from further analysis.

5.2.2. Horizontally averaged profiles

Since the system under consideration is stratified, most quantities will change with depth, z , throughout the domain. Therefore, investigating horizontally averaged profiles with depth provides insight in the system dynamics during the saturated regime.

First, a local turbulent Reynolds number is defined as follows

$$Re_t(z) = \frac{\bar{\rho}(z)l_t(z)u_{rms}(z)}{\sigma C_k}, \quad (5.12)$$

where $\bar{\rho}(z)$ denotes that the density is horizontally averaged as defined in Equation (4.6). Here $u_{rms}(z)$ is the root-mean-square of the fluctuating velocity averaged over the horizontal layers calculated as follows

$$u_{rms}(z) = \frac{1}{N_x N_y} \sum_{x=1}^{N_x} \sum_{y=1}^{N_y} \sqrt{(\mathbf{u}(x, y, z) - \mathbf{U}_0(z))^2}, \quad (5.13)$$

where $\mathbf{U}_0(z)$ is the target velocity profile as defined in Equation (3.14). The turbulent length-scale is taken as

$$l_t(z) = 2\pi \frac{\sum_{k=1}^{k_{max}} x_{max} k^{-1} E(k, z)}{\sum_{k=1}^{k_{max}} E(k, z)}, \quad (5.14)$$

where $k^2 = k_x^2 + k_y^2$ is the horizontal wave number, $k_{max} = (N_x/3 + 1)$ and x_{max} is the length of the domain in x -direction.

The energy spectrum $E(k, z)$ is averaged over horizontal layers such that it takes the form

$$E(k, z) = \frac{1}{4} \sum_{k=1}^{k_{max}} \hat{\mathbf{u}}(k_x, k_y, z) \rho \hat{\mathbf{u}}^*(k_x, k_y, z) + \rho \hat{\mathbf{u}}(k_x, k_y, z) \hat{\mathbf{u}}^*(k_x, k_y, z). \quad (5.15)$$

The resulting Reynolds numbers with depth for the viscous method, the relaxation method with $\tau_0 = 1$ and with $\tau_0 = 10$ after 60 sound-crossing times, which is during the saturated regime, are shown in Fig. 5.4 (a).

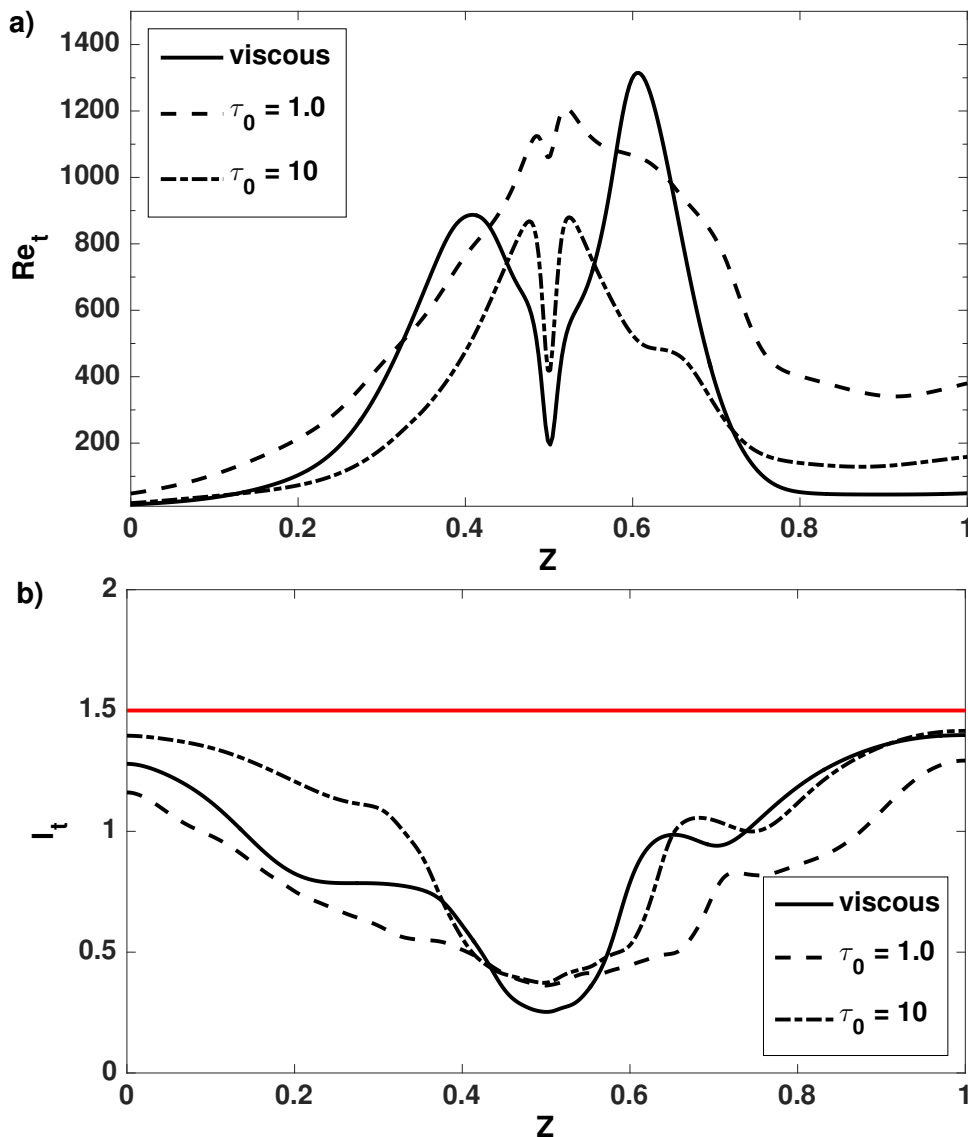


Figure 5.4.: Turbulent Reynolds number and length-scales for three different forcing methods. (a) Re_t , as defined in Equation (5.12). (b) Turbulent length-scales, l_t . The red line indicates the horizontal extent of the domain.

It becomes evident that the flow for all three cases is very different at the late stage of the calculation. The viscous method is characterised by two regions above and below the middle of the domain, where the flow has high Reynolds numbers about 850 and 1300 respectively. The asymmetry is due to significantly denser fluid at the bottom of the domain. For the relaxation method with $\tau_0 = 10$, these two regions are narrower and the maximal Reynolds numbers are approximately 800 and 900. For $\tau_0 = 1.0$ the region of high Re_t is spread with two peaks very close to $z = 0.5$. For all cases a moderate turbulent flow remains confined in the middle of the domain. Fig. 5.4 (b) reveals that for the three methods used the corresponding turbulent length-scales become less than 0.5 around $z = 0.5$ and increase towards the boundaries. For this particular case, using the viscous method leads to smaller turbulent length-scales than using relaxation methods.

I now consider the horizontally averaged velocity profile $\bar{u}_x(z)$ shown in Fig. 5.5 at a time, \tilde{t} , where the system evolves towards a quasi-steady state.

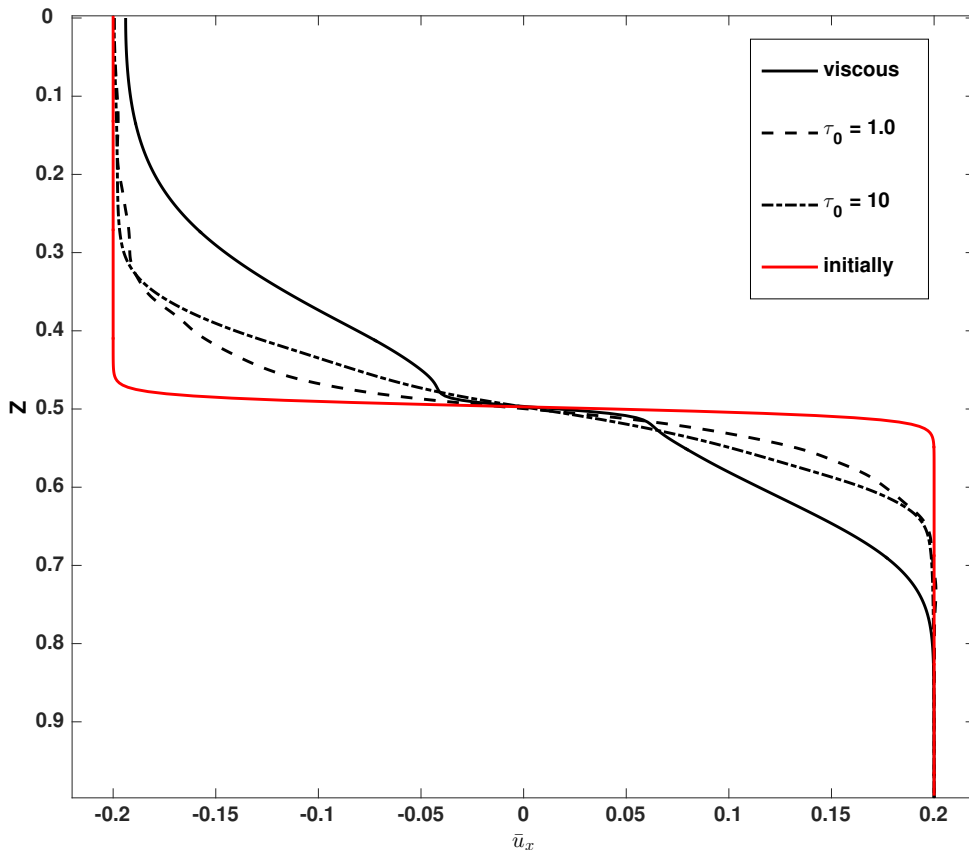


Figure 5.5.: The horizontally averaged u_x profiles at $t \approx 60$ are shown for different forcing methods.

For all methods the shear profile is smoothed out. For the relaxation method $\bar{u}_x(z)$ remains a hyperbolic tangent profile, but for the viscous method a steep transition occurs around $z = 0.5$, which merges into a smoother region at the boundaries. This is caused by the different type of forcing: The force applied in the viscous method is solely defined by the shape of the target profile. Since the initial target profile has a thin width, the second derivative is large in this region, which causes a stronger forcing, compared to the outer parts of the domain. In contrast the relaxation method applies a force that depends on the deviation of the actual mean profile from the target profile, such a back reaction ensures the preservation of a hyperbolic tangent profile.

5.2.3. Energy Budgets from Numerical Calculations

The Kelvin-Helmholtz instability converts kinetic energy that is available to the base horizontal shear flow into vertical fluctuations that need to overcome the stably-stratified atmosphere. The gravitational potential energy of the system is changed during this process. In addition, after saturation the fluid starts to overturn, and is mixed, where irreversible processes change the potential energy. Here I will investigate how the forcing contributes to the different forms of energy in the system. Using separate components responsible for the change in different energy budgets presented in Section 5.1 and tracking the changes of the kinetic energy, internal energy and different gravitational potential energy budgets, I will discuss how the system behaves for different forcings. In the discussion below I will distinguish between four stages of the system's evolution that are summarised in Table 5.1.

Table 5.1.: Time intervals of the different dynamical stages.

Stage:	Viscous	Relaxation Method	
	Method	with $\tau_0 = 1$	with $\tau_0 = 10$
before instability	$0 < t < 2.5$	$0 < t < 3.5$	$0 < t < 4.5$
exponential growth	$2.5 < t < 4.5$	$3.5 < t < 6.5$	$4.5 < t < 10$
saturation	$4.5 < t < 23$	$6.5 < t < 30$	$10 < t < 30$
quasi-steady state	$t > 23$	$t > 30$	$t > 30$

These stages are the time interval before the exponential growth of an instability, the exponential growth phase, the onset of saturation, and a fully saturated quasi-steady state. These stages are at different times for the three calculations that are discussed.

Significant differences between the forcing methods become evident when following different energy budgets normalized by the initial value of the system's total energy with time as shown in Fig. 5.6. Note, three-dimensional calculations were performed only once due to computational limitations. Although, random temperature perturbations were included in the beginning of each calculation, it is not expected that other random initial perturbations will significantly affect the results.

In general the sum of the three energies is increasing due to the external work done by the forcing. First I will focus on the viscous forcing method where the kinetic energy remains almost constant until the instability starts to grow at $\tilde{t} \approx 3$. As the kinetic energy remains almost constant in the beginning, it can be concluded that the amount of energy dissipated is fed back into the system due to external work, W . Then, at $\tilde{t} \approx 3$ the kinetic energy, E_{kin} , begins to decrease. The decrease in the kinetic energy of the system during the exponential growth of the instability is a direct consequence of the Kelvin-Helmholtz instability extracting energy from the large-scale shear flow in order to overcome the potential energy associated with the stably-stratified atmosphere. This amount of energy is partly converted into vertical motion, which contributes to the kinetic energy, and partly exchanged into gravitational potential energy. The term in the energy change rate associated with this exchange is \mathcal{H}_ρ , which leads to a slight increase in E_{pot} . Because the conversion of the mean-flow kinetic energy to vertical motion retains the energy in the kinetic energy budget, the decrease is small. During the saturation phase the negative rate of change in the kinetic energy grows, but start to evolve towards a constant value after saturation.

Moving on to the other energy budgets, the internal energy increases at an almost constant rate from the beginning of the calculation, which is due to viscous heating that extracts kinetic energy via ε in Equation (5.5). However, a plateau is reached just after the exponential growth phase and followed by a steeper increase during the

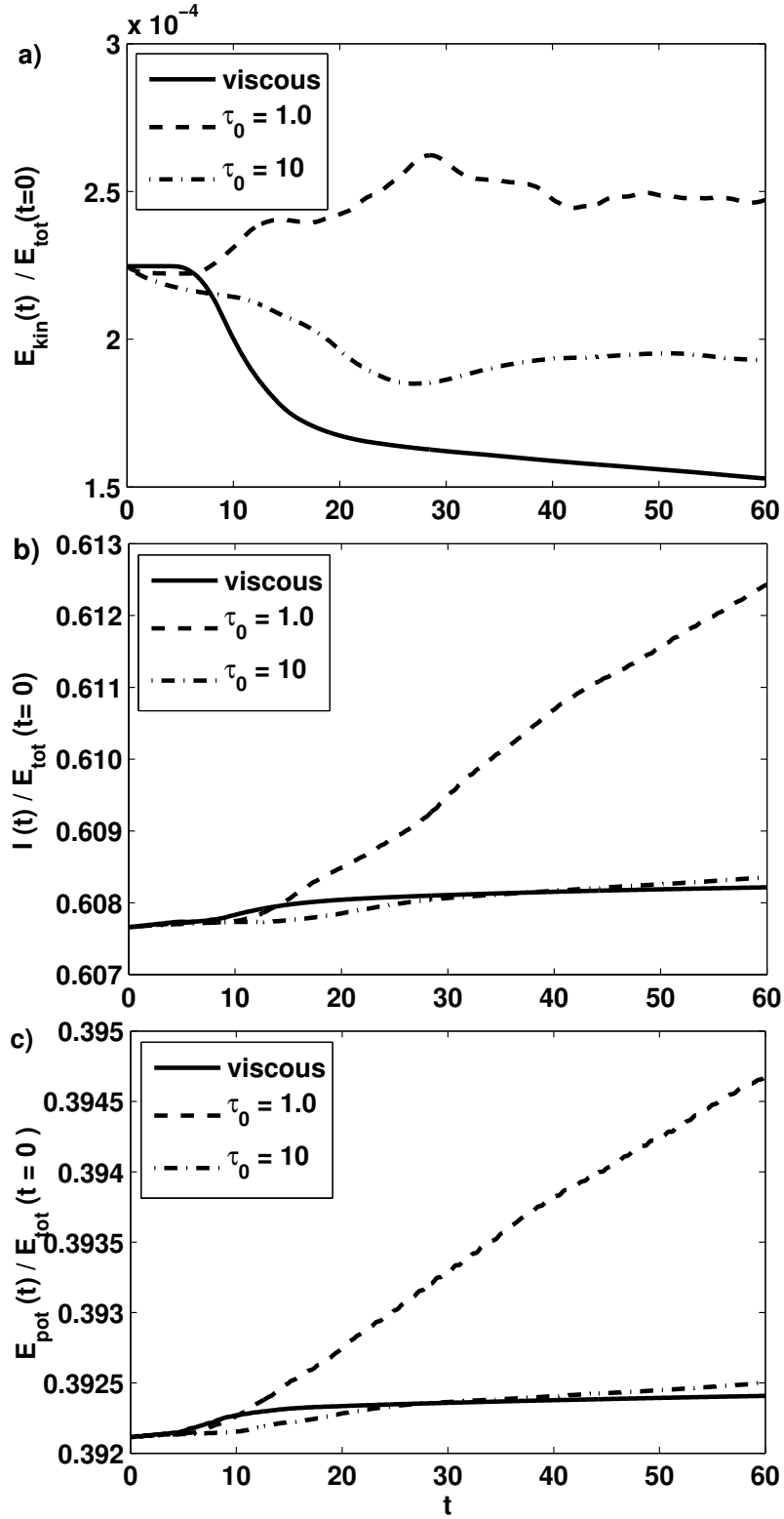


Figure 5.6.: The total kinetic energy, internal energy and the gravitational potential energy evolution for the viscous forcing and relaxation method by using two different τ_0 . All energies are normalised by the initial total amount of the system's energy $E_{tot}(t=0) = 195.81$. (a) $E_{kin}(t)/E_{tot}(t=0)$ with time. (b) $I(t)/E_{tot}(t=0)$. (c) $E_{pot}/E_{tot}(t=0)$.

end of the saturation phase. The gravitational potential energy starts to increase faster from the beginning of the saturation phase, but converges towards a constant value during the long-time evolution. Comparing the gravitational potential energy and the internal energy evolution shows that the changes of the internal energy are similar to the changes in the potential energy but with a time shift and a greater amplitude. The time delay can be explained as follows: In a first step, kinetic energy is transformed reversibly and irreversibly into gravitational potential energy due to the term \mathcal{H}_ρ . This leads to an increase in the gravitational potential energy. Then, in a second step irreversible processes during the feedback of gravitational potential energy into kinetic energy lead to an increase in the internal energy. Eventually a quasi-steady state is reached, where the kinetic energy will decrease very little, but the potential energies will constantly increase due to viscous heating and irreversible mixing processes. Both processes extract kinetic energy due to ε and \mathcal{H}_ρ respectively, but only a part of ε is added to the system by the external force. Therefore, the system will always evolve very slowly, but remain statistically similar for a very long time.

Having looked at the energy evolution for the viscous forcing method I now focus on the calculations where the relaxation method was used. The time evolution of E_{kin} for the relaxation method with $\tau_0 = 10$ is similar to the viscous forcing. However, the early evolution is different because E_{kin} decreases even before the instability starts to develop. This is expected since the kinetic energy initially contained in the initial shear flow is dissipated by viscosity over a short time-scale, and the forcing method is not sufficiently fast to balance for that. Therefore, the exponential growth regime is shifted to later times, where a similar drop in E_{kin} as in the viscous forcing case was found. In both cases, this reduction in kinetic energy corresponds to an increase in the potential energy in the system as shown in Fig. 5.6 (c). Similar to the viscous forcing, for the relaxation method with $\tau_0 = 10$ the background potential energy and internal energy increase slowly until the system starts to saturate. During the saturation phase a steeper increase is present. Then, after several sound crossing times, both potential energies start to converge towards a constant small growth after the system saturated. This behaviour reveals that the energy induced by the forcing principally transfers into internal energy due to dissipation, but does not

contribute to an increase in either kinetic energy or available potential energy for late time evolution. Moreover, in the non-linear regime the system also tends towards a statistically steady state.

Moving on to the calculation with a shorter relaxation time, $\tau_0 = 1.0$, a different behaviour is present compared to the case with $\tau_0 = 10$. The kinetic energy, E_{kin} , increases with the onset of instability. This growth is due to the very intense external forcing present as soon as the averaged velocity profile deviates from the target profile, which is the case when the instability starts growing. For $\tau_0 = 1.0$ this corresponds to a growth in the total kinetic energy over approximately 30 sound crossing times whereby E_{kin} slowly oscillates around a fixed value. In addition, the case with $\tau_0 = 1.0$ shows a constantly large increase of the potential energy even for the saturated stage. Looking back at Fig. 5.6 (a) the kinetic energy converges towards a constant value at large times. This indicates again that the kinetic energy pumped into the system by external forcing, W , is used to balance viscous dissipation and partly converted into gravitational potential and internal energy. Here the amount of externally added energy is significantly greater than for the other two calculations.

In contrast for the calculation with $\tau_0 = 0.1$, which is not displayed here, the kinetic energy grows during the whole duration of the calculation. As discussed earlier, this growth in the kinetic energy of the system in that particular case is associated with a transition between a stably stratified atmosphere (the polytropic index is initially $m = 1.6$) and a convectively unstable atmosphere where large convective cells appear in the upper part of the domain as shown in Fig. 5.3 (c). This transition is driven by the large viscous heating in the central shear region modifying the temperature profile and changing the sign of the Brunt-Väisälä frequency. While the interaction between a large-scale shear flow and thermal convection is of interest (see, for example, Guerrero and Käpylä, 2011; Silvers et al., 2009a), this is beyond the scope of the current study.

In Fig. 5.7 the evolution of the available gravitational potential energy is plotted for the three-dimensional calculations. This part of energy is due to the reversible part of \mathcal{H}_ρ in the energy equations. When looking at the available potential energy

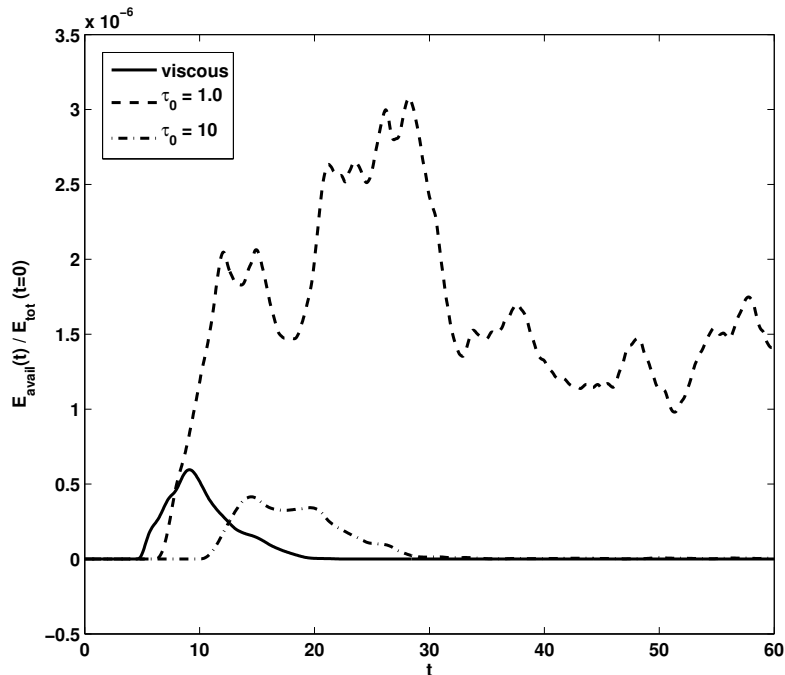


Figure 5.7.: The available gravitational potential energy $E_{avail}(t)/E_{tot}(t=0)$ evolution for both the viscous forcing and relaxation methods by using two different τ_0 .

in Fig. 5.7, no available potential energy is present before the saturation of the shear instability for all cases. Such that the system is in a state of lowest possible potential energy. The E_{avail} for the viscous method and relaxation method with $\tau_0 = 10$ increases similarly, although the arch of E_{avail} is shifted towards later times in the calculation with $\tau_0 = 10$. Looking at Fig. 5.6 (b) and Fig. 5.6 (c) it becomes evident that E_{pot} and E_{avail} increase significantly during saturation, which indicates reversible and irreversible mixing processes. Therefore, I conclude that the fluid is mixed mostly during this stage, where the background density is modified due to the onset of overturning.

After the system saturated, E_{avail} converges towards zero for the viscous method at late times, whereas in the calculation using the relaxation method with $\tau_0 = 10$ the available potential energy oscillates around a small value. Since available potential energy is directly related to mixing (Peltier and Caulfield, 2003), the system evolves towards a state with little mixing. This means that, after a certain modification of the density profile, the overturning settles down and persists at a low level over a long period of time.

In agreement with kinetic energy evolution for the relaxation method with $\tau_0 = 1.0$, the available potential energy starts to grow more rapidly and the system seems to reach a type of quasi-steady state at very late times. However, for both cases where the relaxation method is used with $\tau_0 = 1.0$ and with $\tau_0 = 10$ it remains unclear if the available potential energy is saturated or will eventually decay at some later time, due to current limitation on numerical resources. In order to clarify this, the calculations need to be evolved further. However, for the purposes of comparing the forcing methods in this chapter it is immaterial. By using the relaxation method a long-lived state can be reached and different mixing behaviours exist depending on the relaxation time τ_0 , which persist sufficiently long to study long-time evolution of the generated turbulence.

5.2.4. Comparing Total Viscous Dissipation and External Work

Finally, I will investigate how much of the energy induced into the system by forcing balances the viscous dissipation, which part remains as kinetic energy and what converts into potential energy. To do so, it is useful to study the work done by the forcing, given by W as well as the total viscous dissipation rate, ε , with time. These quantities can be found for all three forcing methods in Fig. 5.8. At the start of the calculation the viscous forcing will always almost exactly balance the viscous dissipation, because the velocity profile does not deviate from the target velocity such that the viscous force cancel the viscous dissipation exactly, as becomes evident from Equation (4.1). This is true until approximately $\tilde{t} \approx 5$ when the instability starts to saturate. After saturation the work done by the viscous forcing is not sufficient to balance the additional dissipation associated with small-scale fluctuations in the system in that case. This is associated with a decrease in the total kinetic energy as already discussed previously. At late times the amount of ε converges towards the work done, as can be seen in Fig. 5.8 (a), and so the system evolves towards a quasi-steady state, where a sustained turbulent flow is present.

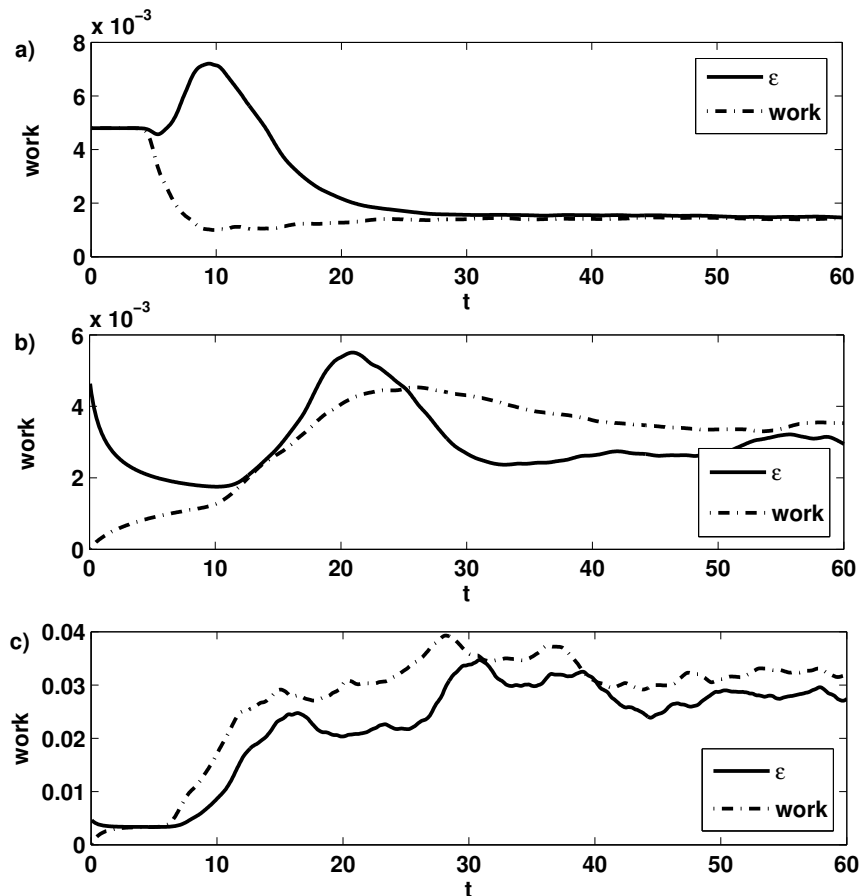


Figure 5.8.: Time evolution of the viscous dissipation rate of momentum, ε , and the work done by the forcing, W . (a) Viscous forcing. (b) Relaxation method with $\tau_0 = 10$. (c) Relaxation method with $\tau_0 = 1.0$.

At the beginning of each calculation, using the relaxation method the work, W , done by the forcing defined in Equation (4.7), is initially zero since the velocity profile exactly matches the target profile. Therefore, depending on τ_0 , viscous dissipation is initially not balanced, as can be seen in Fig. 5.8 (b) and Fig. 5.8 (c). As the initial shear flow diffuses, the associated dissipation decreases until it becomes equal to the external forcing leading to a quasi-steady state. For the case with $\tau_0 = 1.0$ the force increases shortly after the start of the calculation, such that a phase is present, where the viscous dissipation is balanced, before the shear flow instability starts to saturate. After saturation the work done by the forcing is greater than ε , which explains the increase in kinetic energy noticed previously.

Due to the long relaxation time, the case with $\tau_0 = 10$ reveals a distinct behaviour, where W remains less than ε throughout the exponential growth phase. After the exponential growth W matches with ε for a few sound-crossing times as shown in Fig. 5.8 (b). When the total viscous dissipation reaches a peak the work done remains insufficient to balance for the viscous dissipation. At large times when the system is evolving towards a quasi-steady state the total viscous dissipation remains less than the energy input such that turbulence can be sustained.

5.3. Discussion and Conclusion

Turbulent motions driven by a shear flow instability are subject to occur in a wide range of physical systems, where numerical calculations can provide a comprehensive insight to the physical processes. However, the physical mechanism for the generation and maintenance of the differential rotation in stellar interior and especially the tachocline is not well understood (Gough and McIntyre, 1998; Vasil and Brummell, 2009). It is widely believed that external processes such as Reynold stresses, which originated in the convection zone, drives the shear flow in the tachocline (Miesch et al., 2008). However, it is unknown what form the resulting force has that drives the shear flow in the tachocline. Therefore, there are several different forcing methods that have been used to study astrophysical shear flows. Since viscosity is very low in astrophysical objects the aim is to eliminate its effect on the global scale dynamics in numerical calculations. Miesch (2003), Vasil and Brummell (2008), and Silvers et al. (2009b) used a method to balance viscous dissipation by introducing an external force proportional to the viscous term. The other commonly used method is the relaxation method (e.g. Prat and Lignières, 2013), where an external force proportional to the difference between the actual velocity profile and the target shear profile is used. Here direct numerical calculations in three-dimensional Cartesian domains were used to analyse these different forcing methods to maintain a background shear flow.

This research has revealed several characteristics of the different forcing methods: The viscous method provides a well defined localised force, but without control on the resulting velocity profile of the saturated flow. The shear instability can freely

develop further away from the middle of the domain, but no turbulent motions are sustained there. Therefore, modification of the background profiles are solely due to non-linear dynamics of the instability. This results in less control on the resulting averaged velocity profile further away from the middle layer. From energetic considerations it can be concluded that the additional energy, which is added to the system during the late time evolution by external forcing, approaches a constant value. This initially kinetic energy is mostly converted into potential energy via dissipation. Only a small part contributes to the turbulent dynamics by mixing processes.

On the contrary to the viscous method using the relaxation method provides control on the resulting velocity profile, because the force is proportional to the deviation of the horizontally averaged velocity. For the relaxation method an additional parameter, the relaxation time τ_0 , provides control on the strength of the forcing. Due to the form of the relaxation method the target profile is controlled even far away from $z = 0.5$. This corresponds to a global forcing, which can suppresses changes of the background velocity throughout the domain such that modifications of the background profile due to the shear instability are suppressed. However, this also can induce more mixing, which is not initially caused by the instability of the localised shear layer and therefore leads to non-physical behaviour further away from the middle plane.

Significant differences in the system dynamics are revealed when using the relaxation method with different τ_0 . For the choice of τ_0 two typical time-scales are of interest, the turnover time $t_s = L_u/U_0$ and the viscous time-scale $t_\mu = L_u^2/\mu$. For $\tau_0 < t_s$ an instability with almost the same properties as obtained by the EV-solver is triggered (see Section 4.2). However, the energy evolution of the saturated flow reveals that only a τ_0 greater than or of the same order as the viscous time-scale leads to a system that can reach a quasi-steady state. Moreover, choosing τ_0 greater than the viscous time-scale a non-linear evolution like for the viscous forcing method is achieved. Energy induced into the system by the force balances the loss by viscous dissipation, but little additional kinetic and potential energy is obtained. On the contrary a relaxation time τ_0 less than t_μ leads to a system that is constantly forced and develops a turbulent region, which has a greater vertical extent. Such cases

do not tend to evolve towards a quasi-static state, which becomes evident due to their energy evolution. Moreover, the energy induced into the system is significant greater than the loss by dissipation such that the energy overrun is converted into kinetic energy of the disturbances and available potential energy of the system.

Analysing the turbulent Reynolds numbers for late times shows that with decreasing τ_0 the horizontal layer of turbulent flow reaches a larger vertical extent and higher Re numbers. However, for the relaxation method with greater τ_0 and the viscous method, the system develops a small region confined around the middle of the domain with moderate Re numbers. Thus the strength of the forcing has a strong impact on the spread of the resulting turbulent region. Interestingly, the mean flow resulting from viscous forcing develops a peculiar form around the middle plane, where a steep slope is present, while the relaxation method leads to a horizontally averaged velocity profile that generally preserves a hyperbolic tangent profile.

Having compared the non-linear evolution for the viscous forcing and the relaxation method, I conclude that both methods can be used depending on the properties of the dynamics that need to be modelled. For investigations with focus on the resulting velocity profile during the saturated regime the relaxation method is more appropriate, where a careful choice of the relaxation time has to provide that no significant effects from the forcing can induce non-physical behaviour. This should be provided if τ_0 is of the same order as t_μ or greater. On the other hand, if the non-linear evolution of a shear unstable flow is of interest, where the mixing behaviour induced by the shear instability is the main focus, the viscous method provides a more appropriate forcing. Since the viscous method does not significantly affect the turbulent dynamics further away from the shear region, the turbulence induced by the instability can evolve freely. However, since the physical mechanisms driving shear flows in different objects are not known in detail, future global-scale investigations might reveal which of these two forcing methods is more relevant when modelling the tachocline.

6. Non-linear Evolution of the Saturated Phase

In order to develop a complete model of stellar dynamics a comprehensive understanding of the micro- and macrophysical processes present in all stellar regions is required. Main-sequence stars have common dynamical elements, such as large-scale shear flows resulting from differential rotation. However, these shear flows can occur in different regions with different characteristics, i.e. different transport coefficients, thermal stratification, et cetera. As, for example, in the Sun there exist the tachocline, which has a strong shear flow. Recently, considerable effort has been directed towards extending our understanding of the tachocline and its role in the solar dynamo (see Silvers, 2008, and references therein). However, there exist other shear regions in the Sun, such as the near-surface shear layer. This region is located at the upper boundary of the convection zone and is just as important as the tachocline, but has significantly different transport coefficients (Thompson et al., 1996; Miesch and Hindman, 2011; Barekat et al., 2014). In previous chapters of this thesis the main focus was on the stability of shear flows and on differences in numerical models to sustain shear flows. In this chapter I will investigate the properties of the saturated regime to shed light on several questions.

Observations of shear flows, such as the tachocline for example, only provide spatial and time averaged measurements (see for example Kosovichev, 1996; Charbonneau et al., 1999). Therefore, investigations in Section 6.1 shed light on the question of how likely it is that an initially unstable shear flow will result in global flow profiles that suggest a stable system. Second, when focusing on small-scale dynamics such as present in shear-induced turbulence, one would like to understand whether there is a relation between the transport coefficients and the resulting characteristic

length-scales, and velocities of the turbulent saturated state. Moreover, understanding what controls the global properties of the resulting mean flow after saturation, can help to draw a connection between observations of shear flows in astrophysical objects and numerical calculations. In Section 6.2 I will examine how unstable shear flows saturate and evolve into quasi-steady states when transport coefficients are changed. Third, in Section 6.3 the non-linear regime of a diffusive instability is investigated, and compared to a low Péclet number turbulence induced by a classical low Richardson number instability. Finally, a conclusion is drawn in Section 6.4.

6.1. Investigating the Effective Richardson Number

Velocity measurements obtained by helioseismology suggest a hydrodynamically stable tachocline (Miesch, 2007), i.e. the approximated Richardson number is significantly greater than the theoretical stability threshold of $1/4$ (Miles, 1961). However, helioseismology is restricted to large-scale time-averaged measurements (Christensen-Dalsgaard and Thompson, 2007), such that turbulent motions can still be present on small length- and time-scales. Such a scenario, where a hydrodynamically unstable system appears stable on large scales, was suggested by Spiegel and Zahn (1992) and Vasil and Brummell (2009). In order to investigate such a possibility I will focus on shear flows close to the stability threshold and how they evolve into the saturated phase. Then, the saturated regime of two differently stratified systems is analysed in terms of their horizontally averaged profiles and the resulting effective Richardson number. For this purpose, the relaxation method, which is suitable for modelling a target flow in the saturated phase, is used. This method allows the adjustment of the time-scale on which the system is driven towards the initial shear flow.

6.1.1. Setup

In order to investigate if an initially unstable system can reach a saturated state where the horizontally averaged profiles, associated with large-scale averaged measurements, suggest a stable system I will consider two differently stratified cases. Case I, which was investigated in Chapter 5, is strongly stratified but the polytropic

index is chosen such that it is not far from being unstable to convection. Here, rather than focusing on the different forcing methods that could be used, the horizontally averaged profiles during the saturated regime are examined in order to understand if they suggest a stable or unstable system. Case II is weakly stratified but has a large polytropic index to ensure that the system is far from the onset of convection. The Prandtl number is taken $\sigma = 0.1$ for both cases, as $\sigma < 1$ is more relevant for stellar interiors. All relevant parameters are summarised in Table 6.1. Using the relaxation method different relaxation times τ_0 are considered in order to investigate how horizontally averaged profiles are affected. Then, the system is evolved sufficiently long after saturation to reach a statistically steady state.

Table 6.1.: Parameters for the investigated cases, where the resolution of the domain is given by N_x , N_y and N_z . The dynamical viscosity is $C_k\sigma$, where C_k is the thermal diffusivity and σ the Prandtl number. The temperature gradient is denoted as θ and the polytropic index is m . For the initial shear flow the shear amplitude is U_0 and the shear width is controlled by L_u .

Case	$C_k\sigma$	θ	m	U_0	$1/L_u$	N_x	N_y	N_z	Ri
Case I	10^{-4}	5	1.6	0.2	80	256	256	360	0.003
Case II	10^{-5}	0.25	4	0.05	40	256	64	384	0.07

6.1.2. Results

A saturated shear flow instability leads to modified averaged density, temperature and velocity profiles such that at late times the effective minimal Ri number of the system changes. In order to understand if the effective Richardson number is significantly affected by modification of the stratification I will first investigate the changes in the density profile.

The density deviations, $\overline{\delta\rho}$, from the initial density profile is displayed in Fig. 6.1. Although, the absolute time at which the averaged density profiles are taken differs between the two cases, both are taken sufficiently long after the system had saturated. Therefore, both systems are in the same regime when the density deviations are calculated. It is evident that the density profile is not significantly

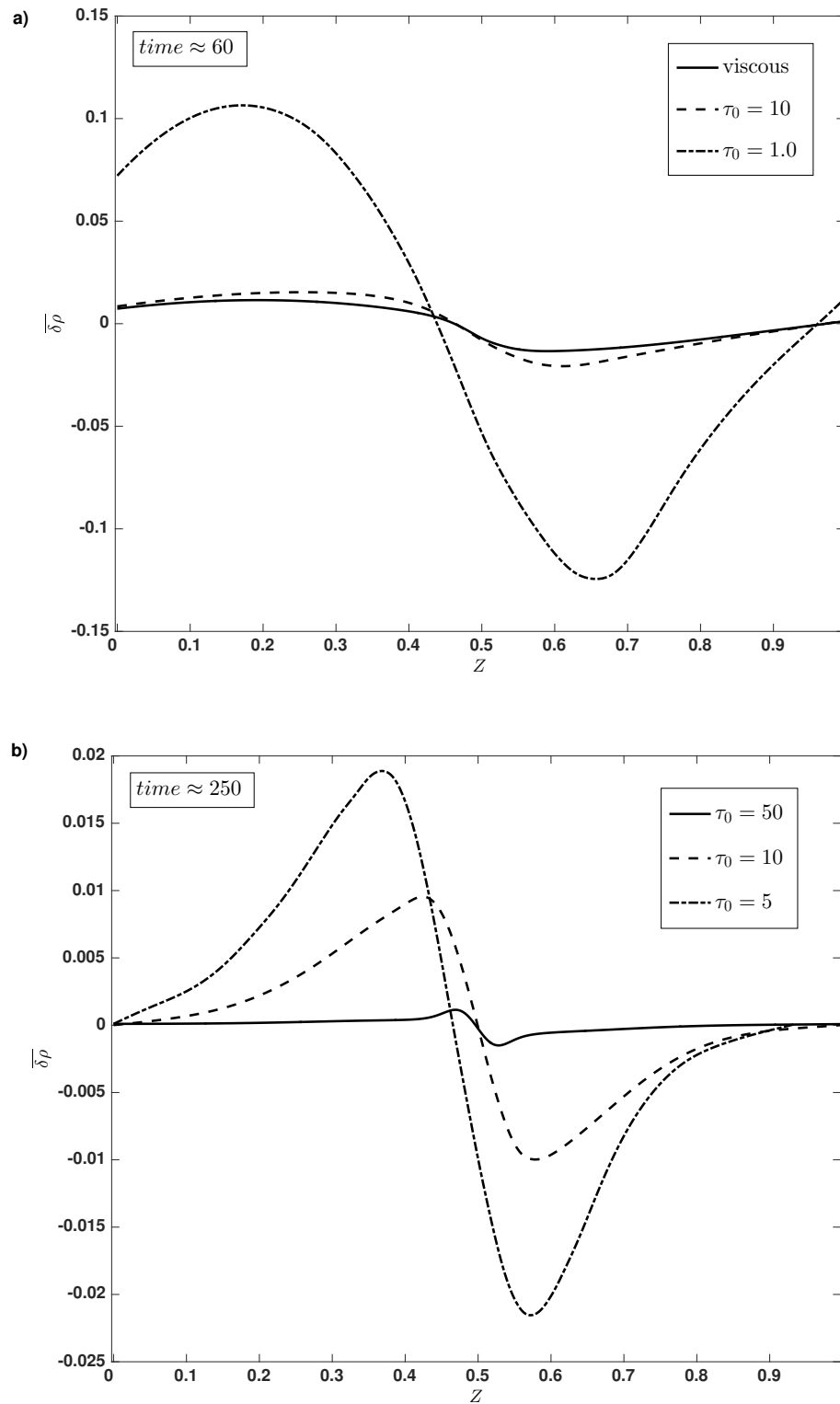


Figure 6.1.: Density deviation from the initial background density profile, $\overline{\delta\rho}$.
 (a) The profiles at $\tilde{t} \approx 60$ for case I and different relaxation times.
 (b) Case II is displayed at $\tilde{t} \approx 250$.

modified. Although even small departures in density can result in a large effect, it is not the case here. The density deviations in a strongly stratified system, displayed in Fig. 6.1 (a), are at least two order of magnitude smaller than the background density. Whereas in a weakly stratified systems, shown in Fig. 6.1 (b), the density deviations are significantly smaller. It reveals that forcing methods with a shorter relaxation time lead to stronger density changes. However, for all cases the positive deviations at the upper half of the domain peak further away from the middle plane, than the negative deviation in the lower and initially denser region. I compared the change in the Brunt-Väisälä frequency to the changes in the overturning rate and found that for both cases the change in the Brunt-Väisälä frequency, due to changes in the averaged density and temperature profiles, remains small compared with the contribution from the velocity profile.

Then, I move on to the minimal effective Richardson number during the evolution of the system, which is based on the averaged profiles. This quantity is calculated directly from the horizontally averaged profiles as follows:

$$\min Ri_{eff} = \min \left[\frac{-\theta(m+1)}{\left(\frac{\partial \bar{u}(z)}{\partial z}\right)^2} \left(\frac{\gamma-1}{\bar{\rho}(z)} \frac{\partial \bar{\rho}(z)}{\partial z} + \frac{\gamma}{\bar{T}(z)} \frac{\partial \bar{T}(z)}{\partial z} \right) \right], \quad (6.1)$$

where the overbar denotes a horizontally averaged quantity. This quantity is compared to the initial minimal Ri in order to understand the change to the system. Investigating Ri_{eff} , for the cases displayed in Fig. 6.2 (a), I find that a maximum is reached when the instability saturates. Afterwards Ri_{eff} oscillates around a lower value, which increases with increasing τ_0 . The late time values are $Ri_{eff} \approx 0.09$ for the relaxation method with $\tau_0 = 10$ and $Ri_{eff} \approx 0.01$ for $\tau_0 = 1.0$. For both runs of case I an effective Ri number that is one order of magnitude greater than the initial $Ri = 0.003$ number is obtained in the statistically steady state.

For case II, see Fig. 6.2 (b), the system is initially closer to the stability threshold. Varying the relaxation time gave rise to a similar trend as in case I, where with increasing τ_0 , the effective Richardson number obtained during the quasi-static regime increases. When using $\tau_0 = 50$ the minimal Ri_{eff} becomes greater than 0.25 shortly after the system starts to saturate. However, it drops down to around 0.2 when

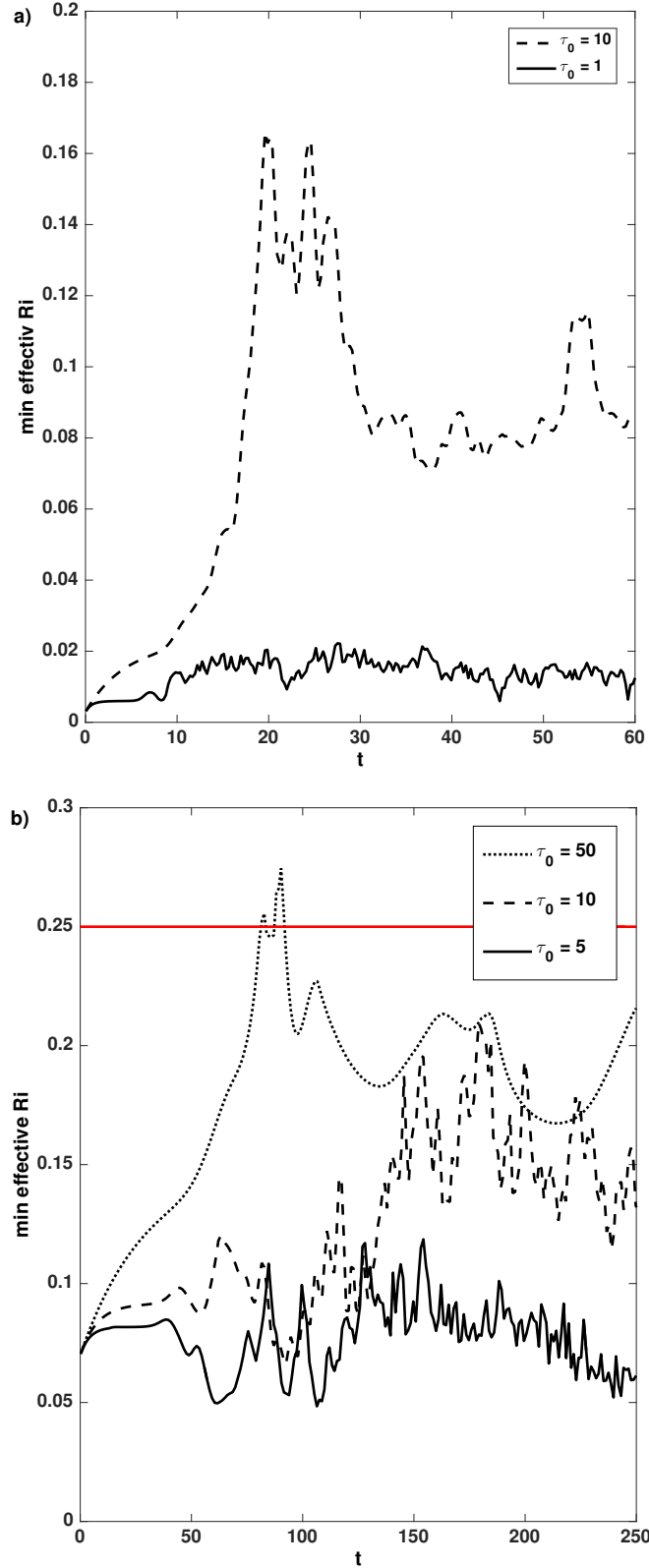


Figure 6.2.: The minimal effective Richardson number obtained from the horizontally averaged profiles as in Equation (6.1) with time. (a) Case I using two different relaxation times τ_0 . (b) Case II with three different relaxation times τ_0 . The red line indicates the 1/4 stability threshold.

the system evolves. This shows that for a few special cases the Kelvin-Helmholtz instability saturates by restoring linear marginal stability (Zahn, 1992; Prat and Lignières, 2014), but no evidence was found for an effective Richardson number larger than the linear stability threshold value during a statistical steady state.

6.2. Investigations of the Saturated Regime

The Péclet number, which is the ratio of advection to temperature diffusion, plays an important role in the linear and non-linear stability of shear flows. In stellar interiors, and depending on the region of interest, the Péclet number can be either small such as in massive stars or very large such as in the tachocline region (Garaud and Kulenthirarajah, 2016).

Recent investigations focus on the conditions under which low Péclet number flows become linearly or non-linearly unstable (see Prat and Lignières, 2013; Garaud et al., 2015) and mixing occur. However, the relevant parameters that determine whether thermal diffusivity has significant impact on the non-linear dynamics of the system are dictated by the typical length and typical velocities in the turbulent regime and so they are not known *a priori*, but can only be determined from fully non-linear hydrodynamical calculations. In stellar interiors these parameters evolve due to complex mechanisms, which are not entirely understood (Miesch, 2003; Garaud and Kulenthirarajah, 2016). Thus, in order to draw a connection between observations and numerical calculations it is crucial to investigate what affects the evolution of these scales.

Previous numerical studies, which exploit the Boussinesq approximation, use a periodic domain in the vertical direction (Garaud and Kulenthirarajah, 2016) or a linear shear profile (Prat and Lignières, 2014). Both approaches correspond to modelling a very localised part of the tachocline region. While they have extended our understanding, it remains unclear if the findings of these approaches persist when extending the domain in order to investigate localised shear transition regions together with their surrounding regions.

The principal focus here will be on classical shear instabilities with different Péclet numbers in order to investigate the resulting saturated regime and what affects the extent of the turbulent region. In addition, the objective is to shed light on whether the properties of the turbulent regime depend on the type of shear considered. This investigation aims to address the following questions: Does viscosity have impact on the spread of a shear flow instability and how are the turbulent length-scales affected? To what extent is the spread of the shear instability controlled by the Richardson number? What effect has thermal dissipation on the resulting turbulent region and characteristics present there?

6.2.1. Results: The Effect of Key Parameters on the Non-Linear Evolution

In order to understand the effect of viscosity and thermal diffusivity on shear induced turbulence, two sets of investigations in a two-dimensional domain with spatial resolution 480×512 are performed. This forms a first study summarised in Table 6.2. Here, a highly supercritical system has been chosen, where $Ri = 0.006$ and the Mach number remains less than 0.1 throughout the domain, which is achieved by taking $U_0 = 0.095$, $1/L_u = 60$ and considering a temperature difference of $\theta = 1.9$. In this investigations and for the following sections of this chapter, the viscous forcing method is used to sustain the shear flow. This choice is made to minimize the effect of the forcing on the non-linear dynamics further away from the middle of the domain.

First, I have varied the viscosity by several orders of magnitude while the thermal diffusivity is fixed in such a way that the Péclet number is greater than unity, which corresponds to changing Re but holding all other parameters fixed (cases A to C in Table 6.2). Second, I have investigated a turbulent system with different Péclet numbers but at a fixed viscosity (cases D to H in Table 6.2). A comparison of five cases with different C_k and σ have been conducted, where C_k is chosen in such a way that the initial Péclet number is varied by one order of magnitude from one case to the other.

Table 6.2.: Comparing typical length-scales, turbulent Reynolds numbers and effective shear width L_{eff} for different transport coefficients. For cases A to H the initial Ri number is fixed to be 0.006, where $\theta = 1.9$, the polytropic index is $m = 1.6$, the shear amplitude $U_0 = 0.095$, and the shear width is $L_u = 0.016$. The effective shear width is calculated after saturation and \bar{Re}_t , \bar{Pe}_t , and \bar{l}_w are averaged in the turbulent region, which depends on the effective L_{eff} , and over a sufficiently long time interval.

Case	σC_k	Pe	ζ_r	k_{max}	L_{eff}	\bar{Re}_t	\bar{Pe}_t	$\min Pe_t$	\bar{u}_{rms}	$\min u_{rms}$	\bar{l}_w	$\min l_w$
Varying viscosity via changing σ												
A	1×10^{-4}	15	0.86 ± 0.03	23.6 ± 3.9	0.61 ± 0.04	1.2×10^3	3.4×10^2	1.0×10^2	0.048	0.02	0.96	0.38
B	1×10^{-5}	15	0.99 ± 0.03	23.6 ± 3.9	0.53 ± 0.05	9.7×10^3	3.0×10^2	1.8×10	0.048	0.009	0.66	0.22
C	5×10^{-6}	15	1.0 ± 0.03	23.6 ± 3.9	0.49 ± 0.03	1.7×10^4	2.7×10^2	1.4×10	0.045	0.006	0.73	0.24
Varying Péclet number via changing C_k												
D	1×10^{-4}	0.01	0.85 ± 0.02	19.6 ± 3.9	0.51 ± 0.02	1.7×10^3	3.5×10^{-1}	1.2×10^{-1}	0.050	0.020	0.91	0.62
E	1×10^{-4}	0.1	0.83 ± 0.02	23.6 ± 3.9	0.43 ± 0.01	1.0×10^3	2.0×10^0	5.2×10^{-1}	0.050	0.020	0.54	0.36
F	1×10^{-4}	1.0	0.83 ± 0.02	27.5 ± 3.9	0.43 ± 0.02	8.0×10^2	1.4×10^1	3.3×10^0	0.049	0.020	0.59	0.29
G	1×10^{-4}	15	0.84 ± 0.03	23.6 ± 3.9	0.65 ± 0.07	9.0×10^2	2.7×10^2	8.7×10^1	0.045	0.024	0.62	0.39
H	1×10^{-4}	150	0.85 ± 0.02	19.6 ± 3.9	0.95 ± 0.16	9.0×10^3	2.8×10^3	1.0×10^3	0.040	0.024	0.78	0.39
Three dimensional low and large Péclet												
3D-I	5×10^{-4}	0.05	0.51 ± 0.01	18.8 ± 2.1	0.36 ± 0.03	2.14×10^2	8.25×10^{-1}	5.00×10^{-1}	0.047	0.039	0.59	0.41
3D-II	5×10^{-4}	1	0.49 ± 0.01	20.9 ± 4.2	0.30 ± 0.03	1.30×10^2	1.17×10^1	8.04×10^0	0.037	0.035	0.50	0.36

For the second study summarised in Table 6.3 the product of Ri and Pe numbers is varied by increasing Pe , but keeping Ri fixed and *vice versa*. The shear width, $L_u = 0.033$, is fixed for all cases. For cases I to K, the shear amplitude is $U_0/2 = 0.15$, but the thermal stratification is varied to increase Ri . To increase the Péclet number the shear amplitude, U_0 , is increased. Accordingly, the thermal stratification needs adjustment to keep $Ri = 0.006$. For all cases in Table 6.2 and Table 6.3 a stable stratification is obtained by setting $m = 1.6$.

Table 6.3.: For all cases $L_u = 0.016$ and $\sigma C_k = 1.0 \times 10^{-4}$. For cases I to K the temperature gradient is varied from $\theta = 0.85$ to $\theta = 6.5$. For cases L to N the Péclet number is varied, but $Ri = 0.006$. The effective shear width L_{eff} is calculated as described in Section 4.3. All turbulent quantities are averaged in time and over the turbulent region indicated by L_{eff} .

Case:	$RiPe$	L_{eff}	$\bar{P}e_t$	min Pe_t	u_{rms}	\bar{l}_w
Varying Richardson number via changing thermal stratification θ						
I	1×10^{-3}	0.87 ± 0.09	52	9.3	0.09	1.18
J	1×10^{-2}	0.45 ± 0.01	25	3.4	0.076	0.68
K	2×10^{-2}	0.23 ± 0.01	22	3.7	0.086	0.42
Varying Péclet number via changing shear amplitude U_0						
L	2.5×10^{-3}	0.27 ± 0.02	8.1	3.4	0.024	0.48
M	5×10^{-3}	0.43 ± 0.02	15	3.3	0.049	0.59
N	1×10^{-2}	0.45 ± 0.01	25	3.4	0.076	0.68

In general before the system reaches a quasi-steady state, the shear flow instability grows exponentially and evolves throughout a saturation phase. After the system has saturated, it enters a regime where statistical quantities fluctuate around a mean value. These regimes can be identified from the time evolution of the volume averaged vertical velocity in two dimensions $\langle w \rangle$, where the brackets were defined in Equation (4.10). Since the general trend of the volume averaged vertical velocity is similar in all unstable systems, the time evolution of $\langle w \rangle$ for cases A to C is shown in Figure 6.3. These three cases are chosen as examples, because they have significantly different viscosities and illustrate its effect on the saturation. In Fig. 6.3 (a) the exponential growth of the instability is displayed, which is almost identical for the

three cases because only the viscosity, which does not affect the instability growth rate, varies.

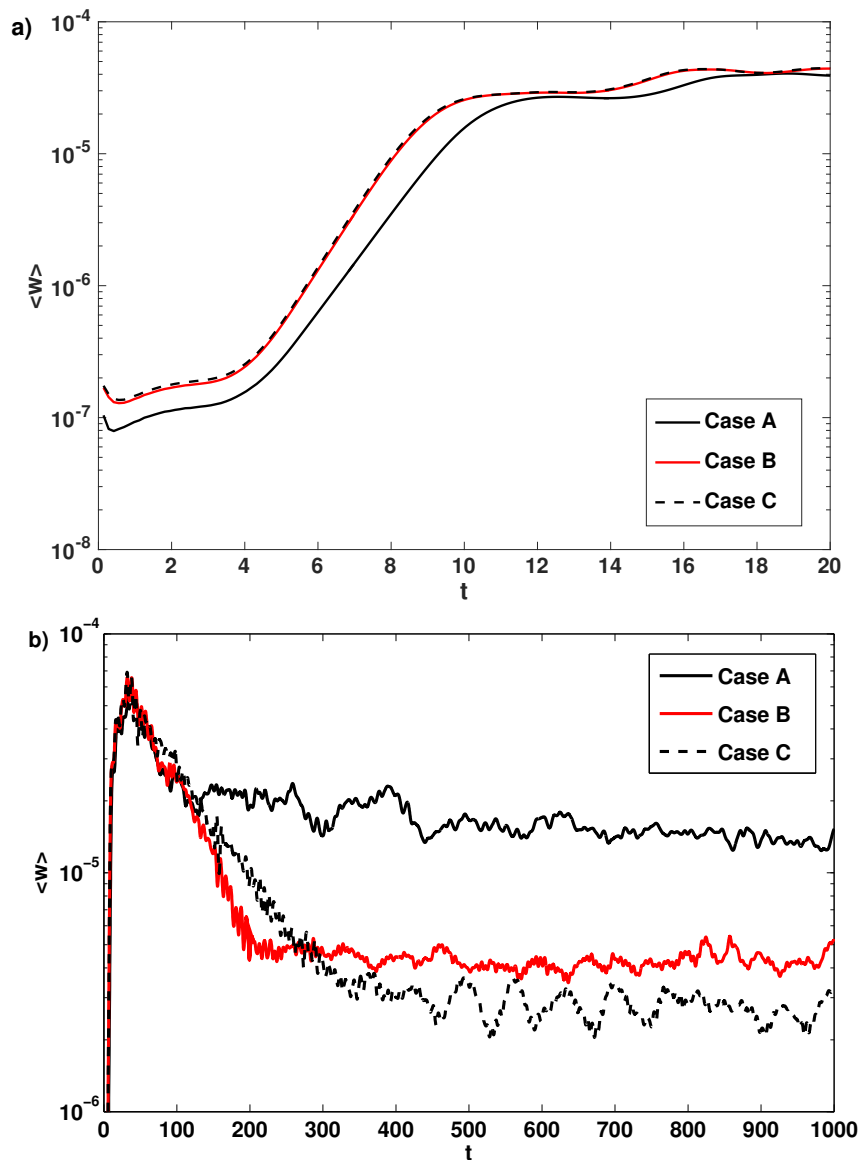


Figure 6.3.: Volume averaged vertical velocity evolution for cases A to C. (a) The exponential growth regime. (b) The long-time evolution.

After approximately nine sound crossing times the system starts to saturate. In Fig. 6.3 (b) it can be seen that this phase persists longer for lower viscosities. Finally, when the volume averaged vertical velocity fluctuates around a mean value the system reaches a statistically steady state. Case A enters the statistically steady state after 150 sound crossing times, but for case C the statistically steady state is approximately after 450 sound crossing times. All statistics presented in this chapter

are time-averaged during the resulting statistical steady state. In order to ensure that the system is evolved for a sufficiently long time the largest diffusive time-scale $t_{\mu,0} = d^2/\mu$ is considered. The calculations are evolved for at least a significant fraction of this time-scale, which is long enough to give meaningful statistics. The largest diffusive time is for case C, where $t_{\mu,0} = 2 \times 10^5$ whereas for most other cases $t_{\mu,0} = 10^4$. All time averages calculated in this chapter are obtained over a long time interval during the saturated quasi-steady regime.

Visualisations and Horizontally Averaged Profiles

A qualitative observation of the flow is obtained, by looking at the total vorticity component perpendicular to the x - z -plane after the exponential growth regime, when the billows start to overturn, and during the statistical steady state (see Fig. 6.4). It can be seen from Fig. 6.4 (a), Fig. 6.4 (c) and Fig. 6.4 (e) that the dynamics significantly alter with decreasing viscosity. In order to exclude that this change in dynamics is a result of a different instability, I compare the characteristic of the linear instability triggered. Note that the wave number k_{max} , summarised in Table 6.2, for the most unstable mode is the same for almost all cases, such that I conclude that the same instability is triggered in all cases (see Table 6.2).

In Fig. 6.4 snapshots for cases A to C are displayed: As the viscosity decreases, total vorticity structures are generated on much smaller spatial scales, as expected. However, it also becomes evident that the height of the horizontal layer in which mixing occurs changes only slightly with decreasing viscosity. In order to estimate the extent of the turbulent region the horizontally averaged velocity, $\bar{u}_x(z)$, in x -direction is calculated as in Equation (4.12). Then, the effective shear width L_{eff} is obtained, as in Section 4.3, by fitting the function in Equation (4.13) to the resulting time averaged $\bar{u}_x(z)$. Investigating this quantity for cases A to C, the effective L_{eff} slightly drops from $L_{eff} \approx 0.6$ to $L_{eff} \approx 0.5$ while viscosity decreases over two orders of magnitude (see Table 6.2). This implies that viscosity has only little effect on the spread of the instability.

Understanding the relevant parameters affecting the vertical extent of the turbulent region generated by a shear instability, as well as the turbulent characteristics, can

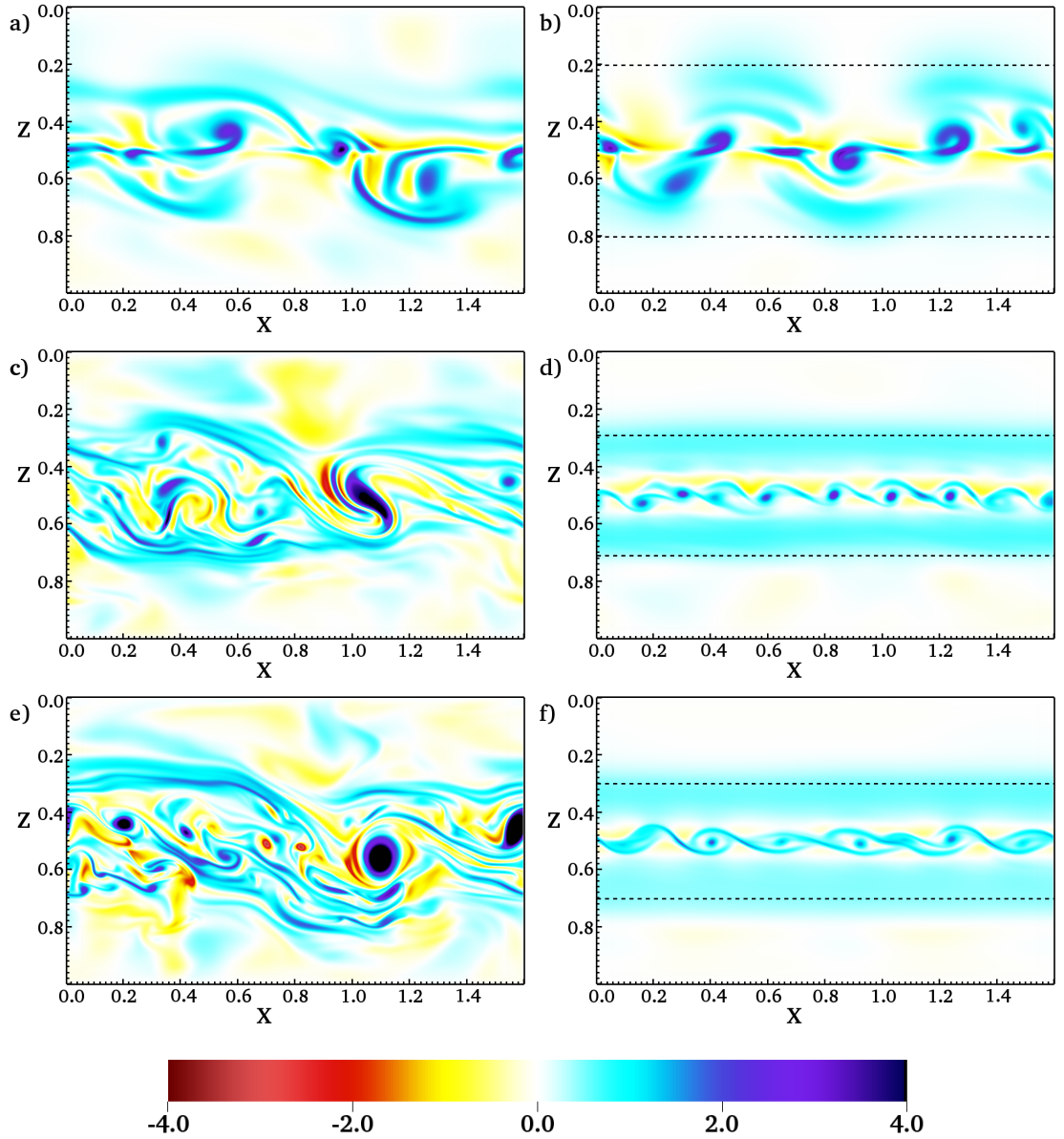


Figure 6.4.: Total vorticity in the x - z -plane for case A to C (see Table 6.2). The left column show cases A to C during saturation at approximately $\tilde{t} \approx 93$. (a) Case A. (c) Case B. (e) Case C. The right column show the same cases during the quasi-steady state at different times (for reference see Fig. 6.3). The dotted lines indicate the extent of the turbulent region of the saturated state as obtained from Equation (4.13).

provide a comprehensive picture of the possible dynamics in stellar interiors. Therefore, the characteristic properties of the turbulent regime, the root-mean-square velocity of the perturbations and the typical turbulent length-scales, are calculated. The system considered is stratified such that most quantities will change with depth, z , throughout the domain. Therefore, investigating horizontally-averaged profiles varying with depth, before averaging over the depth, provides further insight in the dynamics during the saturated regime.

Averaged velocity profiles, as calculated in Equation (4.12), are displayed in Fig. 6.5,

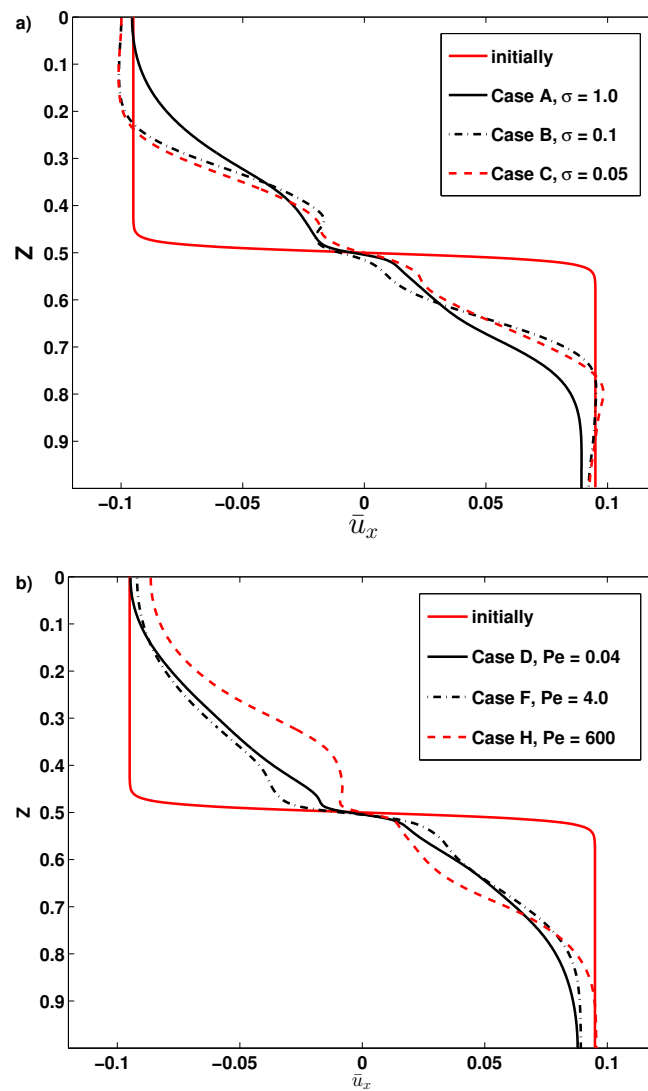


Figure 6.5.: The horizontally averaged and time averaged \bar{u}_x profiles are shown for cases A to H and O to U. In (a) the $\bar{u}_x(z)$ is displayed for cases A to C in (b) the $\bar{u}_x(z)$ for cases D to H are shown.

where asymmetries can occur due to the fact that the system is stratified and only one component of the velocity is considered. For all cases the confinement of the turbulent region is due to the dynamics, where the boundaries have only a negligible effect on the form of the horizontally averaged profiles. In Fig. 6.5 (a), \bar{u}_x is shown for cases A to C. It shows that all cases are very similar to each other despite the difference of three orders of magnitude in viscosity. The effective shear width L_{eff} for these cases, summarised in Table 6.2, confirms this observation. Since the effective width decreases only slightly, as viscosity is changed over two orders of magnitude, it indicates that viscosity variation does not have a significant effect on the vertical extent of the turbulent region.

One possible explanation for the lack of effect of varying the viscosity on the extent of the region comes from energetic considerations, where the only controlling parameter is the initial Ri number. The Richardson number is proportional to the ratio of the potential energy that is needed to overcome the stabilising stratification and the available kinetic energy of the background flow. Since a perturbation loses its initial energy when moving vertically, in the ideal case it will continue to spread as long as it has more energy than needed to overcome the stratification. Therefore, the vertical extent of the turbulent region should increase with decreasing Richardson numbers. To investigate this, I check the effective width obtained for three different Ri numbers, where the viscosity, thermal diffusivity and Péclet number are fixed (cases I, J and K in Table 6.3). Here I changed the Richardson number by two orders of magnitude by only varying the thermal stratification from $\theta = 0.85$ to $\theta = 6.5$. As a result the effective shear width drastically decreases with the Richardson number (see the evolution of L_{eff} in Table 6.3).

In such a complex problem, the Richardson number is unlikely to be the only parameter controlling the global form of the velocity profile. In order to investigate what other factors control the spread of the turbulence, I move on to the second study where only the Péclet number is varied. For cases D to H, the Péclet number is varied by varying the thermal diffusivity C_k , see Table 6.2. In order to examine how the non-linear dynamics change a qualitative comparison of several Péclet numbers is conducted. A visualisation of the total vorticity after the system has saturated is shown in Fig. 6.6. For case D with a Péclet number of order 10^{-2} , displayed

in Fig. 6.6 (a), very strong positive total vorticity in a narrow region around the middle plane is present. Here, patches are stretched along the x-axis with a few small interruptions of negative total vorticity. Positive total vorticity regions are stretched outwards from the middle plane at $z = 0.5$ and are overturning. A significantly different pattern is present in Fig. 6.6 (c), case H, where the Péclet number is of order 10^2 . Here the total vorticity amplitude is notably less than in case D and a vertically extended turbulent region is present, with positive and negative circular regions. Furthermore, smaller scale vortices are present in case H compared to case D and F. Therefore, I conclude that greater thermal diffusivity leads to a different turbulent state, where larger fluid parcels than for cases with lower thermal diffusivity are present. This indicates a complex effect of thermal diffusivity on the length-scales present in the turbulent regime. One possible explanation is that thermal diffusivity weakens the stabilising effect of stratification depending on the typical length of perturbation (Zahn, 1974), and so when C_k is decreased the length-scales for which the Péclet number becomes less than unity become shorter. Since the thermal diffusivity is varied significantly in cases D to H, another quantity, the temperature fluctuations around the initial background temperature, δT , is of interest. A visualisation of δT for cases D, F and H is shown in Fig. 6.7. The absence of small-scale fluctuations in Fig. 6.7 (a) can be explained by the greater thermal dissipation, where smaller scale fluctuations are dissipated faster.

Note, when decreasing the thermal diffusion C_k in the five cases from D to H, the extent of the turbulent layer after saturation decreases gradually from case D to case F, but increases from case F to case H. This is confirmed by the effective shear width, L_{eff} in Table 6.2. Since the dynamical viscosity is fixed, these effects result solely from different C_k . Generally, thermal diffusion becomes important in the system where the thermal time-scale is shorter than the buoyancy time-scale. For that to be satisfied, the Péclet number has to become smaller than unity. In such a system thermal diffusion effectively weakens the stable stratification, i.e. due to the high thermal diffusivity the moving fluid parcel adjusts its temperature to the surrounding quicker than the counteracting thermal stratification acts to restore the system. Therefore, the system becomes less constrained by buoyancy such that

vertical transport is enhanced. Therefore, one has to distinguish between the two limits: Low Péclet numbers and large Péclet numbers.

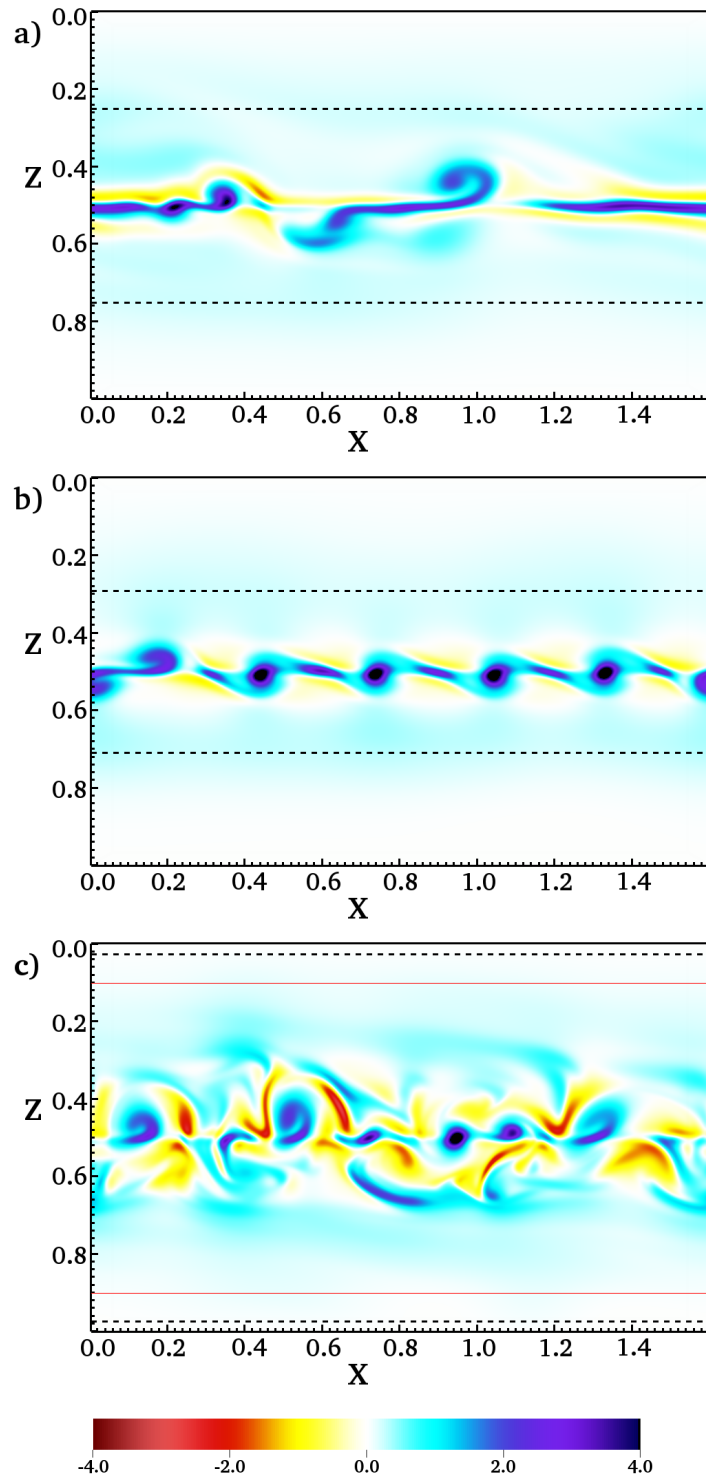


Figure 6.6.: The total vorticity component perpendicular to the x - z -plane shortly after saturation. Dotted lines indicate L_{eff} . (a) case D. (b) case F. (c) case H where the red lines indicate the lower bound of the error for L_{eff} .

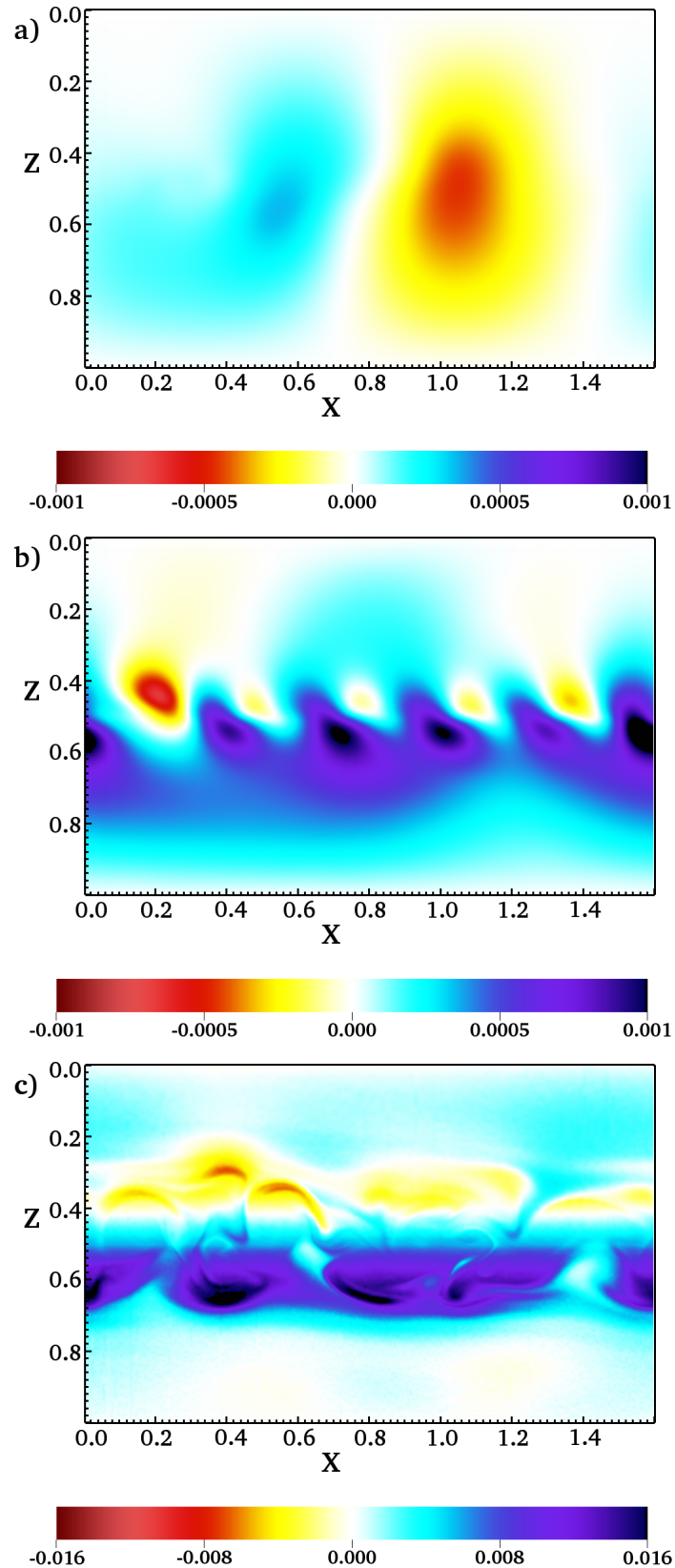


Figure 6.7.: The temperature fluctuations around the initial temperature profile shortly after saturation. (a) Case D. (b) Case F. (c) Case H. Note, the scale in (c) is of one order of magnitude greater, such that small scale disturbances at the middle are not visible.

It becomes evident that in the limit of large Péclet numbers the effective spread increases with increasing Péclet numbers as observed from the effective shear width, L_{eff} in the cases F to H. This shows that thermal diffusivity significantly damps the spread of perturbations. For higher thermal diffusivity the temperature of a fluid blob will adjust to the surrounding temperature faster. Therefore, a part of the kinetic energy is converted into potential energy quicker and so further propagation of the fluid parcels is hindered. However, in the limit of small Péclet numbers the opposite trend is observed, which can be explained as follows: Since the stratification is effectively weakened one might expect that the ‘effective’ Richardson number decreases with decreasing Péclet number, which should result in a larger extent of the turbulent region.

Since the Péclet number is the ratio of the product of velocity and length-scales to the thermal diffusivity, varying the shear flow amplitude is another option to change Pe . This option is investigated separately in case L to case N. Since increasing U_0 affects the Richardson number, it is necessary to fix it, so the thermal stratification is adjusted accordingly. For cases L to N U_0 is increased from 0.05 to 0.15 in two steps (see Table 6.3). As a result, the turbulent region extends vertically with increasing Péclet number.

Therefore, I conclude that there are two parameters controlling the extent of the turbulent region generated by an unstable shear flow in a stratified system, the Richardson number, and the Péclet number. Whereas, varying Re by changing the viscosity has a negligible effect on the spread of the turbulent region.

Statistical Properties

In the following I investigate how the characteristic length-scales and root-mean-square velocities are changed by viscosity, thermal diffusivity and the Richardson number. The overall turbulent length-scale in two-dimensions can be defined in a similar way to Equation (5.14):

$$l_t(z) = 2\pi \frac{\sum_{k_x=1}^{k_{max}} x_{max} k_x^{-1} E(k_x, z)}{\sum_{k_x=1}^{k_{max}} E(k_x, z)}, \quad (6.2)$$

where k_x is the horizontal wave number and $k_{max} = (N_x/3 + 1)$. The corresponding energy spectrum $E(k_x, z)$ is averaged over horizontal layers such that it takes the form

$$E(k_x, z) = \frac{1}{4} \sum_{k_x=1}^{k_{max}} \hat{\mathbf{u}}(k_x, z) \cdot \hat{\rho \mathbf{u}}^*(k_x, z) + \hat{\rho \mathbf{u}}(k_x, z) \cdot \hat{\mathbf{u}}^*(k_x, z), \quad (6.3)$$

where $\hat{\cdot}$ denotes the Fourier transform and the $*$ is used to indicate the complex conjugate. In previous studies the vertical scale of the vertical motion is calculated (Garaud and Kulenthirarajah, 2016). Due to the inherently inhomogeneous nature of the system considered, it is impossible to calculate exactly the same quantity. However, to obtain a comparable quantity the typical horizontal scale of the vertical motion is calculated by taking only the vertical velocity into account in Equation (6.3), such that the energy spectrum

$$E_w(k_x, z) = \frac{1}{4} \sum_{k_x=1}^{k_{max}} \hat{w}(k_x, z) \cdot \hat{\rho w}^*(k_x, z) + \hat{\rho w}(k_x, z) \cdot \hat{w}^*(k_x, z), \quad (6.4)$$

is obtained. The corresponding turbulent length-scale is then given by

$$l_w(z) = 2\pi \frac{\sum_{k_x=1}^{k_{max}} x_{max} k_x^{-1} E_w(k_x, z)}{\sum_{k_x=1}^{k_{max}} E_w(k_x, z)}. \quad (6.5)$$

However, resulting typical length-scales, l_w , are always slightly smaller than the overall turbulent length-scale, l_t , which is due to the fact that the horizontal velocities are excluded. I calculated the same statistical quantities by using l_t and verified that the behaviour that is observed by varying the key parameters remains qualitatively the same. The root-mean-square of the fluctuating velocity $u_{rms}(z)$ is calculate as

$$u_{rms}(z) = \frac{1}{N_x} \sum_{x=1}^{N_x} \sqrt{|\mathbf{u}(x, z) - \mathbf{U}_0(z)|^2}, \quad (6.6)$$

where $\mathbf{U}_0(z)$ is the target velocity profile as defined in Equation (3.14). Here, I averaged over the horizontal layers after the root-mean-square velocity was obtained at each position. In addition, I calculate a local turbulent Reynolds number

$$Re_t(z) = \bar{\rho}(z) l_t(z) u_{rms}(z) / (\sigma C_k), \quad (6.7)$$

where $\bar{\rho}(z)$ is the horizontally averaged density and $l_t(z)$ is the typical length in a two-dimensional domain. It can be seen in Table 6.2 that horizontally and time averaged $\bar{R}e_t$ increases with decreasing σ , as expected. However, the minimum l_w decreases from case A to case B, but increases slightly for case C. This indicates that if viscosity is further decreased the smallest typical length-scales present at the middle of the domain might converge towards a certain value. The u_{rms} summarised in Table 6.2 increases slightly with increasing viscosity and the minimal u_{rms} at the middle of the domain as well. Therefore, varying viscosity by changing the Prandtl number does not lead to significant changes of the global characteristic, but only affects the typical length-scales of the turbulence as expected.

Since the turbulent scales achieved in the non-linear regime can be drastically different to the initial length-scale defined in the initial state, the turbulent Péclet number will differ from the initial Péclet number. The initial Péclet number, as defined in Equation (3.34), depends on the initial shear width. For the saturated regime a turbulent Péclet number is required, for which there are various options what typical length-scale and velocity should be taken into account. In order to make the results comparable to previous investigations as for example by Garaud and Kulenthirarajah (2016), a turbulent Péclet number, $Pe_t = u_{rms}l_w/C_k$ in analogy to Equation (3.34), is calculated by taking the turbulent length-scale l_w and root-mean-square velocity, u_{rms} . Choosing l_t as defined in Equation (6.2) instead of l_w leads to slightly greater turbulent Péclet numbers, but of the same order of magnitude. The resulting turbulent Péclet numbers averaged over the effective vertical extent L_{eff} are summarised in Table 6.2. It becomes evident that the turbulent $\bar{P}e_t$ number averaged over the turbulent region exceeds the initial Pe number by at least one order of magnitude for all cases of the classical shear flow instabilities (cases A to J).

In recent studies either a sinusoidal velocity profile and periodicity in the vertical direction or a linear profile with appropriate boundary conditions (Garaud and Kulenthirarajah, 2016; Prat et al., 2016) were considered. In such investigations the domain develops a homogeneous turbulence in vertical direction. Such a system models a very localised region in stellar interiors where homogeneity can be justified. Since the system considered here is inherently inhomogeneous and anisotropic,

the narrow region around the shear interface has significantly different dynamics and characteristics from the outer parts of the turbulent region. In order to obtain results that can be compared to previous investigations, described above, a very narrow region around the middle of the domain is investigated. Here, the dynamics are similar to a homogeneous turbulent region. The obtained minimum Péclet number in this very localised region is listed for all cases in the corresponding Table. For most cases the minimum turbulent Péclet number at the middle of the domain is close to the initial Péclet number or even smaller. On the contrary the previous study with a sinusoidal velocity profile revealed that the turbulent Péclet number is always smaller than the initial Péclet number (see Garaud and Kulenthirarajah (2016)). In this investigation a sufficiently low viscosity result in minimum Péclet numbers lower than the initial Péclet numbers (see cases A to C in Table 6.2). One explanation for the discrepancy between previous studies and this case is due to the difference in velocity profiles and smaller Reynolds numbers used here.

Moving on to a quantitative comparison for different initial Péclet numbers (cases D to H in Table 6.2). These cases reveal that thermal diffusion significantly affects the typical turbulent length-scale l_w . Similar to the effective spread discussed above, it shows that different trends are present in the two limits of low and large Péclet number cases. Furthermore, the minimum root-mean-square of the velocity perturbations (see Table 6.2) is slightly reduced with increasing thermal diffusion in the limit of large Péclet numbers. This trend is consistent with the recent Boussinesq investigations of the low Péclet number regime (Garaud and Kulenthirarajah, 2016), where the Richardson number was varied. However, in this setup the pressure scale height always exceeds the turbulent length-scale observed, such that the Boussinesq approximation is not valid for the system considered here.

In previous studies the product of the Richardson number and the Péclet number, $RiPe$, has been considered to characterise the system (Garaud and Kulenthirarajah, 2016; Prat and Lignières, 2014). When looking at the $RiPe$ number in the two sets of data in Table 6.3 it becomes evident that they show opposite trends. Whereas in cases I, J and K, the vertical spread L_{eff} , the turbulent length-scale \bar{l}_w , and the \bar{u}_{rms} decrease with increasing $RiPe$, in the other cases L to N all quantities increase. This shows that increasing the number $RiPe$ by changing the Richardson number has the

opposite effect on the non-linear dynamics than increasing $RiPe$ by changing the Péclet number.

Comparing the results obtained here to those results obtained in Garaud and Kulenthirajah (2016), it becomes evident that the decrease of the typical length-scale with increasing $RiPe$, can be recovered in the study where the Ri was varied by changing the thermal stratification (cases I, J and K). This result suggests that the controlling factors are the Richardson number and the relationship between shear flow amplitude and thermal stratification. Viscosity and thermal diffusivity do not significantly affect the turbulent length-scale, if viscosity is sufficiently low, as shown above for cases A to C. Furthermore, the increase of the \bar{u}_{rms} with increasing $RiPe$ observed by Garaud and Kulenthirajah (2016), can be confirmed only for cases, where the Péclet number was increased by the shear amplitude only (cases L to M). However, cases I to K, where the Richardson number only was increased reveal an opposite trend to what was observed for cases L to M. For these cases the \bar{u}_{rms} is significantly affected by the thermal stratification, even when the Richardson number is fixed. Therefore, it is concluded that in stratified systems the product of Ri and Pe can not be used to characterise the saturated dynamics of the system. It is necessary to consider each dimensionless number separately.

6.2.2. Three-Dimensional Long Time Evolution

In previous subsections two-dimensional calculations were conducted to understand the effect of the Prandtl number and thermal diffusivity on the global properties of a saturated regime and characteristic dynamics. So far a two-dimensional model was utilised to considerably reduce the computational cost. As in two dimensions vortex stretching is suppressed, it is important to consider whether the conclusions would be altered if fully three-dimensional calculations are performed. Therefore, while the three-dimensional calculations are extremely numerically demanding and take considerable amount of running time, a few representative calculations are performed and will be discussed in this subsection.

Both small and large Péclet number regimes can occur in stellar interiors depending on the region considered and the type of the star. Here, the aim is to compare the

characteristics of the three-dimensional calculations to the previous two-dimensional calculations. Furthermore, a direct comparison of the non-linear evolution and statistical behaviour of the small and large Péclet number regime calculations will be given to understand the spread of the instability in three dimensions. Therefore, two different Péclet number regimes are considered. Case 3D-I represents the low Péclet number regime with $Pe < 1$ and case 3D-II the large Péclet number regime were $Pe \geq 1$. The calculations are evolved over at least one thermal diffusion time, $t_{thermal} = l_t^2/C_k$. The spatial resolution for these calculations is $N_x = 256$, $N_y = 256$ and $N_z = 320$. For the exact parameter choice see Table 6.2.

Visually the three-dimensional calculations, for which the total vorticity is displayed in Fig. 6.8, show very similar dynamics when comparing them to each other.

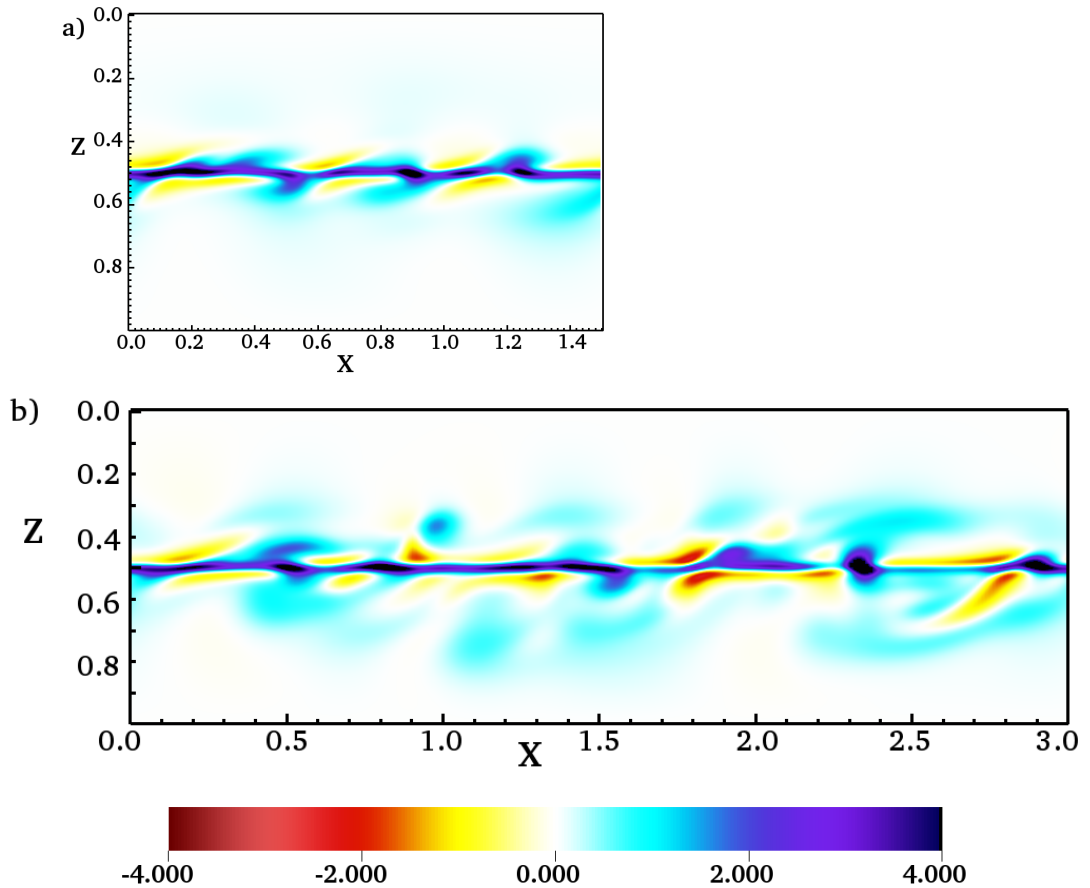


Figure 6.8.: The total vorticity component perpendicular to the x - z -plane. (a) case 3D-II at roughly $\tilde{t} \approx 200$. (b) case 3D-I at roughly $\tilde{t} \approx 120$.

The region of turbulent flow has approximately the same vertical extent. However, the regions of the same total vorticity orientation are more elongated in the x -direction for case 3D-I, where the Péclet number is lower than unity. In the middle horizontal layer positive total vorticity is predominant and only a few patches with weak negative total vorticity are present. This was also observed in two-dimensional calculations, see Fig. 6.6 (a) and Fig. 6.6 (b). When comparing the three-dimensional cases to the corresponding two-dimensional cases the effective shear width L_{eff} is significantly reduced (by approximately 17 %) for the large Péclet number case 3D-II. However, in the low Péclet number regime the effective shear width increases as observed in the two-dimensional cases, but remains slightly less than obtained in the two-dimensional cases D and E. The stronger confinement in both three-dimensional cases might be caused by the different non-linear dynamics present in three dimensions, where a secondary instability can evolve perpendicular to the x -direction.

When focusing on the characteristic of the turbulent regime, different results were obtained in both three-dimensional calculations compared to the two-dimensional cases. However the trend of smaller typical length-scales in the low Péclet number regime is confirmed. Therefore it can be concluded that some differences in three-dimensional calculations are present. As expected, the region of turbulent motions is more confined compared to two-dimensional calculations. In addition, the values for the typical length-scales and root-mean-square velocity are slightly altered. However, the overall trends of these quantities when varying viscosity and thermal diffusivity remain the same as in two-dimensions.

6.3. Diffusive Instability

For a classical shear flow in an ideal fluid the Richardson number, which corresponds to the ratio of the Brunt-Väisälä frequency and the turnover rate of the shear, gives the measure for stability. A low Richardson number, $Ri < 1/4$, is required for the system to become unstable. In previous sections the focus was only on classical shear flow instabilities that can be present within the stellar interiors where Richardson numbers become small. However, in diffusive systems, where the Péclet number is

low, a possible ‘secular’ shear instability can be present. This type of shear flow instability develops even for high Richardson numbers (Dudis, 1974; Zahn, 1974; Garaud et al., 2015), but only if the thermal diffusivity is large enough to weaken the stable stratification (Zahn, 1974; Lignières et al., 1999; Garaud et al., 2015; Witzke et al., 2015). So far studies of low Péclet number shear flows make use of the Boussinesq approximation (Prat et al., 2016), which does not permit the study of a system with large pressure gradients as present in stellar interiors.

Low Péclet numbers are most likely to be present in upper regions of massive stars, where differential rotation is present and ‘secular’ shear instabilities can develop. In recent studies, linear stability analysis of such diffusive systems confirmed the presence of ‘secular’ instabilities (Lignières et al., 1999; Witzke et al., 2015). In order to investigate the evolution during the saturated phase, non-linear studies are required. However, it is extremely difficult to consider small Péclet number regimes using the full set of equations as the time-stepping is restricted by numerical stability constraints related to the diffusion time. Therefore, it has previously been impossible to numerically investigate small Péclet number shear flows without using approximations (as in Prat and Lignières, 2013). However, here it is shown that it is possible to calculate low Péclet and large Richardson number cases in a two-dimensional domain. Here, some calculations are presented with a spatial resolution of 480×512 to investigate the differences between the classical and ‘secular’ instabilities during the saturated phase.

To ensure that the classical KH instability is not triggered, I set $Ri = 0.4$, which is achieved by taking $\theta = 2$, $m = 3.0$, $U_0 = 0.05$ and $1/L_u = 70$. Taking $C_k = 0.05$ leads to an initial Péclet number of order 10^{-2} , such that a ‘secular’ instability can develop due to the destabilising effect of low Péclet numbers. For cases O, P and Q the Prandtl number is varied in order to investigate its effect on the turbulent length-scale and the resulting turbulent Péclet number. In order to study how different Ri numbers affect the dynamics of a ‘secular’ instability, the Richardson number for case U is increased to $Ri = 1.0$. This is achieved by changing $U_0 = 0.035$ and $1/L_u = 60$, and the dynamical viscosity is fixed to be 10^{-5} . All cases are summarised in Table 6.4. The growth rates and most unstable modes predicted by means of a linear stability analysis as used in Chapter 3 is compared to that obtained

Table 6.4.: For the diffusive instability cases O to U the temperature gradient, $\theta = 2.0$, and the polytropic index, $m = 3.0$, are fixed, but the initial Ri number changes from 0.4 for cases O to Q to 1.0 for case U. The effective shear width is calculated after saturation and \bar{Re}_t , \bar{Pe}_t , and \bar{l}_w are averaged in the region of the turbulence, depending on the effective L_{eff} .

Diffusive Instability												
Case:	σC_k	U_0	L_u	Pe	Ri	L_{eff}	\bar{Re}_t	\bar{Pe}_t	$\min Pe_t$	\bar{u}_{rms}	\bar{l}_w	$\min(l_w)$
O	5.0×10^{-5}	0.05	0.014	0.015	0.4	0.076 ± 0.002	8.3×10^2	0.067	0.027	0.013	0.25	0.20
P	3.0×10^{-5}	0.05	0.014	0.015	0.4	0.094 ± 0.002	3.6×10^3	0.11	0.039	0.016	0.37	0.26
Q	1.0×10^{-5}	0.05	0.014	0.015	0.4	0.097 ± 0.001	1.7×10^4	0.21	0.061	0.017	0.50	0.36
U	1.0×10^{-5}	0.035	0.016	0.0125	1.0	0.063 ± 0.001	8.3×10^3	0.13	0.096	0.007	0.96	0.82

in non-linear calculations for all cases of the ‘secular’ instability. Furthermore, I have checked that the instability is a consequence of the destabilising mechanism at low Péclet numbers, by conducting test cases with the same dynamical viscosity as used in cases O to U but $C_k = 0.0002$. This results in an initial $Pe \approx 12$. For these test cases, I find that for both Ri numbers the system remains stable and the initial perturbations decay.

When the instability starts to saturate in any of the cases O to U only very little overturning is observed, which is unlikely to develop into a turbulent regime at least for the Reynolds numbers considered here. Focusing on the vertical spread the horizontally averaged velocity profiles, displayed in Fig. 6.9, reveals that the vertical extent of the instability is significantly smaller than observed in the previous cases in Section 6.2.

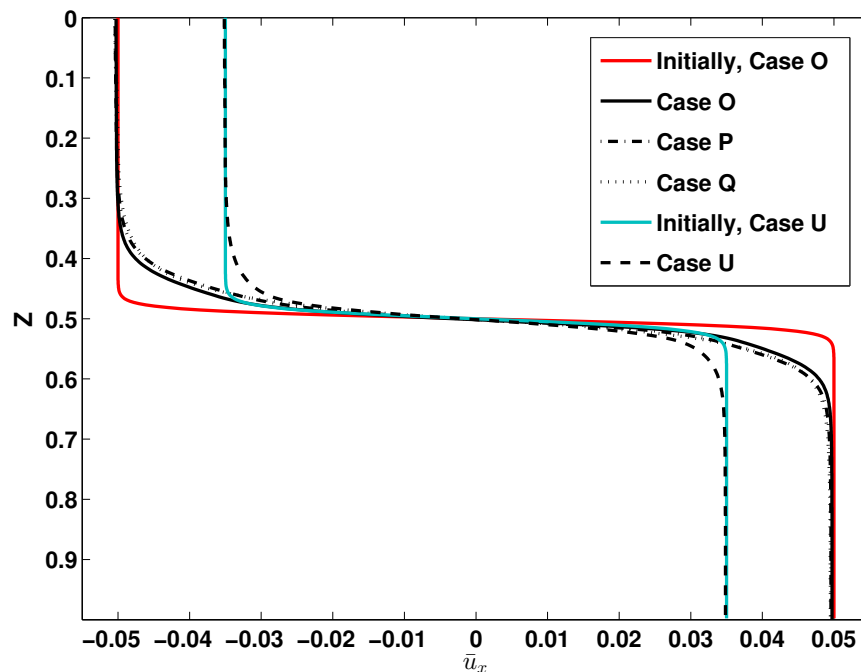


Figure 6.9.: The $\bar{u}_x(z)$ for the diffusive instability cases.

The resulting effective shear width is given in Table 6.4. This observation can be explained by the very large Richardson numbers, where the available kinetic energy for the perturbations is lower. For all cases here, the vertical spread of the temperature perturbations is slightly greater than it is for the vertical velocity during the saturation phase. A similar trend appears for a classical shear instability

in the low Péclet number regime as was shown in Fig 6.6. Looking at Fig. 6.10 (b) it becomes evident that regions of upward and downward motion are stretched along the horizontal direction. A similar pattern of the negative and positive temperature fluctuations is present in Fig. 6.10 (c), where layers are formed.

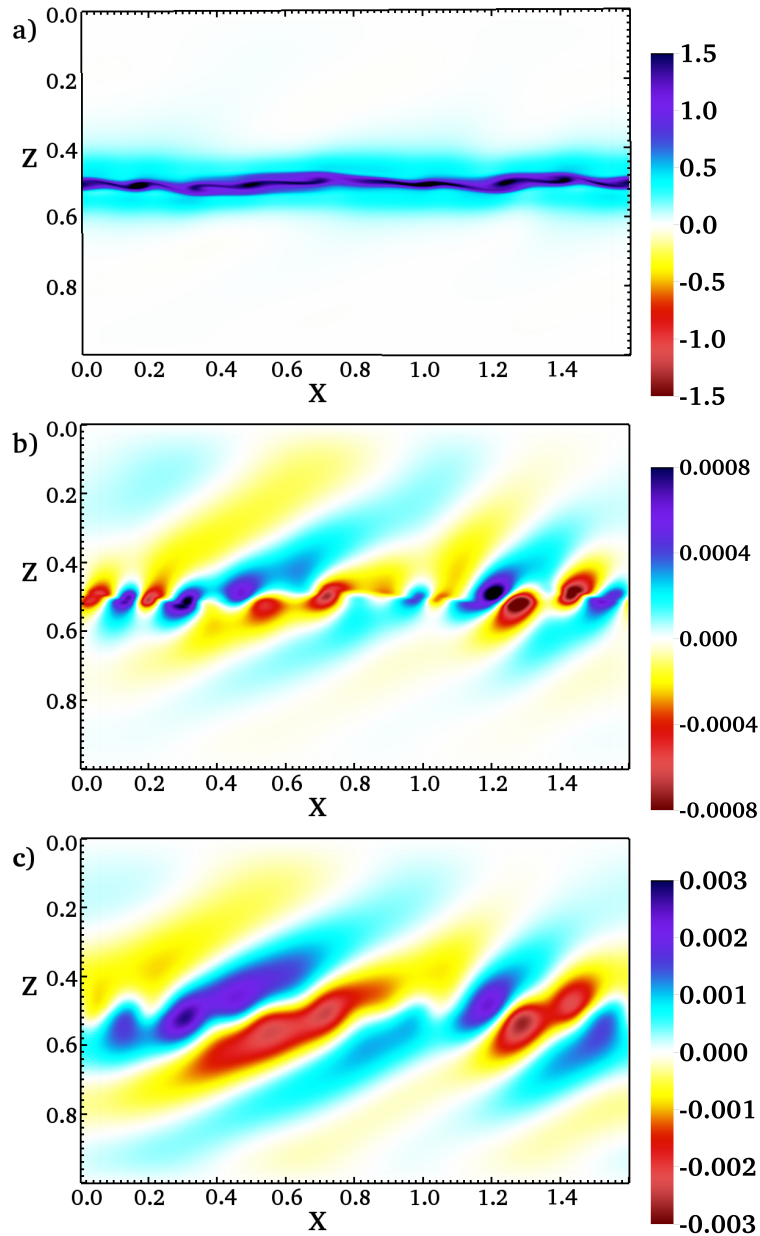


Figure 6.10.: The vorticity component perpendicular to the x - z -plane, the vertical velocity w , and temperature fluctuations around the initial temperature profile for case Q long after saturation. (a) Vorticity. (b) Vertical velocity. (c) Temperature fluctuations.

While there is some similarity in the trend in terms of the spread, there is a marked difference in the patterns observed in the saturated state between the ‘secular’ instabilities and the classical instabilities. Comparing what is seen in Fig. 6.10 (c) to the temperature fluctuations present in Fig. 6.7 (a) for case D, where the Péclet number is of the same order, it shows that for the classical instability no layering occurs.

Turning to the characteristic length-scales during the saturated regime it is observed, from the data in Table 6.4, that decreasing the viscosity results in greater typical turbulent length-scales. The opposite trend was observed in the previous study of a classically unstable system at large Péclet number. The trend for the ‘secular’ instability cases can be explained by the peculiar pattern observed for the vertical velocity and temperature fluctuations as shown in Fig. 6.10. Since the fluctuations are sheared out the typical length-scale between the up and down motions is increased. When the viscosity is decreased it becomes easier for the horizontal movement of the background flow to elongate the fluctuation pattern even more, such that the typical length-scale increases. However, the considered cases do not develop turbulence. Therefore, it is concluded that such layering can develop in systems that are not very far from the stability threshold. Such a behaviour is not only a feature of the diffusive instability, but might be present in a system with Richardson number close to the stability threshold. Finally, for the ‘secular’ instability cases, it is found that the smallest turbulent Péclet number at the middle of the domain drops below its initial value only for larger viscosities.

To summarize, the ‘secular’ shear flow instability in a fully compressible, stratified fluid shows the expected trend for the spread of the instability, which is a very small extent of the instability since the system is close to the stability threshold. Although the cases studied do not become turbulent, a turbulent regime will be eventually reached when considering larger Reynolds numbers. A differences in the trend is observed for typical length-scales during the saturated regime, when compared to classical shear unstable cases. Moreover, peculiar pattern for the temperature fluctuations and vertical velocity fluctuations are present.

6.4. Discussion

In order to obtain a comprehensive understanding of stars in their entirety, it is crucial to understand the complex dynamics in stellar interiors by investigating shear driven turbulence. Shear driven turbulence is a promising candidate in order to explain the missing mixing problem and is important for magnetic field generation.

The first study aims to shed light on the question if a saturated state that suggest a stable system can be achieved. Horizontally averaged profiles reveal a significant increase in the minimal Ri during saturation. It becomes evident that the relaxation time used in the forcing method has a significant effect on the resulting minimal Ri_{eff} during the steady state. Starting with an initially unstable configuration close to the stability threshold can lead to a transient phase where the effective Ri number becomes greater than $1/4$. However, the minimal Ri_{eff} decreases notably below the stability threshold during the long time evolution. So for a pure hydrodynamical system that is initially unstable, but with a connectively stable stratification it is difficult to achieve a turbulent flow that looks stable. Focusing on the tachocline, which is located between a convectively stable and a convectively unstable region, the system is more complex than considered in this model.

Numerical calculations are used to obtain a comprehensive insight to the detailed small-scale dynamics of shear regions. However, due to computational limitations, all calculations to date use modelling parameters that are far from the actual values in stellar interiors. Therefore, it is important to investigate how varying key properties affects our understanding of complex stellar regions. In the second study I focused on understanding the effect of different viscosities and thermal diffusivities on the saturated phase of a shear-driven turbulent flow in a fully compressible polytropic atmosphere. Examining the global properties of the saturated flow of an unstable system revealed that the vertical extent of the mixing region is primarily controlled by the Richardson number, but the thermal diffusivity also plays a key role through the Péclet number. It is found that for greater Richardson numbers the vertical spread of the mixing decreases, which also occurs as thermal diffusivity is increased in the large Péclet number limit. An opposite trend is observed for the small Péclet number limit, where the vertical spread increases with larger thermal diffusivity due

to the effectively weaker stratification. Here, I found that viscosity does not play an important role in the formation of the global shape of the mean flow during the saturated regime.

Turbulent flows can be characterised by the typical length-scale and the root-mean-square velocity of the perturbations. It is shown that viscosity only becomes important if it is sufficiently large to affect the minimal turbulent length-scales present. However, the typical turbulent length-scales were shown to depend on the Richardson number as well as on relationship between velocity amplitude and thermal stratification. An increase in the Richardson number by increasing thermal stratification leads to smaller typical length-scales, whereas larger values of the thermal stratification or velocity amplitude results in a opposite trend for a fixed Richardson number. Therefore, it can be concluded that the product of the input Péclet number and the Richardson number can not be used in strongly stratified systems to extract any information on the characteristics of the turbulence. A similar trend to what is seen for the typical length-scales is found for the root-mean-square velocity, but it is also found that thermal diffusivity has a significant effect. In summation the turbulent regime of a shear flow instability depends on several parameters and these can counteract each other. The properties of the saturated regime can only be broadly predicted from the input parameters.

The research presented in the last section focus on the low Péclet number regime. While for large Péclet numbers the initial flow requires low Ri numbers to become unstable, for low Péclet numbers it is possible to destabilise a high Richardson number shear flow (Lignières et al., 1999; Witzke et al., 2015). Therefore, cases were examined that are unstable against ‘secular’ shear instabilities. A different dependency is found, where the typical length-scale increases with decreasing viscosity, which is not the case in large Péclet number regimes. In addition, the turbulent Péclet number either remains less, or approximately the same as the initial Péclet number.

Having established a better understanding of what parameters significantly affect the global properties of saturated shear flow instabilities, future studies of the mixing behaviour and momentum transport of shear-driven turbulence can now be con-

ducted. In order to gain a more comprehensive picture of the complex dynamics in stellar interiors, it is crucial to include magnetic field interactions. Investigations with magnetic fields will help to inform how magnetic fields affect the turbulent regime. Moreover, the results obtained can be used to seek for a shear induced turbulence that is capable of driving a magnetic dynamo, which will be discussed in Chapter 7.

7. Shear-Driven Kinematic Dynamo

It is widely established that solar activity can be explained by the evolution of magnetic fields, where both the poloidal and toroidal components of the magnetic field are regenerated by a magnetohydrodynamic dynamo (for example Moffatt, 1978; Parker, 1979; Ruzmaikin and Feynman, 2001; Mason et al., 2002; Cameron et al., 2016). Current models of a solar dynamo require two components: The generation of toroidal fields can be obtained from poloidal magnetic fields by differential rotation, which is called the ω -effect (see for example Jones, 2011a; Hughes and Proctor, 2013, and references therein). In order to regenerate poloidal fields another process has to close the loop, otherwise no dynamo can operate (Cattaneo and Hughes, 2001; Mason et al., 2002). A possible mechanism for which helical flows are essential (Mason et al., 2002; Hughes and Proctor, 2013) is the so-called α -effect. This mechanism was first proposed by Parker (1955). Moreover, several investigations have shown, that an α -effect can also produce toroidal fields (see Rädler and Bräuer, 1987; Schubert and Zhang, 2000; Schrunner et al., 2011, and references therein). So different types of dynamo action are possible depending on which effect dominates the generation of toroidal magnetic fields (Jones, 2011b). A more detailed discussion on possible, large-scale, dynamos will be presented in Section 7.1.

Large-scale dynamos generate magnetic fields on larger length-scales compared to typical length-scales of the dynamics (Favier and Bushby, 2012; Brandenburg et al., 2012). In contrast, small-scale dynamos operate on scales smaller or comparable to the typical length-scale of the turbulent eddies (Brandenburg et al., 2012; Weiss and Proctor, 2014; Bhat et al., 2016). Small-scale dynamos can be achieved in fully isotropic turbulence if the conductivity is sufficiently high (Brandenburg et al., 2012; Borrero et al., 2015). Therefore, small-scale dynamos are important for many astrophysical objects, such as galaxy-clusters (Subramanian et al., 2006; Vazza et al.,

2014) and stellar surfaces (Petrovay and Szakaly, 1993; Pietarila Graham et al., 2010). So there has been a recent drive towards understanding small-scale dynamos in general and their contribution towards large-scale magnetic field generation (Ossendrijver, 2003; Schekochihin et al., 2004; Pietarila Graham et al., 2010).

In the previous chapters properties of shear-driven turbulence were investigated in order to obtain an extensive description of detailed small-scale dynamics in stellar interiors. However, stellar interiors possess magnetic fields. This fact leads us to the question how magnetic fields interact with turbulent motions and whether such complex dynamics can generate and sustain large-scale magnetic fields. Building upon the results so far, in this chapter I will start to include background magnetic fields in order to study the possibility of a kinematic dynamo. In these investigations I aim to shed light on the question whether magnetic field amplification and generation can occur in shear-driven turbulence without convection and on what scales magnetic fields are sustained. Since, different types of magnetohydrodynamic dynamos exist, a brief review on current results on magnetic dynamo action in different setups will be given in Section 7.1. Then, the setup will be introduced in Section 7.2, where I aim to investigate under what conditions a small-scale dynamo can operate in a shear-driven turbulent regime. The results are presented in Section 7.3 and Section 7.4. Finally a discussion will be given in Section 7.5.

7.1. Magnetic Field Generation

Magnetic fields are ubiquitous in astrophysical objects including planetary and stellar interiors, galaxies, and galaxy clusters (see for example Silvers, 2008; Tobias et al., 2011a; Beck and Wielebinski, 2013). The essential concept of the magnetohydrodynamic dynamo, proposed by Larmor (1919), provides an established theory that explains the time variation and the persistence of magnetic fields in astrophysical objects (Childress and Gilbert, 1995). Although, the observed temporal changes of the magnetic fields in most planets and stars imply dynamo action (Moffatt, 1978; Parker, 1993; Zeldovich et al., 1983), detailed observations of the fluid dynamics are not available, and so the exact dynamo processes is not understood. Therefore, extensive effort towards understanding magnetic fields in galaxies, stars and planets

over several decades led to a comprehensive theory of magnetic field generation in such objects. This section provides a brief review on the basic ideas of the magnetohydrodynamic dynamo in Subsection 7.1.1, where the mean-field approach and different types of dynamos are introduced. Furthermore, different possible dynamo scenarios for the Sun are discussed in Subsection 7.1.2 and differences to other stars are pointed out in Subsection 7.1.3.

7.1.1. Magnetohydrodynamic Dynamos

In an electrically conducting fluid, such as a plasma, magnetic fields interact with the fluid. Due to electrical resistivity, magnetic fields are dissipated. Generally, investigations concerning the process of sustaining a magnetic field against dissipation in an electrically conducting fluid are referred to as the magnetohydrodynamic dynamo problem (Childress and Gilbert, 1995). In the MHD approximation the evolution of the magnetic fields is governed by the induction equation, see Equation (2.30), which was derived in Section 2.3. The simplest form of a dynamo problem is testing if a magnetic field is amplified and sustained by a prescribed velocity field when employing the induction equation. This is called the kinematic dynamo problem, as no back-reaction of the magnetic field on the fluid motion is taken into account (Moffatt, 1978; Parker, 1975). On the contrary the non-linear dynamo theory comprise the coupled problem, where the back-reaction of the magnetic field due to Lorentz force on the flow is considered. In such a system the magnetic fields need to be maintained in a self-consistent manner (Moffatt, 1978; Parker, 1975).

For a kinematic dynamo, there exist two important types, depending on whether the growth rate is related to magnetic diffusivity in the limit of vanishing magnetic diffusivity or not. These two types of dynamo solutions were introduced by Vainshtein and Zel'dovich (1972). For the so-called slow dynamo, the growth rate becomes zero or negative in the limit of a perfectly conducting fluid (Fitzpatrick, 2014). Whereas, if the growth rate is independent of the magnetic diffusivity and remains positive for vanishing magnetic diffusivity, the dynamo is called 'fast dynamo' and the growth rate is comparable with the turnover time (Childress and Gilbert, 1995). Fast dynamos lead to several questions, concerning the properties of the required motion for their existence as well as the properties of generated magnetic fields. A more de-

tailed discussion on slow and fast dynamos is given in Childress and Gilbert (1995).

Focusing on potential dynamos in astrophysical objects, Parker (1955) proposed that convective motion in the solar interior together with the Sun's rotation would result in helical motion. These small-scale fluid motion twist toroidal magnetic fields to form small-scale poloidal fields, which then give rise to a large-scale poloidal field (Priest, 2014). Parker's idea triggered the formulation of the mean-field dynamo (MFD), which was derived by the Potsdam group (Steenbeck et al., 1966; Krause and Rädler, 1980), in order to explain the generation of large-scale fields due to small-scale motion in a more systematic mathematical description (Priest, 2014).

In the mean-field approach the evolution of large-scale fields is studied. For that the magnetic field $\mathbf{B} = \overline{\mathbf{B}} + \mathbf{b}'$ and the velocity field $\mathbf{u} = \overline{\mathbf{u}} + \mathbf{u}'$ are decomposed in a mean-field denoted by the overbar and small fluctuations denoted by $'$. The mean-field is either time averaged or averaged over a particular scale that separates small-scales and large-scales (Rädler, 2007). With this expansion the homogeneous, isotropic, mean-field induction equation becomes

$$\frac{\partial \overline{\mathbf{B}}}{\partial t} = \nabla \times (\overline{\mathbf{U}} \times \overline{\mathbf{B}}) + \nabla \times \alpha \overline{\mathbf{B}} + (\eta + \beta) \nabla^2 \overline{\mathbf{B}}, \quad (7.1)$$

where the α -term in this equation corresponds to the α -effect anticipated by Parker (1955) and is only possible for turbulence that is not reflectionally symmetric, and hence helicity is present (Rädler, 2007; Hughes and Proctor, 2013). The β -term corresponds to a turbulent diffusivity. The mean-field equation is used to study large-scale dynamo models. The concept of decomposing fields into a mean-field and fluctuations can be used to analyse the magnetic field evolution in numerical calculation of the full set of equations. While in general the α and β terms can be always computed, the interpretation using the mean-field approach is not always applicable (Cattaneo and Hughes, 2009). For a historical review, derivation and discussion of the mean-field dynamo formalism see Rädler (2007).

While the mean-field approach introduced above focuses on the evolution of large-scale magnetic fields, random motions even of an isotropic turbulence can produce

small-scale magnetic fields. By small-scales we mean length-scales much smaller than the scale of the energy carrying eddies (Parker, 1979; Zeldovich et al., 1983; Blackman, 2003). Such ‘fluctuation’ dynamos were explained by Kazantsev (1968) and Kraichnan (1968) independently, but they were predicted earlier (Batchelor, 1950; Biermann and Schlüter, 1951; Elsasser, 1956). Small-scale dynamos can amplify random magnetic fields at a fast growth rate, which is of the order of the eddy turnover time-scale (Blackman, 2003; Brandenburg et al., 2012). When investigating the conditions for magnetohydrodynamic dynamos, a non-dimensional number, the magnetic Reynolds number $Re_M = U_t l_t / \eta$, is introduced, where U_t is the typical turbulent velocity and l_t a typical turbulent length-scale. The magnetic Reynolds number gives a measure of the ratio of the induction to the dissipation of magnetic fields (Charbonneau, 2014). It was shown that for large enough magnetic Reynolds numbers small-scale magnetic fields can be generated regardless of the properties of the turbulence (see Charbonneau, 2014, and reference therein).

In numerical calculations it is not straight forward to distinguish between large-scale dynamo action and small-scale dynamo action. Especially in the early stage both dynamos produce a similar magnetic energy spectrum regardless if the turbulence is helical or non-helical (Brandenburg et al., 2012). However, in the saturated regime, for helical turbulence the magnetic energy will develop a peak at large scales due to an inverse cascade of magnetic energy, which indicates that a large-scale dynamo is present (Frisch et al., 1975). Whereas, a small-scale dynamo will produce magnetic fields at scales smaller than the energy injection scale even during the saturated regime. The absence of large-scale magnetic field generation during the linear regime indicates that the responsible process is non-linear in nature (Herault et al., 2011; Brandenburg et al., 2012). However, the role of small-scale dynamos in the generation of large-scale magnetic fields is not entirely understood (Tobias et al., 2011b). Especially, in the context of solar dynamo action there is increased interest in investigating small-scale dynamo contributions (e.g. Cattaneo, 1999; Stein and Nordlund, 2006; Vögler and Schüssler, 2007; Borrero et al., 2015).

7.1.2. Solar Dynamo Models

Focusing on the Sun, the ingredients necessary for a MHD dynamo to operate are present. First, there is differential rotation, which can convert poloidal into toroidal magnetic fields by the ω -effect. Second, turbulent motions in the interior due to convection are not reflectionally symmetric and inhomogeneous, because of rotation and stratification respectively (Charbonneau, 2014). Therefore, in principal, an α -effect can regenerate poloidal fields from toroidal. However, processes involved in the magnetic field evolution in the Sun are not entirely understood and the models developed over the last decades do not match some observed properties (Ossendrijver, 2003; Choudhuri, 2015). Hence, the challenge is to model detailed features of the solar cycle (Priest, 2014).

In the early stage of solar dynamo research, investigations mostly focused on improving kinematic α - ω dynamos, where the induction equation only was taken into account (Cowling, 1981; Priest, 2014). Simple kinematic dynamo models eventually cleared the way for more complex models. For example models including the equation of motion or models where a significant portion of the magnetic fields is generated at the base of the convection zone were developed (Priest, 2014). It is widely accepted that generation of toroidal fields due to differential rotation occurs at the base of the convection zone. However, the generation of poloidal fields remains controversial (Weiss, 2010; Chatterjee et al., 2011; Charbonneau, 2014). Although, there exist several dynamo models, they are divided into two classes: Interface dynamos, where all magnetic field generation is located near the tachocline (Parker, 1993; Tobias, 1996; MacGregor and Charbonneau, 1997), and flux-transport dynamos in which meridional circulation is necessary in order to transport poloidal fields that are created near the surface (Charbonneau and Dikpati, 2000; Weiss, 2010; Choudhuri, 2015).

Tachocline Dynamos

In the past, it was assumed that the ω -effect as well as the α -effect operate in the convection zone. However, Parker (1975) showed that magnetic fields cannot be amplified sufficiently fast in the convection zone before they rise due to convection

and magnetic buoyancy. This led to the overshoot dynamo model (Spiegel and Weiss, 1980) and later on to the interface dynamo model (Parker, 1993), where in both models the magnetic fields are generated at the base of the convection zone. This is required in order to store magnetic fields in the stably stratified region until they are sufficiently strong (Soward et al., 2005). Later on, after the tachocline was discovered such type of dynamos got support, because the tachocline is believed to be a good candidate for the ω -effect to occur (Priest, 2014). Moreover, in order to obtain the sign for the magnetic field orientation, the α -effect caused by cyclonic convection needs to be located deep in the convection zone (Mason et al., 2002). For the interface dynamo model the α -effect can operate either due to cyclonic convection or due to a dynamical α -effect from instabilities affected by rotation (see Mason et al., 2002, and references therein).

Fig. 7.1 illustrates all key ingredients for a potential interface dynamo. At stage (0) magnetic flux has to be present, which then has to be regenerated by some small-scale mechanism in (1) (Priest, 2014).

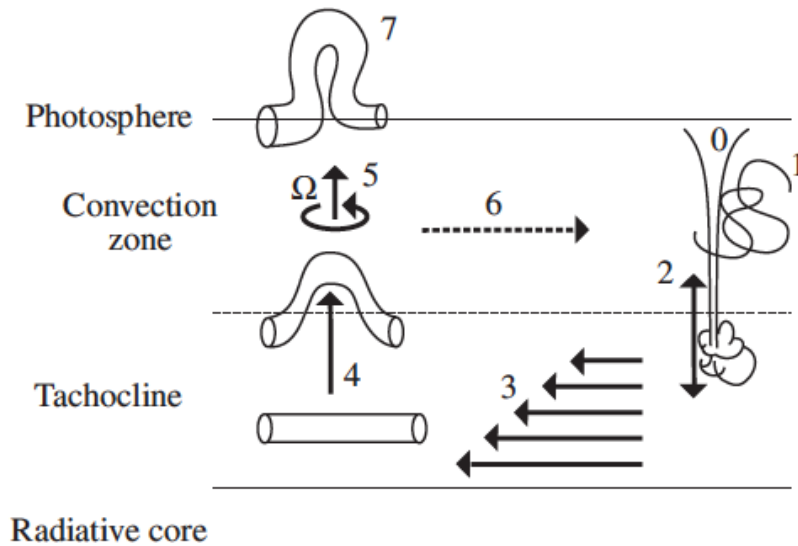


Figure 7.1.: A sketch of the scenario for potential tachocline dynamos, where the stages are explained in the text. Taken from Priest (2014).

In the next step (2) magnetic fields are transported downwards into the tachocline, where Parker suggested turbulent diffusion, but other processes such as magnetic

pumping can be also responsible for a downward transport (Tobias et al., 2001). Subsequently, strong shear in the tachocline (3) generates toroidal fields, which make their way up to the convection zone by either buoyancy or turbulent diffusion (4). However, at this stage it is crucial that there is a reduced upwards transport of the magnetic fields, such that they can be sufficiently amplified (Soward et al., 2005). In the convection zone (5), poloidal fields can be generated by the α -effect and some magnetic fields enter back into the cycle (6). However, some part of the toroidal field rises up to the solar surface and triggers active regions (7).

From Babcock-Leighton to Flux-transport Dynamos

An alternative to tachocline models are flux-transport dynamos, where meridional flows form an essential part of the model. The idea for such dynamos was developed from the Babcock-Leighton model (Babcock, 1961; Leighton, 1969). This model was motivated by the observed migration of the surface flux (Priest, 2014). The poloidal flux generated at the equator is transported towards the poles and reverses the pre-existing poloidal fields (Weiss, 2010). In such a model both dynamo components operate near the solar surface, where the so-called near-to surface shear layer (NSSL) has a strong radial shear. Due to observations of the NSSL, the logarithmic radial gradient of the rotation rate there was recently corrected to be $d\ln\Omega/d\ln r = -1$ (Barekat et al., 2014). Such a gradient is of the same order as for the steepest gradient measured in the tachocline (see Fig. 8 in Charbonneau et al., 1999). The role of the NSSL for the solar dynamo was studied for example by Dikpati et al. (2002), where it was found that the effect of NSSL radial shear on the flux transport dynamo is sub-dominant. In the work of Mason et al. (2002) the competitive production of poloidal fields at the base and at the surface of the convection zone was studied. The aim of their work was to compare the effectiveness of the Babcock-Leighton model against the interface model by using mean-field models. It was found that the tachocline is more efficient to provide the α -effect to reproduce poloidal fields at the base of the convection zone. However, an additional α -effect at the surface can have minor effects on the magnetic field evolution.

A modified version of the flux-transport dynamo assumes that the poloidal fields are generated at the surface, but the ω -effect is located at the base of the convection

zone (Wang et al., 1991; Dikpati and Choudhuri, 1994; Durney, 1995). In such a model, a transport mechanism to and from the base of the convection zone is necessary. Therefore, it was assumed that the meridional flow can transport poloidal fields downwards and toroidal fields upwards (Charbonneau and Dikpati, 2000; Mason et al., 2002). Since flux-transport dynamo models depend significantly on the form and strength of the meridional circulation (Jouve, L. and Brun, A. S., 2007; Dikpati and Gilman, 2009; Hazra et al., 2014), current numerical and observational investigations aim to shed light on the properties of meridional circulation (Küker et al., 2011; Miesch et al., 2012). Current observational investigations found evidence of an equatorward meridional flow located at shallow depths (Hathaway, 2012; Zhao et al., 2013). Whereas (Schad et al., 2013) found that the return flow reaches down to the base of the convection zone, but has a complex multi-cell structure. Although, flux-transport dynamos have several advantages, such as potential to reproduce many observational features of the solar cycle, they do not determine the flow consistently. The velocity field is imposed through a term that is obtained from observations.

7.1.3. Different Stars

Stellar magnetic fields were accurately detected for the first time by Robinson Jr. (1980), where an advanced measuring method based on emission line broadening due to the Zeeman effect was introduced. Currently, due to more detailed observations of different stars, which differ in mass, rotation, and convection from the Sun, it became evident that a plethora of stars have magnetic fields and stellar activity (Priest, 2014). Although, magnetic activity was found in all types of stars, it is more common in low mass stars than in massive or intermediate-mass stars (Grunhut and Neiner, 2015; Stello et al., 2016). Moreover, young stars with high rotation rates appear to be very active (Barnes, 2003; Brown et al., 2010), but a cyclic activity, similar to our Sun, has been found in stars with slow rotation (Weiss and Tobias, 2000).

Differential rotation and the convective motions are key ingredients for magnetic activity in various stars (Dobler, 2005; Brown, 2011). Main-sequence stars of all masses possess convection zones, but the location of one or even two convection

zones differs for the different types of stars (Augustson et al., 2012). Fig. 7.2 shows a schematic sketch of possible locations of a convection zone in different stars.

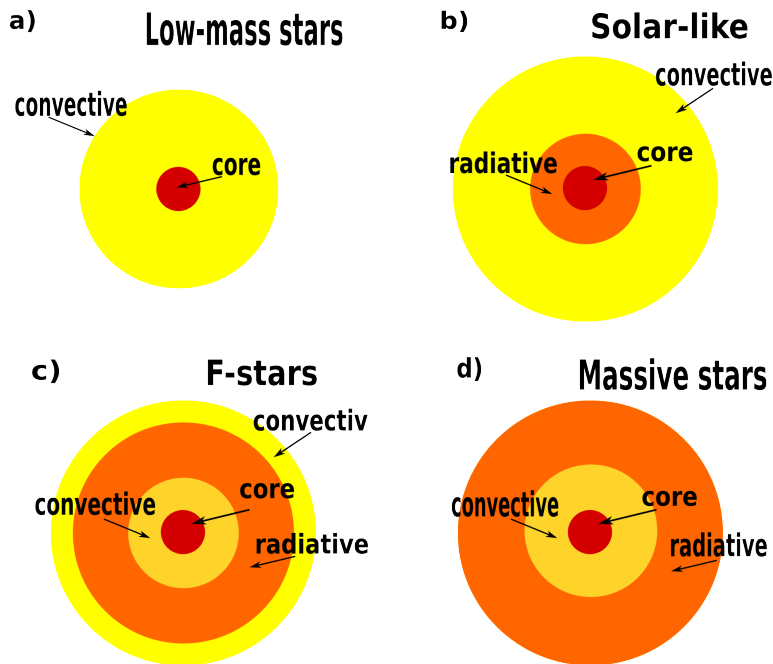


Figure 7.2.: Schematic illustration of the structure in different main-sequence stars.

(a) Fully convective, low mass stars. (b) Solar-like stars with a deep convection zone. (c) Stars with two convection zones. (d) Massive stars with inner convection zones.

Besides the location of the convection zone, the existence and location of a tachocline or a NSSL is of interest, because the role of a strong shear region in stellar magnetohydrodynamic dynamos is not understood (Browning et al., 2006; Guerrero et al., 2016). For example, for low mass stars with a fully convective interior a different process is required to explain magnetic field generation (Donati et al., 2006; Priest, 2014). Therefore, investigations of low mass stars focus on the question of how dynamo action can be achieved without a tachocline (see for example Browning, 2008). Whereas for solar-like and massive stars the role of shear regions requires comprehensive investigations (Augustson et al., 2013; Kosovichev et al., 2015; Guerrero et al., 2016).

The model considered in this chapter assumes a stable stratified systems with a strong unstable shear flow, which is applicable to solar-like and more massive stars

(Augustson et al., 2013; Guerrero et al., 2016). Moreover, different Péclet number regimes will be studied, which can occur in different stars. Low Péclet numbers are more likely to be present in massive stars, and large Péclet numbers are present in solar-like stars and intermediate mass stars (Meynet and Maeder, 2000; Garaud and Kulenthirarajah, 2016). However, since low mass stars have either a tachocline that is significantly deeper within the interior, or no tachocline at all (Wright and Drake, 2016), the setup considered here is not applicable to such stars.

7.2. Setting up a Kinematic Dynamo

In the following sections I will shed light on the question if shear-driven turbulence in a stably stratified system can generate and sustain a magnetic dynamo. Starting with the simplest scenario, I will neglect back-reaction of the magnetic field on the flow, which corresponds to a kinematic dynamo setup. For the initial seed magnetic field a configuration with zero net flux across the domain is chosen. A flux free field ensures that no imposed magnetic field is present and the obtained setup is a kinematic dynamo problem (as seen in for example Favier and Bushby, 2013; Hughes and Proctor, 2009). This seed magnetic field is then introduced at a time when the initially unstable shear flow has reached a saturated phase.

There exist two possible boundary conditions for the magnetic field, as discussed in Subsection 2.3.2. The first option is given in Equation (2.37) and it is called pseudo-vacuum, where the magnetic field is normal to the boundary. In the second Equation (2.38) the magnetic field is tangent to the boundary. It was shown that in the asymptotic regime the growth rate of a kinematic dynamo will be the same for either of the two boundary conditions (Favier and Proctor, 2013). However, in general there is no obvious advantage to chose one set of boundary conditions over the other. So I chose the boundary conditions as formulated in Equation (2.37) for the problem at hand. In this case I take $B_x = 0$, $B_y = 0$ due to boundary conditions and set

$$B_z(x, y, z) = A_m \cos\left(F_m \frac{2\pi x}{x_{max}}\right), \quad (7.2)$$

where A_m is the magnetic field amplitude and it will be set to unity, F_m gives the number of oscillations within the domain along the x -direction with $x \in [0 : x_{max}]$.

Since magnetic fields on smaller scales will decay more quickly than magnetic fields on larger scales, an initial magnetic field with more oscillations in the domain will lead to a faster onset of the exponential regime. Therefore, in all investigations F_m is set to 5 in order to ensure a quicker response. It remains to be checked that the magnetic flux, Φ_B , which is define as

$$\Phi_B = \oint_S \mathbf{B} \cdot \hat{\mathbf{n}} dS, \quad (7.3)$$

where S is the surface of the domain, is indeed zero. Inserting the magnetic field in Equation (7.2) the magnetic flux becomes

$$\Phi_B = \int_x \int_y A_m \cos\left(F_m 2\pi \frac{x}{x_{max}}\right) dx dy \quad (7.4)$$

$$= \int_x y_{max} A_m \cos\left(F_m 2\pi \frac{x}{x_{max}}\right) dx \quad (7.5)$$

$$= y_{max} A_m F_m \frac{x_{max}}{2\pi} \sin\left(F_m 2\pi \frac{x}{x_{max}}\right) \Big|_0^{x_{max}} = 0. \quad (7.6)$$

No magnetic field back-reaction on the velocity implies that $f = |\mathbf{B}|^2 / \mu_0 P_t$ has to be set to zero and the magnetic field amplitude can be unity, which is satisfied by the assumption $A_m = 1$. Another possibility is to investigate a system where the back-reaction is negligible. This can be achieved by setting $f = 1$, but taking a magnetic field amplitude of at least six orders of magnitude smaller than the velocity amplitude ($A_m \sim 10^{-6} U_0$). Here, the first option is considered.

For dynamo action to occur the magnetic Reynolds number, $Re_m = Re\sigma_m$, has to be large (Brandenburg et al., 2012). There exist a critical $Re_{m,crit}$ such that below this value no small-scale dynamo can operate, for large-scale dynamos this critical value is significantly lower. Since $\sigma_m = \mu/\eta = \sigma/\zeta$, it is necessary to vary ζ in order to investigate small and large magnetic Prandtl number regimes. For a low magnetic Prandtl number regime $\sigma_m \leq 1$, where in astrophysical objects the magnetic Prandtl number is $\sim 10^{-4}$ (Brandenburg et al., 2012). Whereas for the large Prandtl number regime, $\sigma_m > 1$, a small-scale magnetic dynamo is more likely to operate. In Table 7.1 all cases that are considered in the following are summarised. I will distinguish between four different series with low to moderate Péclet numbers,

for which I will study different magnetic Prandtl numbers and check if a magnetic dynamo exist.

7.3. Seeking Dynamo Action: Preliminary Results

In order to obtain a better understanding about if dynamo action is possible in shear-driven turbulence, I start by including a seed magnetic field defined in Equation (7.2) into three-dimensional calculations previously obtained in Chapter 5 and Chapter 6. Testing several low magnetic Prandtl numbers that are summarized in the first part of Table 7.1, I observe whether the magnetic fields decay away exponentially or grow. For that, the magnetic energy evolution is studied, where the volume averaged magnetic energy density is calculated as follows

$$E_{mag} = \langle \mathbf{B}^2 \rangle = \frac{x_{max}y_{max}}{N_z N_x N_y} \sum_{x=1}^{N_x} \sum_{y=1}^{N_y} \sum_{z=1}^{N_z} \mathbf{B}^2, \quad (7.7)$$

where N_x , N_y and N_z are the resolution in x , y and z direction respectively and x_{max} and y_{max} are the extent of the domain in x and y direction. For most all of the cases in the first and second part of Table 7.1 a decay of the magnetic energy is observed, where some examples are shown in Fig. 7.3. In Fig. 7.3 (b) it can be seen that for some cases the magnetic energy increases slightly just after the seed magnetic field is induced, before it enters the exponential decay.

This increase is due to the quick amplification by the background shear. Therefore, in order to obtain an accurate decay rate, the magnetic energy evolution slightly after the onset is fitted to an exponential function

$$f(t) = ae^{\zeta_r t}, \quad (7.8)$$

where ζ_r is the growth or decay rate. The obtained decay rates are listed in Table 7.1 and show that even for a magnetic Prandtl number of order unity, as in case 1b, the decay rate remains large.

Although, the viscous method provides a more suitable method to study the free evolution of shear-driven turbulence, and therefore it will be used in this investigation,

Table 7.1.: The values of various parameters for all cases considered together with the decay rates for each. For all cases the polytropic index is set to $m = 1.6$ and the dynamic viscosity $\mu = 5 \times 10^{-4}$. In part 1 calculations that were used in Chapter 5 with different forcing methods are studied. Part 2 shows low and moderate Péclet number cases used in Chapter 6. In part 3 a new case is set up.

Case	forcing	σ	C_k	θ	U_0	L_u	Pe	ξ	Pr_m	ζ_r
Part I										
1a	viscous	0.1	0.005	5	0.2	0.0125	0.5	0.2	0.5	-1.07
1b	viscous	0.1	0.005	5	0.2	0.0125	0.5	0.1	1	-0.65
1c	relaxation, $\tau_0 = 10$	0.1	0.005	5	0.2	0.0125	0.5	0.15	0.67	-0.79
1d	relaxation, $\tau_0 = 1$	0.1	0.005	5	0.2	0.0125	0.5	0.15	0.67	-0.72
Part II										
2a	viscous	0.316	0.00158	1.9	0.095	0.0166	1	0.632	0.5	-0.95
2b	viscous	0.316	0.00158	1.9	0.095	0.0166	1	0.316	1	-0.495
2c	viscous	0.316	0.00158	1.9	0.095	0.0166	1	0.15	2.1	-0.256
2d	viscous	0.316	0.00158	1.9	0.095	0.0166	1	0.0316	10	-0.077
3a	viscous	0.0158	0.0316	1.9	0.095	0.0166	0.05	0.0158	1	-0.166
3b	viscous	0.0158	0.0316	1.9	0.095	0.0166	0.05	0.0032	5	-0.04
3c	viscous	0.0158	0.0316	1.9	0.095	0.0166	0.05	0.0008	20	growth
Part III										
4a	viscous	0.5	0.001	1	0.095	0.0166	1.5	2.5	0.2	-1.3
4b	viscous	0.5	0.001	1	0.095	0.0166	1.5	0.5	1	-0.28
4c	viscous	0.5	0.001	1	0.095	0.0166	1.5	0.1	5	-0.085
4d	viscous	0.5	0.001	1	0.095	0.0166	1.5	0.05	10	growth
4e	viscous	0.5	0.001	1	0.095	0.0166	1.5	0.0333	15	0.016
4f	viscous	0.5	0.001	1	0.095	0.0166	1.5	0.025	20	0.018

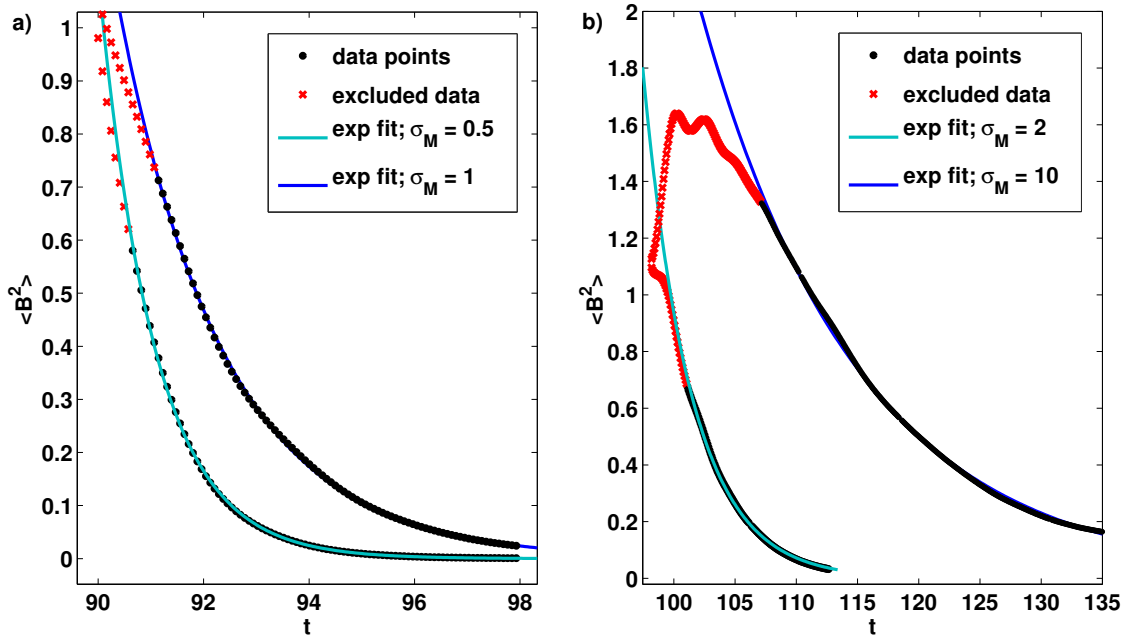


Figure 7.3.: Magnetic energy with time together with and exponential curve fit. a) Case 2a and case 2b, which have low Prandtl numbers. b) The two large Prandtl number cases 2c and 2d.

a couple of test calculations using the relaxation method and including a magnetic field were performed. These tests aim to answer if a different forcing method can potentially provide a saturated non-linear regime, where magnetic field generation is obtained more easily. The two runs listed in Table 7.1 for the relaxation method with $\tau_0 = 10$ and with $\tau_0 = 1$ show very similar decay rates, such that I conclude that the forcing has potentially little effect on the magnetic field generation.

Moderate and Low Péclet numbers

Here, I focus on low and moderate Péclet number regimes. A seed magnetic field is induced after the unstable flow has saturated. Four different magnetic Prandtl numbers for case 2, which has a Péclet number of unity, are investigated. In Fig. 7.3 the magnetic energy density evolution together with the corresponding exponential fit to the data is shown. Even for a large magnetic Prandtl number, $\sigma_m = 10$, the seed magnetic field decays away, as shown in Fig. 7.3 (b). However, comparing the decay rates for the run with $\sigma_m = 0.5$ and $\sigma_m = 1$ for case 1 and case 2, it seems that for case 1 it is potentially more difficult to generate magnetic fields.

In order to understand what might affect the magnetic field generation the characteristics of the non-linear dynamics in these two cases are compared. For that, the turbulent Reynolds number and the typical length-scale with depth as defined in Equation (5.12) and Equation (5.14) respectively are calculated and displayed in Fig. 7.4. Both quantities are time-averaged during the saturated phase. It becomes

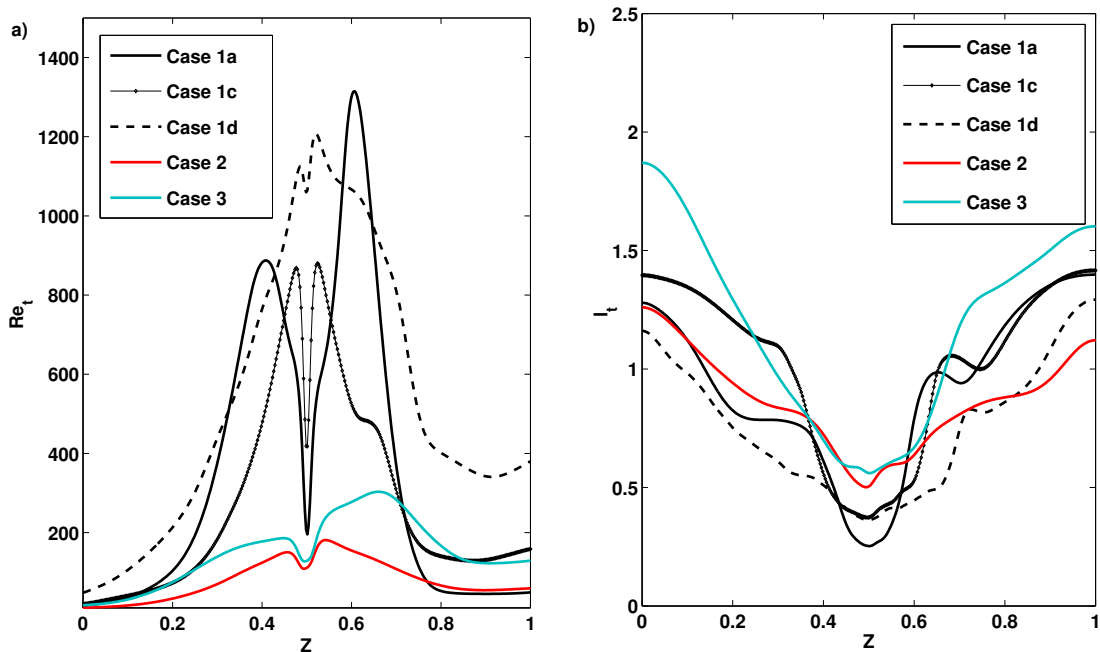


Figure 7.4.: Turbulent Reynolds numbers and typical length-scales with depth. The vales are horizontally and time averaged during the saturated regime for all three cases and different forcing methods. (a) $Re_t(z)$. (b) $l_t(z)$.

evident that the magnetic Reynolds numbers for case 1 are significantly greater than for case 2 and case 3. This seems to contradict previous investigations, where one would expect that larger magnetic Reynolds numbers are important for small-scale dynamo action. However, for case 1 the density around the middle of the domain is significantly higher. It is more plausible that the typical length-scales of the turbulence and the root-mean square velocity affect magnetic field generation. Therefore, comparing l_t in Fig. 7.4 (b) indicates that for cases, where more energy is stored in larger length-scales the seed magnetic field does not decay as fast as for cases with smaller typical length-scales. Moreover, the extent of the turbulent region might have an impact on potential dynamo action, as it determines the region in which small-scale dynamo action can take place. However, comparing the effective

spread of the turbulence in the two cases, where $L_{eff} = 0.35$ for case 1 when using the viscous method and $L_{eff} = 0.30$ in Case 2, suggests that L_{eff} does not play an important role.

Turning to case 3, which has a low Péclet number and was used in Chapter 6, three different magnetic Prandtl numbers are investigated. Here I only focus on cases with $\sigma_m \geq 1$, since from previous cases it became evident that for $\sigma_m < 1$ dynamo action is unlikely. The magnetic field evolution for case 3b and case 3c is displayed in Fig. 7.5. It becomes evident that for $\sigma_m = 5$ the system might be marginally stable, but for $\sigma_m = 20$ a magnetic dynamo is present. Unfortunately, such a low Péclet number regime results in very small time steps due to the high thermal diffusion, and so it is numerically not feasible in order to investigate the long-time evolution of the magnetic field. Comparing the characteristics of the turbulence and the spread, the typical length-scales are greater than in case 1 and case 2, the extent of the turbulent region, $L_{eff} = 0.36$ is also larger than for case 1 and case 2. Therefore, I conclude that a new case needs to be set up that is numerically easier to run, but has potentially greater typical length-scale in the saturated regime and a more extended turbulent region.

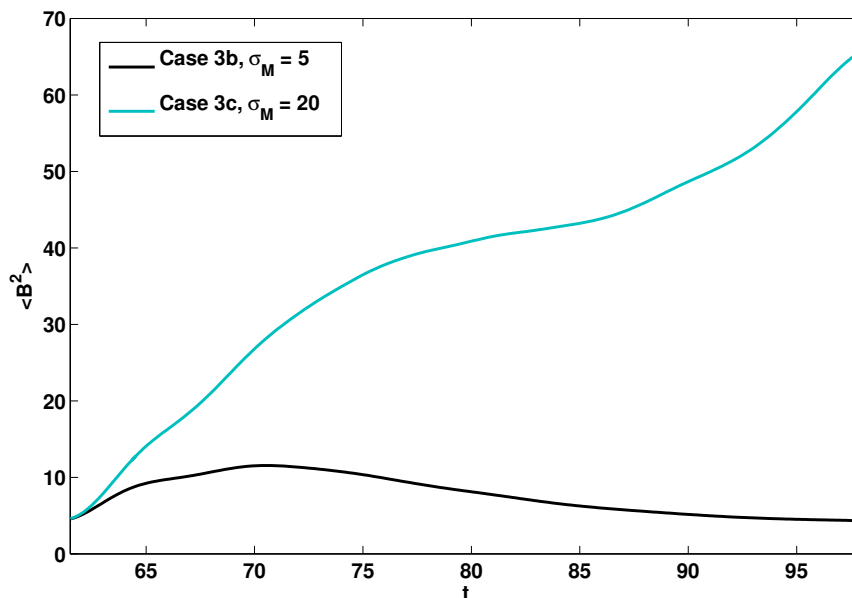


Figure 7.5.: Magnetic energy evolution for case 3b and case 3c.

7.4. Small-scale Dynamo Action

As found in the previous section, low Péclet number regime calculations are numerically not feasible, therefore I focus on greater Péclet numbers in the large Péclet number regime. A slightly greater initial Pe is achieved by decreasing C_k . In addition, I decrease the initial Richardson number to $Ri = 0.002$, because it was found that smaller Ri will result in a greater spread of the turbulent region. Then, the new case 4 is summarised in the third part of Table 7.1, where cases with $\sigma_m = 0.2, 1, 5, 10, 15, 20$ are studied and their decay rate is obtained for the first three cases.

Before I move on to analyse the magnetic field evolution it is useful to investigate an additional property of the saturated turbulent regime. Since mean-field theory requires the flow to be helical in order to generate large-scale magnetic fields, a mean relative kinetic helicity is defined (Favier and Bushby, 2012) as

$$\mathcal{H}(z) = \frac{\langle \mathbf{u} \cdot \nabla \times \mathbf{u} \rangle_z}{\langle \mathbf{u}^2 \rangle_z^{1/2} \langle (\nabla \times \mathbf{u})^2 \rangle_z^{1/2}}. \quad (7.9)$$

In Fig. 7.6 the time averaged relative helicity, \mathcal{H} , for all cases is shown.

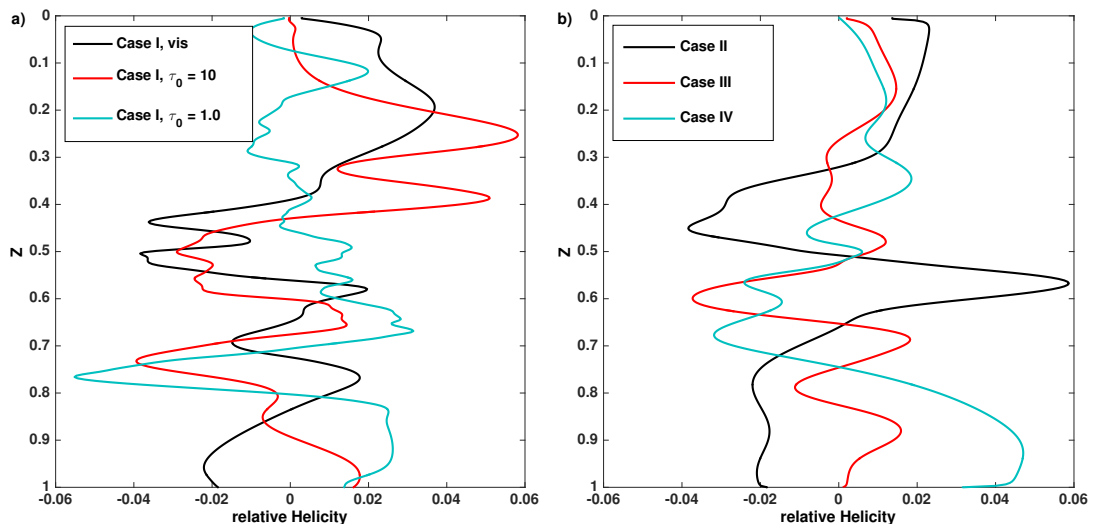


Figure 7.6.: Time averaged relative helicity, $\mathcal{H}(z)$, as defined in Equation (7.9) for all cases. a) Helicity obtained for case 1 and for all three different forcing methods is shown. b) Helicity for case 2 to case 4 is displayed.

The horizontally averaged quantity is averaged over approximately 10 sound-crossing times after the seed magnetic field was introduced. Comparing the relative helicity with depth for each case, no systematic pattern can be established. Moreover, the sign changes several times along the z -direction. Although, the horizontally averaged profile of the relative helicity differs for each case, the maximum deviation from zero is of the same order in all cases. The helicity for case 1 tends to be positive at the upper half and negative at the lower half. A different behaviour is observed for the other three cases where overall more positive helicity is present. While in all cases the turbulent flow possesses helicity it remains unclear if a large-scale dynamo can be obtained and if a relationship between helicity and magnetic field generation in these cases can be established.

I start the analysis of magnetic fields by looking at the magnetic energy evolution for the three cases with $\sigma_m \geq 10$, where dynamo action is present, displayed in Fig. 7.7.

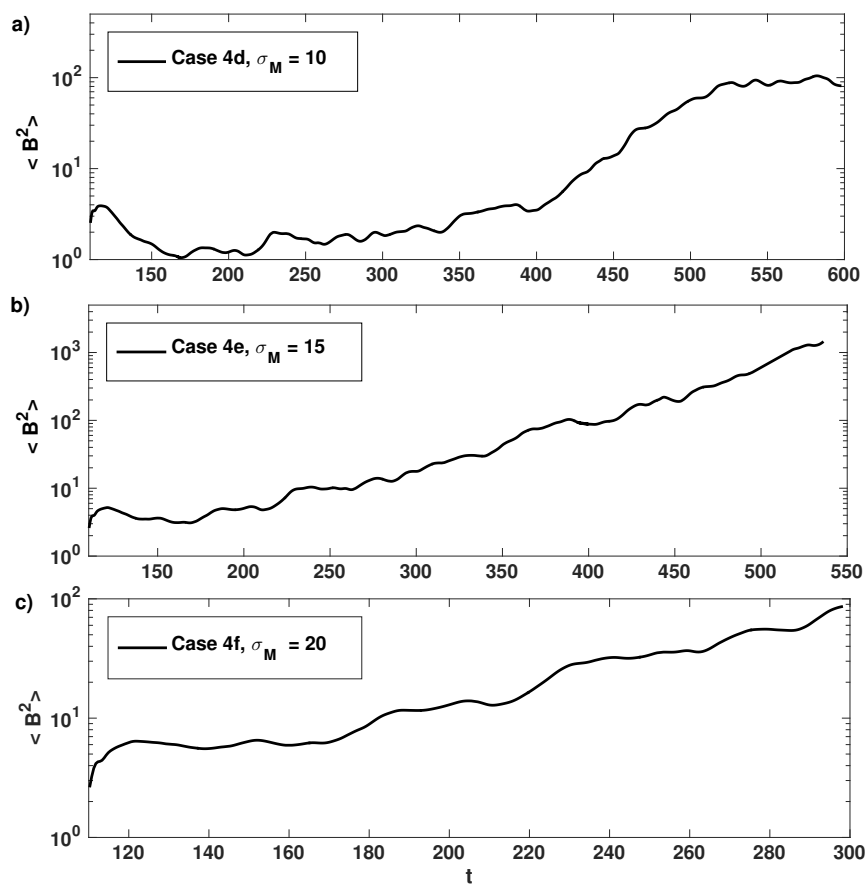


Figure 7.7.: Magnetic energy density evolution with time for large magnetic Prandtl numbers of case 4. a) Case 4d with $\sigma_m = 10$. b) Case 4e. c) Case 4f.

No clear exponential growth in the total magnetic energy density, E_{mag} , can be identified for case 4d. For the other two cases the growth rate, ζ_r , is obtained by fitting a linear function $f(t) = \zeta_r \ln(\langle B^2 \rangle) + c$ to the logarithm of the magnetic energy density. The obtained values are summarised in Table 7.1. It becomes evident that for $\sigma_m = 10$, the system is close to stability and for a long time, $150 < t < 350$, the total magnetic energy increases with a small growth rate. After $t \approx 350$ a greater growth in magnetic energy is observed. Some jumps in the growth rate are present for the case with $\sigma_m = 15$ and the case with $\sigma_m = 20$. However, a mean growth rate can be found. In order to find a critical magnetic Reynolds number, which can be obtained by interpolation, more calculations are needed. However, the nature of the magnetic field generation can be partly studied at this stage. As mentioned above, it is crucial to distinguish between small-scale dynamos and large-scale dynamos: For large-scale dynamos the typical length-scales of the generated magnetic fields are larger than the typical length of the energy carrying eddies (see for example Weiss and Proctor, 2014) and *vice versa*.

To analyse if only a small-scale dynamo operates or also large-scale magnetic fields are produced in case 4d and case 4e, it is possible to study if a significant amount of mean-magnetic field is generated. For that the time evolution of the mean-field, $B_{mean} = \sqrt{\langle \mathbf{B} \rangle^2}$, shown in Fig. 7.8 for the cases with $\sigma_m = 10$ and $\sigma_m = 15$, is studied.

It becomes evident that the mean-magnetic field increases. In contrast to the total magnetic field energy density evolution displayed in Fig. 7.7, there is no sharp transition to greater growth rates at $t \approx 350$. This indicates a continuous generation of some mean-magnetic field. Comparing the averaged B_x and B_y components of the magnetic field in the two cases (case 4d and case 4e) reveals a very similar evolution among the two cases as can be seen in Fig. 7.9. The B_x component in both cases follows almost the same curve with a slight difference. The same is observed for the B_y component, where a greater difference is present at $t > 300$. The B_z component, not shown here, oscillates around zero, where the deviation from zero is greater for the case with $\sigma_m = 15$. Taking into account that both the magnetic field energy and the mean-field are significantly greater for the case with $\sigma_m = 15$, it can be concluded that for this case the magnetic field amplitude is greater, but the magnetic

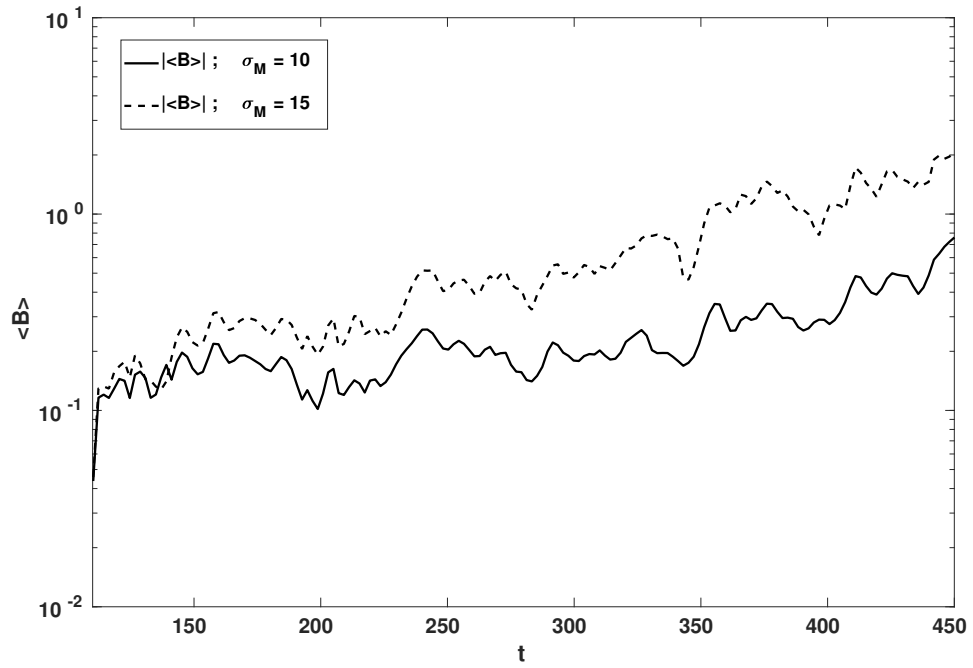


Figure 7.8.: Time evolution of B_{mean} for the cases 4d and 4e with time.

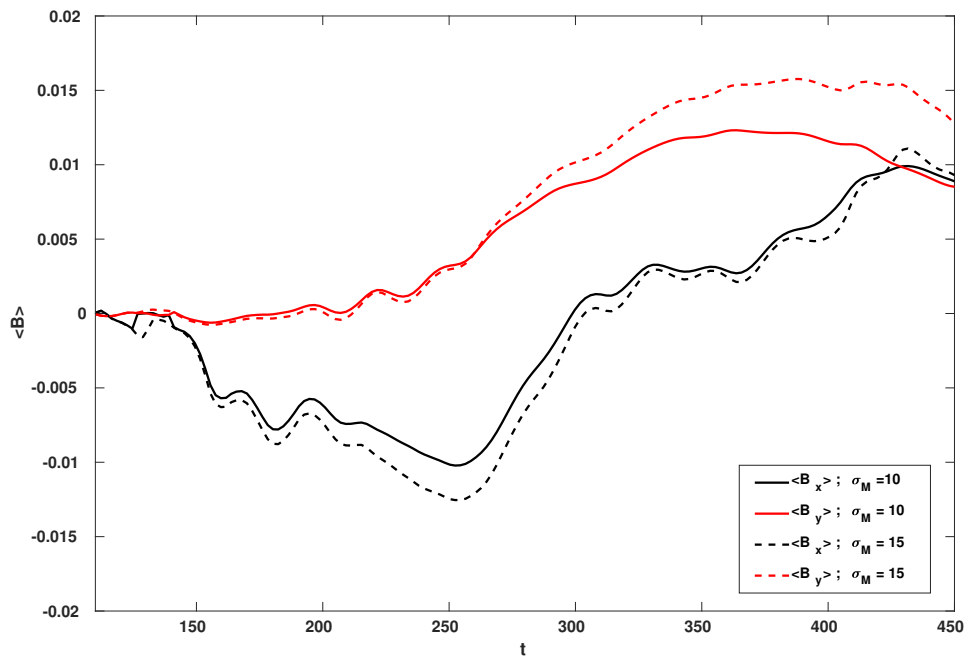


Figure 7.9.: Time evolution of the horizontal magnetic field components $\langle B_x \rangle$ and $\langle B_y \rangle$ for the cases 4d and 4e with time.

field structure similar. Therefore, I conclude that for future investigations it will be sufficient to focus only on one case in the long-time evolution.

Moving on to the question if significant large-scale magnetic fields are produced, a quantity that gives the ratio of the energy in the mean-field to the total magnetic field energy is defined (see for example Cattaneo and Hughes, 2006; Favier and Bushby, 2012):

$$\Gamma(z) = \frac{\langle \mathbf{B} \rangle_z^2}{\langle \mathbf{B}^2 \rangle_z}. \quad (7.10)$$

In Fig. 7.10 this quantity is displayed for case 4e for each depth over a range of times. $\Gamma(z)$ becomes at most about 0.1, which indicates that some large-scale magnetic fields are generated, but it is not a significant amount. It can be seen that regions with higher Γ are formed at some distance in both directions from the middle of the domain. After approximately $t \approx 200$ these regions become more extended and migrate further away from the middle of the domain with time. At the current stage, at $t \approx 440$, the small-scale dynamo dominates the magnetic field generation, where only some large-scale magnetic field is formed.

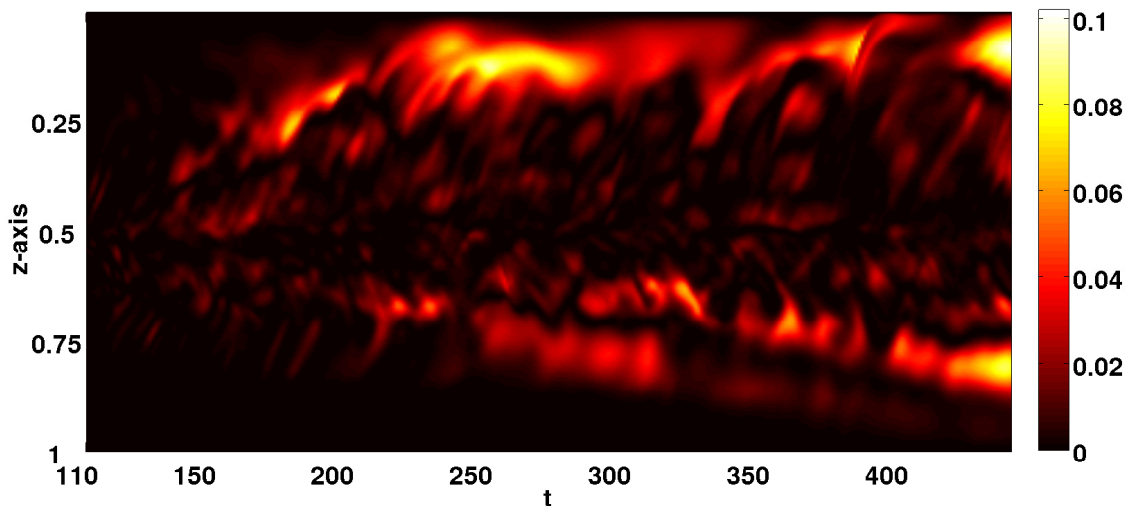


Figure 7.10.: $\Gamma(z)$ as a function of depth and time for case 4e.

7.5. Summary and Future Work.

To study potential dynamo action in the tachocline in order to gain a more detailed understanding of magnetic field evolutions in stars, in this chapter I have started to

include seed magnetic fields in our previously investigated hydrodynamical systems. Several preliminary results of potential kinematic dynamo action in shear-driven turbulence were presented in this chapter. Examining several cases at small and large magnetic Prandtl numbers revealed that only for $\sigma_m > 1$ dynamo action can be established. In the large magnetic Prandtl number regime a small-scale dynamo is more likely to operate. However, the constant but slow increase in the mean magnetic field indicates that some large-scale magnetic fields are produced. A few more calculations are needed to find a critical magnetic Reynolds number. This is part of ongoing and future investigations due to the lengthy computational times involved. Moreover, a non-linear magnetic setup incorporating the back-reaction of the magnetic field on the turbulence dynamics is planned in order to obtain a comprehensive analysis of potential magnetic field generation.

8. Discussions and Conclusions

Current stellar evolution models as well as stellar dynamo models are challenged by some discrepancies between theory and observations. Observed surface abundances of lithium and carbon indicate more mixing in stars than can be explained by current stellar models. In this context it is crucial to obtain a detailed understanding of all micro- and macro-physical processes that contribute to mixing in stellar interiors. It is also the case that magnetic dynamo models still cannot explain magnetic field generation and temporal evolution in a self-consistent way. While more sophisticated dynamo models include many important dynamical features of stars, stellar interior dynamics in general are still not entirely understood.

The aim of my research has been to provide a more detailed understanding of potential small-scale dynamics in astrophysical shear regions, especially in stars. This is important in the context of understanding mixing behaviour in stars as well as magnetic field generation. Measurements obtained by using helioseismic techniques are not sufficiently accurate to resolve the gas dynamics at the base of the solar convection zone, in the tachocline. Therefore, use of analytical and numerical calculations helps to develop a better understanding of a potentially unstable shear flow. In this volume I have completed comprehensive investigations of linear and non-linear evolution of shear flows, where the primary focus was on pure hydrodynamical systems.

In order to achieve a better understanding of small-scale dynamics in stellar interiors, it was necessary to undertake several investigations: Starting with a linear stability analysis of a fully compressible fluid in a stratified polytropic atmosphere, in Chapter 3 the stability of shear flows in stellar interiors was investigated. In this study the effect of compressibility and high thermal diffusivity in weakly and strongly stratified systems was examined. This is particularly relevant in order to

understand if compressibility has a significant effect on the stability threshold. It was shown that the stability of shear flows is only affected for moderate to high Mach number flows, where it has a stabilising effect. This is potentially important in upper regions in stars. As in stellar interiors the flow has low Mach numbers, the effect of compressibility is negligible there. Furthermore, the destabilising effect of high thermal diffusivity, which has been studied in the Boussinesq approximation so far, was confirmed for fully compressible fluids. This is especially relevant for massive stars, as thermal diffusivity can become very high in such stars and affect the linear and non-linear stability of shear flows. In addition, I demonstrated that this effect is weaker in more strongly stratified systems.

Having established a better insight of linear stability of shear flows in stellar interiors, I moved on to the non-linear evolution of unstable shear flows. Focusing on the long-time evolution of saturated shear-driven turbulence, unforced shear flows would result in a finite life time of a quasi-static regime. Therefore, in the first step a detailed comparison of possible numerical methods to sustain non-linear shear flows against viscous dissipation was performed in Chapter 4 and Chapter 5. In these investigations two types of forcing methods were distinguished: For static forcing methods no back-reaction of the actual state of the system is incorporated, whereas in the case of dynamic forcing methods the forcing adapts according to the flow. In the latter, an additional parameter, the relaxation time, provides a mechanism regulating how quickly the forcing responds to a changed velocity profile. For an extensive analysis of four forcing methods I used diverse analysing techniques. In addition, different energy budgets with separate contributions from, for example, buoyancy flux, viscous dissipation and work done by the forcing were studied. It was established that the viscous method, or the perturbation method, which both are static methods, can be used for studies in which the free evolution of a shear instability is crucial. Although, the flow is strongly forced around regions of large shear curvature, non-linear evolution away from these narrow regions is not affected by the forcing. This results in a peculiar horizontally averaged velocity profile, but ensures that the turbulence evolves freely. On the contrary, for studies where a particular mean flow during the quasi-static phase is desired, the average relaxation method is more suitable. Due to a forcing that is proportional to the difference be-

tween the target velocity profile and the actual horizontally averaged velocity profile, a global forcing drives the flow towards the desired flow on an adjustable relaxation time-scale. I investigated how different relaxation time-scales affect the linear and non-linear evolution of the system. I found that the relaxation time-scale needs to be of order or greater than the viscous time-scale to achieve a quasi-static state and avoid non-physical effects due to overly strong forcing. These results contribute to the understanding of how forcing methods affect shear-driven turbulence and provide insights into what forcing method is suitable for a particular problem.

Moving on to the question of how shear flows can help us to understand the complex dynamics in stellar interiors, the third project targeted global properties of shear-driven turbulence and was discussed in Chapter 6. In stellar interiors the global shear profile and turbulent length-scales evolve freely due to unknown mechanisms. Therefore, it is crucial to investigate what affects these scales. Primarily, the question of how key parameters affect the typical length-scales and velocities in a saturated regime and the extent of the turbulent region is addressed. It shows that viscosity has little effect on the spread of the turbulent region, whereas for increasing thermal diffusivity the turbulent region is either squeezed or enlarged, depending on the Péclet number regime. I show that turbulence characteristics in stratified systems, obtained in the non-linear calculations, depend on several dimensionless numbers, which indicates that the problem is more complex in stratified systems than in some previous Boussinesq studies. The results provide a better understanding of what controls the global properties of the resulting mean flow after saturation, which helps to draw a connection between observations of shear flows in astrophysical objects and numerical calculations.

Having conducted detailed investigations of the non-linear evolution of pure hydrodynamical systems extended insights into the dynamics and the influence of transport coefficients were gained in Chapter 6. Until this point I have fully considered pure hydrodynamic systems. However, in stars the presence and temporal variation of magnetic fields require an understanding of stellar dynamo models. To address these questions, it is crucial to study how magnetic fields interact with turbulent motions and whether such complex dynamics can generate and sustain large-scale magnetic fields. Thus, the possibility of a kinematic dynamo in shear-driven turbu-

lence is studied in Chapter 7. Magnetic dynamo action was found for large magnetic Prandtl numbers, which indicates that small-scale magnetic field generation takes place. However, due to computational time restrictions this research remains ongoing and requires further investigations in order to clarify if large-scale magnetic field generation is possible. Moreover, back-reaction of magnetic fields on the fluid dynamics needs to be considered to ensure a more self-consistent model.

Limitations of Current Investigations

In general, it is worth noting that even with the currently available computational facilities, numerical investigations of stellar interior dynamics cannot be performed with the actual observed viscosity, thermal diffusivity and Prandtl number. Such that at least two of these parameters differ several orders of magnitude from the measured value. Using much higher viscosity and Prandtl number, in order to get a tractable system, allows to investigate dynamics similar to realistic astrophysical shear flows. However, the numerically obtained dynamics will necessarily lead to some differences. Therefore, results obtained by numerical simulations need to be verified by observations of the relevant objects.

In this study the system only considers a local Cartesian geometry in order to investigate small-scale dynamics. Such a model is not self-consistent as the initial dynamics are modelled and external forces are assumed to drive a shear flow. Currently, global-scale studies aim to understand what processes form and drive the strong shear flow in the tachocline (Brun and Toomre, 2002; Miesch et al., 2008). Although, global-scale models are essentially important such models cannot resolve the range of length-scales in its entirety and have to rely on artificially large transport coefficients or subgrid-scale models. Therefore, in my opinion future work is needed to close the gap between these two approaches.

Future Investigations

Having conducted the investigations so far, several questions have been partially answered and require further investigations at a later stage. In Chapter 6 I shed light on the question of whether an unstable shear flow can possibly lead to a saturated regime that suggests a stable system, when looking at horizontally averaged

properties. In this study I concluded that this is impossible to achieve in a pure hydrodynamic system. However, stellar interiors possess strong magnetic fields, especially at the base of the convection zone. Therefore, starting with an unstable shear flow and including magnetic fields that interact with the dynamics due to Lorentz force is a natural extension of the conducted study, where the strength of the magnetic field has to be varied in order to investigate how the non-linear dynamic is affected. Furthermore, taking into account previous investigations, only very unstable shear flows were considered where the KH instability dominated the saturated phase (Silvers et al., 2009a). However, shear flows with Richardson numbers significantly closer to the stability threshold might eventually lead to a quasi-static state that looks stable when considering averaged profiles and needs to be checked in future studies.

A second point to note is that in this work several simplifications were made in order to study the effect of key parameters on the linear and non-linear evolution of shear flows. I assumed a stably stratified fluid without rotation. However, stellar shear regions are not necessary stably stratified, in particular the tachocline overlaps with the base of the convection zone. Therefore, in a local approach, in order to make progress, the interface of the tachocline and the convection zone has to be taken into account. In such a setup the lower part of the domain is stably stratified and the upper part becomes unstable against convection. Similar systems have been investigated in the context of magnetic buoyancy and magnetic dynamo action (see for example Tobias et al., 2008; Silvers et al., 2009a; Brummell et al., 2010). However, previous investigations focused on the question of what conditions are necessary to obtain magnetic buoyancy when the horizontal magnetic field is generated by the shear flow (Vasil and Brummell, 2008), where it was shown that magnetic buoyancy was only present for very strong, initially unstable shear flows. Therefore in future, a setup can be considered where an upper layer is unstable to convection but the lower layers are stably stratified. Starting with a shear flow that is unstable but results in mean profiles that suggest stability when magnetic fields are included, I would suggested to test if magnetic buoyancy can be achieved when varying the distance of the shear from the unstable upper layer. As the overlap of the tachocline with the base of the convection zone changes with latitude (Basu and Antia, 2001;

Forgács-Dajka and Petrovay, 2002), a more extended overshoot region can favour magnetic buoyancy at higher latitudes, whereas the amplification and storage of toroidal magnetic fields takes place at lower latitudes. Future investigations are needed to clarify if such a complex system possibly explains helioseismic observations of a stable tachocline and some key ingredients of an interface dynamo.

Finally, it was assumed that rotation will have negligible effect on the local dynamics, which is a valid assumption for a slow rotator like the Sun. However, even in a slow rotating star, Coriolis forces will affect the non-linear evolution and need to be considered in order to obtain a full picture of the complex interior dynamics. In a rotating system other instabilities such as the baroclinic instability might be triggered (see Gilman and Dikpati, 2014, and reference therein). Particularly in faster rotating stars rotation is potentially important. Therefore, future investigations need to include rotation and study potential instabilities and the effect on dynamo action.

The suggested future research directions help to develop a complete model of stellar interior dynamics and magnetic field generation. This is particularly important in order to obtain a model that cannot only explain the observed stellar phenomena, but ultimately predict the stellar evolution self-consistently.

A. Derivation of Linearised Equations

A.1. Zero order equations

In order to derive zero order and first order MHD equations, all quantities are decomposed in the following manner $\mathbf{f} = \mathbf{f}_0 + \delta\mathbf{f}$, where zero denotes the zero order or basic state and δ the first order deviation from that. The continuity equation in zero order has the form

$$\partial_t \rho_0 = -\partial_x (\rho_0 u_0) + \partial_y (\rho_0 v_0) - \partial_z (\rho_0 w_0). \quad (\text{A.1})$$

The zero order Navier-Stokes equation takes the form

$$\begin{aligned} \partial_t (u_0 \rho_0) &= -\partial_x \left(p_0 + \frac{\alpha}{2} |\mathbf{B}_0|^2 \right) - \rho_0 (u_0 \partial_x + v_0 \partial_y + w_0 \partial_z) u_0 \\ &\quad + \alpha (B_{x,0} \partial_x + B_{y,0} \partial_y + B_{z,0} \partial_z) B_{x,0} \\ &\quad + \sigma C_k \left(\nabla^2 u_0 + \frac{1}{3} \partial_x (\partial_x u_0 + \partial_y v_0 + \partial_z w_0) \right) \\ \partial_t (v_0 \rho_0) &= -\partial_y \left(p_0 + \frac{\alpha}{2} |\mathbf{B}_0|^2 \right) - \rho_0 (u_0 \partial_x + v_0 \partial_y + w_0 \partial_z) v_0 \\ &\quad + \alpha (B_{x,0} \partial_x + B_{y,0} \partial_y + B_{z,0} \partial_z) B_{y,0} \\ &\quad + \sigma C_k \left(\nabla^2 v_0 + \frac{1}{3} \partial_y (\partial_x u_0 + \partial_y v_0 + \partial_z w_0) \right) \\ \partial_t (w_0 \rho_0) &= -\partial_z \left(p_0 + \frac{\alpha}{2} |\mathbf{B}_0|^2 \right) - \rho_0 (u_0 \partial_x + v_0 \partial_y + w_0 \partial_z) w_0 \\ &\quad + \theta (m + 1) \rho_0 \\ &\quad + \alpha (B_{x,0} \partial_x + B_{y,0} \partial_y + B_{z,0} \partial_z) B_{z,0} \\ &\quad + \sigma C_k \left(\nabla^2 w_0 + \frac{1}{3} \partial_z (\partial_x u_0 + \partial_y v_0 + \partial_z w_0) \right). \end{aligned} \quad (\text{A.2})$$

The temperature evolution equation in zero order becomes

$$\begin{aligned} \partial_t T_0 = & - (u_0 \partial_x + v_0 \partial_y + w_0 \partial_z) T_0 - T_0 (\gamma - 1) (\partial_x u_0 + \partial_y v_0 + \partial_z w_0) \\ & + \frac{\gamma C_k}{\rho_0} \nabla^2 T_0 + \frac{C_k (\gamma - 1)}{\rho_0} \left(\frac{\sigma}{2} \|\tau\|^2 + \alpha \xi \nabla \times \mathbf{B}_0 \right), \end{aligned} \quad (\text{A.3})$$

where $\|\tau\|^2$ is

$$\begin{aligned} \|\tau\|^2 = & 4 \left[(\partial_x u_0)^2 + (\partial_y v_0)^2 + (\partial_z w_0)^2 \right] - 4/3 (\partial_x u_0 + \partial_y v_0 + \partial_z w_0)^2 \\ & + 2 \left[(\partial_x v_0 + \partial_y u_0)^2 + (\partial_x w_0 + \partial_z u_0)^2 + (\partial_y w_0 + \partial_z v_0)^2 \right]. \end{aligned} \quad (\text{A.4})$$

The induction equation in zero order takes the form

$$\begin{aligned} \partial_t B_{x,0} = & \xi C_k \nabla^2 B_{x,0} + \partial_y (u_0 B_{y,0} - v_0 B_{x,0}) - \partial_z (w_0 B_{x,0} - u_0 B_{z,0}) \\ \partial_t B_{y,0} = & \xi C_k \nabla^2 B_{y,0} + \partial_z (v_0 B_{z,0} - w_0 B_{y,0}) - \partial_x (u_0 B_{y,0} - v_0 B_{x,0}) \\ \partial_t B_{z,0} = & \xi C_k \nabla^2 B_{z,0} + \partial_x (w_0 B_{x,0} - u_0 B_{z,0}) - \partial_y (v_0 B_{z,0} - w_0 B_{y,0}). \end{aligned} \quad (\text{A.5})$$

Now, assuming that the basic state only varies along the z direction, the above derived equations can be reduced. The continuity equations is

$$\partial_t \rho_0 + \partial_z (\rho_0 w_0) = 0. \quad (\text{A.6})$$

The Navier-Stokes equation becomes

$$\begin{aligned} \partial_t (u_0 \rho_0) + \rho_0 w_0 \partial_z (u_0) = & \sigma C_k (\partial_z^2 u_0) + \alpha B_{z,0} \partial_z B_{x,0} \\ \partial_t (v_0 \rho_0) + \rho_0 w_0 \partial_z (v_0) = & \sigma C_k (\partial_z^2 v_0) + \alpha B_{z,0} \partial_z B_{y,0} \\ \partial_t (w_0 \rho_0) + \rho_0 w_0 \partial_z (w_0) = & \frac{4\sigma C_k}{3} \partial_z^2 w_0 - \partial_z \left(p_0 + \frac{\alpha}{2} |\mathbf{B}_0|^2 \right) \\ & + \theta (m + 1) \rho_0 + \alpha B_{z,0} \partial_z B_{z,0}. \end{aligned}$$

The temperature equation takes the form

$$\begin{aligned} \partial_t T_0 = & - w_0 \partial_z T_0 - T_0 (\gamma - 1) \partial_z w_0 + \frac{\gamma C_k}{\rho_0} \partial_z^2 T_0 \\ & + \frac{C_k (\gamma - 1)}{\rho_0} \left(\frac{\sigma}{2} \|\tau\|^2 + \alpha \xi \left((-\partial_z B_{y,0})^2 + (\partial_z B_{x,0})^2 \right) \right), \end{aligned} \quad (\text{A.7})$$

where $||\tau||^2$ is

$$||\tau||^2 = 2 \left[4/3(\partial_z w_0)^2 + (\partial_z u_0)^2 + (\partial_z v_0)^2 \right]. \quad (\text{A.8})$$

Finally the induction equation is

$$\begin{aligned} \partial_t B_{x,0} &= \xi C_k \partial_z^2 B_{x,0} - \partial_z (w_0 B_{x,0} - u_0 B_{z,0}) \\ \partial_t B_{y,0} &= \xi C_k \partial_z^2 B_{y,0} + \partial_z (v_0 B_{z,0} - w_0 B_{y,0}) \\ \partial_t B_{z,0} &= \xi C_k \partial_z^2 B_{z,0}. \end{aligned} \quad (\text{A.9})$$

For the equilibrium state we seek for a system that has only velocity in horizontal directions. Furthermore, we restrict ourself to a velocity profile just in the x -direction. This assumption (there are several reason to set the vertical velocity initially to zero) reduces the equations such that it follows that the density is stationary $\partial_t \rho_0 = 0$ and the Navier-Stokes equations are

$$\begin{aligned} \partial_t (u_0 \rho_0) &= \sigma C_k (\partial_z^2 u_0) + \alpha B_{z,0} \partial_z B_{x,0} \\ \partial_t (v_0 \rho_0) &= \sigma C_k (\partial_z^2 v_0) + \alpha B_{z,0} \partial_z B_{y,0} \\ 0 &= -\partial_z (p_0 + \alpha/2(B_{x,0}^2 + B_{y,0}^2 + B_{z,0}^2)) + \theta (m+1) \rho_0 + \alpha B_{z,0} \partial_z B_{z,0} \end{aligned} \quad (\text{A.10})$$

The temperature equation takes the form

$$\partial_t T_0 = \frac{\gamma C_k}{\rho_0} \partial_z^2 T_0 + \frac{C_k (\gamma - 1)}{\rho_0} (\sigma [(\partial_z u_0)^2 + (\partial_z v_0)^2] + \alpha \xi ((-\partial_z B_{y,0})^2 + (\partial_z B_{x,0})^2)). \quad (\text{A.11})$$

The induction equation becomes

$$\begin{aligned} \partial_t B_{x,0} &= \xi C_k \partial_z^2 B_{x,0} + \partial_z (u_0 B_{z,0}) \\ \partial_t B_{y,0} &= \xi C_k \partial_z^2 B_{y,0} + \partial_z (v_0 B_{z,0}) \\ \partial_t B_{z,0} &= \xi C_k \partial_z^2 B_{z,0}. \end{aligned} \quad (\text{A.12})$$

A.2. First Order Equations

In this section the first order equations are derived. Here we assume that the basic state does not depend on x , y , or time. Furthermore, the initial velocity \mathbf{u}_0 has only horizontal components. Assuming the initial equilibrium magnetic field of the

form $\mathbf{B}_0 = (B_x(z), B_y(z), B_z(z))$ and denoting $\delta\mathbf{u} = (u, v, w)$ leads to the following linearised equations.

The continuity equation in first order is

$$\partial_t \delta\rho = -(U_0 \partial_x + V_0 \partial_y) \delta\rho - \rho_0 (\partial_x u + \partial_y v + \partial_z w) - w \partial_z \rho_0. \quad (\text{A.13})$$

The first order in perturbations Navier-Stokes equations are:

$$\begin{aligned} \rho_0 \partial_t u = & -\alpha (B_{y,0} \partial_x b_y + B_{z,0} \partial_x b_z) - \partial_x p - \rho_0 w \partial_z U_0 - \rho_0 (U_0 \partial_x + V_0 \partial_y) u \\ & + \alpha (B_{y,0} \partial_y b_x + B_{z,0} \partial_z b_x + b_z \partial_z B_{x,0}) \\ & + \sigma C_k \left(\frac{4}{3} \partial_x^2 u + \partial_y^2 u + \partial_z^2 u + \frac{1}{3} \partial_x \partial_y v + \frac{1}{3} \partial_x \partial_z w \right) \end{aligned}$$

$$\begin{aligned} \rho_0 \partial_t v = & -\alpha (B_{x,0} \partial_y b_x + B_{z,0} \partial_y b_z) - \partial_y p - \rho_0 w \partial_z V_0 - \rho_0 (U_0 \partial_x + V_0 \partial_y) v \\ & + \alpha (B_{x,0} \partial_x b_y + B_{z,0} \partial_z b_y + b_z \partial_z B_{y,0}) \\ & + \sigma C_k \left(\partial_x^2 v + \frac{4}{3} \partial_y^2 v + \partial_z^2 v + \frac{1}{3} \partial_y \partial_x u + \frac{1}{3} \partial_y \partial_z w \right) \end{aligned}$$

$$\begin{aligned} \rho_0 \partial_t w = & -\alpha \partial_z (B_{x,0} b_x + B_{y,0} b_y) - \partial_z p - \rho_0 (U_0 \partial_x + V_0 \partial_y) w \\ & + \alpha (B_{x,0} \partial_x b_z + B_{y,0} \partial_y b_z) + \rho \theta (m + 1) \\ & + \sigma C_k \left(\partial_x^2 w + \partial_y^2 w + \frac{4}{3} \partial_z^2 w + \frac{1}{3} \partial_z \partial_x u + \frac{1}{3} \partial_z \partial_y v \right) \end{aligned}$$

The heat equation becomes

$$\begin{aligned} \partial_t \delta T = & \frac{\gamma C_k}{\rho_0} (\partial_x^2 + \partial_y^2 + \partial_z^2) \delta T - (\gamma - 1) T_0 (\partial_x u + \partial_y v + \partial_z w) \\ & + \frac{C_k (\gamma - 1)}{\rho} \sigma (\partial_z V_0 (\partial_y w + \partial_z v) + \partial_z U_0 (\partial_x w + \partial_z u)) \\ & + \frac{C_k (\gamma - 1) \alpha \xi}{\rho} (\partial_z B_{x,0} (\partial_z b_x - \partial_x b_z) - \partial_z B_{y,0} (\partial_y b_z - \partial_z b_y)). \end{aligned}$$

And the induction equation takes the form

$$\begin{aligned}
 \partial_t b_x &= (B_{x,0} \partial_x u + B_{y,0} \partial_y u + B_{z,0} \partial_z u) + b_z \partial_z U_0 - B_{x,0} (\partial_x u + \partial_y v + \partial_z w) \\
 &\quad - U_0 \partial_x b_x - V_0 \partial_y b_x - w \partial_z B_{x,0} + \xi C_k (\partial_x^2 + \partial_y^2 + \partial_z^2) b_x \\
 \partial_t b_y &= (B_{x,0} \partial_x v + B_{y,0} \partial_y v + B_{z,0} \partial_z v) + b_z \partial_z V_0 - B_{y,0} (\partial_x u + \partial_y v + \partial_z w) \\
 &\quad - U_0 \partial_x b_y - V_0 \partial_y b_y - w \partial_z B_{y,0} + \xi C_k (\partial_x^2 + \partial_y^2 + \partial_z^2) b_y \\
 \partial_t b_z &= (B_{x,0} \partial_x w + B_{y,0} \partial_y w + B_{z,0} \partial_z w) - B_{z,0} (\partial_x u + \partial_y v + \partial_z w) \\
 &\quad - U_0 \partial_x b_z - V_0 \partial_y b_z - w \partial_z B_{z,0} + \xi C_k (\partial_x^2 + \partial_y^2 + \partial_z^2) b_z.
 \end{aligned}$$

Assuming that (u, v, w) , $\delta\rho$ and δT can be written in form of Fourier modes, i.e. any $\delta f \propto \exp(ikx + ily + \zeta t)$, then the continuity equation can be rewritten as:

$$\zeta \delta\rho = -(ikU_0 + ilV_0) \delta\rho - \rho_0(iku + ilv + \partial_z w) - w \partial_z \rho_0 \quad (\text{A.14})$$

The Navier-Stokes equations become

$$\begin{aligned}
 \zeta \rho_0 u &= -\alpha (ikB_{y,0} b_y + ikB_{z,0} b_z) - ikp - \rho_0 w \partial_z U_0 - \rho_0 (ikU_0 + ilV_0) u \\
 &\quad + \alpha (ilB_{y,0} b_x + B_{z,0} \partial_z b_x + b_z \partial_z B_{x,0}) \\
 &\quad + \sigma C_k \left(-\frac{4}{3} k^2 u - l^2 u + \partial_z u - \frac{1}{3} klv + \frac{1}{3} ik \partial_z w \right) \\
 \zeta \rho_0 v &= -\alpha (ilB_{x,0} b_x + ilB_{z,0} b_z) - ilp - \rho_0 w \partial_z V_0 - \rho_0 (U_0 ikv + V_0 ilv) \\
 &\quad + \alpha (ikB_{x,0} b_y + B_{z,0} \partial_z b_y + b_z \partial_z B_{y,0}) \\
 &\quad + \sigma C_k \left(-k^2 v - \frac{4}{3} l^2 v + \partial_z^2 v - \frac{1}{3} klu + \frac{1}{3} il \partial_z w \right) \\
 \zeta \rho_0 w &= -\alpha \partial_z (B_{x,0} b_x + B_{y,0} b_y) - \partial_z p - \rho_0 (U_0 ikw + V_0 ilw) \\
 &\quad + \alpha (ikB_{x,0} b_z + ilB_{y,0} b_z) + \rho \theta (m + 1) \\
 &\quad + \sigma C_k \left(-k^2 w + -l^2 w + \frac{4}{3} \partial_z^2 w + \frac{1}{3} \partial_z iku + \frac{1}{3} \partial_z ilv \right).
 \end{aligned}$$

The heat equation becomes

$$\begin{aligned} \zeta \delta T = & \frac{\gamma C_k}{\rho_0} (-k^2 - l^2 + \partial_z^2) \delta T - (\gamma - 1) T_0 (iku + ilv + \partial_z w) \\ & + \frac{C_k(\gamma - 1)}{\rho} \sigma (\partial_z V_0 (ilw + \partial_z v) + \partial_z U_0 (ikw + \partial_z u)) \\ & \frac{C_k(\gamma - 1)\alpha\xi}{\rho} (\partial_z B_{x,0} (\partial_z b_x - ikb_z) - \partial_z B_{y,0} (ilb_z - \partial_z b_y)). \end{aligned}$$

Making use of form of Fourier mode representation, the induction equation becomes

$$\begin{aligned} \zeta b_x = & (ikB_{x,0}u + ilB_{y,0}u + B_{z,0}\partial_z u) + b_z \partial_z U_0 - B_{x,0}(iku + ilv + \partial_z w) \\ & - ikU_0 b_x - ilV_0 b_x - w \partial_z B_{x,0} + \xi C_k (-k^2 - l^2 + \partial_z^2) b_x \\ \zeta b_y = & (ikB_{x,0}v + ilB_{y,0}v + B_{z,0}\partial_z v) + b_z \partial_z V_0 - B_{y,0}(iku + ilv + \partial_z w) \\ & - ikU_0 b_y - ilV_0 b_y - w \partial_z B_{y,0} + \xi C_k (-k^2 - l^2 + \partial_z^2) b_y \\ \zeta b_z = & (ikB_{x,0}w + ilB_{y,0}w + B_{z,0}\partial_z w) - B_{z,0}(iku + ilv + \partial_z w) \\ & - ikU_0 b_z - ilV_0 b_z - w \partial_z B_{z,0} + \xi C_k (-k^2 - l^2 + \partial_z^2) b_z. \end{aligned}$$

The divergence free requirement of the magnetic field, which has the linearised form

$$0 = \partial_x b_x + \partial_y b_y + \partial_z b_z = ikb_x + ilb_y + \partial_z b_z, \quad (\text{A.15})$$

can be rearranged such that $b_x = -(l/k)b_y + (i/k)\partial_z b_z$.

Substituting this expression for b_x into the Navier-Stokes equations, the heat equation and the induction equation lead to the following set of coupled linear differential equations:

$$\begin{aligned}
 \zeta \delta \rho &= -(ikU_0 + ilV_0)\delta\rho - \rho_0(iku + ilv + \partial_z w) - w\partial_z \rho_0 \\
 \zeta \rho_0 u &= -\alpha(ikB_{y,0}b_y + ikB_{z,0}b_z) - ikp - \rho_0 w \partial_z U_0 - \rho_0(U_0 \partial_x + V_0 \partial_y)u \\
 &\quad + \alpha \left(B_{z,0} \partial_z \left(\frac{i}{k} \partial_z b_z - \frac{l}{k} b_y \right) - B_{y,0} \left(\frac{l}{k} \partial_z b_z + \frac{il^2}{k} b_y \right) + b_z \partial_z B_{x,0} \right) \\
 &\quad + \sigma C_k \left(\frac{4}{3} \partial_x^2 u + \partial_y^2 u + \partial_z^2 u + \frac{1}{3} \partial_x \partial_y v + \frac{1}{3} \partial_x \partial_z w \right) \\
 \zeta \rho_0 v &= -\alpha \left(ilB_{z,0}b_z - B_{x,0} \left(\frac{l}{k} \partial_z b_z + \frac{il^2}{k} b_y \right) \right) - ilp - \rho_0 w \partial_z V_0 - \rho_0(U_0 ikv + V_0 ilv) \\
 &\quad + \alpha(ikB_{x,0}b_y + B_{z,0} \partial_z b_y + b_z \partial_z B_{y,0}) \\
 &\quad + \sigma C_k \left(-k^2 v - \frac{4}{3} l^2 v + \partial_z^2 v - \frac{1}{3} klu + \frac{1}{3} il \partial_z w \right) \\
 \zeta \rho_0 w &= -\alpha \partial_z \left(B_{x,0} \left(\frac{i}{k} \partial_z b_z - \frac{l}{k} b_y \right) + B_{y,0} b_y \right) - \partial_z p - \rho_0(U_0 ikw + V_0 ilw) \\
 &\quad + \alpha(ikB_{x,0}b_z + ilB_{y,0}b_z) + \rho\theta(m+1) \\
 &\quad + \sigma C_k \left(-k^2 w + -l^2 w + \frac{4}{3} \partial_z^2 w + \frac{1}{3} \partial_z iku + \frac{1}{3} \partial_z ilv \right) \\
 \zeta \delta T &= \frac{\gamma C_k}{\rho_0} (-k^2 - l^2 + \partial_z^2) \delta T - (\gamma - 1)T_0(iku + ilv + \partial_z w) \\
 &\quad + \frac{C_k(\gamma - 1)}{\rho} \sigma (\partial_z V_0(ilw + \partial_z v) + \partial_z U_0(ikw + \partial_z u)) \\
 &\quad + \frac{C_k(\gamma - 1)\alpha\xi}{\rho} \left(\partial_z B_{x,0} \left(\partial_z \left(\frac{i}{k} \partial_z b_z - \frac{l}{k} b_y \right) - ikb_z \right) - \partial_z B_{y,0}(ilb_z - \partial_z b_y) \right) \\
 \zeta b_y &= (ikB_{x,0}v + ilB_{y,0}v + B_{z,0} \partial_z v) + b_z \partial_z V_0 - B_{y,0}(iku + ilv + \partial_z w) \\
 &\quad - ikU_0 b_y - ilV_0 b_y - w \partial_z B_{y,0} + \xi C_k (-k^2 - l^2 + \partial_z^2) b_y \\
 \zeta b_z &= (ikB_{x,0}w + ilB_{y,0}w + B_{z,0} \partial_z w) - B_{z,0}(iku + ilv + \partial_z w) \\
 &\quad - ikU_0 b_z - ilV_0 b_z - w \partial_z B_{z,0} + \xi C_k (-k^2 - l^2 + \partial_z^2) b_z.
 \end{aligned}$$

These equations can be represented by

$$\zeta \mathbf{f} = \mathbf{A} \mathbf{f}, \tag{A.16}$$

where the matrix A contains the finite difference coefficients applied to the discretised eigenfunctions $\mathbf{f} = (\delta\rho, u, v, w, \delta T, b_y, b_z)^T$. These procedure reduces the problem to a matrix equation, as it was done in Section 3.2 for a simplified set of linearised equations.

B. Useful Vector Identities

In the following any tensor of rank two will be denoted by a capital letters, as for example \mathbf{T} , and tensor of rank one by any small letter, such as \mathbf{a} .

B.1. Vector Identities I

In order to derive the vector identity

$$\mathbf{a} \cdot (\nabla \cdot \mathbf{T}) = \nabla \cdot (\mathbf{T} \cdot \mathbf{a}) - (\mathbf{T}^T \cdot \nabla) \cdot \mathbf{a}, \quad (\text{B.1})$$

where T denotes that the tensor \mathbf{T} is transposed, it is necessary to use the following known identities:

$$(\nabla \cdot \mathbf{T})_i = \partial^j T_{ji} \quad (\text{B.2})$$

$$(\mathbf{M} \cdot \mathbf{a})_i = M_{ij} a^j, \quad (\text{B.3})$$

where we use the Einstein summation convention and sum over repeated indices.

Starting with $\mathbf{a} \cdot (\nabla \cdot \mathbf{T})$ it can be rewritten as

$$a^i (\nabla \cdot \mathbf{T})_i = a^i \partial^j T_{ji} = \partial^j \underbrace{(a^i T_{ji})}_{=B_j} - T_{ji} \partial^j a^i \quad (\text{B.4})$$

$$= \partial^j B_j - T_{ji} \partial^j a^i = \nabla \cdot \mathbf{B} - (\mathbf{T}^T \cdot \nabla) \cdot \mathbf{a}, \quad (\text{B.5})$$

where $\mathbf{B} = \mathbf{T} \cdot \mathbf{a}$.

B.2. Vector identities II

It can be shown that

$$\frac{1}{2} \mathbf{u} \cdot \nabla |\mathbf{u}^2| = [(\mathbf{u}\mathbf{u}) \cdot \nabla] \cdot \mathbf{u} \quad (\text{B.6})$$

by rewriting the left side of the equation

$$\frac{1}{2} u_i \partial^i u_j u^j = \frac{1}{2} 2 u_i u_j \partial^i u^j = \underbrace{u_i u_j}_{=(\mathbf{u}\mathbf{u})_{ij}} \partial^i u^j = [(\mathbf{u}\mathbf{u}) \cdot \nabla] \cdot \mathbf{u} \quad (\text{B.7})$$

B.3. Vector identities III

The Frobenius (or Hilbert-Schmidt) norm of a second rank tensor \mathbf{A} can be calculated from the trace of matrix product of the tensor \mathbf{A} with its transposed \mathbf{A}^T :

$$\|\mathbf{A}\|^2 = \text{tr} (\mathbf{A}^T \mathbf{A}), \quad (\text{B.8})$$

Another definition of the Frobenius norm is

$$\|\mathbf{A}\|^2 = A_{ji} A^{ij}. \quad (\text{B.9})$$

Note, there exist various other matrix norms, which are not used here.

C. Energy Budgets Detailed Calculations

In this section a more detailed derivation for the energy change in the kinetic energy, the gravitational potential energy, and the internal energy will be shown. The change of the kinetic energy can be expressed, by using the Equations (2.13) - (2.15), where the external forcing term in the momentum equation is set to zero:

$$\begin{aligned}
\partial_t E_{kin} &= \partial_t \left(\frac{1}{2} \int_V \mathbf{u} \cdot \mathbf{u} \rho dV \right) \\
&= \int_V \partial_t(\rho \mathbf{u}) \cdot \mathbf{u} dV - \frac{1}{2} \int_V \mathbf{u} \cdot \mathbf{u} \partial_t(\rho) dV \\
&= \int_V \mathbf{u} \cdot \left(\underbrace{\sigma C_k \left(\nabla^2 \mathbf{u} - \frac{1}{3} \nabla(\nabla \cdot \mathbf{u}) \right)}_{=\nabla \cdot \boldsymbol{\tau}} - \nabla p - \rho \theta(m+1) \hat{\mathbf{z}} - \nabla \cdot (\rho \mathbf{u} \mathbf{u}) \right) dV \\
&\quad + \frac{1}{2} \int_V \mathbf{u} \cdot \mathbf{u} \nabla \cdot (\rho \mathbf{u}) dV \\
&= \underbrace{\sigma C_k \oint_S \boldsymbol{\tau} \cdot \mathbf{u} \cdot \hat{\mathbf{n}} dS}_{=0} - \underbrace{\sigma C_k \int_V \epsilon' dV}_{=\epsilon} - \underbrace{\int_V \mathbf{u} \cdot \nabla p dV}_{=\mathcal{H}_p} \\
&\quad + \underbrace{\int_V \theta(m+1) \rho w dV}_{=\mathcal{H}_b} - \underbrace{\int_V \mathbf{u} \cdot \nabla \cdot (\rho \mathbf{u} \mathbf{u}) dV + \frac{1}{2} \int_V \mathbf{u} \cdot \mathbf{u} \nabla \cdot (\rho \mathbf{u}) dV}_{=\mathcal{H}_a} \\
&= -\epsilon - \mathcal{H}_p + \mathcal{H}_b - \mathcal{H}_a,
\end{aligned} \tag{C.1}$$

where $\epsilon' = \tau_{ij} \frac{\partial u_i}{\partial x_j}$, such that it gives the energy dissipation rate per volume due to viscosity (see Landau and Lifshitz, 1987) and ϵ represents its volume integral. The second term represents the advected pressure change within the domain. \mathcal{H}_p denotes

the reversible exchange of energy through buoyancy flux and appears in the kinetic energy changes as well as in the gravitational potential energy change, which means that there is a direct exchange of energy in both directions. The last term \mathcal{H}_a can be rearranged using the identities in Section B.1 and Section B.2:

$$\mathcal{H}_a = \int_V \frac{1}{2} |\mathbf{u}|^2 \nabla \cdot (\rho \mathbf{u}) - \mathbf{u} \cdot \nabla \cdot (\rho \mathbf{u} \mathbf{u}) dV \quad (\text{C.2})$$

$$= \frac{1}{2} \int_V \nabla \cdot (\rho |\mathbf{u}|^2 \mathbf{u}) - \rho \mathbf{u} \cdot \nabla |\mathbf{u}|^2 dV \quad (\text{C.3})$$

$$- \int_V \nabla \cdot (\rho (\mathbf{u} \mathbf{u}) \cdot \mathbf{u}) - \rho (\mathbf{u} \mathbf{u}) \cdot \nabla \cdot \mathbf{u} dV \quad (\text{C.4})$$

where the vector identity derived in Section (B.1) was used. The second and fourth term cancel each other due to the vector identity shown in Section (B.2). The first and third term contract, because $(\mathbf{u} \mathbf{u}) \cdot \mathbf{u} = |\mathbf{u}|^2 \mathbf{u}$. Then, the advective term becomes

$$\mathcal{H}_a = -\frac{1}{2} \int_V \nabla \cdot (\rho |\mathbf{u}|^2 \mathbf{u}) dV = -\frac{1}{2} \oint_S \rho |\mathbf{u}|^2 \mathbf{u} \cdot \hat{\mathbf{n}} dS \quad (\text{C.5})$$

where S is the volume's surface and $\hat{\mathbf{n}}$ is the normal vector on the surface.

For the numerical implementation all components of the ε term are derived in detail:

$$\begin{aligned} \varepsilon &= \sigma C_k \int_V \epsilon' dV \\ &= \sigma C_k \int_V -\frac{2}{3} (\nabla \cdot \mathbf{u})^2 + \frac{1}{2} \nabla^2 (\mathbf{u} \cdot \mathbf{u}) - \mathbf{u} \cdot (\nabla^2 \mathbf{u}) + \nabla \cdot (\mathbf{u} \cdot \nabla \mathbf{u}) - \mathbf{u} \cdot \nabla (\nabla \cdot \mathbf{u}) dV \\ &= -\frac{2}{3} \sigma C_k \int_V (\nabla \cdot \mathbf{u})^2 dV \\ &\quad + 2\sigma C_k \int_V (\partial_x u)^2 + (\partial_y v)^2 + (\partial_z w)^2 + \partial_x w \partial_z u + \partial_y w \partial_z v + \partial_x v \partial_y u dV \\ &\quad + \sigma C_k \int_V (\partial_y u)^2 + (\partial_z v)^2 + (\partial_x v)^2 + (\partial_z v)^2 + (\partial_x w)^2 + (\partial_y w)^2 dV \end{aligned} \quad (\text{C.6})$$

For the two potential energies, first the time derivative of the gravitational potential energy is derived by using the continuity equation:

$$\begin{aligned}
\partial_t E_{pot} &= \partial_t \left(- \int_V \theta(m+1) \rho z dV \right) \\
&= + \theta(m+1) \int_V z \nabla \cdot (\rho \mathbf{u}) \\
&= \theta(m+1) \int_V \nabla \cdot (z \rho \mathbf{u}) dV - \int_V \theta(m+1) \rho \mathbf{u} \cdot \nabla z dV \\
&= \underbrace{\theta(m+1) \oint_S z \rho \mathbf{u} \cdot \hat{\mathbf{n}} dS}_{=0} - \underbrace{\int_V \theta(m+1) \rho w dV}_{=\mathcal{H}_\rho}
\end{aligned} \tag{C.7}$$

where the surface integral corresponds to advective fluxes through the boundary and \mathcal{H}_ρ represents the buoyancy flux. As our system is closed and the net mass flux across the surface vanished, the only term that contributes is the buoyancy flux \mathcal{H}_ρ . To account for the total potential energy it is necessary to analyse the change in the internal energy of the system. For an ideal gas the internal energy is defined as $I = c_v \int T \rho dV$ and changes according to

$$\begin{aligned}
\partial_t \left(c_v \int_V T \rho dV \right) &= c_v \int_V \partial_t(T) \rho dV + c_v \int_V T \partial_t(\rho) dV \\
&= c_v \int_V \rho \left(\frac{\gamma C_k}{\rho} \nabla^2 T - (\gamma - 2) T \nabla \cdot \mathbf{u} - \nabla \cdot (T \mathbf{u}) + \mathbf{q} \right) dV \\
&\quad - c_v \int_V T \nabla \cdot (\rho \mathbf{u}) dV \\
&= c_v \int_V (\gamma C_k \nabla^2 T - \rho (\gamma - 1) T \nabla \cdot \mathbf{u} - \rho \mathbf{u} \cdot \nabla (T) + \mathbf{q}) dV \\
&\quad - c_v \int_V T \nabla \cdot (\rho \mathbf{u}) dV \\
&= c_v \underbrace{\oint_S \gamma C_k \nabla T dS}_{=\Phi_{temp}} + c_v \underbrace{\int_V \rho \mathbf{q} dV}_{=\varepsilon} - c_v \int_V T \nabla \cdot (\rho \mathbf{u}) dV \\
&\quad - c_v \int_V (\gamma - 1) \nabla \cdot (\rho T \mathbf{u}) - (\gamma - 1) \mathbf{u} \cdot \nabla \rho T + \nabla \cdot (\rho T \mathbf{u}) - T \nabla \cdot (\rho \mathbf{u}) dV \\
&= c_v \Phi_{temp} + \varepsilon + c_v (\gamma - 1) \underbrace{\int_V \mathbf{u} \cdot \nabla \rho T dV}_{=\mathcal{H}_p} \\
&= c_v \Phi_{temp} + \varepsilon - c_v (\gamma - 1) \mathcal{H}_p,
\end{aligned} \tag{C.8}$$

where $\mathbf{q} = \frac{C_k \sigma (\gamma - 1)}{2\rho} |\tau|^2$ and τ is the strain rate tensor, such that ε is due to viscous heating and cause irreversible changes. There is a surface flux, Φ_{temp} , which accounts for the temperature flux through the boundaries and does not vanish. The advective term transports the pressure change and it is denoted by \mathcal{H}_p . The internal energy is changed by three types of processes, dissipation, flux through boundaries and internal local compression and expansion.

Additional Terms for the MHD Equations

For the sake of completeness the additional energy contributions obtained from magnetic field interaction are derived. For this purpose it is necessary to derive the energy changes using the set of Equations (2.32) - (2.36). Then, for the internal energy change, $\partial_t I$, derived in Equation (C.8) only one additional term has to be considered.

$$\begin{aligned}
\partial_t \left(c_v \int_V T \rho dV \right) &= -\varepsilon - \mathcal{H}_p + \mathcal{H}_\rho - \mathcal{H}_a + c_v \int_V C_k (\gamma - 1) f \xi |\nabla \times \mathbf{B}|^2 dV \\
&= -\varepsilon - \mathcal{H}_p + \mathcal{H}_\rho - \mathcal{H}_a + \underbrace{\int_V C_k f \xi |\nabla \times \mathbf{B}|^2 dV}_{\mathcal{D}_{ohmic}} \\
&= -\varepsilon - \mathcal{H}_p + \mathcal{H}_\rho - \mathcal{H}_a + \mathcal{D}_{ohmic}
\end{aligned} \tag{C.9}$$

where \mathcal{D}_{ohmic} is the internal energy increase induced by ohmic heating.

Then, taking Equation (C.1) into account the kinetic energy change, $\partial_t E_{kin}$, becomes

$$\begin{aligned}
\partial_t E_{kin} &= -\varepsilon - \mathcal{H}_p + \mathcal{H}_\rho - \mathcal{H}_a + \int_V f \nabla \cdot (\mathbf{B}\mathbf{B}) \cdot \mathbf{u} - \frac{f}{2} \nabla |\mathbf{B}|^2 \cdot \mathbf{u} dV \\
&= -\varepsilon - \mathcal{H}_p + \mathcal{H}_\rho - \mathcal{H}_a + \underbrace{\int_V f (\mathbf{B} \cdot \nabla \mathbf{B}) \cdot \mathbf{u} dV}_{\mathcal{B}_t} - \underbrace{\int_V \frac{f}{2} \nabla |\mathbf{B}|^2 \cdot \mathbf{u} dV}_{\mathcal{B}_\perp} \\
&= -\varepsilon - \mathcal{H}_p + \mathcal{H}_\rho - \mathcal{H}_a + \mathcal{B}_t - \mathcal{B}_\perp
\end{aligned} \tag{C.10}$$

where both terms \mathcal{B}_\perp and \mathcal{B}_t are due to magnetic pressure parallel to the velocity field. The term \mathcal{B}_\perp represents all changes made by the pressure perpendicular to the magnetic field lines and proportional to the magnetic field strength. The other

term is due to the magnetic tension force that counteracts bent magnetic field lines to straighten them out.

D. Parallel Sorting

In order to calculate the background potential energy, introduced in Section 5.1, in a parallelised code, it is necessary to sort the density array across several layers. The straight forward option is to gather all arrays on one core and to use an efficient sorting algorithm. Afterwards the arrays are distributed to perform subsequent calculations. However, for high resolutions it becomes impossible to gather the initially distributed array to one core and perform the sorting there. Therefore, it was necessary to develop an efficient algorithm to sort the local arrays globally. In Fig. D.1 a visualisation of the procedure is shown where an array is distributed across four cores.

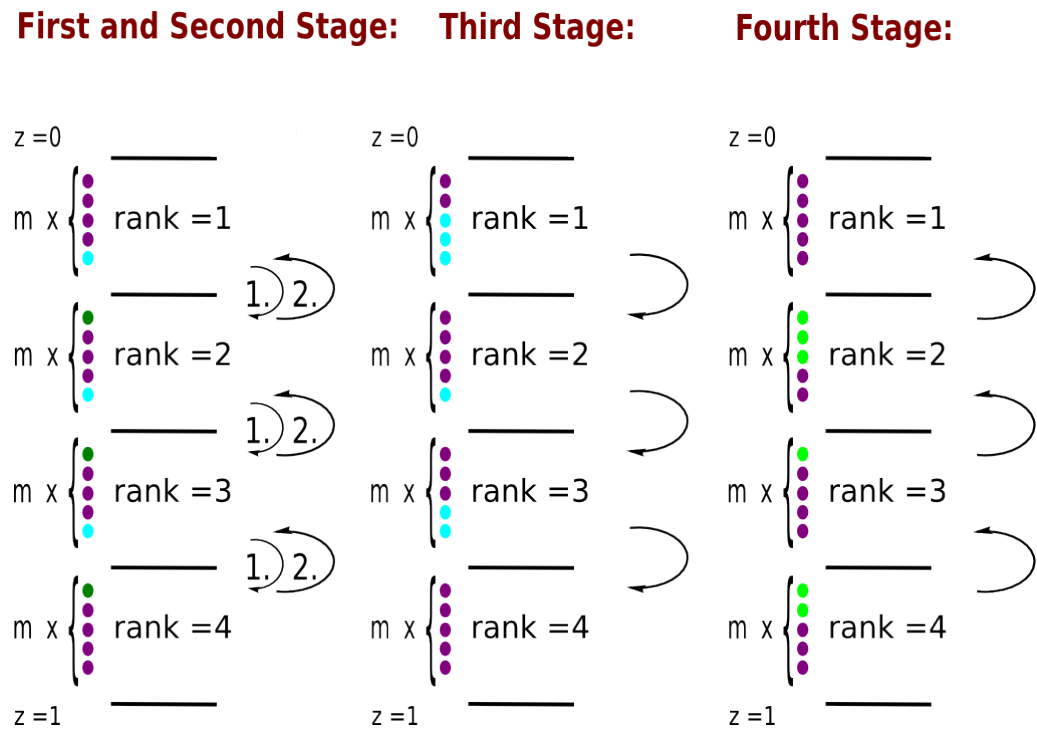


Figure D.1.: Illustration of a sorting procedure for an array, which is distributed on several cores. In this example z indicates the vertical coordinate.

To commence the procedure on each core the density is copied to a one-dimensional array, $\rho(m)$, because one is only interested in the distribution with depth. During the first and second stage shown on the left in Fig. D.1 the density array with m points is sorted locally on each of the four cores and the two boundary points are sent to their neighbouring layer (as indicated by the arrows). On each core the received point is compared to the boundary point and it is determined if and how many points need to be swapped to the corresponding core. During the third stage, displayed in the middle of Fig. D.1, the bottom points that need to be swapped are sent one layer down and stored with the top of the layer. Then, this array is sorted on each core. To complete the swap in the fourth stage, the top points that need to be send up are copied from the resorted array at each core and send one core up. This is shown in the right graphic in Fig. D.1. Then the density array is sorted on each core again. To make sure that the global array is sorted the boundary point are compared again, if it needs further sorting the whole procedure is repeated. Below the pseudo code in Algorithm 1 sketches a general parallelisation for a sorting task across several layers, where it is assumed that the array has to be sorted in an ascending order.

Algorithm 1 Parallel Sorting

```
1: procedure PARALLELSORT( $R$ )
2:   Input:  $r(m)$        $\rightarrow$   $r$  is distributed on  $n$  cores each of size  $m$ 
3:   global variable: rank       $\rightarrow$  specifies the core rank
4:   declare integer  $p, q(n,2)$    $\rightarrow$   $q$  counts points to swap at top ( $q(\text{rank},1)$ )
   and bottom ( $q(\text{rank},2)$ ) for each layer
5:   declare allocatable stop, sbottom, rtop, rbottom, sortr
6:   set  $p = 0$ 
7:   set  $q = 0$ 
8:
9:   while  $\maxval(q) > 0$  Or  $p = 0$  do
10:     $p = 1$ 
11:    if  $q(\text{rank}, 1) > 0$  Or  $q(\text{rank} + 1, 2) > 0$  then
12:      allocate stop( $q(\text{rank},1)$ ), sbottom( $q(\text{rank},2)$ )
13:      allocate rtop( $q(\text{rank},2)$ ), rbottom( $q(\text{rank},1)$ )
14:      allocate sortr( $2*q(\text{rank},1)$ )
15:
16:      if  $q(\text{rank}, 1) > 0$  then
17:        assign and send stop to the layer above ( $\text{rank}=(n-1)$ )
18:        receive rbottom
19:        copy rbottom to  $r(1:q(\text{rank},1))$ 
20:      end if
21:
22:      if  $q(\text{rank}, 2) > 0$  then
23:        receive rtop layer from core with  $\text{rank}=n+1$ 
24:        copy  $r((m-q(\text{rank},2)):m)$  to sortr and rtop to sortr
25:        sort sortr by using quicksort routine
26:        copy sortr( $1:q(\text{rank},2)$ ) to  $r((m-q(\text{rank},2)): m)$ 
27:        copy sortr( $q(\text{rank},2) + 1:2*q(\text{rank},2)$ ) to sbottom
28:        send sbottom to the next layer with  $\text{rank} = (n+1)$ 
29:      end if
30:    end if
31:    sort  $r$  on each core
32:    send last top and bottom point receive last bottom and top point
33:    if  $\text{top} > r(1)$  Or  $\text{bottom} < r(m)$  then
34:      count how many points need to be exchanged
35:      assign  $q(\text{rank},1)$  and  $q(\text{rank},2)$ 
36:    else
37:       $q(\text{rank},*) = 0$ 
38:    end if
39:    get all  $q$  entries from all ranks
40:  end while
41:  return sorted  $r$ 
42: end procedure
```

Bibliography

- Anderson, E., Bai, Z., Bischof, C., Blackford, S., Demmel, J., Dongarra, J., Du Croz, J., Greenbaum, A., Hammerling, S., McKenney, A., and Sorensen, D., 1999. *LA-PACK Users' Guide: Third Edition*. Software, Environments, and Tools. Society for Industrial and Applied Mathematics. 49
- Appenzeller, I., 2012. *Introduction to Astronomical Spectroscopy*, Chapter 2. Cambridge University Press. 4
- Arlt, R., 2009. Instabilities in the Magnetic Tachocline. In: M. Dikpati, T. Arentoft, I. González Hernández, C. Lindsey, and F. Hill, eds., *Solar-Stellar Dynamos as Revealed by Helio- and Asteroseismology: GONG 2008/SOHO 21*, volume 416 of *Astronomical Society of the Pacific Conference Series*, p. 467. 5
- Augustson, K. C., Brown, B. P., Brun, A. S., Miesch, M. S., and Toomre, J., 2012. Convection and Differential Rotation in F-type Stars. *Astrophys. J.*, 756, pp.169-146
- Augustson, K. C., Brun, A. S., and Toomre, J., 2013. Dynamo Action and Magnetic Cycles in F-type Stars. *Astrophys. J.*, 777, pp.153-146, 147
- Babcock, H. W., 1961. The Topology of the Sun's Magnetic Field and the 22-Year Cycle. *Astrophys. J.*, 133, pp.572-144
- Baines, P. G. and Mitsudera, H., 1994. On the Mechanism of Shear Flow Instabilities. *J. Fluid Mech.*, 276, pp.327-342. 41
- Balbus, S. A. and Hawley, J. F., 1991. A Powerful Local Shear Instability in Weakly Magnetized Disks. I - Linear analysis. II - Nonlinear evolution. *Astrophys. J.*, 376, pp.214-233. 6, 34

- Barekat, A., Schou, J., and Gizon, L., 2014. The Radial Gradient of the Near-Surface Shear Layer of the Sun. *Astron. Astrophys.*, 570, pp.L12. 104, 144
- Barker, A. J., Silvers, L. J., Proctor, M. R. E., and Weiss, N. O., 2012. Magnetic Buoyancy Instabilities in the Presence of Magnetic Flux pumping at the Base of the Solar Convection Zone. *Mon. Not. R. Astron. Soc.*, 424, pp.115–127. 65, 67
- Barnes, S. A., 2003. On the Rotational Evolution of Solar- and Late-Type Stars, Its Magnetic Origins, and the Possibility of Stellar Gyrochronology. *Astrophys. J.*, 586, pp.464–479. 145
- Basu, S. and Antia, H. M., 2001. A Study of Possible Temporal and Latitudinal Variations in the Properties of the Solar Tachocline. *Mon. Not. R. Astron. Soc.*, 324, pp.498–508. 12, 164
- Batchelor, G. K., 1950. On the Spontaneous Magnetic Field in a Conducting Liquid in Turbulent Motion. *Proc. R. Soc. A*, 201(1066), pp.405–416. 141
- Beck, R. and Wielebinski, R., 2013. Magnetic Fields in Galaxies. In: T. D. Oswalt and G. Gilmore, eds., *Planets, Stars and Stellar Systems. Volume 5: Galactic Structure and Stellar Populations*, p. 641. Springer Netherlands. 138
- Bhat, P., Subramanian, K., and Brandenburg, A., 2016. A Unified Large/Small-Scale Dynamo in Helical Turbulence. *Mon. Not. R. Astron. Soc.*, 461, pp.240–247. 137
- Biermann, L. and Schlüter, A., 1951. Cosmic Radiation and Cosmic Magnetic Fields. II. Origin of Cosmic Magnetic Fields. *Phys. Rev.*, 82, pp.863–868. 141
- Blackman, E. G., 2003. Recent Developments in Magnetic Dynamo Theory. In: Falgarone, E. and Passot, T., eds., *Turbulence and Magnetic Fields in Astrophysics*, volume 614 of *Lecture Notes in Physics*, Berlin Springer Verlag, pp. 432–463. 141
- Blumen, W., 1970. Shear Layer Instability of an Inviscid Compressible Fluid. *J. Fluid Mech.*, 40, pp.769–781. 53
- Borrero, J. M., Jafarzadeh, S., Schüssler, M., and Solanki, S. K., 2015. Solar Magnetoconvection and Small-Scale Dynamo - Recent Developments in Observation and Simulation. *Space Sci. Rev.*, pp. 1–42. 137, 141

- Boussinesq, J., 1903. *Théorie Analytique de la Chaleur*, volume 2. Gauthier-Villars. 18
- Brandenburg, A., Nordlund, A., Stein, R. F., and Torkelsson, U., 1995. Dynamo-generated Turbulence and Large-Scale Magnetic Fields in a Keplerian Shear Flow. *Astrophys. J.*, 446, pp.741. 6, 34, 42
- Brandenburg, A., Sokoloff, D., and Subramanian, K., 2012. Current Status of Turbulent Dynamo Theory. From Large-Scale to Small-Scale Dynamos. *Space Sci. Rev.*, 169, pp.123–157. 137, 141, 148
- Brown, B., 2011. Dynamos in Stellar Convection Zones: Of Wreaths and Cycles. *J. Phys. Conf. Ser.*, 271(1), pp.012064. 145
- Brown, B. P., Browning, M. K., Brun, A. S., Miesch, M. S., and Toomre, J., 2010. Persistent Magnetic Wreaths in a Rapidly Rotating Sun. *Astrophys. J.*, 711(1), pp.424. 145
- Brown, B. P., Vasil, G. M., and Zweibel, E. G., 2012. Energy Conservation and Gravity Waves in Sound-Proof Treatments of Stellar Interiors. Part I. Anelastic Approximations. *Astrophys. J.*, 756, pp.109. 19
- Browning, M. K., 2008. Simulations of Dynamo Action in Fully Convective Stars. *Astrophys. J.*, 676, pp.1262–1280. 146
- Browning, M. K., Miesch, M. S., Brun, A. S., and Toomre, J., 2006. Dynamo Action in the Solar Convection Zone and Tachocline: Pumping and Organization of Toroidal Fields. *Astrophys. J. Lett.*, 648, pp.L157–L160. 146
- Brüggen, M. and Hillebrandt, W., 2001. Mixing through Shear Instabilities. *Mon. Not. R. Astron. Soc.*, 320, pp.73–82. 43
- Brummell, N., Tobias, S., and Cattaneo, F., 2010. Dynamo Efficiency in Compressible Convective Dynamos with and without Penetration. *Geophys. Astro. Fluid.*, 104, pp.565–576. 164
- Brun, A. S. and Toomre, J., 2002. Turbulent Convection under the Influence of Rotation: Sustaining a Strong Differential Rotation. *Astrophys. J.*, 570, pp.865–885. 8, 13, 163

- Brunt, D., 1927. The Period of Simple Vertical Oscillations in the Atmosphere. *Q. J. R. Meteorol. Soc.*, 53(221), pp.30–32. 88
- Butcher, J. C., 2008. Numerical Differential Equation Methods. In: *Numerical Methods for Ordinary Differential Equations*, pp. 51–135. John Wiley & Sons, Ltd. 29
- Cameron, R. H., Dikpati, M., and Brandenburg, A., 2016. The Global Solar Dynamo. *Space Sci. Rev.*. 137
- Canuto, C., Hussaini, M. Y., Quarteroni, A., and Zang, T. A., 1988. *Spectral Methods in Fluid Dynamics*. Springer. 27
- Canuto, C., Hussaini, M. Y., Quarteroni, A., and Zang, T. A., 2006. *Spectral Methods. Fundamentals in Single Domains*. Springer. 27, 28
- Cattaneo, F., 1999. On the Origin of Magnetic Fields in the Quiet Photosphere. *Astrophys. J. Lett.*, 515, pp.L39–L42. 141
- Cattaneo, F. and Hughes, D. W., 2001. Solar Dynamo Theory: A New Look at the Origin of Small-Scale Magnetic Fields. *Astron. Geophys.*, 42(3), pp.3.18. 137
- Cattaneo, F. and Hughes, D. W., 2006. Dynamo Action in a Rotating Convective Layer. *J. Fluid Mech.*, 553, pp.401–418. 158
- Cattaneo, F. and Hughes, D. W., 2009. Problems with Kinematic Mean Field Electrodynamics at High Magnetic Reynolds Numbers. *Mon. Not. R. Astron. Soc.*, 395(1), pp.L48. 140
- Caulfield, C. P. and Peltier, W. R., 2000. The Anatomy of the Mixing Transition in Homogeneous and Stratified Free Shear Layers. *J. Fluid Mech.*, 413, pp.1–47. 8, 65
- Chandrasekhar, S., 1961. *Hydrodynamic and Hydromagnetic Stability*. Oxford: Clarendon Press. 35, 38
- Charbonneau, P., 2014. Solar Dynamo Theory. *Annu. Rev. Astron. Astr.*, 52(1), pp.251–290. 141, 142

- Charbonneau, P., Christensen-Dalsgaard, J., Henning, R., Larsen, R. M., Schou, J., Thompson, M. J., and Tomczyk, S., 1999. Helioseismic Constraints on the Structure of the Solar Tachocline. *Astrophys. J.*, 527, pp.445–460. 5, 104, 144
- Charbonneau, P. and Dikpati, M., 2000. Stochastic Fluctuations in a Babcock-Leighton Model of the Solar Cycle. *Astrophys. J.*, 543, pp.1027–1043. 142, 145
- Charney, J. G., 1947. The Dynamics of Long Waves in a Baroclinic Westerly Current. *J. Meteorol.*, 4, pp.135–162. 7
- Chatterjee, P., Guerrero, G., and Brandenburg, A., 2011. Magnetic Helicity Fluxes in Interface and Flux Transport Dynamos. *Astron. Astrophys.*, 525, pp.A5. 142
- Chen, Z. and Huang, J., 2015. *Fundamentals of Nonlinear Systems*, Chapter 2, pp. 15–65. Springer International Publishing, Cham. 34
- Childress, S. and Gilbert, A. D., 1995. *Stretch, Twist, Fold: The Fast Dynamo*. Springer-Verlag Berlin Heidelberg. 138, 139, 140
- Choudhuri, A. R., 2015. A critical assessment of the flux transport dynamo. *J. Astrophys. Astron.*, 36(1), pp.5–14. 142
- Christensen-Dalsgaard, J. and Thompson, M. J., 2007. Observational Results and Issues concerning the Tachocline. In: D. W. Hughes, R. Rosner, and N. O. Weiss, eds., *The Solar Tachocline*, pp. 53–86. Cambridge University Press. 5, 12, 33, 105
- Cline, K. S., Brummell, N. H., and Cattaneo, F., 2003a. Dynamo Action Driven by Shear and Magnetic Buoyancy. *Astrophys. J.*, 599, pp.1449–1468. 42
- Cline, K. S., Brummell, N. H., and Cattaneo, F., 2003b. On the Formation of Magnetic Structures by the Combined Action of Velocity Shear and Magnetic Buoyancy. *Astrophys. J.*, 588, pp.630–644. 43
- Cohen, J. G., 2009. Lecture notes in structure and evolution of stars. [online] Available at: <http://www.astro.caltech.edu/~jspineda/ay123/notes/2011/ay123_polytropes_sep2010.pdf> [Accessed: 08 Apr 2016]. 11
- Collins, G. W., 2003. *The Fundamentals of Stellar Astrophysics*, Chapter 2, 5. W H Freeman & Co. 11

- Cowling, T. G., 1981. The Present Status of Dynamo Theory. *Annu. Rev. Astron. Astr.*, 19, pp.115–135. 142
- Cox, J. P. and Giuli, R. T., 1968. *Principles of Stellar Structure: Applications to Stars*. Principles of Stellar Structure. Gordon and Breach. 10, 11
- D. H. Hathaway, 2015. The Solar Interior. [online] Available at: <<https://solarscience.msfc.nasa.gov/interior.shtml>> [Accessed: 02 Jan 2017]. 5
- Davidson, P. A., 2001. Dynamics at Moderate to High Magnetic Reynolds' Number. In: *An Introduction to Magnetohydrodynamics*, pp. 159–221. Cambridge University Press. Cambridge Books Online. 6
- Dikpati, M. and Choudhuri, A. R., 1994. The Evolution of the Sun's Poloidal Field. *Astron. Astrophys.*, 291, pp.975–989. 145
- Dikpati, M., Corbard, T., Thompson, M. J., and Gilman, P. A., 2002. Flux Transport Solar Dynamos with Near-Surface Radial Shear. *Astrophys. J. Lett.*, 575(1), pp.L41. 144
- Dikpati, M. and Gilman, P. A., 2009. Flux-transport solar dynamos. *Space Sci. Rev.*, 144(1), pp.67–75. 145
- Dirac, P. A. M., 1958. *The Principles of Quantum Mechanics*, Chapter 11. Clarendon Press. 6
- Dobler, W., 2005. Stellar Dynamos - Theoretical Aspects. *Astron. Nachr.*, 326(3-4), pp.254–264. 145
- Donati, J.-F., Forveille, T., Collier Cameron, A., Barnes, J. R., Delfosse, X., Jardine, M. M., and Valenti, J. A., 2006. The Large-Scale Axisymmetric Magnetic Topology of a Very-Low-Mass Fully Convective Star. *Science*, 311, pp.633–635. 146
- Drazin, P. G. and Reid, W. H., 2004. *Hydrodynamic Stability*. Cambridge Mathematical Library. Cambridge University Press. 7, 34, 35, 36, 37

- Dubrulle, B., Marié, L., Normand, C., Richard, D., Hersant, F., and Zahn, J.-P., 2005. An Hydrodynamic Shear Instability in Stratified Disks. *Astron. Astrophys.*, 429, pp.1–13. 42
- Dudis, J. J., 1974. The Stability of a Thermally Radiating Stratified Shear Layer, including Self-Absorption. *J. Fluid Mech.*, 64, pp.65–83. 7, 42, 55, 70, 129
- Duraiswami, R., 2010. Computational Methods. [PDF file] Available at: <http://www.umiacs.umd.edu/~ramani/cmssc460/Lecture22_ODE_2010.pdf> [Accessed: 25 Oct 2016]. 30
- Durbin, P. A. and Reif, B. A. P., 2010. Reynolds Averaged Navier-Stokes Equations. In: *Statistical Theory and Modeling for Turbulent Flows*, pp. 45–56. John Wiley & Sons, Ltd. 24
- Durney, B. R., 1995. On a Babcock-Leighton Dynamo Model with a Deep-Seated Generating Layer for the Toroidal Magnetic Field. *Sol. Phys.*, 160, pp.213–235. 145
- Elliott, J. R. and Gough, D. O., 1999. Calibration of the Thickness of the Solar Tachocline. *Astrophys. J.*, 516, pp.475–481. 5
- Elsasser, W. M., 1956. Hydromagnetic Dynamo Theory. *Rev. Mod. Phys.*, 28, pp.135–163. 141
- Favier, B. and Bushby, P. J., 2012. Small-scale Dynamo Action in Rotating Compressible Convection. *J. Fluid Mech.*, 690, pp.262–287. 25, 137, 154, 158
- Favier, B. and Bushby, P. J., 2013. On the Problem of Large-Scale Magnetic Field Generation in Rotating Compressible Convection. *J. Fluid Mech.*, 723, pp.529–555. 25, 147
- Favier, B., Jouve, L., Edmunds, W., Silvers, L. J., and Proctor, M. R. E., 2012. How can Large-Scale Twisted Magnetic Structures Naturally emerge from Buoyancy Instabilities? *Mon. Not. R. Astron. Soc.*, 426, pp.3349–3359. 49
- Favier, B. and Proctor, M. R. E., 2013. Growth Rate Degeneracies in Kinematic Dynamos. *Phys. Rev. E*, 88(3), pp.031001. 24, 147

- Fitzpatrick, R., 2014. *Plasma Physics: An Introduction*. CRC Press. 139
- Fletcher, L., Dennis, B. R., Hudson, H. S., Krucker, S., Phillips, K., Veronig, A., Battaglia, M., Bone, L., Caspi, A., Chen, Q., Gallagher, P., Grigis, P. T., Ji, H., Liu, W., Milligan, R. O., and Temmer, M., 2011. An observational overview of solar flares. *Space Sci. Rev.*, 159(1), pp.19. 4
- Forgács-Dajka, E. and Petrovay, K., 2002. Dynamics of the Fast Solar Tachocline. I. Dipolar Field. *Astron. Astrophys.*, 389, pp.629–640. 12, 165
- Frisch, U., Pouquet, A., Liorat, J., and Mazure, A., 1975. Possibility of an Inverse Cascade of Magnetic Helicity in Magnetohydrodynamic Turbulence. *J. Fluid Mech.*, 68, pp.769–778. 141
- Garaud, P., Gallet, B., and Bischoff, T., 2015. The stability of stratified spatially periodic shear flows at low pécelet number. *Phys. Fluids*, 27(8). 110, 129
- Garaud, P. and Kulenthirarajah, L., 2016. Turbulent Transport in a Strongly Stratified Forced Shear Layer with Thermal Diffusion. *Astrophys. J.*, 821, pp.49. 110, 123, 124, 125, 126, 147
- Garnier, E., Adams, N., and Sagaut, P., 2009. *Large Eddy Simulation for Compressible Flows*. Springer. 24
- Gilman, P. and Dikpati, M., 2014. Baroclinic Instability in the Solar Tachocline. *Astrophys. J.*, 787(1), pp.60. 165
- Goldreich, P. and Lynden-Bell, D., 1965. II. Spiral Arms as Sheared Gravitational Instabilities. *Mon. Not. R. Astron. Soc.*, 130, pp.125. 42
- Goode, P. R., Dziembowski, W. A., Korzennik, S. G., and Rhodes, Jr., E. J., 1991. What we know about the Sun's Internal Rotation from Solar Oscillations. *Astrophys. J.*, 367, pp.649–657. 5
- Gough, D., 2007. An introduction to the solar tachocline. In: Hughes, D. W., Rosner, R., and Weiss, N. O. E., eds., *The Solar Tachocline*, Chapter 1, pp. 3–30. Cambridge University Press. 12

- Gough, D. O., Kosovichev, A. G., Toomre, J., Anderson, E., Antia, H. M., Basu, S., Chaboyer, B., Chitre, S. M., Christensen-Dalsgaard, J., Dziembowski, W. A., Eff-Darwich, A., Elliott, J. R., Giles, P. M., Goode, P. R., Guzik, J. A., Harvey, J. W., Hill, F., Leibacher, J. W., Monteiro, M. J. P. F. G., Richard, O., Sekii, T., Shibahashi, H., Takata, M., Thompson, M. J., Vauclair, S., and Vorontsov, S. V., 1996. The Seismic Structure of the Sun. *Science*, 272(5266), pp.1296–1300. 5
- Gough, D. O. and McIntyre, M. E., 1998. Inevitability of a Magnetic Field in the Sun’s Radiative Interior. *Nature*, 394, pp.755–757. 79, 101
- Griffies, S. M., 2004. *Fundamentals of Ocean Climate Models*. Princeton University Press. 81
- Grunhut, J. H. and Neiner, C., 2015. Magnetic Fields in Early-Type Stars. In: K. N. Nagendra, S. Bagnulo, R. Centeno, and M. Jesús Martínez González, eds., *Polarimetry*, volume 305 of *IAU Symposium*, pp. 53–60. 145
- Guerrero, G. and Käpylä, P. J., 2011. Dynamo Action and Magnetic Buoyancy in Convection Simulations with Vertical Shear. *Astron. Astrophys.*, 533, pp.A40. 69, 97
- Guerrero, G., Smolarkiewicz, P. K., de Gouveia Dal Pino, E. M., Kosovichev, A. G., and Mansour, N. N., 2016. On the Role of Tachoclines in Solar and Stellar Dynamos. *Astrophys. J.*, 819, pp.104. 146, 147
- Guillard, H. and Murrone, A., 2004. On the Behavior of Upwind Schemes in the Low Mach Number Limit: II. Godunov Type Schemes. *Comput. Fluids*, 33(4), pp.655 – 675. 51
- Hansen, C. J. and Kawaler, S. D., 1999a. *Stellar Interiors: Physical Principles, Structure, and Evolution*, Chapter 9. Astronomy and Astrophysics Library. Springer New York. 1
- Hansen, C. J. and Kawaler, S. D., 1999b. *Stellar Interiors: Physical Principles, Structure, and Evolution*, Chapter 3. Astronomy and Astrophysics Library. Springer New York. 14
- Hathaway, D. H., 2010. The Solar Cycle. *Living Rev. Sol. Phys.*, 7(1). 4

- Hathaway, D. H., 2012. Supergranules as Probes of the Sun's Meridional Circulation. *Astrophys. J.*, 760, pp.84. 145
- Hawley, J. F., Balbus, S. A., and Winters, W. F., 1999. Local Hydrodynamic Stability of Accretion Disks. *Astrophys. J.*, 518, pp.394–404. 6, 34, 42
- Hazra, G., Karak, B. B., and Choudhuri, A. R., 2014. Is a Deep One-Cell Meridional Circulation Essential for the Flux Transport Solar Dynamo? *Astrophys. J.*, 782(2), pp.93. 145
- Herault, J., Rincon, F., Cossu, C., Lesur, G., Ogilvie, G. I., and Longaretti, P.-Y., 2011. Periodic Magnetorotational Dynamo Action as a Prototype of Nonlinear Magnetic-Field Generation in Shear Flows. *Phys. Rev. E*, 84(3), pp.036321. 141
- Hirsch, C., 2007a. Chapter 4 - the finite difference method for structured grids. In: *Numerical Computation of Internal and External Flows*, pp. 145 – 201. Butterworth-Heinemann, Oxford, 2nd edition. 25
- Hirsch, C., 2007b. Chapter 5 - finite volume method and conservative discretization with an introduction to finite element method. In: *Numerical Computation of Internal and External Flows*, pp. 203 – 248. Butterworth-Heinemann, Oxford, 2nd edition. 26, 27
- Holmboe, J., 1962. On the Behaviour of Symmetric Waves in Stratified Shear Layers. *Geophys. Publ.*, 24, pp.67–113. 7, 41
- Holt, S. E., Koseff, J. R., and Ferziger, J. H., 1992. A Numerical Study of the Evolution and Structure of Homogeneous Stably Stratified Sheared Turbulence. *J. Fluid Mech.*, 237, pp.499–539. 65, 67
- Hou, T. Y. and Li, R., 2007. Computing Nearly Singular Solutions using Pseudo-Spectral Methods. *J. Comput. Phys.*, 226, pp.379–397. 28
- Hughes, D. W. and Proctor, M. R. E., 2009. Dynamo Action in the Presence of an Imposed Magnetic Field. *Proc. R. Soc. A*, 465(2105), pp.1599–1616. 147
- Hughes, D. W. and Proctor, M. R. E., 2013. The Effect of Velocity Shear on Dynamo Action due to Rotating Convection. *J. Fluid Mech.*, 717, pp.395–416. 43, 137, 140

- Hughes, D. W., Rosner, R., and Weiss, N. O., 2007. *The Solar Tachocline*. Cambridge University Press. 6
- Hughes, D. W. and Tobias, S. M., 2001. On the Instability of Magnetohydrodynamic Shear Flows. *Proc. R. Soc. A*, 457, pp.1365. 43
- Itsweire, E. C., Koseff, J. R., Briggs, D. A., and Ferziger, J. H., 1993. Turbulence in Stratified Shear Flows: Implications for Interpreting Shear-induced Mixing in the Ocean. *J. Phys. Oceanogr.*, 23(7), pp.1508–1522. 34
- Jackson, A., Sheyko, A., Marti, P., Tilgner, A., Cébron, D., Vantieghem, S., Simatev, R., Busse, F., Zhan, X., Schubert, G., Takehiro, S., Sasaki, Y., Hayashi, Y.-Y., Ribeiro, A., Nore, C., and Guermond, J.-L., 2014. A Spherical Shell Numerical Dynamo Benchmark with Pseudo-Vacuum Magnetic Boundary Conditions. *Geophys. J. Int.*, 196(2), pp.712–723. 24
- Jackson, J. D., 1975. *Classical Electrodynamics*, Chapter 5. Wiley. 6
- Jacobitz, F. G., Sarkar, S., and van Atta, C. W., 1997. Direct Numerical Simulations of the Turbulence Evolution in a Uniformly Sheared and Stably Stratified Flow. *J. Fluid Mech.*, 342, pp.231–261. 65, 67
- JAXA/NASA/PPARC, H., 2010. Hinode Views the Sun’s Surface. [online] Available at: https://www.nasa.gov/mission_pages/hinode/solar_013.html [Accessed: 30 Nov 2016]. v, 4
- Jones, C. A., 1977. The Onset of Shear Instability in Stars. *Geophys. Astro. Fluid*, 8(1), pp.165–184. 7, 42, 55, 57
- Jones, C. A., 2011a. Dynamo theory. *Dynamos: Lecture Notes of the Les Houches Summer School 2007*, 88, pp.45. 137
- Jones, C. A., 2011b. Planetary Magnetic Fields and Fluid Dynamos. *Annu. Rev. Fluid Mech.*, 43(1), pp.583–614. 137
- Jones, C. A., Boronski, P., Brun, A. S., Glatzmaier, G. A., Gastine, T., Miesch, M. S., and Wicht, J., 2011. Anelastic convection-driven dynamo benchmarks. *Icarus*, 216(1), pp.120 – 135. 31

- Jouve, L. and Brun, A. S., 2007. On the Role of Meridional Flows in Flux Transport Dynamo Models. *Astron. Astrophys.*, 474(1), pp.239–250. 145
- Kardashev, N. S., 1992. *Astrophysics on the Threshold of the 21st Century*. Gordon and Breach Science Publishers. 6
- Karttunen, H., Kröger, P., Oja, H., Poutanen, M., and Donner, K. J. E., 2007. *Fundamental Astronomy*. Springer Berlin Heidelberg New York, 5th edition. 1, 2, 3
- Kazantsev, A. P., 1968. Enhancement of a Magnetic Field by a Conducting Fluid. *J. Exp. Theor. Phys.*, 26, pp.1031. 141
- Kelvinsong, 2012. The Structure of the Sun. [online] Available at: <https://upload.wikimedia.org/wikipedia/commons/d/d4/Sun_poster.svg> [Accessed: 26 Jul 2014]. v, 3
- Kippenhahn, R. and Möllenhoff, C., 1975. *Elementare Plasmaphysik*. Bibliographisches Institut. 21
- Kitchatinov, L. L. and Rüdiger, G., 2009. Stability of Latitudinal Differential Rotation in Stars. *Astron. Astrophys.*, 504, pp.303–307. 6, 34
- Kosovichev, A., Guerrero, G., Smolarkiewicz, P., Gouveia Dal Pino, E., and Mansour, N. N., 2015. Effects of Tachocline in Solar-Stellar Dynamo Simulations. *IAU General Assembly*, 22, pp.2258507. 146
- Kosovichev, A. G., 1996. Helioseismic Constraints on the Gradient of Angular Velocity at the Base of the Solar Convection Zone. *Astrophys. J. Lett.*, 469, pp.L61. 5, 104
- Kosovichev, A. G., Schou, J., Scherrer, P. H., Bogart, R. S., Bush, R. I., Hoeksema, J. T., Aloise, J., Bacon, L., Burnette, A., De Forest, C., Giles, P. M., Leibbrand, K., Nigam, R., Rubin, M., Scott, K., Williams, S. D., Basu, S., Christensen-Dalsgaard, J., Däppen, W., Duvall, T. L., Rhodes, J., Howe, R., Thompson, M. J., Gough, D. O., Sekii, T., Toomre, J., Tarbell, T. D., Title, A. M., Mathur, D., Morrison, M., Saba, J. L. R., Wolfson, C. J., Zayer, I., and Milford, P. N.,

1997. Structure and Rotation of the Solar Interior: Initial Results from the MDI Medium-L Program. *Sol. Phys.*, 170(1), pp.43–61. 5, 33
- Kraichnan, R. H., 1968. Small-Scale Structure of a Scalar Field Convected by Turbulence. *Phys. Fluids*, 11(5), pp.945–953. 141
- Krause, F. and Rädler, K.-H., 1980. Chapter 2 - Basic Ideas of Mean-Field Electrodynamics. In: F. Krause and K.-H. Rädler, eds., *Mean-Field Magnetohydrodynamics and Dynamo Theory*, pp. 15 – 18. Pergamon. 140
- Küker, M., Rüdiger, G., and Kitchatinov, L. L., 2011. The Differential Rotation of G Dwarfs. *Astron. Astrophys.*, 530, pp.A48. 145
- Kuzmin, D., 2015. Introduction to CFD. [online] Available at: <<http://www.mathematik.uni-dortmund.de/~kuzmin/cfdintro/lecture8.pdf>> [Accessed: 17 Oct 2016]. 29
- Landau, L. D. and Lifshitz, E. M., 1987. *Fluid Mechanics*, volume 6. Pergamon Press. 81, 176
- Larmor, J., 1919. How could a Rotating Body such as the Sun become a Magnet? *Rep. Brit. Assoc. Adv. Sci.*, A 159. 138
- Leighton, R. B., 1969. A Magneto-Kinematic Model of the Solar Cycle. *Astrophys. J.*, 156, pp.1. 144
- Leprovost, N. and Kim, E.-J., 2008. Analytical Theory of Forced Rotating Sheared Turbulence: The Perpendicular Case. *Phys. Rev. E*, 78, pp.016301. 65
- Lignières, F., Califano, F., and Mangeney, A., 1999. Shear Layer Instability in a Highly Diffusive Stably Stratified Atmosphere. *Astron. Astrophys.*, 349, pp.1027–1036. 7, 42, 55, 57, 64, 70, 129, 135
- Lopes, I. P., 2002. Probing the Dark Matter within the Solar Interior. In: *New worlds in astroparticle physics. Proceedings, 4th International Workshop, Faro, Portugal, September 5-7, 2002*, pp. 306–318. 5

- Lord Rayleigh, Strutt, J. W., 1883. Investigation of the Character of the Equilibrium of an Incompressible Heavy Fluid of Variable Density. *Proc. London Math. Soc.*, 14, pp.170–177. 87
- MacGregor, K. B. and Charbonneau, P., 1997. Solar Interface Dynamos. I. Linear, Kinematic Models in Cartesian Geometry. *Astrophys. J.*, 486, pp.484–501. 142
- Mahajan, S. M. and Rogava, A. D., 1999. What Can the Kinematic Complexity of Astrophysical Shear Flows Lead To? *Astrophys. J.*, 518, pp.814–820. 65
- Mason, J., Hughes, D. W., and Tobias, S. M., 2002. The Competition in the Solar Dynamo between Surface and Deep-Seated α -Effects. *Astrophys. J. Lett.*, 580, pp.L89–L92. 137, 143, 144, 145
- Matthews, P. C., Proctor, M. R. E., and Weiss, N. O., 1995. Compressible Magnetoconvection in Three Dimensions: Planforms and Nonlinear Behaviour. *J. Fluid Mech.*, 305, pp.281–305. 23, 25, 29, 61
- Meynet, G. and Maeder, A., 2000. Stellar Evolution with Rotation. V. Changes in all the Outputs of Massive Star Models. *Astron. Astrophys.*, 361, pp.101–120. 147
- Michaud, G. and Zahn, J.-P., 1998. Turbulent Transport in Stellar Interiors. *Theor. Comp. Fluid Dyn.*, 11, pp.183–193. 64
- Miczek, F., 2013. *Simulation of Low Mach Number Astrophysical Flows*. PhD thesis, Technical University of Munich. 42
- Miesch, M. S., 2003. Numerical Modeling of the Solar Tachocline. II. Forced Turbulence with Imposed Shear. *Astrophys. J.*, 586(1), pp.663. 65, 67, 101, 110
- Miesch, M. S., 2007. Turbulence in the Tachocline. In: D. W. Hughes, R. Rosner, and N. O. Weiss, eds., *The Solar Tachocline*, pp. 109–128. Cambridge University Press. 33, 105
- Miesch, M. S., Brun, A. S., De Rosa, M. L., and Toomre, J., 2008. Structure and Evolution of Giant Cells in Global Models of Solar Convection. *Astrophys. J.*, 673, pp.557–575. 8, 13, 101, 163

- Miesch, M. S., Featherstone, N. A., Rempel, M., and Trampedach, R., 2012. On the Amplitude of Convective Velocities in the Deep Solar Interior. *Astrophys. J.*, 757, pp.128–145
- Miesch, M. S. and Hindman, B. W., 2011. Gyroscopic Pumping in the Solar Near-surface Shear Layer. *Astrophys. J.*, 743, pp.79–104
- Miki, K., 2008. *Simulation of Magnetohydrodynamics Turbulence with Application to Plasma-assisted Supersonic Combustion*. PhD thesis, Georgia Institute of Technology. 24
- Miles, J. W., 1961. On the Stability of Heterogeneous Shear Flows. *J. Fluid Mech.*, 10, pp.496–508. 7, 38, 40, 46, 105
- Moffatt, H. K., 1978. *Magnetic Field Generation in Electrically Conducting Fluids*. Cambridge University Press, 1978. 137, 138, 139
- Narayan, R., Goldreich, P., and Goodman, J., 1987. Physics of Modes in a Differentially Rotating System - Analysis of the Shearing Sheet. *Mon. Not. R. Astron. Soc.*, 228, pp.1–41. 42
- NASA/CXC/SAO, 2015. The H-R Diagram. [online] Available at: <http://chandra.harvard.edu/edu/formal/variable_stars/bg_info.html> [Accessed: 30 Nov 2016]. v, 2
- NASA/SDO, 2016. A Solar Eruptive Prominence as Seen in Extreme UV Light on March 30, 2010 with Earth Superimposed for a Sense of Scale. [online] Available at: <https://www.nasa.gov/mission_pages/sunearth/spaceweather/index.html> [Accessed: 30 Nov 2016]. v, 4
- Orszag, S. A., 1971. Numerical Simulation of Incompressible Flows within Simple Boundaries: I. Galerkin (Spectral) Representations. *Stud. Appl. Math.*, 50, pp.293–327. 27
- Ossendrijver, M., 2003. The Solar Dynamo. *Astron. Astrophys. Rev.*, 11, pp.287–367. 138, 142

- Parker, E. N., 1955. The Formation of Sunspots from the Solar Toroidal Field. *Astrophys. J.*, 121, pp.491–513, 140
- Parker, E. N., 1975. The Generation of Magnetic Fields in Astrophysical Bodies. X - Magnetic Buoyancy and the Solar Dynamo. *Astrophys. J.*, 198, pp.205–209. 139, 142
- Parker, E. N., 1979. *Cosmical Magnetic Fields: Their Origin and Their Activity*. Oxford: Clarendon Press. 137, 141
- Parker, E. N., 1993. A Solar Dynamo Surface Wave at the Interface between Convection and Nonuniform Rotation. *Astrophys. J.*, 408, pp.707–719. 6, 138, 142, 143
- Paternò, L., 2010. The Solar Differential Rotation: A Historical View. *Astrophys. Space Sci.*, 328(1), pp.269–277. 65
- Paterson, A. R., 1983. *A First Course in Fluid Dynamics*. Cambridge University Press. 34, 35, 36
- Peltier, W. R. and Caulfield, C. P., 2003. Mixing Efficiency in Stratified Shear Flows. *Annu. Rev. Fluid Mech.*, 35(1), pp.135–167. 41, 80, 83, 98
- Peltier, W. R. and Smyth, W. D., 1989. The Transition between Kelvin-Helmholtz and Holmboe Instability: An Investigation of the Overreflection Hypothesis. *J. Atmos. Sci.*, 46, pp.3698 – 3720. 7, 41
- Petrovay, K. and Szakaly, G., 1993. The Origin of Intranetwork Fields: A Small-Scale Solar Dynamo. *Astron. Astrophys.*, 274, pp.543–551. 138
- Pietarila Graham, J., Cameron, R., and Schüssler, M., 2010. Turbulent Small-Scale Dynamo Action in Solar Surface Simulations. *Astrophys. J.*, 714, pp.1606–1616. 138
- Pradhan, A. K. and Nahar, S. N., 2011. *Atomic Astrophysics and Spectroscopy*. Cambridge University Press. 12

- Prat, V., Guilet, J., Viallet, M., and Müller, E., 2016. Shear Mixing in Stellar Radiative Zones. II. Robustness of Numerical Simulations. *Astron. Astrophys.*, 592, pp.A59. 124, 129
- Prat, V. and Lignières, F., 2013. Turbulent Transport in Radiative Zones of Stars. *Astron. Astrophys.*, 551, pp.L3. 65, 69, 101, 110, 129
- Prat, V. and Lignières, F., 2014. Shear Mixing in Stellar Radiative Zones. I. Effect of Thermal Diffusion and Chemical Stratification. *Astron. Astrophys.*, 566, pp.A110. 110, 125
- Priest, E., 2014. *Magnetohydrodynamics of the Sun*. Cambridge University Press. ix, 3, 140, 142, 143, 144, 145, 146
- Priest, E. R., 2012. *Solar Magnetohydrodynamics*. Geophysics and Astrophysics Monographs. Springer Netherlands. 4
- Rädler, K.-H., 2007. Mean-field dynamo theory: Early ideas and today's problems. In: S. Molokov and R. Moreau and K. Moffatt, eds., *Magnetohydrodynamics: Historical Evolution and Trends*, pp. 55–72. Springer Netherlands, Dordrecht. 140
- Rädler, K.-H. and Bräuer, H.-J., 1987. On the Oscillatory Behaviour of Kinematic Mean-Field Dynamos. *Astron. Nachr.*, 308(2), pp.101–109. 137
- Robinson Jr., R. D., 1980. Magnetic Field Measurements on Stellar Sources - A New Method. *Astrophys. J.*, 239, pp.961–967. 145
- Rogava, A. D., Poedts, S., and Mahajan, S. M., 2000. Shear-Driven Wave Oscillations in Astrophysical Flux Tubes. *Astron. Astrophys.*, 354, pp.749–759. 65
- Ruzmaikin, A. and Feynman, J., 2001. Strength and Phase of the Solar Dynamo during the last 12 Cycles. *J. Geophys. Res. Space Phys.*, 106(A8), pp.15783–15789. 137
- Ruzmaikin, A. A., Shukurov, A. M., and Sokoloff, D. D., 1988. *Magnetic Fields of Galaxies*. Astrophysics and Space Science Library. Springer. 6

- Schad, A., Timmer, J., and Roth, M., 2013. Global Helioseismic Evidence for a Deeply Penetrating Solar Meridional Flow Consisting of Multiple Flow Cells. *Astrophys. J. Lett.*, 778, pp.L38. 145
- Schatzman, E., Zahn, J.-P., and Morel, P., 2000. Shear Turbulence beneath the Solar Tachocline. *Astron. Astrophys.*, 364, pp.876–878. 33
- Schekochihin, A. A., Cowley, S. C., Taylor, S. F., Maron, J. L., and McWilliams, J. C., 2004. Simulations of the Small-Scale Turbulent Dynamo. *Astrophys. J.*, 612(1), pp.276. 138
- Schmieder, B., Aulanier, G., and Török, T., 2008. Solar prominences. *Proc. Int. Astron. Union*, 4(S257), pp.223–232. 4
- Schochet, S., 1994. Fast Singular Limits of Hyperbolic PDEs. *J. Differ. Equations*, 114(2), pp.476–512. 51
- Schrinner, M., Petitdemange, L., and Dormy, E., 2011. Oscillatory Dynamos and their Induction Mechanisms. *Astron. Astrophys.*, 530, pp.A140. 137
- Schubert, G. and Zhang, K., 2000. Spherical Oscillatory α^2 Dynamo Induced by Magnetic Coupling between a Fluid Shell and an Inner Electrically Conducting Core: Relevance to the Solar Dynamo. *Astrophys. J. Lett.*, 532, pp.L149–L151. 137
- Scinocca, J. F., 1995. The Mixing of Mass and Momentum by Kelvin-Helmholtz Billows. *J. Atmos. Sci.*, 52, pp.2509 – 2530. 80
- Shizgal, B., 2015. *Spectral Methods in Chemistry and Physics*. Springer. 27
- Silvers, L. J., 2008. Long-term Nonlinear Behaviour of the Magnetorotational Instability in a Localized Model of an Accretion Disc. *Mon. Not. R. Astron. Soc.*, 385(2), pp.1036–1044. 42
- Silvers, L. J., 2008. Magnetic fields in astrophysical objects. *Phil. Trans. R. Soc. A*, 366, pp.4453–4464. 6, 33, 104, 138

- Silvers, L. J., Bushby, P. J., and Proctor, M. R. E., 2009a. Interactions between Magnetohydrodynamic Shear Instabilities and Convective Flows in the Solar Interior. *Mon. Not. R. Astron. Soc.*, 400, pp.337–345. 25, 61, 97, 164
- Silvers, L. J., Vasil, G. M., Brummell, N. H., and Proctor, M. R. E., 2009b. Double-Diffusive Instabilities of a Shear-Generated Magnetic Layer. *Astrophys. J. Lett.*, 702, pp.L14–L18. 61, 65, 67, 101
- Smyth, W. D. and Moum, J. N., 2000. Anisotropy of turbulence in stably stratified mixing layers. *Phys. Fluids*, 12(6), pp.1343–1362. 8, 65
- Smyth, W. D. and Winters, K. B., 2003. Turbulence and Mixing in Holmboe Waves. *J. Phys. Oceanogr.*, 33, pp.694–711. 8, 65
- Solanki, S. K., 2003. Sunspots: An overview. *Astron. Astrophys. Rev.*, 11(2), pp.153–286. 4, 6
- Soward, A. M., Jones, C. A., Hughes, D. W., and Weiss, N. O., 2005. *Fluid Dynamics and Dynamos in Astrophysics and Geophysics*. The Fluid Mechanics of Astrophysics and Geophysics. CRC Press. 12, 143, 144
- Spiegel, E. A. and Veronis, G., 1960. On the Boussinesq Approximation for a Compressible Fluid. *Astrophys. J.*, 131, pp.442. 18
- Spiegel, E. A. and Weiss, N. O., 1980. Magnetic Activity and Variations in Solar Luminosity. *Nature*, 287, pp.616. 143
- Spiegel, E. A. and Zahn, J.-P., 1992. The solar tachocline. *Astron. Astrophys.*, 265, pp.106–114. 5, 105
- Squire, H. B., 1933. On the Stability for Three-Dimensional Disturbances of Viscous Fluid Flow between Parallel Walls. *Proc. R. Soc. A*, 142(847), pp.621–628. 37, 69
- Steenbeck, M., Krause, F., and Rädler, K.-H., 1966. Berechnung der Mittleren Lorentz-Feldstärke $\overline{\mathbf{b} \times \mathbf{B}}$ für ein Elektrisch Leitendes Medium in Turbulenter, durch Coriolis-Kräfte beeinflusster Bewegung. *Z. Naturforsch. A*, 21, pp.369. 140
- Stein, R. F. and Nordlund, Å., 2006. Solar Small-Scale Magnetoconvection. *Astrophys. J.*, 642, pp.1246–1255. 141

- Stello, D., Cantiello, M., Fuller, J., Huber, D., García, R. A., Bedding, T. R., Bildsten, L., and Aguirre, V. S., 2016. A Prevalence of Dynamo-Generated Magnetic Fields in the Cores of Intermediate-Mass Stars. *Nature*, 529(7586), pp.364–367A. 145
- Sturrock, P. A., 1985. *Physics of the Sun: Volume I: The Solar Interior*. Geophysics and Astrophysics Monographs. Springer Netherlands. 3
- Subramanian, K., Shukurov, A., and Haugen, N. E. L., 2006. Evolving Turbulence and Magnetic Fields in Galaxy Clusters. *Mon. Not. R. Astron. Soc.*, 366, pp.1437–1454. 137
- Sundberg, T., Boardsen, S. A., Slavin, J. A., Blomberg, L. G., and Korth, H., 2010. The Kelvin-Helmholtz Instability at Mercury: An Assessment. *Planet. Space Sci.*, 58(11), pp.1434 – 1441. 34
- Tailleux, R., 2013. Irreversible Compressible Work and Available Potential Energy Dissipation in Turbulent Stratified Fluids. *Phys. Scripta*, 2013(T155), pp.014033. 83, 84
- Thompson, M. J., Toomre, J., Anderson, E. R., Antia, H. M., Berthomieu, G., Burtonclay, D., Chitre, S. M., Christensen-Dalsgaard, J., Corbard, T., DeRosa, M., Genovese, C. R., Gough, D. O., Haber, D. A., Harvey, J. W., Hill, F., Howe, R., Korzennik, S. G., Kosovichev, A. G., Leibacher, J. W., and Pijpers, F. P., 1996. Differential Rotation and Dynamics of the Solar Interior. *Science*, 272(5266), pp.1300–1305. 104
- Thorpe, S. A., 1987. Transitional Phenomena and the Development of Turbulence in Stratified Fluids: A Review. *J. Geophys. Res. Oceans*, 92(C5), pp.5231–5248. 80
- Tobias, S. M., 1996. Diffusivity Quenching as a Mechanism for Parker’s Surface Dynamo. *Astrophys. J.*, 467, pp.870. 142
- Tobias, S. M., 2004. The solar tachocline: Formation, stability and its role in the solar dynamo. In: A. M. Soward, C. A. Jones, D. W. Hughes, and N. O. Weiss,

- eds., *Fluid Dynamics and Dynamos in Astrophysics and Geophysics*, pp. 193–234. CRC. 5, 33
- Tobias, S. M., Brummell, N. H., and Toomre, J., 2001. Magnetic Pumping at the Base of the Solar Convection Zone. In: Brekke, P., Fleck, B., and Gurman, J. B., eds., *Recent Insights into the Physics of the Sun and Heliosphere: Highlights from SOHO and Other Space Missions*, volume 203 of *IAU Symposium*, p. 156. 144
- Tobias, S. M., Cattaneo, F., and Boldyrev, S., 2011a. MHD Dynamos and Turbulence. *ArXiv e-prints*. 138
- Tobias, S. M., Cattaneo, F., and Brummell, N. H., 2008. Convective Dynamos with Penetration, Rotation, and Shear. *Astrophys. J.*, 685, pp.596–605. 164
- Tobias, S. M., Cattaneo, F., and Brummell, N. H., 2011b. On the Generation of Organized Magnetic Fields. *Astrophys. J.*, 728, pp.153. 141
- Tobias, S. M. and Hughes, D. W., 2004. The Influence of Velocity Shear on Magnetic Buoyancy Instability in the Solar Tachocline. *Astrophys. J.*, 603, pp.785–802. 42, 49
- Väisälä, V., 1925. Über die Wirkung der Windschwankungen auf pilot Beobachtungen. *Soc. Sci. Fennica, Commentations Phys. Math II*, 2. 87
- Vasil, G. M. and Brummell, N. H., 2008. Magnetic Buoyancy Instabilities of a Shear-Generated Magnetic Layer. *Astrophys. J.*, 686(1), pp.709. 43, 65, 101, 164
- Vasil, G. M. and Brummell, N. H., 2009. Constraints on the Magnetic Buoyancy Instabilities of a Shear-Generated Magnetic Layer. *Astrophys. J.*, 690(1), pp.783. 79, 101, 105
- Vainshtein, S. I. and Zel'dovich, Y. B., 1972. Reviews of Topical Problems: Origin of Magnetic Fields in Astrophysics (Turbulent “Dynamo” Mechanisms). *Sov. Phys. Usp.*, 15, pp.159–172. 139
- Vazza, F., Brüggem, M., Gheller, C., and Wang, P., 2014. On the Amplification of Magnetic Fields in Cosmic Filaments and Galaxy Clusters. *Mon. Not. R. Astron. Soc.*, 445, pp.3706–3722. 137

- Vöglér, A. and Schüssler, M., 2007. A Solar Surface Dynamo. *Astron. Astrophys.*, 465, pp.L43–L46. 141
- Wang, Y.-M., Sheeley Jr., N. R., and Nash, A. G., 1991. A New Solar Cycle Model including Meridional Circulation. *Astrophys. J.*, 383, pp.431–442. 145
- Weiss, N. O., 2010. Solar and stellar dynamos. *Proc. Int. Astron. Union*, 6(S271), pp.247–260. 142, 144
- Weiss, N. O. and Proctor, M. R. E., 2014. Basic MHD. In: *Magnetoconvection*, pp. 9–37. Cambridge University Press, Cambridge. 137, 156
- Weiss, N. O. and Tobias, S. M., 2000. Physical causes of solar activity. *Space Sci. Rev.*, 94(1), pp.99–112. 145
- Wesseling, P., 2009. *Principles of Computational Fluid Dynamics*, Chapter 1. Springer Series in Computational Mathematics. Springer Berlin Heidelberg. 14
- Winters, K. B., Lombard, P. N., Riley, J. J., and D’Asaro, E. A., 1995. Available Potential Energy and Mixing in Density-Stratified Fluids. *J. Fluid Mech.*, 289, pp.115–128. 83
- Witzke, V., Silvers, L. J., and Favier, B., 2015. Shear Instabilities in a Fully Compressible Polytropic Atmosphere. *Astron. Astrophys.*, 577, pp.A76. 129, 135
- Wright, N. J. and Drake, J. J., 2016. Solar-type Dynamo Behaviour in Fully Convective Stars without a Tachocline. *Nature*, 535(7613), pp.526 – 528. 147
- Yu, H., 2015. Spectral and High-Order Numerical Methods. [online] Available at: <<http://math.mit.edu/~stevenj/fft-deriv.pdf>> [Accessed: 17 Oct 2016]. 27, 28
- Zahn, J.-P., 1974. Stellar instability and evolution. In: P. Ledoux, A. Noels, A. W. Rodgers, and International Astronomical Union and International Astronomical Union. Commission 27 and International Astronomical Union. Commission 35, eds., *Stellar Instability and Evolution*. Springer. 7, 42, 70, 119, 129
- Zahn, J.-P., 1992. Circulation and Turbulence in Rotating Stars. *Astron. Astrophys.*, 265, pp.115–132. 110

Zeldovich, I. B., Ruzmaikin, A. A., and Sokolov, D. D., 1983. *Magnetic Fields in Astrophysics*, volume 3. New York, Gordon and Breach Science Publishers. 138, 141

Zhao, J., Bogart, R. S., Kosovichev, A. G., Duvall, Jr., T. L., and Hartlep, T., 2013. Detection of Equatorward Meridional Flow and Evidence of Double-cell Meridional Circulation inside the Sun. *Astrophys. J. Lett.*, 774, pp.L29. 145